# The critical current of high temperature superconducting inclined-substrate coated conductors under biaxial strain.

GURNHAM, CHARLES,WILLIAM,ANDREW

**How to cite:**

GURNHAM, CHARLES,WILLIAM,ANDREW (2023) *The critical current of high temperature superconducting inclined-substrate coated conductors under biaxial strain.*, Durham theses, Durham University. Available at Durham E-Theses Online: http://etheses.dur.ac.uk/15171/

# The critical current of high temperature superconducting inclined-substrate coated conductors under biaxial strain.

## Charles William Andrew Gurnham

### Abstract

A new biaxial strain probe which allows *in situ* $x$-strain variation and independent fixed $y$-strains has been commissioned and biaxial strain measurements of critical current density ($J_\mathrm{c}$) of an inclined-substrate high temperature superconducting coated conductor (CC) completed.

The first measurements of the effect of strain on interplanar currents with a $c$-directed component are presented, showing no strong difference in behaviour from $ab$-oriented currents. This indicates the effect of inter-plane coupling on $J_\mathrm{c}$ does not change dramatically with strain at 77 K.

Measurements of $J_\mathrm{c}$ were made using mechanical scribing to reduce the cross section of the CCs. It was shown the decrease in critical current is proportional to the sample width from 12 mm down to 1 mm, enabling higher critical current densities to be measured.

Short samples (12 mm long) were investigated at high currents to enable rotation of samples on the strain board, although current shunting prevented reliable measurements at larger strains.

Calculations of self-field in thin superconducting tapes were made using a Josephson junction model for local $J_\mathrm{c}(B)$, and self-consistent current and field spatial distributions derived, that explain the low-field behaviour of CCs.

A theoretical model for the strain behaviour of CCs is presented which uses single-crystal strain measurements and elastic constants from the literature to calculate $\frac{1}{J_\mathrm{c}(0)}\frac{\mathrm{d}J_\mathrm{c}}{\mathrm{d}\varepsilon}$ for both current and strain along and perpendicular to the tape length on a copper-beryllium sample holder. Qualitative agreement is found between the model values of between +1.0 and -9.2 and between +1.9 and -4.0 for the two geometries considered, compared to experimental measurements of -7.0(3) and -7.6(13) respectively.

The model results suggest crystallographic normal strains determine the strain behaviour of $J_\mathrm{c}$ in CCs in contrast to deviatoric strain that is known to control $Nb_3Sn$. These results suggest different mechanisms operate in these two materials.

Supervisors: Prof. Damian Hampshire, Dr. Mark Raine and Prof. Del Atkinson

# The critical current of high temperature superconducting inclined-substrate coated conductors under biaxial strain.

**Charles William Andrew Gurnham**

A thesis presented for the degree of
*Doctor of Philosophy*

Department of Physics
Durham University
2023

# Contents

# List of Abbreviations

| | | |
|---|---|---|
| **APC** | artificial pinning centre | 11 |
| **BCS** | Bardeen-Cooper-Schrieffer | 17 |
| **CC** | coated conductor | 2 |
| **DFT** | density functional theory | 36 |
| **DT** | deuterium-tritium | 8 |
| **EBPVD** | electron-beam physical vapour deposition | 30 |
| **FEA** | finite element analysis | 49 |
| **Fusion CDT** | EPSRC centre for doctoral training in the science and technology of fusion energy | 127 |
| **GL** | Ginzburg-Landau | 17 |
| **HLW** | high level waste | 9 |
| **HTS** | high temperature superconductor | 1 |
| **IBAD** | ion-beam assisted deposition | 30 |

|  |  |  |
|---|---|---|
| **ICF** | inertial confinement fusion | 7 |
| **ILW** | intermediate level waste | 8 |
| **ISD** | inclined-substrate deposition | 31 |
| **JJ** | Josephson junction | 17 |
| **LHC** | large hadron collider | 4 |
| **LTS** | low temperature superconductor | 1 |
| **MCF** | magnetic confinement fusion | 5 |
| **MOCVD** | metalorganic chemical vapour deposition | 30 |
| **MRI** | magnetic resonance imaging | 4 |
| **PLD** | pulsed laser deposition | 30 |
| **PPMS** | physical properties measurement system | 47 |
| **RCE-DR** | reactive co-evaporation by deposition and reaction | 30 |
| **RF** | radio frequency | 14 |
| **STEM** | scanning transmission electron microscopy | 91 |
| **SQUID** | superconducting quantum interference device | 13 |

# Declaration

The work in this thesis is based on research carried out at Durham University Superconductivity Group, Department of Physics, University of Durham, England. No part of this thesis has been submitted elsewhere for any other degree or qualification, and it is the sole work of the author unless referenced to the contrary in the text.

Some of the work presented in this thesis has been previously published in journals [1, 2] and presented at conferences - the relevant publications and conferences are listed below.

## Publications

Self-field effects in a Josephson junction model for $J_\mathrm{c}$ in REBCO tapes, C W A Gurnham and D P Hampshire; *IEEE Trans. Appl. Supercond.* **32**(4) 8000205 (2022)

Angular $J_\mathrm{c}$ measurements at 77 K in-field, on an ISD REBCO coated conductor using a straightforward mechanical scribing technique to reduce tape width, C W A Gurnham, V Große and D P Hampshire; *J. Phys.: Conf. Ser.* **1559** 012036 (2020)

## Conference Presentations

Self-field effects in a Josephson junction model for $J_c$ in REBCO tapes (Poster), C W A Gurnham and D P Hampshire, EUCAS 2021, Virtual (September, 2021)

Angular measurements of $J_c$ in ISD coated conductors with mechanical scribing to reduce cross-section (Poster), C W A Gurnham, V Große and D P Hampshire, EUCAS 2019, Glasgow, UK (September, 2019)

The strain dependence of critical current density in superconducting REBCO coated superconductors (Poster), C W A Gurnham and D P Hampshire, CCFE PhD Showcase, Culham, UK (July, 2019)

The strain dependence of critical current density in REBCO high temperature superconductors (Poster), C W A Gurnham and D P Hampshire, Frontiers of Fusion, York, UK (May, 2019)

*3rd September 2023*

Charles William Andrew
Gurnham

# Statement of Copyright

# Acknowledgements

I would like to thank my supervisory team, Damian Hampshire, Mark Raine and Del Atkinson for all their support, expertise and wisdom guiding me through this PhD. Thanks to all of my fellow group members over my time in Durham: Alex Blair, Jack Greenwood, Andy Smith, Simon Chislett-McDonald, Adel Nader, Brad Din, Charles Haddon, Emma Gillard, Rollo Hutson and Daniel Scobbie for many interesting and fruitful discussions. Particular thanks to Jack and Mark for their help with experimental work, getting me up to speed in the lab and helping to trouble shoot on the many occasions where something was not working as expected. I would also like to thank my friends and family for their support during these particularly difficult years, helping me to get through multiple lockdowns and many other difficult times while working on this PhD.

I would like to thank Veit Große from THEVA Dünnschichttechnik GmbH for the supply of the coated conductor samples measured in this work.

This work is funded by EPSRC grant EP/L01663X/1 that supports the EPSRC Centre for Doctoral Training in the Science and Technology of Fusion Energy. Data and supporting material can be found at `http://doi:10.15128/r2f4752g77z`.

Chapter 1

# Introduction

## 1.1 Background

Superconductors have a wide range of technological and scientific applications and enable a number of technologies. Superconductors are often used as the current-carrying material in high-performance electromagnets, but they can also be used for power transmission as well as other applications which exploit key features of superconductivity such as their highly non-linear current-voltage relationship.

Superconductors have been known about for over a century and have been used in technological applications for several decades now, and more superconducting materials continue to be discovered. The specific superconducting material which has been measured in this thesis is a rare-earth barium copper oxide (REBCO), a class of high temperature superconductors (HTS) which was discovered in the 1980s. Due to practical challenges in manufacture (discussed in section 4.1.1), high-quality long lengths of the material have only been available more recently, and a better understanding of them is still needed before REBCO becomes used as widely as the more technologically mature low temperature superconductors (LTS) such as NbTi and $Nb_3Sn$.

Some key benefits of REBCO (which also apply some other HTS materials such as BiSCCO) over LTS are use in much stronger magnetic fields [3], and at higher temperatures. The current densities can in principal be much higher than LTS materials as well, although in practice more additional material is required in practical conductors, both for mechanical support and for electrical and thermal stability, so the overall ‘engineering’ current density may not be significantly better than high-performance LTS. A high magnetic field is particularly useful when building strong superconducting magnets. The possibility to operate at higher temperatures is also useful in some situations to reduce the cooling requirements. For many applications, however, HTS would still be used at low temperatures of 10 K and below, as the possible magnetic field and current density is higher at low temperatures.

Chapter 2 covers some of the key applications of superconductors, outlining many of the current applications and some exciting future applications, with a particular focus on the role of superconductors for nuclear fusion reactors. Chapter 3 gives a general overview of superconductivity and some of the key theoretical tools used to understand

and describe their critical properties and behaviour. Chapter 4 looks in more detail at coated conductors (CCs), providing a review of the relevant existing literature for the work undertaken in this thesis.

The later sections of the thesis contain the new experimental and theoretical results. In chapter 5, a design and prototype for a miniaturised strain applicator for resistivity measurements is outlined. Chapter 6 describes the experimental apparatus and modifications made for transport current measurements, and presents some characterisation and other preliminary measurements. Chapter 7 describes theoretical work undertaken to explain the behaviour of CCs in low applied fields, using numerical calculations and comparisons to experimental data. Chapter 8 includes the strain measurements made on CCs and measurements on interplanar currents. Also in chapter 8 is a model to explain the strain behaviour of CCs in more detail using data from single-crystal measurements. Comparisons are made to different tape architectures which provide different constraints on the model for strain response. Finally, in chapter 9, possible avenues for future work to continue and build on the findings of this thesis are presented.

Chapter 2

# Applications

## 2.1 Introduction

Superconductors are a key enabling technology for a wide range of applications. These applications are significant motivators for research to better categorise and improve the performance of superconductors. This chapter outlines some of the applications for superconductors which provides context and motivation for the work presented in this thesis. High temperature superconductors (HTS) are particularly exciting materials, which are now possible to manufacture in long lengths but are yet to be used in a number of key applications of superconductivity. By better understanding their properties, HTS can be used in applications to increase the current density, operating field and/or operating temperature compared to LTS. This often has significant advantages, either by increasing the performance or reducing the operating cost of the application.

## 2.2 Superconducting magnet applications

### 2.2.1 Research magnets

Resistive high-field electromagnets have a high energy consumption due to the Ohmic losses from the large currents needed to reach a high magnetic field. This means that superconducting magnets can be much cheaper to operate, particularly if a magnetic field needs to be sustained for a long period. For this reason, many universities and national research facilities use superconducting magnets to generate the large fields needed for some areas of scientific research. Here in Durham, we have a 17 T vertical superconducting magnet and a 15 T split-pair horizontal magnet with a $Nb_3Sn$ coil [4]. International high-field facilities have even stronger superconducting magnets, such as the 25 T cryogen-free superconducting magnet in Sendai, Japan [5] and a 32 T magnet in Tallahassee, USA [6]. Superconducting coils can also be combined with resistive coils to create hybrid magnets, such as the 45 T hybrid magnet in Tallahassee, USA [7].

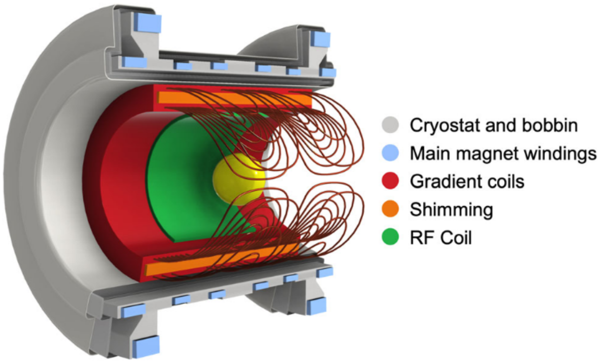

Figure 2.1: Cross-section of an MRI scanner showing the superconducting magnet coils. The patient lies in the centre of the bore, with the measurement region shown in yellow. Figure from [12].

### 2.2.2 Particle accelerators

A major research application of superconducting magnets is in particle accelerators. The magnets are used to shape the particle beam, and high-energy accelerators like the large hadron collider (LHC) at CERN need a large number of high-field magnets. The superconducting magnets in the LHC are being upgraded from NbTi to $Nb_3Sn$ [8] to increase the magnetic field they can generate for the high-luminosity upgrade to the LHC.

### 2.2.3 MRI

Superconductors are a key enabling technology for magnetic resonance imaging (MRI). MRI scanners need an extremely stable magnetic field for high-resolution imaging [9], which superconductors excel at. The superconducting magnet is in persistent mode, where the zero-resistance of the superconductor allows the electromagnet to be disconnected from the current source and the current to flow without decaying. This removes the small fluctuations generated by any current source, allowing for a much greater degree of magnetic field stability. MRI is a highly effective diagnostic tool for medical care as it can effectively image soft tissues within the human body and it is widely used in hospitals, with just over 3.5 million MRI scans performed in England in the year from November 2021-October 2022 (the most recent period with data published by the NHS) [10]. A cross-section of an MRI scanner is shown in figure 2.1.

The majority of MRI scanners use NbTi, partly due to its ductility. A ductile material is far easier to work with than a brittle one, and NbTi gives the best critical currents and fields of known ductile superconductors. The magnetic fields are typically relatively low in scanners, especially compared to HTS, with magnetic fields above 1 T considered ‘high field’ and 3 T ‘very high field’ [11], so LTS are typically used instead of brittle HTS materials.

## 2.3 Fusion

Fusion reactors are a major upcoming application for superconductors. The largest prototype fusion reactor under construction, ITER, uses primarily $Nb_3Sn$ superconducting magnets, and if many more fusion reactors are built, this would be a major use of superconductors. The primary motivator for use of superconductors in a fusion reactor is the ability to carry large currents with very low resistance. The resistive losses from conventional resistive magnets would significantly increase the recirculating power of a fusion reactor, dramatically decreasing the net power output.

The most technologically mature design for a fusion reactor is the tokamak (a Russian acronym for ‘toroidal chamber with magnetic coils’). A tokamak uses a toroidal cavity with a combination of toroidal and poloidal magnets to contain a plasma. A schematic of the ITER tokamak is shown in figure 2.2.

Magnetic confinement fusion (MCF) devices such as tokamaks require strong magnetic fields that are produced over a large volume. For example ITER provides a $5\,\mathrm{T}$ field in a plasma volume of $840\,\mathrm{m}^3$ [13] and other devices are considering considerably higher field strengths [14, 15], which would require a prohibitive power to use resistive magnets. The quantity of superconductor can be considerable, with 500 tonnes of $Nb_3Sn$ used in ITER [16], and even more needed in larger scale devices. The superconductor could contribute to more than 20% of the electricity cost of a power plant purely from the capital cost of the magnets [17]. The large cost of these magnets is a strong motivation for minimising the quantity of superconductor required, which naturally leads to the requirement for improvements in the critical current density ($J_\mathrm{c}$) of the superconductors.

ITER and several other fusion devices use LTS due to their technological maturity, comparatively low cost and ease of use. However, their relatively low critical fields prevent their use in very high-field applications, for which HTS are needed. In practice, all magnet strands will experience strain, from thermal strains when cooling and from the Lorentz forces from the magnetic fields present. These forces become particularly challenging in high-field compact devices. Understanding the biaxial strain dependence is crucial to magnet design as the operational stress state should be tailored to achieve the maximum possible critical currents, allowing a smaller superconducting cross-section to be used, and a better understanding of how much mechanical support is required to control the strain state.

Charged particles in a magnetic field have a much higher velocity along magnetic field lines than perpendicular to them, which allows for plasma confinement by magnetic fields. Plasma stability can only be achieved with an additional magnetic field in the poloidal direction. This cannot be generated by external magnets in a toroidal configuration, so a plasma current is induced to generate the required magnetic field. This current is typically very large, with MAST (mega-amp spherical tokamak) in Culham named for the MA plasma currents it is designed to generate.

The plasma current is often generated by a time varying magnetic field from a central solenoid, which makes the tokamak a pulsed device as the plasma is only contained

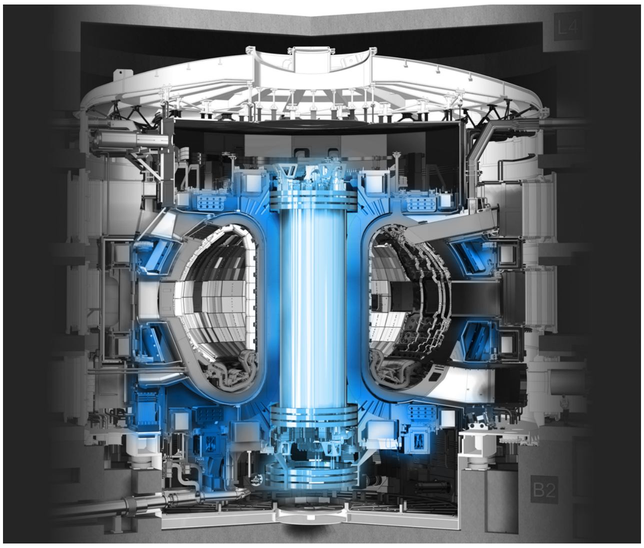

Figure 2.2: Schematic the ITER tokamak, with the magnet systems highlighted in blue. The plasma is contained within the toroidal cavity by the strong magnetic fields generated by the superconducting magnets. Figure from [13].

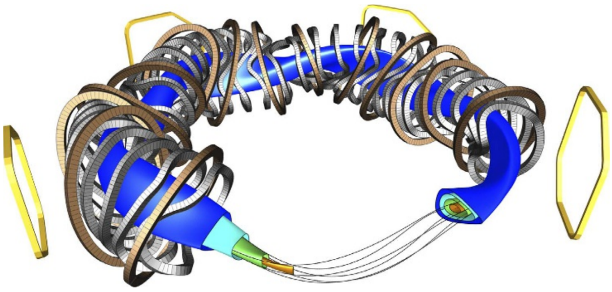

Figure 2.3: Schematic of Wendelstein 7-X, a stellerator. The blue surface is a magnetic field surface, and the silver and bronze-coloured rings are the magnetic field coils. Figure from [18].

while the magnetic field continues ramping in a single direction. To achieve longer pulses or steady state operation, an alternative method to generate the current is required. Contributions to this current can come from neutral beam injection and so-called ‘bootstrap currents’, but careful control of the plasma is required to reach long pulse-lengths.

An alternative to the inherent instability of tokamaks is to design a more complicated geometry where the required magnetic field configuration is generated by steady-state magnets. This is known as a stellerator, and the largest example of this is Wendelstein 7-X in Greifswald, Germany. The cylindrical symmetry of the tokamak is broken, and both the design and construction of a stellerator is considerably more complicated than for a tokamak (see figure 2.3 for the design of a stellerator), although in principal the plasma stability can be better than for a tokamak.

Both tokamaks and stellerators are examples of MCF, but other methods of plasma confinement are also possible. Gravitational confinement, which occurs in the sun, is not feasible on earth, but inertial confinement could be used.

The principle of inertial confinement fusion (ICF) is to use an imploding plasma to reach sufficiently temperatures that fusion reactions occur and sufficiently high densities that the $\alpha$-particles created collide with unreacted fuel at a high enough rate to maintain the fusion reaction. The high pressure present in the high density reacting region means that the reaction is only on very short timescales, but a relatively large amount of energy can be released in this time.

Thermonuclear warheads operate on the same basic principle as ICF, with a fissile nuclear explosion producing X-rays that compress the fusion fuel to the required density for significant burn-through [19]. The fusion reaction both contributes directly to the total yield of the weapon and acts as a source of energetic neutrons which can further increase the fissile yield. While thermonuclear weapons remain to date the only fusion devices which produce net energy, they are hardly practical for electricity generation. At the national ignition facility (NIF) in the USA, a large number of high-power lasers are used to generate the required densities. NIF recently announced a milestone of more energy produced than was delivered by the laser light to the target, indicating that ignition has been achieved [20]. However, the energy produced (3.15 MJ) is much lower than the total energy required to drive the experiment (322 MJ), primarily because the lasers used are only about 1% efficient. While the research on ICF is in large part driven by nuclear weapons research, ICF is sometimes presented as a potential future energy source.

### 2.3.1 Nuclear fusion within the energy sector

Nuclear fusion is a high-energy-density and low-carbon energy source, which makes it, like fission, potentially very attractive and often discussed in the context of decarbonisation to tackle climate change.

Anthropogenic climate change is possibly the greatest threat facing our planet and our species - we are already at 1.09 K of warming compared to the 1850-1900 average [21] due to greenhouse gas emissions since the industrial revolution, which are in large part from ‘fossil fuels’ burned for heating, transport and electricity generation. We are already seeing the adverse effects of the climate emergency, with deadly heatwaves and other extreme weather events happening more frequently. Indeed, here in Durham in July 2022 the local all-time temperature record was exceeded by an astonishing 4 K [22].

Globally, we are continuing to burn fossil fuels faster than ever before and if we fail to curb emissions or worse continue to increase global consumption, the consequences will be catastrophic, with widespread ecological collapse and the worst human effects felt by those living in the historically (and currently) exploited regions near the equator. The worst case scenario considered in the IPCC 2022 report [21], SSP5-8.5 or ‘fossil-fuelled development’ where fossil fuels continue to be used to drive economic growth predicts a warming of 4.5 K by 2100, and an upper bound of 7.2 K.

Rapid global political action is essential if we are to avert these catastrophic consequences. We need to simultaneously change the makeup of our energy sources and dramatically reduce overall energy consumption, particularly in regions such as Europe and North

America with exceptionally high per-capita emissions and disproportionate contributions to historical carbon emissions.

To achieve rapid decarbonisation, proven technologies are required that can be deployed at scale immediately, so technologies that will not be viable within a few decades at the latest should not be considered part of a realistic climate change strategy.

Fusion research promotes itself as a source of ‘safe, non-carbon emitting and virtually limitless energy’ [13], but does not meet the criteria for a widespread rapid implementation of the sort that is likely to be required to mitigate the worst effects of climate breakdown. This means that fusion energy is not a solution to climate change and significant structural, societal and economic change is required instead. Fusion is only likely to play a significant role in our energy landscape in the more distant future when we (hopefully) already have majority low-carbon energy production.

### 2.3.2 Fusion and fission

Deuterium-tritium (DT) fusion reactions have the largest reactivities and fusion cross-sections of viable fusion reactions except at extremely high temperatures ($< 10^{10}$ K) [23]. A key threshold for viable fusion reactions is for the heating from fusion reactions to exceed the radiative losses from the plasma so the fusion reaction is self-sustaining. This condition is much harder to achieve from reactions other than DT in low-density plasmas such as those typical in MCF. In higher density plasmas, this threshold can be exceeded but a change to a fusion reaction with lower reactivity still significantly increases the confinement requirements of the device.

DT fusion produces an alpha particle and a neutron and an energy yield of 17.6 MeV. As the lighter product, the majority of this energy (14.1 MeV) is carried by the neutron.

The fusion plasma is largely transparent to these neutrons, so they reach the walls of the device and are the primary source of heating the coolant from which electricity would be generated. Unfortunately these neutrons also cause significant damage to any component near the plasma, both by displacing atoms and through transmutation. Displaced atoms in particular degrade the physical properties of structural materials, leading to embrittlement and a finite lifetime. Transmutation can affect structural properties, but most critically creates radioactive isotopes which cause problems for maintenance and disposal.

EU-DEMO, which is conceived as a prototype fusion powerplant to be constructed in the second half of this century, is predicted to generate approximately 7000 t of intermediate level waste (ILW) [24], of which 3000 t remains ILW after 100 years and approximately 1000 t after 1000 years, although with more variation between designs considered at longer times.

For comparison, the projected ILW generated on shutdown of the new Hinkley C reactor is 3000 t [25], which is approximately 0.15 t/GWhe for the 60 year lifetime of the plant, where the e denotes electrical energy to the grid rather than thermal energy produced. While EU-DEMO is not expected to output energy to the grid, we can estimate the equivalent figure using a 200 MWe output to give roughly 10 t/GWhe, a factor of 70 worse than Hinkley C. While future designs may have a lower recirculating power than has been assumed here, and improved materials or structural design to reduce activation, there is a lot of improvement needed to achieve an equivalent ILW production to existing fission reactors. It is important to note that fission reactors do produce significantly more high level waste (HLW) than fusion reactors, mostly in the form of spent fuel rods. While the near absence of HLW is undoubtedly favourable for fusion, ILW is still categorised as highly activated, with the distinction being that HLW requires heat management to be considered for storage. Any long-lived ILW or HLW will require disposal in a dedicated storage facility, preferably a deep geological disposal facility or similar that does not require any active management. Geological storage is currently employed for low level waste (LLW) and ILW at several sites. For HLW, the waste isolation pilot plant, USA, only stores nuclear weapons waste and not power plant waste [26]. Other facilities have been proposed, such as Cigéo in France [27].

Fusion researchers have stated a goal of no ILW after 100 years [13], on the basis that it is politically acceptable to manage near-surface waste facilities on this time frame. For longer timescales, relying on political stability or potentially even continued knowledge of the nature of the waste becomes less viable, so a storage facility which is filled and shut permanently, inaccessible from the surface, stable to tectonic activity and far below ground-water level is required. Once we have constructed such a facility for our existing nuclear waste, it would likely be the best repository for long-lived fusion waste as well, so the volume of ILW produced is significant for the capacity required in such a facility.

Low-activation steels such as EUROFER are designed to mitigate the long-lived waste, but at present the carbon-14 produced from nitrogen and carbon in the steel is at too high concentrations to qualify as low level waste [24].

Nuclear fusion is primarily competing with fission as a high density, low carbon fuel which could deliver predictable and continuous power. The key advantages for fusion are the lack of extremely long-lived HLW, the stronger safety case and fission's risk of nuclear proliferation from its reliance on uranium enrichment.

Fission is unlikely to make significant improvements on proliferation resistance in the medium term, but there are designs which use a significantly higher proportion of the fuel and can burn the fission products as well. Known as fast reactors, these could significantly reduce the quantity of long-lived HLW produced [28]. Given the long time frame for fusion to deployed at scale, the relevant comparison is to these advanced concept fission reactors, generally labelled as Gen-IV.

Fusion is intrinsically safe to runaway reactions as the reaction conditions are so specific and hard to maintain that a disruption to operations would instead lead to plasma collapse. The biggest safety concern for a fusion reactor is likely a loss of tritium containment. As a hydrogen isotope, tritium can easily displace hydrogen atoms in water and organic compounds, which makes it extremely dangerous if it is released into the environment and comes into contact with water, with a median lethal dose of $T_2O$ being 0.6 mg and much lower if aerosolised [29].

The comparison to fission is not a conclusive one on radiation. The absence of extremely long-lived HLW is certainly an advantage over existing fission reactors, but may not be such a great advantage compared to fast-reactors at a similar level of technological maturity.

A widespread implementation of fusion power would require either a long-term irradiated waste disposal facility, or to tolerate more highly activated waste in our existing facilities than is currently permitted by regulation in the UK.

## 2.4 Superconductors in a fusion environment

Superconducting magnets will be exposed to harsh conditions in fusion reactors, predominantly from the 14.1 MeV neutrons produced in the DT reaction. In present test reactors, the neutron dose is negligible compared to projected energy-producing tokamaks, even in the limited number of machines which run on DT. There is almost no operational experience of superconductors in an irradiated environment, so the community are forced at present to rely on fission neutron or ion irradiation experiments to understand how a fusion magnet would behave in practice.

### 2.4.1 NbTi

NbTi is found to have a very small drop in critical temperature ($T_\mathrm{c}$) on irradiation and a shallow decrease in critical current, leading to a degradation in performance but typically by less than 10% over ITER lifetime fluence [30, 31], although Topchishvili & Naskidashvili [32] find that the radiation resistance is dependent on wire design, with a factor of two decrease in $J_\mathrm{c}$ after similar fluences seen in multiwires, explained by contamination from matrix atoms displaced by irradiation. The drop in $J_\mathrm{c}$ is explained by Weber [30] to be from neutron cascades disturbing the near-optimum existing pinning site distribution from Titanium precipitates.

Parkin & Sweedler [33] report only a 20% decrease in $J_\mathrm{c}$ after irradiation of $10^{24}\,\mathrm{m}^{-2}$, two orders of magnitude more than ITER's design lifetime. Both $Nb_3Sn$ and REBCO, discussed in subsequent sections, become completely unuseable well before this limit, so NbTi looks ideal for use in high-radiation environments. While comparatively small, the drop does need to be considered as an extra ~10% wire area may be needed to ensure continued functioning later in the plant lifetime. The relatively small drop in performance makes NbTi an attractive superconducting material for irradiated applications.

### 2.4.2 $Nb_3Sn$

A number of studies [33, 34, 35, 36, 37, 38] find an increase in $J_\mathrm{c}$ upon initial irradiation, up to $\mathcal{O}(10^{22})\ \mathrm{m}^{-2}$ neutrons, with the specific value varying possibly due to differing manufacturing methods and initial defect concentration. The increased disorder from neutron cascades decreases the critical temperature [30, 34, 38, 39] decreasing low field/high temperature critical currents.

The pinning mechanism in un-irradiated $Nb_3Sn$ is predominantly from grain boundaries, so the point-defects introduced by neutron cascades change the pinning mechanism and correspondingly the form of the pinning force, seen by [40]. As the majority of grain boundaries are unaffected by neutron damage (at fluences of interest), the additional pinning from cascades is a stronger effect than disruption of grain-boundary pinning.

More recent studies, such as Baumgartner *et al.* [41] and Nishimura *et al.* [37] find higher fluences can be reached before performance drops compared to earlier samples (increase in $J_c$ up to the maximum 2.5 and $5 \times 10^{22}\,\mathrm{m}^{-2}$ tested respectively), higher than the predicted ITER lifetime and comparable to the projected DEMO lifetime fluence. This implies that performance could be improved by including more artificial defects as the defect concentration remains below optimal well after ITER lifetime fluence, and Baumgartner *et al.* suggest inclusion of $ZrO_2$ precipitates.

After $10^{23} - 10^{24}\ \mathrm{m}^{-2}$ fast neutron fluence [30, 33, 42] the disorder is sufficient to significantly impair superconducting properties and $Nb_3Sn$ ceases to be useable. This sets a minimum limit on shielding in a fusion power plant to have an adequate magnet lifetime.

### 2.4.3 REBCO

Fast neutrons create damage cascades in REBCO of average 2.5 nm diameter with corresponding strain fields $\sim$ 6 nm diameter [43]. Frischhertz finds the defect density and size to be independent of temperature between the two irradiation temperatures used of 5 K and 40 °C, which is promising for the applicability of irradiation studies at room temperature. The coherence length (vortex core diameter) in the *ab*-plane $\sim$ 7 nm at 77 K [43] and smaller at lower temperatures, so neutron cascades are ideal size pinning sites for $B \parallel c$. The effect of an isotropic distribution of neutron cascades is not necessarily isotropic, with Chudy *et al.* [44] finding strong peaks after irradiation. This could be due to interaction with existing defects, and that the coherence length varies with orientation and so the pinning strength from the defects will also vary.

Improvements in performance from radiation damage were noted in early work on single crystals which have particularly stark improvements [45] due to the low density of pinning sites in high purity single crystals. Irradiation damage has been proposed as a mechanism for introducing pinning, such as ion irradiation carried out by Hensel *et al.* [46]. Civale [47] reviews the improvements seen from ion irradiation, which produces columnar defects in the *c*-direction with a similar pinning mechanism to modern BZO artificial pinning centres (APCs), and a consequent increase in $J_c$ when $B$ is parallel to the *c*-axis [48] at high fields, although a reduction in low field performance on increasing irradiation. Columnar pinning sites give an improvement over a range of angles [49] due to the flexibility of fluxons which can pin for a section of their length even when the field is non-parallel. Point defects have no preferred direction so provide greater improvements away from $B \parallel ab$. The different defect geometry and pinning interaction means ion irradiation results are not directly comparable to neutron irradiation damage seen in fission reactors.

Neutron cascades will provide additional pinning sites for $B \parallel ab$, but may also disrupt the CuO chains and decrease intrinsic pinning. Chudy *et al.* [50] and Eisterer *et al.* [51] both find an increase in $J_c$ away from $B \parallel ab$ up to $10^{22}\,\mathrm{m}^{-2}$ on samples without APCs but a decrease at $B \parallel ab$ (at 77 & 64 K). This implies that intrinsic pinning is being disrupted, particularly at higher fluence where the drop in $J_c$ with $B \parallel ab$ is considerable over the ITER lifetime. Chudy *et al.* also find a decrease in the transition index, $N$, on neutron irradiation. Emhofer *et al.* [52] similarly saw a drop in *ab*-pinning on irradiation and an increase in *c*-pinning (on a material without APCs). Thermal neutrons were not shielded in this experiment, likely leading to a greater $T_c$ decrease, and vastly changing the results for GdBCO due to the high neutron capture cross section of gadolinium. Nevertheless, the angular dependence in the YBCO results (which should be less affected by thermal neutrons) show the expected increased isotropy of response after irradiation.

Numerous neutron irradiation studies on REBCO tapes [51, 50, 53, 54, 55] show a temperature dependent effect. High temperature performance decreases while low temperature improves, attributed to the drop in $T_c$ from increased disorder. The irreversibility line is very steep near the transition temperature, so any change in $T_c$ will dominate the effect on critical field or $J_c$ at high temperatures. At lower temperatures, an improvement in pinning outweighs the loss from a drop in $T_c$, so better radiation performance is observed at lower operational temperatures.

Performance at low fields is found to worsen while high fields improve [51], attributed to the transition from grain-boundary moderated pinning to in-grain pinning mechanisms. At low fields, where grain-boundaries dominate, the breakdown of grain-boundaries on irradiation is used to explain the observed decrease in $J_c$. At higher fields, the increase in pinning-sites in grains dominates the behaviour, causing an increase in $J_c$ [56]. This is similar to the effect seen by Civale *et al.* [48] with ion irradiation.

Fischer *et al.* [57] see an earlier onset of radiation degradation with $B \parallel c$ in samples with APCs (see figure 2.4), arguing that the neutron cascades act in the same manner as the APCs as pinning defects, with degradation occurring once the critical defect density has been reached. The drop in $T_c$ is not found to be affected by APCs, so the temperature dependence should be equivalent. Jirsa *et al.* [54] similarly find an improvement in performance with radiation for tapes without APCs but a decrease in performance over $2 \times 10^{22}\,\mathrm{m}^{-2}$ in tapes with APCs, although unfortunately do not specify the field direction for the post-irradiation methods so it is not clear which pinning mechanism is affected.

If the samples have artificial spherical pinning sites, these may act in much the same way as a neutron cascade. A well-optimised sample would be expected to decrease performance on irradiation as any extra pinning sites would degrade the existing pinning. The decreased radiation resistance of more technologically advanced samples implies that REBCO tapes for use under irradiation need to be designed with this in mind rather than purely for peak (pristine) performance. Initial defect concentrations below the optimum would be preferable for increased lifetime, and it may be that cylindrical APCs are at optimum density but spherical inclusions are deliberately below the concentration for peak performance.

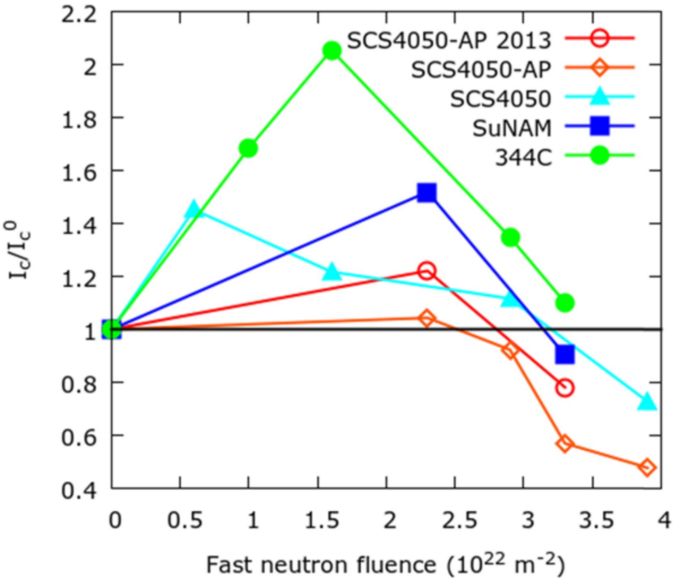

Figure 2.4: The normalised critical current with fast neutron fluence from several REBCO tapes with $B \parallel c$. The tapes with APCs (open shapes) have a lower threshold for the critical current decreasing relative to unirradiated, although their initial $J_c$ is higher than tapes without APCs. Figure from [57].

### 2.4.4 Suppression of superconductivity during irradiation

In addition to a permanent change in the ionic distribution of the REBCO lattice due to irradiation, a temporary electronic disruption is likely to occur in the vicinity of a damage cascade. As the superconducting magnets will see a neutron flux during operation, the degree to which the superconducting state in the conductors is disrupted is critical. A recent study on ion irradiation [58] finds a reduction in the critical current of REBCO by a factor of 3 when the ion beam is switched on compared to after irradiation with the beam off. Unfortunately the authors were not able to directly measure the temperature of the CC, but report that nearby thermometers have much smaller beam heating than would be required to account for the degree of $J_c$ suppression seen. If the effect is indeed not due to beam heating, this is a very significant reduction which if reproduced in a tokamak would require a dramatic change in magnet design. As the authors point out, a neutron will not interact with the superelectrons as strongly as the charged ions used in the measurement, but a neutron interaction creates a large number of knock-on atoms which are charged and may cause a similar reduction in critical current. Further work is needed to determine the effect of irradiation rate, and how neutron irradiation compares to ion experiments.

## 2.5 Other applications

While many applications for superconductors are as the conductor in electromagnets, there are a number of other applications. Some non-magnetic applications use the zero-resistance of superconductors, such as power transmission lines. Other applications use other properties of superconductors, such as fault current limiters, RF-cavities and superconducting quantum interference devices (SQUIDs).

### 2.5.1 Power transmission lines

The zero-resistance of superconductors can be exploited to remove resistive losses present in power transmission cables. Superconducting cables would require energy expenditure to maintain the cryogenic temperatures required for operation, but as the cooling requirements for HTS are much lower than LTS, they can be significantly lower than the resistive losses in large-scale power transmission. Another benefit of superconducting transmission lines is that they are smaller than conventional transmission lines for the same capacity, reducing environmental disruption [59]. As power transmission lines do not operate in a large magnetic field, the self-field behaviour of HTS cables is highly relevant for this application.

### 2.5.2 Fault current limiters

The strongly non-linear $I$-$V$ behaviour of superconductors near a superconducting-normal transition can be exploited for technological applications, such as fault current limiters. A fault current limiter performs the same function as a fuse, but typically for much larger currents. In a superconducting fault current limiter, a superconductor is placed in parallel to a shunt. When a current greater than the critical current of the superconductor is flowing, the superconducting transition causes additional current to flow through the shunt which is designed to dissipate a large amount of energy. Additionally, the heating caused by the transition depresses the critical current in nearby regions of the superconductor, leading to a quench of the whole superconductor and a large proportion of the current flowing through the shunt [60]. By tuning the critical current of the superconductor to the desired operational current, the nonlinear transition is used to remove additional current in the event of a fault or short circuit. This is of particular use in power generation and distribution where large currents are possible in the event of a short circuit.

### 2.5.3 RF cavities

Superconductors are also used to accelerate particles, such as in the radio frequency (RF) cavities in the LHC [61]. An RF source which matches the resonant frequency of the cavity is used to generate large accelerating voltages across the cavity. When a number of cavities are connected in series, this allows for electrons to be accelerated to high energies by the large (MV) electric fields in the cavities. These accelerated electrons can then be injected into the main particle accelerator for a final acceleration up to the maximum beam energy. The resonant cavity also helps with bunching, where particles with too high momentum are decelerated so the beam produced has well controlled momentum. Superconductors are used to construct the cavities as losses are related to the resistance of the cavity material, with higher resistance materials having a deeper skin depth and greater losses. The greater efficiency of superconducting RF cavities more than offsets the increased cooling requirements so they allow for larger beam energies to be reached [62].

### 2.5.4 SQUIDs

SQUIDs make use of the Josephson effect (discussed further in section 3.5) to make extremely sensitive magnetic measurements. The very high sensitivity is ideal for detecting very weak magnetic fields, such as those in biological measurements and for mineral prospecting [63].

## 2.6 Conclusions

Superconductors have a wide range of applications for a number of scientific fields and are an immensely important technology in fields ranging from particle physics to medicine. The main applications of interest for this thesis are electromagnets, such as research magnets, particle accelerators and fusion reactors. These applications are particularly relevant as electromagnets produce strain in the conductor from Lorentz forces, and measurements of the critical parameters with applied magnetic field are most relevant to in-field applications. The calculations on self-field behaviour of superconductors (see chapter 7) will also be relevant to low-magnetic field high current applications such as power transmission lines.

Chapter 3

# Overview of Superconductivity

## 3.1 Introduction

Superconductivity is defined by two key properties: zero electrical resistance and the expulsion of magnetic field. The first of these was discovered by Kamerlingh Onnes [64] who found in 1911 that the electrical resistance of mercury abruptly dropped to zero at 4.2 K. Expulsion of magnetic field was discovered in 1933 by Meissner and Ochsenfeld [65].

Superconductivity has since been discovered in many other metals, notably NbTi (critical temperature 10 K) in 1962 [66], and $Nb_3Sn$ (critical temperature 18 K) in 1954 [67].

These are widely used for technological applications due to their relatively high critical temperatures and fields, with brittle $Nb_3Sn$ used for high-field applications, and NbTi as a ductile material is easier to work with for less demanding applications.

Many theoretical descriptions of superconductivity were proposed in the years following its discovery, such as the 1935 work by London & London [68], but the two most important models were not developed until the 1950s: The Ginzburg-Landau (GL) theory which provides a phenomological description from a field theory of the phase transition [69], and the microscopic description of Bardeen-Cooper-Schrieffer (BCS) theory [70].

BCS theory predicts that superconductors should not exist above approximately 30 K, but materials with significantly higher critical temperatures have been discovered, known as HTS. Wu *et al.* [71] discovered that $YBa_2Cu_3O_{7-\delta}$ (YBCO) is superconducting in 1987, with a critical temperature of 92 K. The cuprate superconductors also include other rare-earth barium copper oxides (REBCO) and $Bi_2Sr_2Ca_{n-1}Cu_nO_{2n+4+x}$ (BSCCO) and other classes of HTS have been discovered since, such as the pnictides discovered to be superconducting in 2006 [72]. Higher critical temperatures have been found at large applied pressures, with a contested [73, 74] record of 217.7(12) K observed in $(H_2S)_{2-x}(CH_4)_xH_2$ at 267(10) GPa [75]. This chapter reviews the London, GL and BCS theories, and a Josephson junction (JJ) model for critical currents.

## 3.2 Ginzburg-Landau theory

GL theory stems from the 1950 paper [69]. The free energy density is expanded as a power series of the complex order parameter, $\psi$:

$$f(\mathbf{r}) = f_n + \alpha|\psi(\mathbf{r})|^2 + \frac{1}{2}\beta|\psi(\mathbf{r})|^4 + \gamma|\nabla\psi(\mathbf{r})|^2. \tag{3.2.1}$$

The equilibrium position is found by minimising this free energy. The $\psi^4$ term is needed with positive $\beta$ to ensure stability of the solution when $\alpha < 0$, as $f \mapsto -\infty$ is unphysical and no bounded minimum exists. Higher terms can be neglected as they do not change the physics at small order parameters. Linear terms in the order parameter are excluded as one can assume the minimum free energy occurs at $\psi = 0$ for $\alpha > 0$, and the solution is symmetric with $\psi$ so terms in $\psi^3$ can be neglected.

The minimum of the free energy occurs at finite $\psi$ when $\alpha < 0$, which we can interpret as a phase transition to a superconducting state, with the temperature at which $\alpha = 0$ being the critical temperature, $T_\mathrm{c}$. For temperatures close to $T_\mathrm{c}$, the temperature dependence of $\alpha$ can be approximated as linear and proportional to $(T - T_\mathrm{c})$, and $\beta$ and $\gamma$ approximated as temperature independent.

As superconductivity is known experimentally to be magnetic-field dependent, magnetic field terms need to be included in the expansion. This is done by making the transformation [76]

$$\nabla \to \nabla - \frac{iq}{\hbar}\boldsymbol{A}, \tag{3.2.2}$$

and including the magnetic energy

$$\frac{\boldsymbol{B}^2}{2\mu_0} - \frac{\mu_0\boldsymbol{H}_0^2}{2} \tag{3.2.3}$$

where the term in $H_0$ describes the magnetic energy of an applied field. The Gibbs free energy density is therefore given by

$$g(\mathbf{r}) = f_n + \alpha|\psi|^2 + \frac{1}{2}\beta|\psi|^4 + \frac{1}{2m}|(-i\hbar\boldsymbol{\nabla} - q\boldsymbol{A})\psi|^2 + \frac{B^2}{2\mu_0} - \boldsymbol{H}_0\cdot\boldsymbol{B} + \frac{\mu_0\boldsymbol{H}_0^2}{2}, \tag{3.2.4}$$

noting that $q$ and $m$ are the charge and effective mass of the charge carriers, which are Cooper pairs, a bound pair of electrons with opposite spins and momenta [70]. A Cooper pair has quantised charge $q = -2e$, noting that the elementary charge, $e$ is always taken to be a positive quantity and has $m = 2m_\mathrm{e}^*$. Some authors explicitly insert $m = 2m_\mathrm{e}^*$, which is a matter of convention.

The GL equations are found by minimising $G = \int g(\mathbf{r})\mathrm{d}^3\mathbf{r}$ using the Euler-Lagrange equations

$$\frac{\partial g}{\partial f} - \sum_j \frac{\partial}{\partial x_j}\frac{\partial g}{\partial(\frac{\partial f}{\partial x_j})} = 0 \tag{3.2.5}$$

for each of the functions $f = \psi$, $\psi^*$ and $\boldsymbol{A}$. The minimisation with respect to $\psi^*$ gives

$$\alpha\psi + \beta|\psi|^2\psi + \frac{1}{2m}(-i\hbar\boldsymbol{\nabla} - q\boldsymbol{A})^2\psi = 0, \tag{3.2.6}$$

known as the 1st GL equation.

The 2nd GL equation is found by minimising with respect to $\boldsymbol{A}$:

$$\boldsymbol{J} = -\frac{iq\hbar}{2m}(\psi^*\nabla\psi - \psi\nabla\psi^*) - \frac{q^2}{m}|\psi^2|\boldsymbol{A}. \tag{3.2.7}$$

Setting $\boldsymbol{A} = \boldsymbol{0}$ in equation 3.2.6 gives

$$\xi^2\nabla^2\psi + \psi + \frac{\beta}{\alpha}|\psi|^2\psi = 0, \qquad \xi = \sqrt{\frac{-\hbar^2}{2m\alpha}}. \tag{3.2.8}$$

By considering the case of a homogeneous superconductor where $\boldsymbol{J} = \boldsymbol{A} = \boldsymbol{0}$, it can be seen that the only non-trivial solution ($\psi \neq 0$) is for $\frac{-\alpha}{\beta} = |\psi|^2$. The quantity $\xi$ is known as the coherence length, which gives the length-scale over which the order parameter varies.

### 3.2.1 The London equations

In the case of a uniform wavefunction ($|\psi(\boldsymbol{r})|^2 = |\psi_0|^2 = -\alpha/\beta$), equation 3.2.7 reduces to:

$$\frac{q^2}{m}|\psi_0|^2\boldsymbol{A} + \boldsymbol{J} = \boldsymbol{0}, \tag{3.2.9}$$

Taking the curl of this equation, and noting that $\nabla \times \boldsymbol{B} = \mu_0\boldsymbol{J}$, and $\nabla \cdot \boldsymbol{B} = 0$ from Maxwell's equations:

$$\frac{q^2}{m}|\psi_0|^2\boldsymbol{B} - \frac{1}{\mu_0}\nabla^2\boldsymbol{B} = \boldsymbol{0} \tag{3.2.10}$$

This can be rewritten as:

$$\nabla^2\boldsymbol{B} = \frac{\boldsymbol{B}}{\lambda^2}, \qquad \lambda = \sqrt{\frac{m}{\mu_0 q^2|\psi_0|^2}}. \tag{3.2.11}$$

with $\lambda$ known as the London penetration depth, first described by London & London in 1935 [68]. This means that the magnetic field inside a superconductor decays with the characteristic length scale $\lambda$, so the superconductor perfectly screens an applied magnetic field for distances much further from the edge than $\lambda$. This field exclusion is known as the Meissner effect, after its discovery by Meissner and Ochsenfeld in 1933 [65].

### 3.2.2 Type-I & type-II superconductors

We consider a superconductor in the Meissner state with a cylindrical region in the normal state running through it. With no applied current, regions much greater than $\lambda$ from the normal region and the edges of the system will have no current through them.

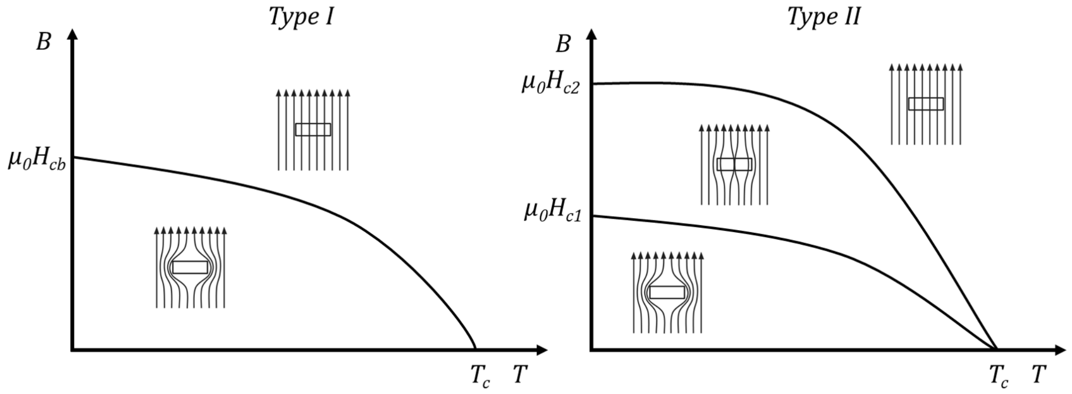

Figure 3.1: A schematic of the $B$-$T$ phase diagram of type-I and type-II superconductors. Figure from [79].

Equation 3.2.7 can be written in terms of a phase:

$$\boldsymbol{J} = \frac{q\hbar}{m}|\psi^2|\boldsymbol{\nabla} S - \frac{q^2}{m}|\psi^2|\boldsymbol{A}. \tag{3.2.12}$$

For a continuous phase, $\oint \boldsymbol{\nabla} S \cdot \mathrm{d}\boldsymbol{l} = 2n\pi,\ n \in \mathbb{Z}$. Performing a closed line integral around the normal region, far enough away that the currents can be neglected, and using Stoke's theorem,

$$\iint_S \boldsymbol{B} \cdot \mathrm{d}\boldsymbol{S} = \frac{2\pi\hbar n}{q}, \tag{3.2.13}$$

which tells us that the magnetic flux through the normal region is quantised. Using $|q| = 2e$, we can define the flux quantum as $\Phi_0 = h/2e = 2.07 \times 10^{-15}\,\mathrm{Wb}$.

The existence of a normal region is energetically favourable if the reduced screening of the applied field, over a volume which scales with $\lambda^2$, outweighs the penalty for creation of the normal state, over a volume which scales with $\xi^2$. A critical parameter is therefore the ratio, $\kappa = \lambda/\xi$. Normal regions within the superconductor become energetically favourable when $\kappa > 1/\sqrt{2}$. Superconductors below this threshold are known as type-I, which only exhibit the Meissner state. Materials with $\kappa > 1/\sqrt{2}$ are type-II, as a mixed state with strings of quantised flux, known as fluxons, can exist. Figure 3.1 shows a schematic phase diagram for these types of superconductor. The vortices present in a type-II superconductor repel each other, so form a 2-D triangular lattice in the absence of microstructural constraints [77]. An energetic consideration shows that vortices with higher multiples of the flux quantum are unfavourable [78].

For a type-I superconductor, we can find an expression for the maximum magnetic field that can be excluded by equating the reduction in free energy from the superconducting state in eq. 3.2.4 to the energy density of the field that would have been present. For the homogeneous, current free case, this condition gives the solution

$$B_\mathrm{c} = \frac{\Phi_0}{2\sqrt{2}\pi\lambda\xi}. \tag{3.2.14}$$

For a type-II superconductor, the critical field at which vortices appear is given by [80]

$$B_{\mathrm{c1}} = \frac{\Phi_0 \ln\kappa}{4\pi\lambda^2}. \tag{3.2.15}$$

The upper critical field, which is the maximum field at which the mixed state is possible is given by

$$B_{\mathrm{c2}} = \frac{\Phi_0}{2\pi\xi^2}. \tag{3.2.16}$$

### 3.2.3 Anisotropic superconductors

Many superconductors, including REBCO, have anisotropic properties. A simple way to modify GL theory to include this anisotropy is to replace the effective mass with a tensor which describes the directional dependence of the effective mass. This approach assumes that local variations in superconducting properties are smaller than the coherence length, which would typically mean that the crystallographic unit cell is smaller than the coherence length.

The London equation (eq. 3.2.11) is modified to [81]

$$\boldsymbol{B} = -\frac{1}{\mu_0 q^2 |\psi_0|^2} \boldsymbol{\nabla} \times (\boldsymbol{m} \cdot (\boldsymbol{\nabla} \times \boldsymbol{B})), \tag{3.2.17}$$

where $\boldsymbol{m}$ is the effective mass tensor. Using a similar modification to the GL equations, an anisotropic coherence length and penetration depth can be defined, and equation 3.2.16 becomes [82]

$$B_{\mathrm{c2},c} = \frac{\Phi_0}{2\pi\xi_{ab}^2} \tag{3.2.18}$$

$$B_{\mathrm{c2},ab} = \frac{\Phi_0}{2\pi\xi_{ab}\xi_c}. \tag{3.2.19}$$

It should be noted that the critical fields are determined by the orthogonal length-scales, $\xi$ and $\lambda$, as the screening currents induced are orthogonal to the applied field.

### 3.2.4 Dimensionless variables

It may be convenient for computation to work with dimensionless variables. An obvious normalisation for a superconducting system would be to normalise length scales to the coherence length, the wavefunction to $\psi_0$ and the magnetic field to $B_{\mathrm{c2}}$. The full list is given in table 3.1. Dimensionless quantities are denoted by a tilde.

From here we can recast the GL equations in dimensionless units:

$$\tilde{\psi}(|\tilde{\psi}|^2 - 1) + (-i\tilde{\boldsymbol{\nabla}} + \tilde{\boldsymbol{A}})^2\tilde{\psi} = 0, \tag{3.2.20}$$

| Description | Definition |
|---|---|
| Position vector | $\boldsymbol{r} = \xi\tilde{\boldsymbol{r}}$ |
| Magnetic flux density | $\boldsymbol{B} = B_{\mathrm{c2}}\tilde{\boldsymbol{B}}$ |
| Order parameter | $\psi = \psi_0\tilde{\psi} = \sqrt{\frac{-\alpha}{\beta}}\tilde{\psi}$ |
| Gradient operator | $\boldsymbol{\nabla} = \frac{1}{\xi}\tilde{\boldsymbol{\nabla}}$ |
| Magnetic vector potential | $\boldsymbol{A} = \frac{\Phi_0}{2\pi\xi}\tilde{\boldsymbol{A}}$ |
| Current density | $\boldsymbol{J} = \frac{\Phi_0}{2\pi\mu_0\kappa^2\xi^3}\tilde{\boldsymbol{J}}$ |
| Relative condensation parameter | $\tilde{\alpha}_{\mathrm{n}} = \frac{\alpha_{\mathrm{n}}}{\alpha_{\mathrm{s}}}$ |
| Relative nonlinearity parameter | $\tilde{\beta}_{\mathrm{n}} = \frac{\beta_{\mathrm{n}}}{\beta_{\mathrm{s}}}$ |
| Relative effective mass | $\tilde{m}_{\mathrm{n}} = \frac{m_{\mathrm{n}}}{m_{\mathrm{s}}}$ |
| Relative 'upsilon' parameter | $\tilde{\Upsilon}_{\mathrm{n}} = \frac{\Upsilon_{\mathrm{n}}}{\Upsilon_{\mathrm{s}}}$ |

Table 3.1: Definition of units used in the normalised GL equations, and normalised normal state properties for Josephson junctions. A subscript s refers to the superconducting material and a subscript n to the normal material in the junction.

$$\tilde{\boldsymbol{J}} = \frac{i}{2}(\tilde{\psi}^*\tilde{\boldsymbol{\nabla}}\tilde{\psi} - \tilde{\psi}\tilde{\boldsymbol{\nabla}}\tilde{\psi}^*) - |\tilde{\psi}|^2\tilde{\boldsymbol{A}}. \tag{3.2.21}$$

In the case where a normal material is present, such as in a JJ (section 3.5), it can be convenient to express the normal region properties in terms of the properties superconducting region. Quantities with a tilde and a subscript n refer to the normal-region and are normalised by the superconducting region's values. These quantities are also listed in table 3.1.

## 3.3 BCS microscopic theory

A detailed microscopic model of superconductivity was first presented by Bardeen, Cooper and Schrieffer in 1957 [70]. The theory is presented here in the language of 'second quantisation', which was not used in the original description but has become widely used since then. BCS theory considers weakly bound spin-singlet pairs of electrons near the Fermi surface, which is sufficient to explain the behaviour of LTS.

One of the key discoveries which prompted the theory was the isotope effect, seen in mercury by Maxwell [83] and Reynolds *et al.* [84], where the critical temperature is sensitive to the mass of the lattice ions. This dependence on ion mass suggests that the superconducting state arises from an electron-phonon interaction since the phonon frequency is mass dependent.

The potential for the interaction where a phonon is emitted by one electron and absorbed by another has the form [85]:

$$V(\mathbf{k},\, \mathbf{k'},\, \mathbf{q}) = \frac{g^2\hbar\omega_{\mathbf{q}}}{(\varepsilon_{\mathbf{k+q}} - \varepsilon_{\mathbf{k}})^2 - (\hbar\omega_{\mathbf{q}})^2}, \tag{3.3.1}$$

which is attractive for $|\varepsilon_{\mathbf{k+q}} - \varepsilon_{\mathbf{k}}| < \hbar\omega_{\mathbf{q}}$. The electron-phonon coupling constant, $g$, needs to be high for this interaction to be strong, so high-temperature resistivity is also expected to be high for metallic superconductors.

Bardeen *et al.* solve a simplified interaction potential

$$V_{\mathbf{kk'}} = \begin{cases} -|g| & |\varepsilon_{\mathbf{k}}| < \hbar\omega_D \text{ and } |\varepsilon_{\mathbf{k'}}| < \hbar\omega_D \\ 0 & \text{otherwise.} \end{cases} \tag{3.3.2}$$

For a uniform density of states, the number of states satisfying the condition for $V_{\mathbf{kk'}} \neq 0$ has a sharp peak when $\mathbf{k} = -\mathbf{k'}$, so the interaction is strongest for electrons of opposite momenta. The BCS wavefunction is given by

$$|\Psi_{BCS}\rangle = \prod_k (u_k + v_k a^\dagger_{k\uparrow} a^\dagger_{-k\downarrow}) \, |\text{Vacuum}\rangle \,, \tag{3.3.3}$$

which is the product of all permitted pair creation operators with s-wave symmetry (opposite spins). These pairs of electrons with opposite momenta and spin are known as Cooper pairs, first described in detail by Cooper in 1956 [86], having been suggested previously by others [87]. These cooper pairs are the charge carriers for superconductivity, explaining the use of $q = -2e$ and $m = 2m_e^*$ in the GL formulation (equation 3.2.4).

The Hamiltonian is

$$H = \sum_k \begin{pmatrix} a^\dagger_{k\uparrow} & a_{-k\downarrow} \end{pmatrix} \begin{pmatrix} \xi_k & -\Delta \\ -\Delta^* & -\xi_k \end{pmatrix} \begin{pmatrix} a_{k\uparrow} \\ a^\dagger_{-k\downarrow} \end{pmatrix}, \tag{3.3.4}$$

where $\Delta = \frac{|g|}{V} \sum_k \langle a_{-k\downarrow} a_{k\uparrow} \rangle$, and can be found from the self-consistent equation

$$1 = N(0)|g| \int_0^{\varepsilon_c} d\xi \frac{\tanh\left(\frac{\sqrt{\xi^2 + \Delta(T)^2}}{2k_{\mathrm{B}}T}\right)}{\sqrt{\xi^2 + \Delta(T)^2}}. \tag{3.3.5}$$

This energy gap can be found numerically to be $\Delta(T = 0) \simeq 2\varepsilon_c \exp \frac{-1}{N(0)|g|} \simeq 1.76 k_{\mathrm{B}} T_{\mathrm{c}}$ for $N(0)|g| \ll 1$, where $N(0)$ is the density of states at the Fermi surface.

The excitation energy spectrum is given by $E_k = \sqrt{\xi_k^2 + |\Delta|^2}$, so excitations of energy less than the gap $\Delta$ are not permitted, allowing lossless transport of current through the material whenever $\Delta \geq 0$.

The bound state wavefunction is symmetric to electron exchange, so the spin-state must be antisymmetric. The transition predicted by this model is second-order, having a discontinuity in the heat capacity, in agreement with experimental results [88].

Gor'kov was able to show in 1959 that for temperatures close to $T_{\mathrm{c}}$, the GL equations can be derived from the microscopic BCS framework [89]. Although BCS theory describes LTS extremely well, it is unable to explain HTS. The assumptions of weak phonon coupling and *s*-wave symmetry are no longer applicable for the *d*-wave superconductivity found in the cuprates [90].

## 3.4 Critical current and flux pinning

For current carrying applications, the limits of the superconducting state are typically defined in terms of the onset of resistance, rather than a thermodynamic phase change. In a type-II superconductor, resistance occurs when the Lorentz force on fluxons exceeds the pinning force on the flux lattice, leading to dissipative flux motion. The pinning force is determined by the properties of the flux lattice and microstructural features.

For many applications, the temperature and field are specified by the operational requirements, so critical current may be the most relevant quantity to determine. Transport measurements are made to determine $I_\mathrm{c}$ by increasing the current passed through a sample while measuring the electric field across some gauge region. The onset of resistance from flux motion produces an electric field that can be measured by a sensitive voltmeter. The transition is determined by an arbitrary electric-field threshold, typically $100\,\mu\mathrm{V\,m^{-1}}$. Typical experimental traces from $I_\mathrm{c}$ measurements made in this work are shown in figure 3.2.

A key measure of a superconducting transition is the '$N$-value', or transition index. This parameter is found by fitting the power law expression [91, 92]

$$E \propto J^N \tag{3.4.1}$$

over a range of $E$-fields. This gives the sharpness of the transition, and can be used as a figure of merit for engineering applications. A relatively large scatter in $N$-values for REBCO has been seen by some authors [93, 94].

The effective upper critical field $B_\mathrm{c2}^*$, also known as the irreversibility field, is defined as the field at which $J_\mathrm{c}$ drops to zero. This is in practice much easier to measure than the thermodynamic $B_\mathrm{c2}$ and will frequently be used in later analysis.

The current density in commercial high temperature superconducting tapes is now so high that the self-field of even single 4 mm wide tapes can be tens of mT at 77 K and an order of magnitude larger at low temperatures. This means that homogeneous tapes of different widths and thicknesses have different values of current density in self-field, which can be a concern when, for example, batch testing tapes of different geometry from different suppliers for use in magnets.

## 3.5 Josephson junctions

A possible model for a real superconducting system is to consider it as a series of JJs [95], that is superconducting-normal-superconducting (SNS) interfaces. When the normal layer is sufficiently thin, supercurrent can travel through it with a strong dependence on the phase change of the order parameter across the junction. These JJs would represent microstructural features such as grain boundaries or defects along the current path that locally suppress superconductivity.

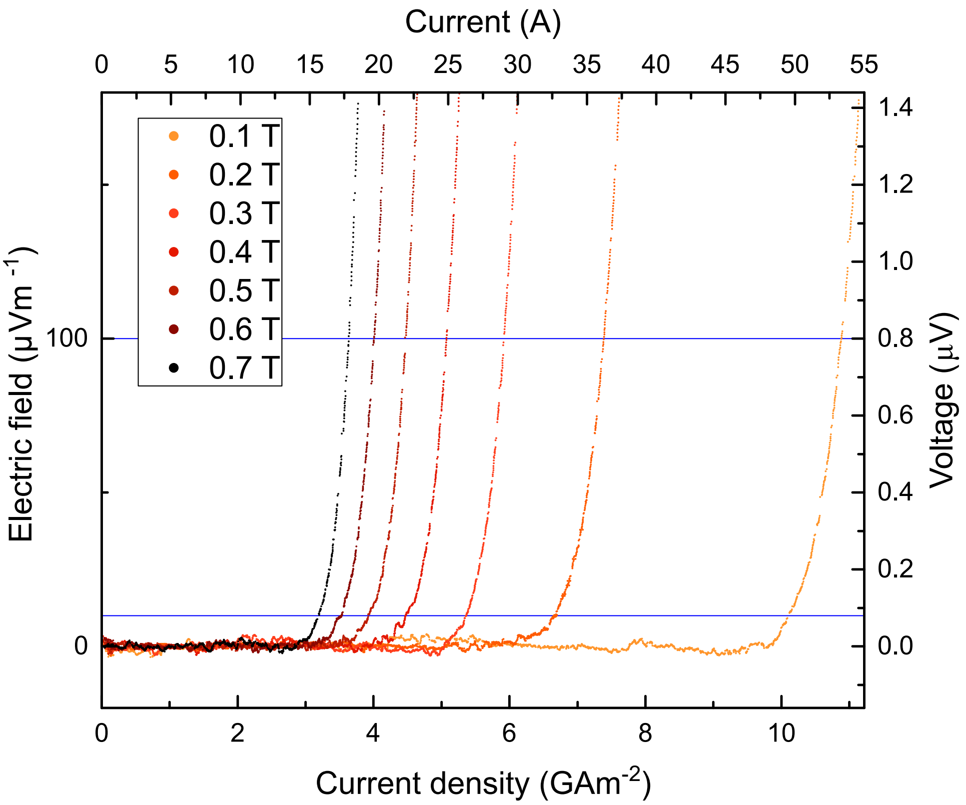

Figure 3.2: $E-J$ measurements on a THEVA 2100 coated conductor at a range of applied field strengths. In each case, the applied field is perpendicular to the tape surface. The blue lines define the transition region, with $I_c$ at the upper blue line, $100\,\mu\mathrm{V\,m^{-1}}$.

For weakly coupled superconductors, the Josephson equations for current across the junction are [96]:

$$I(t) = I_0 \sin(\Delta\gamma) \tag{3.5.1}$$

$$\frac{\partial \Delta\gamma}{\partial t} = \frac{2\pi V(t)}{\Phi_0} \tag{3.5.2}$$

where $\Delta\gamma$ is the phase difference across the junction.

Solutions for a thin, wide junction in applied magnetic have been found by Clem [97]. The current is assumed to be small compared to screening currents such that self-field can be neglected. The coherence length is tacitly assumed to be small as the order parameter changes discontinuously from 0 in the junction to 1 in the bulk; and the system is sufficiently thin such that the lengthscale for variation in the magnetic field, in this case the Pearl length $\Lambda = 2\lambda^2/t$ [98], is much larger than the system.

The solutions are of the form

$$J_c = J_{\mathrm{DJ}} \left| \int \cos\left( B_a \sum_{n=0} \frac{-8\pi}{a\varphi_0 k_n^3} (-1)^n \tanh\left(\frac{k_n L}{4}\right) \sin(k_n y) \right) \mathrm{d}y \right| \tag{3.5.3}$$

with $k_n = \frac{2\pi}{W}(n+1/2)$.

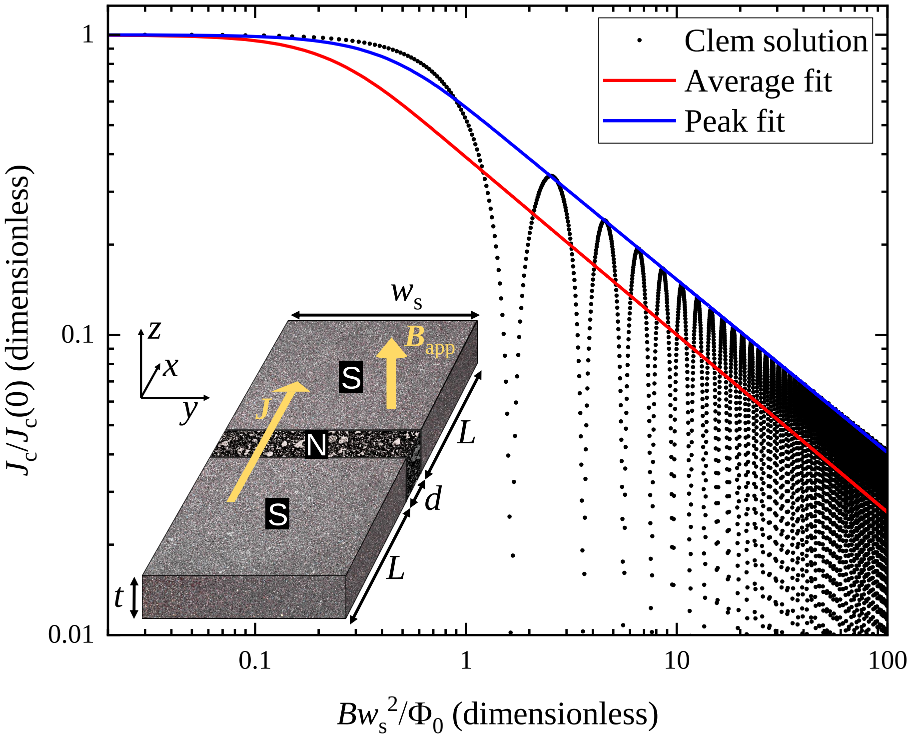

Figure 3.3: Fit to Clem's solution [97] for the critical current density through a Josephson junction as a function of magnetic field for superconducting electrodes with an aspect ratio of 1 (see equation 7.2.1). Fits are shown both through the peaks and through field averaged data. Inset: Josephson junction geometry, with square electrodes that have an aspect ratio of 1.

These solutions describe how the phase associated with fluxons in the junction controls the critical current through the junction, but does not include the behaviour of the zero-field current, $J_{\mathrm{DJ}}$. Figure 3.3 shows these solutions for a junction where $L = w_{\mathrm{s}}$.

Recent work by Blair & Hampshire [99] has generalised the solutions found by Fink [100] in zero applied field for a very narrow and thick JJ, to arbitrary applied field and shown using time-dependent Ginzburg-Landau simulations that these solutions have a wide range of validity [99].

In narrow (rather than very narrow) junctions, where the vortex separation defines the effective junction width, Blair & Hampshire's solutions for $J_{\mathrm{DJ}}$ are

$$J_{\mathrm{DJ}}(B,T) = \frac{4J_0}{\tilde{s}\tilde{v}}\left(1-\tilde{B}\right)^{\frac{3}{2}}\left(1-\sqrt{1-\tilde{s}\tilde{f}^{2}_{\frac{\mathrm{d}}{2}}}\right)\mathrm{e}^{-\frac{d}{\xi_{\mathrm{n}}}}, \tag{3.5.4}$$

$$\tilde{v} = \frac{\tilde{m}_{\mathrm{n}}\tilde{\xi}_{\mathrm{n}}}{\tilde{\Upsilon}_{\mathrm{n}}}\sqrt{1-\tilde{B}}, \quad \tilde{s} = \frac{\tilde{\beta}_{\mathrm{n}}\left(1-\tilde{B}\right)}{\left(\tilde{\alpha}_{\mathrm{n}} - \frac{\tilde{\Upsilon}_{\mathrm{n}}}{\tilde{m}_{\mathrm{n}}}\tilde{B}\right)}, \tag{3.5.5}$$

$$\tilde{\xi}_{\mathrm{n}} = \frac{\xi_{\mathrm{n}}}{\xi_{\mathrm{s}}} = \sqrt{\frac{\tilde{\Upsilon}_{\mathrm{n}}}{\tilde{m}_{\mathrm{n}}\left(-\tilde{\alpha}_{\mathrm{n}} + \frac{\tilde{\Upsilon}_{\mathrm{n}}}{\tilde{m}_{\mathrm{n}}}\tilde{B}\right)}}, \tag{3.5.6}$$

$$\text{and } \tilde{f}^{2}_{\frac{\mathrm{d}}{2}} = \frac{\tilde{v}^2 + 1 - \sqrt{\tilde{v}^2(2-\tilde{s}) + 1}}{\tilde{v}^2 + \tilde{s}}, \tag{3.5.7}$$

| | $T_c$(K) | $B_{c2}(0)$(T) | $\kappa(0)$ | $\xi(0)$(nm) |
|---|---|---|---|---|
| NbTi | 8.99 [101] | 15.7(11) [101] | 48 [82] | 3.40 [82] |
| $Nb_3Sn$ | 17.8(3) [102] | 29.5(3) [102] | 34 [82] | 2.73 [82] |
| $MgB_2$ | 38.6 [103] | $ab$: 25.5 [103]<br>$c$: 9.2 [103] | $ab$: 13.7 [82]<br>$c$: 116 [82] | $ab$: 7.07 [82]<br>$c$: 2.44 [82] |
| $Bi_2Sr_2Ca_2Cu_3O_{10}$ | 108 [104] | $c$: 297 [104] | $ab$: 58 [82] | $ab$: 2.86 [82] |
| REBCO | 90 [105] | $ab$: 250 [3]<br>$c$: 120 [106] | $ab$: 105 [82]<br>$c$: 2400 [82] | $ab$: 1.29 [82]<br>$c$: 0.378 [82] |

Table 3.2: Critical properties of some technological superconductors.

where in Blair & Hampshire's original work $\tilde{\Upsilon}_n$ was taken to be 1. $d$ is the junction thickness, and $\tilde{\alpha}_n$, $\tilde{\beta}_n$, $\tilde{m}_n$ and $\tilde{\Upsilon}_n$ are defined in table 3.1. Blair & Hampshire extend this solution to wide junctions using a parameterisation of the Clem solution

$$J_c(B,T) = C_0 \left(\frac{\Phi_0}{Bw_s^2}\right)^{C_1} J_{DJ}(B,T), \tag{3.5.8}$$

where $C_0$ and $C_1$ are constants. The first factor in (3.5.8) that includes $C_0$ and $C_1$ follows from the high field forms of $J_c$ that include the sinc function for low aspect ratio superconducting electrodes in the JJ, and the Bessel function for the high aspect ratio electrodes, as derived by Clem [97].

## 3.6 Technological superconductors

Superconductors have a wide variety of uses, several of which will be discussed in chapter 2. A few superconducting materials are of particular interest and applicability due to their desirable critical properties, which are summarised in table 3.2, and a comparison of $J_c(B)$ for a range of superconductors is shown in figure 3.4. Materials selection will depend on a number of factors, including cost, ease of use and operational requirements. NbTi in particular is frequently used for its ductility when the operational magnetic field is not too large ($< 10\,\mathrm{T}$).

## 3.7 Conclusions

This chapter has outlined some of the key theoretical tools used to understand superconductivity, including the phenomenological GL theory which uses a linearised free-energy approach to describe the behaviour near to $T_c$, and the microscopic BCS theory. GL theory is presented for anisotropic superconductors, such as REBCO, and in dimensionless units suitable for numerical calculations. A brief introduction is given to the theory of Josephson junctions, which are the foundation for the critical current model used in chapter 7. Finally, an introduction to flux pinning and technological superconductors has been given, with some key parameters of commonly used superconductors.

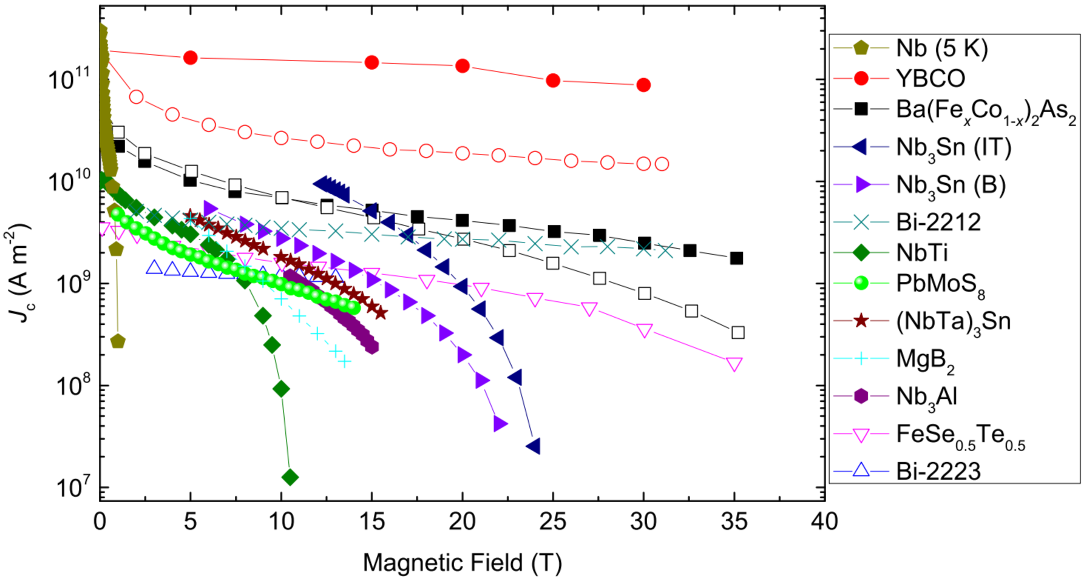

Figure 3.4: Critical current density with magnetic field strength for various technological superconductors. Figure taken from [82]. $J_c$ was measured at 4.2 K unless otherwise specified. Note that the engineering current density, i.e. using the whole strand cross-section, may be significantly lower, particularly for coated conductors.

Chapter 4

# Review of Coated Conductors

## 4.1 Introduction

One of the most promising HTS materials is REBCO, due to its very high critical temperature and field. REBCO stands for rare-earth barium copper oxide, with the chemical formula (RE)$Ba_2Cu_3O_{7-\delta}$. Rare-earth (RE) elements are the lanthanides plus Y and Sc, with common choices for REBCO including Y, Gd and Eu, or a mixture of elements. The crystal structure is orthorhombic, with three orthogonal crystallographic axes of different lengths in the unit cell. The *a*- and *b*-dimensions are similar, at roughly 3.8 Å, and the *c*-axis length is 12 Å. The REBCO unit cell has regions of strong superconductivity in the CuO planes aligned with the *a*- and *b*-axes, with regions of weaker superconductivity around the cations between them. This leads to a strong anisotropy in the superconductivity with significant changes in behaviour with angle of applied magnetic field. The REBCO unit cell is shown in figure 4.1.

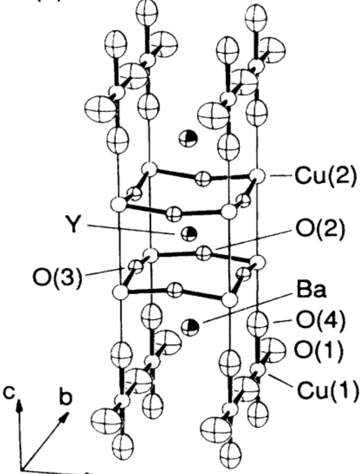

Figure 4.1: REBCO unit cell structure. The CuO planes lie in the *ab*-planes and the CuO chains are aligned with the *b*-axis. Figure from [107].

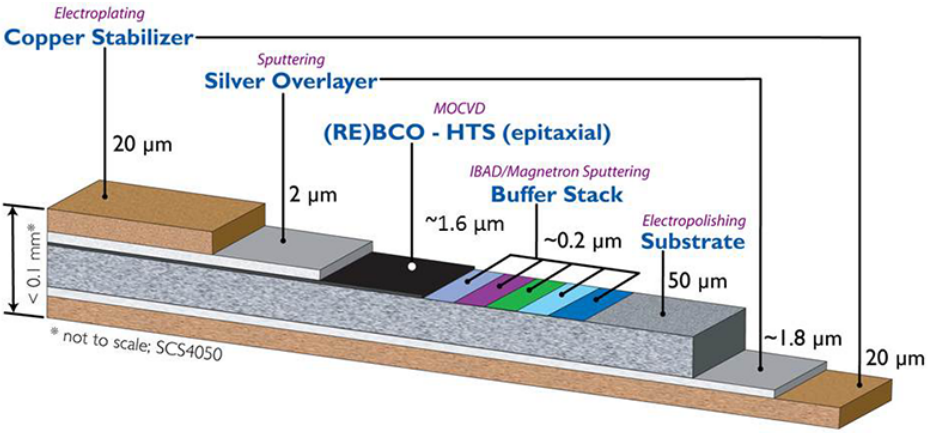

Figure 4.2: Structure of a REBCO coated conductor produced by SuperPower Inc. Figure from [110].

### 4.1.1 Fabrication methods

The short coherence length in HTS can pose problems for manufacture, as any defect that is of comparable thickness to the coherence length that intersects the conduction path causes a significant decrease in $J_c$. For REBCO, grain boundaries can be a few nm thick [108], which is comparable to the coherence length (see table 3.2), and therefore need careful consideration.

Measurements on bicrystals [109] show that grain boundaries in REBCO with a misalignment greater than approximately 5° cause a signifcant suppression of $J_c$. This large suppression suggests that the superconducting state is suppressed over a longer distance than the cation disorder, possibly due to oxygen depletion near the grain boundary.

In order to make high-performance conductors from REBCO, high-angle grain boundaries need to be avoided altogether, which requires a high degree of control over the crystallographic texture. To control the crystallographic orientation, REBCO is grown on a textured substrate, leading to a thin REBCO coating, typically a few micrometers thick. This is known as a coated conductor (CC). This results in a REBCO pseudo-single-crystal which is roughly 1 μm thick, 1 cm wide and can be several km long. Many companies now manufacture CCs, such as SuperPower in the USA, SuNAM in South Korea, SuperOx in Russia and THEVA in Germany. A summary of the properties of CCs from a range of manufacturers is given in table 4.1. An example CC construction is shown in figure 4.2.

There are a number of methods of controlling the texture of the substrate, which often use several intermediate buffer layers to carefully match the REBCO unit cell parameters to that of the substrate. Some common substrate texturing technologies are rolling-assisted biaxially-textured substrates (RABiTS), which uses mechanical rolling of a metal substrate, and ion-beam assisted deposition (IBAD) [111], where ion bombardment introduces texture to one of the buffer layers during its growth [112]. The REBCO layer can be deposited on the buffer layers by a variety of methods, including pulsed laser deposition (PLD), electron-beam physical vapour deposition (EBPVD), metalorganic chemical vapour deposition (MOCVD), and reactive co-evaporation by deposition and reaction (RCE-DR) [113].

| | Rare-Earth | Manufacture | Thickness (µm) | APC |
|---|---|---|---|---|
| SuperPower Inc. | Y & Gd [105] | IBAD, MOCVD | 1-1.6 [116] | BZO |
| THEVA GmbH | Gd [117] | ISD, EBPVD | 3.5 | available |
| SuNAM Co. | Gd | IBAD, RCE-DR | 1.3-1.8 [113] | none |
| Fujikura Ltd. | Gd or Eu | IBAD, PLD | 2-2.5 | BHO [105] |
| SuperOx | Y [118] | IBAD, PLD | 3-4 [114] | $Y_2O_3$ [105] |

Table 4.1: A summary of some commercially available REBCO CCs. Many of these manufacturers produce tapes both with and without APCs. BZO and BHO APCs produce columnar defects, while the $Y_2O_3$ APCs in the SuperOx tapes give spherical point-like defects.

Typically the REBCO layer is formed with the *a*- and *b*-axes within the plane of the tape, and the *c*-axis perpendicular to the tape surface. A drawback of this configuration is the comparatively slow *c*-axis growth rate of REBCO and the increased likelihood of defects with *c*-axis growth, which decreases $J_c$ with thickness [114].

One solution to this issue is inclined-substrate deposition (ISD), notably used by THEVA, where the MgO buffer layer is sprayed on at an angle to the metallic substrate, which changes the angle of the *c*-axis to the tape surface. For THEVA CCs this is approximately 30°. This enables the manufacture of thicker REBCO layers as thickness can now be obtained through *a*- and *b*-axis growth. Using ISD, Dürrschnabel *et al.* were able to produce CCs up to 7.51 µm thick with no loss in $J_c$ [115].

## 4.2 General properties of HTS materials

### 4.2.1 Oxygen content

REBCO is a non-stoichimetric superconductor, meaning that instead of having an integer ratio between element concentrations, the superconducting state depends on the degree of doping. For REBCO, the dopant is typically oxygen vacancies, with the oxygen deficiency given by $\delta$ in the chemical formula $\mathrm{(RE)Ba_2Cu_3O_{7-\delta}}$.

The peak $T_c$ in single crystals occurs when $\delta = 0.06$ [119, 120], but this is not necessarily the preferred oxygen deficiency. Other properties, including $B_{c2}$, are observed to monotonically decrease with oxygen deficiency [119, 121].

Oxygen concentration is important for REBCO growth and manufacture, but in a laboratory setting, it is also important to understand when applying heat. As REBCO tapes are often soldered for mechanical attachment to a strain device or for electrical contact to instrumentation, it is important to know whether the applied heat will affect the superconducting properties of the tape.

The oxygen ions in REBCO are mobile at elevated temperatures, which can cause the oxygen deficiency to change from optimal, depending on the temperature, timescale and oxygen concentration in the atmosphere or chemical barrier adjacent to the REBCO.

Degradation in soldering conditions has been investigated by Preuss *et al.* [122], who measured the change in $I_c$ of a range of REBCO tapes with copper stabilisers submerged

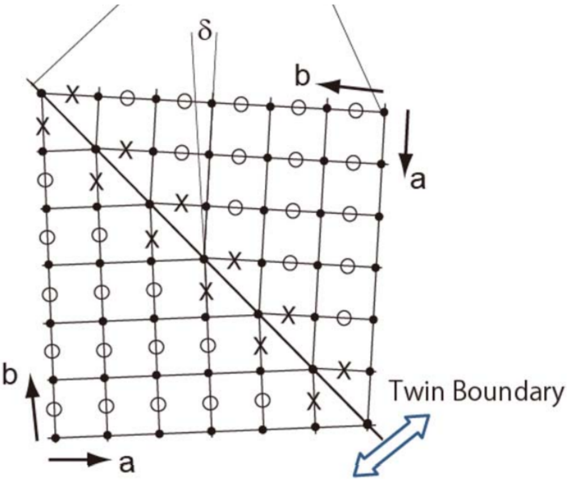

Figure 4.3: Schematic of a twin boundary in REBCO. Figure from [126].

in molten solder, finding an Arrhenius-like relation between $I_c$-decay time and temperature with an activation energy of 0.94 eV. They find that 5% of $I_c$ is lost after 10 minutes at 225 °C but just 30 s at 300 °C. Measurements in large applied fields after heat treatments [123] show onset of degradation at 4.2 K, 8.5 T at lower heat-treatment temperatures than when measured at 77 K, self field. They find a more than 10% decrease in 4.2 K, 8.5 T $I_c$ after 2 h at 175 °C with no apparent change at 77 K, self field. This is of concern when undertaking long heat treatments such as strain-gauge glue curing, which may affect low-temperature measurements but not be observed in liquid nitrogen measurements.

Lead-tin solder has a melting point of at least 183 °C (often closer to 190 °C, depending on composition) [124] which allows for several minutes soldering time if the temperature is kept fairly close above the melting point. Conventional lead-free solders, such as Ag-Sn (melting point $\geq$ 221 °C) give a much greater risk of sample degradation.

Low-temperature solders are also possible, although several of these are much more brittle than PbSn, making them unsuitable for strain application [125].

### 4.2.2 Crystallographic orientation and twin boundaries

The similarity in the *a*- and *b*-dimensions of REBCO mean that there is not a strong preference for which is aligned with the substrate texture. For entropic reasons, REBCO forms twin boundaries so that the *a*- and *b*-axes frequently switch over, with the twin boundary as a plane of mirror symmetry. A schematic of this is shown in figure 4.3. This frequent change of *a*- and *b*-axes has a number of implications that differentiate CCs from single-crystals. The regions between the twin boundaries are referred to as domains, and for CCs where the *a*- or *b*-axis is aligned with the current flow direction, they are known as *a*- and *b*-domains respectively. The *a*-domain fraction, $f$, has implications for the strain behaviour of CCs, discussed in section 4.3.5.

The regions of weak superconductivity between the *ab*-planes provide strong pinning sites for vortices, which have a large energy penalty to cross the *ab*-planes. This means that the pinning force is stronger, and therefore critical current is higher, when vortices are closely

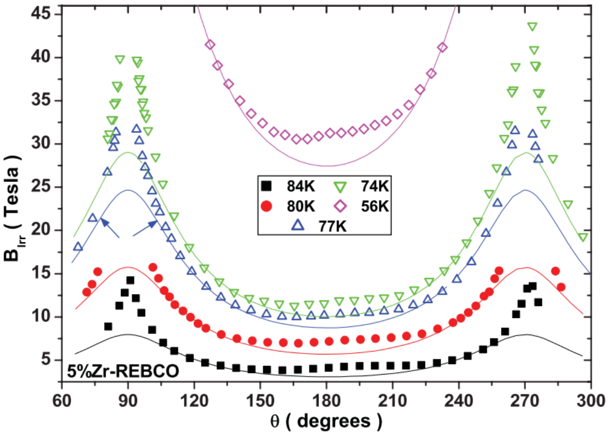

Figure 4.4: Angular variation of the irreversibility field for a coated conductor with artificial pinning centres. The peaks at 90° and 270° are from the intrinsic pinning of the *ab*-planes. The weaker peak at 180° is due to the BZO nanorods. Figure from [127]. The fits are from an anisotropic GL model, with deviations attributed to microstructural pinning.

aligned with the *ab*-planes, and weaker when vortices are perpendicular to the *ab*-planes. As the average vortex orientation is the same as the applied field, this means that there is a strong peak in $J_c$ when $B \parallel ab$.

### 4.2.3 Artificial pinning centres

A number of manufacturers produce CCs with APCs to improve performance. APCs are non-REBCO inclusions designed to improve flux pinning. These can be roughly spherical, or columnar inclusions such as BZO ($BaZrO_3$) nanorods. Columnar APCs are typically aligned with the *c*-axis to counteract the reduced pinning in this orientation. The angular variation of the irreversibility field for a typical CC is shown in figure 4.4, with a small peak at 180° from columnar APCs and a sharper peak at 90° from the *ab*-planes.

### 4.2.4 Inclined substrate deposition

As well as allowing for increased thickness of the REBCO layer, ISD CCs changes a number of key properties of the tape when compared to other manufacturing methods. The THEVA ISD tapes have the *a*- and *b*-axes at 45° to the current flow direction (as do the non-ISD Fujikura tapes), which has implications for their strain behaviour, discussed in section 4.3.5. The change in alignment of the *ab*-planes changes the response to the angle of the applied magnetic field, with pinning features from the *ab*-planes no longer aligned with surface pinning and geometric effects. This has implications for magnet and cable design as the optimum angle of the tape to the external magnetic field is different to other CCs.

One of the most interesting features of ISD CCs from a scientific perspective is the possibility of measuring current flow in the *c*-axis direction. The conventional current direction is still entirely parallel to the *ab*-planes, but with the *c*-axis not perpendicular to the tape surface, applying current through the width of the tape forces current with a *c*-axis component, which travels through the weakly superconducting regions between the *ab*-planes. This allows for the study of a layered superconductor which could be considered as a series of JJs. This ‘interplanar’ current has been measured by Lao *et al.* [128], who found only a modest reduction in $J_{\mathrm{c}}$ of 30% at 77 K, self-field, indicating that the planes are closely coupled at this temperature.

The $J_{\mathrm{c}}$ anisotropy can also be measured with remanent magnetisation, where the spatial variation of magnetisation is measured after a large applied field is removed. The angle of the ‘rooftop’ magnetisation pattern seen at the corners of a rectangular sample indicates the relative $J_{\mathrm{c}}$ along the principal axes. This has been observed to give a ratio of 1.3 in liquid nitrogen conditions [129], in agreement with the 30% reduction seen in direct transport measurements [128].

Such a small decrease suggests that an anisotropic model may be appropriate rather than a layered model. Calculations by Smith *et al.* [130] using an anisotropic GL model and a Klemm model for a layered superconductor [131] suggest that REBCO CCs are 3D (i.e. without strong effects from layering) at all temperatures in low fields. These calculations use fits to angular $B_{\mathrm{c2}}$ data, and while the conclusions for low temperatures rely on significant extrapolations, the data at 77 K is well described by the anisotropic GL model with no correction for a layered structure.

A clear feature of the interplanar current measurements is a local minimum in $J_{\mathrm{c}}$ for angles close to $B \parallel ab$ [128, 132], attributed to a phenomenon known as flux channelling. When the applied field is parallel to the *ab*-planes, fluxons do not have to cross the *ab*-planes and predominantly sit in the weakly-superconducting regions between planes. As the interplanar current generates a Lorentz force component parallel to the *ab*-planes, fluxons can glide parallel to the planes with minimal resistance. This feature is not seen with *ab*-current as there is no Lorentz force component parallel to the planes. The local minima appear against a broader peak when the field is rotated in the maximum-Lorentz force configuration.

## 4.3 Electromechanical properties of HTS

### 4.3.1 Single-crystal strain measurements

A useful tool for understanding the strain behaviour of macroscopic systems is to look at the behaviour in single-crystals.

Table 4.2 lists a selection of single-crystal strain measurements. Note that in many of the papers referenced, the strain sensitivity is given in terms of applied pressure, which has the opposite sign to applied stress, as tensile stress is by convention always taken to be positive.

These measurements are made in a variety of ways, some with directly applied pressure and either magnetic or resistive measurements of $T_{\mathrm{c}}$. Other authors have calculated the strain sensitivity using the Ehrenfest relation from heat capacity and thermal expansivity measurements [133, 134, 135, 136]. Expansivity can be determined by a capacitive

| | $T_{\mathrm{c}}$(K) | $\frac{\mathrm{d}T_{\mathrm{c}}}{\mathrm{d}\sigma_a}$ | $\frac{\mathrm{d}T_{\mathrm{c}}}{\mathrm{d}\sigma_b}$ | $\frac{\mathrm{d}T_{\mathrm{c}}}{\mathrm{d}\sigma_c}$ | $\frac{\mathrm{d}T_{\mathrm{c}}}{\mathrm{d}p}$ | Method |
|---|---|---|---|---|---|---|
| Meingast 1991 [134] | 90.9 | 1.9 | -2.2 | 0 | 0.3* | $\Delta\alpha, \Delta C_p$ |
| Murayama 1991 [137] | 91.4 | - | - | - | 0.66 | resistivity |
| Benischke 1992 [138] | 92.5 | - | - | - | 0.4 | susceptibility |
| Welp 1992 [139] | 91.5(5) | 2.0(2) | -1.9(2) | 0.3(1) | $-0.4(3)^*$ | susceptibility |
| Kraut 1993 [135] | 89.7(4) | 2.7 | -3.1 | 0.64 | - | $\Delta\alpha, \Delta C_p$ |
| Kund 1993 [136] | 89.4(8) | 1.24 | -1.55 | 0 | 0.31* | $\Delta\alpha, \Delta C_p$ |
| Fietz 2005 [140] | 89.55 | 1.00 | -1.18 | 0.164 | 0.01* | susceptibility |

Table 4.2: Strain measurements for REBCO single crystals. Due to the strong sensitivity to oxygen content, only crystals with $T_{\mathrm{c}} > 89\,\mathrm{K}$ are included. All strain sensitivities are given in $\mathrm{K\,GPa^{-1}}$. The change in $T_{\mathrm{c}}$ from hydrostatic pressure is calculated as $\frac{\mathrm{d}T_{\mathrm{c}}}{\mathrm{d}p} = -\sum_i \frac{\mathrm{d}T_{\mathrm{c}}}{\mathrm{d}\sigma_i}$ where not measured explicitly and all crystallographic axes are measured on the same sample, marked with an asterisk. The measurement method is specified: $\Delta\alpha, \Delta C_p$ is a calculation from expansivity and heat capacity measurements; 'susceptibility' and 'resistivity' both have direct pressure application and $T_{\mathrm{c}}$ measured by AC magnetic susceptibility or electrical resistivity respectively.

measurement which in principal allows for a high degree of accuracy, although a direct measurement with applied pressure can show the range over which a linear gradient applies. Applying pressure along multiple axes independently is more challenging due to the large crystal size required.

There is a strong sensitivity of pressure dependence to oxygen concentration [135, 138], with pressure sensitivity much greater for single crystals with larger oxygen deficiency. This strain sensitivity to *c*-axis pressure is understood to be due to hole mobility. Measurements on doped YBCO, where oxygen content is varied and other dopants such as Ca are added to access the overdoped region, show that $T_{\mathrm{c}}$ is parabolic with hole concentration, and that $\frac{\mathrm{d}T_{\mathrm{c}}}{\mathrm{d}\sigma_c}$ and $\frac{\mathrm{d}T_{\mathrm{c}}}{\mathrm{d}p}$ are proportional to the gradient of $T_{\mathrm{c}}$ with hole concentration [120, 135, 140, 141, 142]. This implies that *c*-axis pressure is changing the hole concentration by motion of oxygen atoms. Close to optimal doping, *c*-axis pressure only has a small effect, but further away from optimal, an the change in hole concentration from applied pressure has a significant effect on $T_{\mathrm{c}}$. This is supported by measurements showing that there is a strong link between oxygenation temperature [143, 144], *c*-axis length and $T_{\mathrm{c}}$, showing that the oxygen content of the REBCO changes the equilibrium *c*-axis length.

Near optimal doping, the effect of *a*- and *b*-axis pressure is much stronger than along the *c*-axis, but the effects are similar in magnitude and opposite signs, so nearly cancel out in measurements with applied hydrostatic pressure. The strong *a*- and *b*-axis dependence leads to a strong sensitivity to the angle of an applied strain relative to the crystallographic axes.

### 4.3.2 Detwinned tapes

Some REBCO tapes have been annealed under strain to remove twin boundaries [145, 146]. Changing the lattice parameter generates a preference for a either the *a*- or *b*-axis to be aligned with the current direction. Suzuki *et al.* [145] achieved a domain fraction of

| | $C_{11}$ | $C_{22}$ | $C_{33}$ | $C_{12}$ | $C_{13}$ | $C_{23}$ | Note |
|---|---|---|---|---|---|---|---|
| Reichardt 1988 [147] | 230 | 230 | 150 | 100 | 100 | 100 | Exp |
| Ledbetter 1991 [148] | 223 | 244 | 138 | 37 | 89 | 93 | Exp |
| Lei 1993 [149] | 231 | 268 | 186 | 132 | 71 | 95 | Exp |
| Murphy 2020 [150] | 215.97 | 232.4 | 142.55 | 109.24 | 58.03 | 57.16 | DFT |
| Favre 2021 [151] | 299.8 | 314.9 | 246.2 | 141.7 | 80.1 | 78.8 | DFT |

Table 4.3: Elastic constants for REBCO from various authors. All values are given in GPa. Experimental (Exp) and calculations (using DFT) are noted.

94% for both $a$- and $b$-domains on the respective tapes, and found a linear change in $T_\mathrm{c}$ with strain for the $b$-domain and a gently curving variation for the $a$-domain, both of which have similar gradients to the single-crystal measurements [140] (see table 4.2). Awaji *et al.* [146] measure non-linear behaviour for both crystallographic orientations, and suggest that from extrapolation of both samples that the optimum $T_\mathrm{c}$ for REBCO would be when the $a$ and $b$ lattice constants are equal. As the strain range available on a tape is much greater than has been measured on single-crystals, the non-linear behaviour is entirely consistent with the linear behaviour observed over the small strain range on single crystals. Unfortunately in both detwinned measurements, there is a significant reduction in $J_\mathrm{c}$ relative to the pristine sample, which the authors attribute to micro-cracks, but may also be a consequence of the extended heat treatment of 3 h at 300 °C which may cause significant degradation through oxygen loss [122]. Suzuki *et al.* found $J_\mathrm{c}$ to be 30% ($a$) and 3.4% ($b$) of the pristine sample. If the heat treatment has degraded $T_\mathrm{c}$, this would cast doubt on the applicability of their findings due to the large sensitivity of strain-response to oxygen concentration.

### 4.3.3 Stiffness tensor

As an orthotropic material, REBCO has in general 9 independent components to its stiffness tensor. In the generalised Hooke's law, $\boldsymbol{\sigma} = \boldsymbol{C}\boldsymbol{\varepsilon}$, this can be represented using Voigt notation as:

$$\begin{pmatrix} \sigma_{xx} \\ \sigma_{yy} \\ \sigma_{zz} \\ \sigma_{zy} \\ \sigma_{xz} \\ \sigma_{xy} \end{pmatrix} = \begin{pmatrix} C_{11} & C_{12} & C_{13} & 0 & 0 & 0 \\ C_{12} & C_{22} & C_{23} & 0 & 0 & 0 \\ C_{13} & C_{23} & C_{33} & 0 & 0 & 0 \\ 0 & 0 & 0 & G_{yz} & 0 & 0 \\ 0 & 0 & 0 & 0 & G_{zx} & 0 \\ 0 & 0 & 0 & 0 & 0 & G_{xy} \end{pmatrix} \begin{pmatrix} \varepsilon_{xx} \\ \varepsilon_{yy} \\ \varepsilon_{zz} \\ 2\varepsilon_{zy} \\ 2\varepsilon_{xz} \\ 2\varepsilon_{xy} \end{pmatrix} \tag{4.3.1}$$

Literature values for REBCO elastic constants are summarised in table 4.3, including measured values from neutron scattering and calculated values from density functional theory (DFT).

The elastic constants can be used to convert between stress and strain, and therefore relate changes in $T_\mathrm{c}$ with stress to with strain [139]:

$$\frac{\partial T_\mathrm{c}}{\partial \varepsilon_i} = C_{ij}\frac{\partial T_\mathrm{c}}{\partial \sigma_j}. \tag{4.3.2}$$

### 4.3.4 1D chain model for $J_\mathrm{c}$

As REBCO tapes are pseudo-single-crystals with well-controlled crystallographic texture, it may expected that there are many similarities to the single-crystal measurements.

The strain response of twinned REBCO has been explained using a model known as the 'chain model' [152, 153]. This describes the system in terms of two competing domain types in series along the conducting path. Typically these domains would be each region between twin boundaries where the *a*- or *b*-axis is aligned with the tape, labelled as *a*- and *b*-domains respectively. By matching the electric fields in each domain, an expression for the critical current of the whole tape in terms of the strain sensitivity of each domain can be found:

$$J_\mathrm{c}(\varepsilon) = J_\mathrm{c}(0)(fJ_{\mathrm{c},a}^{-N} + (1-f)J_{\mathrm{c},b}^{-N})^{-\frac{1}{N}} \tag{4.3.3}$$

where $f$ is the *a*-domain fraction, and $J_{\mathrm{c},i}$ can be related using a scaling law (eq. 4.5.1) from the single-crystal $T_\mathrm{c}$ data. The $T_\mathrm{c}$ of each domain is assumed to be linear with strain: $T_{\mathrm{c},i}(\varepsilon) = T_\mathrm{c}(0)(1 + g_i\varepsilon)$ where $g_i, i = a, b$ is the strain sensitivity of each domain.

When the crystallographic axes are aligned with the tape, there is a decrease in $J_\mathrm{c}$ in both directions away from zero strain, as the behaviour is dominated by the domain with lower $J_\mathrm{c}$. In one direction the $J_\mathrm{c}$ of the *a*-domains decreases and in the other direction that of the *b*-domains decreases, from the roughly opposite response of single crystals to *a*- and *b*-oriented strain. This prediction matches well with experimental measurements of uniaxial strain [92].

### 4.3.5 Effect of twin orientation

Some REBCO tapes have the *a*- and *b*-axes aligned at 45° to the current flow rather than being parallel or perpendicular to it, notably tapes manufactured by Fujikura [126] and ISD tapes, such as those manufactured by THEVA [152]. Within the chain model, these tapes are expected to have an almost flat strain response, with no significant change in $T_\mathrm{c}$ on application of uniaxial strain in the current flow direction [152]. This is because both domain types will see an equal *a*- and *b*-strain, which from the single-cyrstal data are expected to almost cancel. This is supported by uniaxial measurements on ISD [152, 154, 155, 156, 157, 158] and Fujikura tapes [159] which find a linear change in $T_\mathrm{c}$ with shallow gradient.

van der Laan *et al.* [152] have measured uniaxial strain at a range of angles, by rotating a small sample on a strain board and patterning small current-bridges to ensure the current flow remains parallel to the applied strain. They find the strain sensitivity, $a = \frac{\mathrm{d}T_\mathrm{c}}{\mathrm{d}\varepsilon}$ varies with strain angle, $\alpha$, and is well described by

$$a(\alpha) = a(0)|\cos(\alpha) - \sin(\alpha)|, \tag{4.3.4}$$

which gives the steepest strain responses when strain is aligned with the $a$- and $b$-axes, and no change in $T_\mathrm{c}$ with strain when strain is at 45° to the axes.

### 4.3.6 2D strain measurements

Measurements with multiple strain axes have been made on a SuperPower CC by Greenwood *et al.* [160, 161]. Unfortunately these measurements do not have *in situ* strain control, creating a relatively large scatter due to a thermal cycle between all strain points. Nevertheless, these results support the chain model with single-crystal-like $a$- and $b$-domains, with strain sensitivities of $g_a = 1.8(1)\,\mathrm{K}\,\%^{-1}$ and $g_b = -1.3(1)\,\mathrm{K}\,\%^{-1}$.

## 4.4 Deviatoric strain

The deviatoric strain approach is a particular method of understanding the strain tensor by decomposing it into strain invariants [162], which are independent of coordinate system. Deviatoric strain has been used to describe the strain response of $Nb_3Sn$, particularly by the group at Twente [163, 164].

The general definition of an invariant of a tensor is any scalar function of that tensor that does not change on a transformation by an orthogonal tensor such that $f(\mathbf{A}) = f(\mathbf{R}^\mathrm{T}\mathbf{A}\mathbf{R})$ for all $\mathbf{R}^\mathrm{T}\mathbf{R} = \mathbf{I}$. Orthogonal tensors include all rotations and coordinate transformations that don't rescale the system, so the invariant, $f$, has the same value in all coordinate systems.

The principal invariants, $I_i$, of a tensor are defined from the characteristic polynomial of the tensor, $\det(\mathbf{A} - \lambda\mathbf{I}) = 0$, which for three-dimensional rank-two tensors can be expressed as $\lambda^3 - I_1\lambda^2 + I_2\lambda - I_3 = 0$ where [165]

$$I_1 = \mathrm{tr}(\mathbf{A}) = \lambda_1 + \lambda_2 + \lambda_3 \tag{4.4.1}$$

$$I_2 = \frac{1}{2}((\mathrm{tr}(\mathbf{A})^2 - \mathrm{tr}(\mathbf{A}^2)) = \lambda_1\lambda_2 + \lambda_1\lambda_3 + \lambda_2\lambda_3 \tag{4.4.2}$$

$$I_3 = \det(\mathbf{A}) = \lambda_1\lambda_2\lambda_3. \tag{4.4.3}$$

These principal invariants can be combined to define other invariant quantities, such as $\mathbf{A} : \mathbf{A} = I_1^2 - 2I_2 = \lambda_1^2 + \lambda_2^2 + \lambda_3^2$, where the double dot product is defined as $\boldsymbol{A} : \boldsymbol{B} = A_{ij}B_{ij}$.

Material properties should be independent of coordinate system, which is a good reason for using strain invariants as they are also independent of coordinate system. However, because they are invariant on all rotations, strain invariants do not capture any information about the relative orientation of the strain to the material. For this reason, information about the relative orientation of the strain to the material may be required to understand an anisotropic material.

For an isotropic material such as polycrystaline $Nb_3Sn$, if external or geometric effects are neglected, only invariants of the strain should have an effect on the properties. A sensible starting point would be to describe the response in terms of some linear combination of the principal invariants, although in general the description could be any function of any invariant, not just the principal invariants. A useful set of invariants is likely to be one which produces a simple mathematical model for the strain response.

Several authors have used the deviatoric strain to construct invariants, labelled here as $J_i$. Deviatoric strain is defined as the traceless component of the strain, $\boldsymbol{\varepsilon}_{\text{dev}} = \boldsymbol{\varepsilon} - \frac{\text{tr}(\boldsymbol{\varepsilon})}{3}\boldsymbol{I} = \boldsymbol{\varepsilon} - \frac{I_1}{3}\boldsymbol{I}$.

The deviatoric strain invariants often used in the literature for superconductors [162] are

$$J_1 = \text{tr}(\boldsymbol{\varepsilon}_{\text{dev}}) = 0 \tag{4.4.4}$$

$$J_2 = \frac{1}{2}\boldsymbol{\varepsilon}_{\text{dev}} : \boldsymbol{\varepsilon}_{\text{dev}} = \frac{I_1^2}{3} - I_2 \tag{4.4.5}$$

$$J_3 = \det(\boldsymbol{\varepsilon}_{\text{dev}}), \tag{4.4.6}$$

where as the deviatoric strain is traceless, the first principal invariant of the total strain, $I_1$ is used to replace $J_1$.

Several authors have used these deviatoric strain invariants to explain the behaviour in $Nb_3Sn$, with a reasonable agreement for $B_{\text{c2}} \propto \sqrt{J_2}$ [163, 164, 166, 167]. These measurements have applied two independent strain directions by changing the Poisson ratio of the material the $Nb_3Sn$ is mounted to when uniaxial strain is applied, but more degrees of freedom in the measured strain state would be needed to rule out other models for strain behaviour. Some analyses also incorporate $J_3$ [162, 168, 169, 170] to more precisely explain experimental results.

### 4.4.1 Polycrystalline materials

It is desirable to understand how the macroscopic behaviour of a polycrystalline material relates to the behaviour of individual grains. We may be able to infer from measurements of the polycrystalline material information about the mechanism for changes in superconducting properties.

Welch [171] outlines a method for predicting the polycrystalline behaviour from some single-crystal strain response. He uses a model where (in Voigt notation)

$$\Delta T_{\text{c}} = \underline{\Gamma} \cdot \underline{\varepsilon} + \frac{1}{2}\underline{\varepsilon} \cdot \underline{\underline{\Delta}} \cdot \underline{\varepsilon}, \tag{4.4.7}$$

where the tensor $\underline{\underline{\Delta}}$ has the same number of independent elements as the stiffness tensor.

This model for $T_{\text{c}}$ of the single crystal is then operated on by an appropriate rotation matrix and integrated over all possible angles [172]:

$$\langle \Delta T_{\mathrm{c}} \rangle = \frac{1}{8\pi^2} \int_{\theta=0}^{\pi} \int_{\varphi=0}^{2\pi} \int_{\chi=0}^{2\pi} \Delta T_{\mathrm{c}}(\theta, \varphi, \chi) \sin(\theta) \mathrm{d}\theta \mathrm{d}\varphi \mathrm{d}\chi, \tag{4.4.8}$$

where $\varphi$, $\theta$, and $\chi$ are the Euler angles.

This step in the calculations assumes that a bulk polycrystalline superconductor will have a change in $T_{\mathrm{c}}$ on applied strain that is equal to the mean of the changes in $T_{\mathrm{c}}$ of the individual grains. This is somewhat of a simplification as the width of the distribution of $T_{\mathrm{c}}$ will change as different grains with different orientations respond differently. In the case where all grains start with an identical $T_{\mathrm{c}}$, the initial $T_{\mathrm{c}}$ distribution is a delta function, but when a strain is applied this will broaden. The effective $T_{\mathrm{c}}$ of the bulk material is not necessarily at the mean of its $T_{\mathrm{c}}$ distribution, depending on the degree of percolative connectivity within the sample.

Welch simplifies the calculation by only considering a cubic material, which reduces the number of independent coefficients in $\underline{\underline{\Delta}}$ to 3, and only considers a shear-free applied strain state. Welch obtains

$$\begin{aligned} \langle \Delta T_{\mathrm{c}} \rangle = &(\varepsilon_{xx} + \varepsilon_{yy} + \varepsilon_{zz})\Gamma_1 + (\varepsilon_{xx}^2 + \varepsilon_{yy}^2 + \varepsilon_{zz}^2)\frac{3\Delta_{11} + 2\Delta_{12} + \Delta_{44}}{10} + \\ &(\varepsilon_{xx}\varepsilon_{yy} + \varepsilon_{xx}\varepsilon_{zz} + \varepsilon_{yy}\varepsilon_{zz})\frac{2\Delta_{11} + 8\Delta_{12} - \Delta_{44}}{10}. \end{aligned} \tag{4.4.9}$$

We can relate the coefficients of the two strain dependence tensors used by Welch to partial differentials of $T_{\mathrm{c}}$ with strain:

$$\begin{aligned} \Gamma_1 &= \frac{1}{3}\frac{\partial T_{\mathrm{c}}}{\partial \varepsilon_{aa}} \\ \Delta_{11} &= \frac{1}{3}\frac{\partial^2 T_{\mathrm{c}}}{\partial \varepsilon_{aa}^2} \\ \Delta_{12} &= \frac{1}{6}\frac{\partial^2 T_{\mathrm{c}}}{\partial \varepsilon_{aa}\partial \varepsilon_{bb}} \\ \Delta_{44} &= \frac{1}{3}\frac{\partial^2 T_{\mathrm{c}}}{\partial \varepsilon_{ab}^2}. \end{aligned} \tag{4.4.10}$$

We can extend this solution by considering a general orthotropic material, where the only symmetry reducing the solution is $\varepsilon_{ij} = \varepsilon_{ij}$, which is equivalent to requiring symmetry on a 180° rotation. For a non-orthotropic material (i.e. with non-orthogonal crystallographic axes), this symmetry does not apply.

For this general case, the change in $T_{\mathrm{c}}$ is written as a second order expansion (now in tensor notation rather than the Voigt notation used by Welch):

$$\Delta T_{\mathrm{c}} = \sum_{j \geq i} \sum_{i} \sum_{l \geq k,j} \sum_{k} \left( \frac{\partial T_{\mathrm{c}}}{\mathrm{d}\varepsilon_{ij}} \left(\mathbf{R}\boldsymbol{\varepsilon}_{\mathrm{app}}\mathbf{R}^{\mathrm{T}}\right)_{ij} + \frac{1}{2}\frac{\partial^2 T_{\mathrm{c}}}{\partial \varepsilon_{ij}\partial \varepsilon_{kl}} \left(\mathbf{R}\boldsymbol{\varepsilon}_{\mathrm{app}}\mathbf{R}^{\mathrm{T}}\right)_{ij} \left(\mathbf{R}\boldsymbol{\varepsilon}_{\mathrm{app}}\mathbf{R}^{\mathrm{T}}\right)_{kl} \right), \tag{4.4.11}$$

Performing the angular integration for this general expansion, and considering a general applied strain including shear components, we obtain:

$$\begin{aligned}
\langle \Delta T_\mathrm{c} \rangle = {} & \frac{1}{3}(\varepsilon_{xx} + \varepsilon_{yy} + \varepsilon_{zz}) \left( \frac{\partial T_\mathrm{c}}{\partial \varepsilon_{aa}} + \frac{\partial T_\mathrm{c}}{\partial \varepsilon_{bb}} + \frac{\partial T_\mathrm{c}}{\partial \varepsilon_{cc}} \right) + \\
& \frac{1}{30} \Bigg( (\varepsilon_{xy}^2 + \varepsilon_{xz}^2 + \varepsilon_{yz}^2) \left\{ 4 \left( \frac{\partial^2 T_\mathrm{c}}{\partial \varepsilon_{aa}^2} + \frac{\partial^2 T_\mathrm{c}}{\partial \varepsilon_{bb}^2} + \frac{\partial^2 T_\mathrm{c}}{\partial \varepsilon_{cc}^2} \right) + 3 \left( \frac{\partial^2 T_\mathrm{c}}{\partial \varepsilon_{ab}^2} + \frac{\partial^2 T_\mathrm{c}}{\partial \varepsilon_{ac}^2} + \frac{\partial^2 T_\mathrm{c}}{\partial \varepsilon_{bc}^2} \right) \right. \\
& \qquad \left. -2 \left( \frac{\partial^2 T_\mathrm{c}}{\partial \varepsilon_{aa} \partial \varepsilon_{bb}} + \frac{\partial^2 T_\mathrm{c}}{\partial \varepsilon_{aa} \partial \varepsilon_{cc}} + \frac{\partial^2 T_\mathrm{c}}{\partial \varepsilon_{bb} \partial \varepsilon_{cc}} \right) \right\} + \\
& (\varepsilon_{xx}^2 + \varepsilon_{yy}^2 + \varepsilon_{zz}^2) \left\{ 3 \left( \frac{\partial^2 T_\mathrm{c}}{\partial \varepsilon_{aa}^2} + \frac{\partial^2 T_\mathrm{c}}{\partial \varepsilon_{bb}^2} + \frac{\partial^2 T_\mathrm{c}}{\partial \varepsilon_{cc}^2} \right) + \frac{\partial^2 T_\mathrm{c}}{\partial \varepsilon_{ab}^2} + \frac{\partial^2 T_\mathrm{c}}{\partial \varepsilon_{ac}^2} + \frac{\partial^2 T_\mathrm{c}}{\partial \varepsilon_{bc}^2} \right. \\
& \qquad \left. + \frac{\partial^2 T_\mathrm{c}}{\partial \varepsilon_{aa} \partial \varepsilon_{bb}} + \frac{\partial^2 T_\mathrm{c}}{\partial \varepsilon_{aa} \partial \varepsilon_{cc}} + \frac{\partial^2 T_\mathrm{c}}{\partial \varepsilon_{bb} \partial \varepsilon_{cc}} \right\} + \\
& (\varepsilon_{xx}\varepsilon_{yy} + \varepsilon_{xx}\varepsilon_{zz} + \varepsilon_{yy}\varepsilon_{zz}) \left\{ 2 \left( \frac{\partial^2 T_\mathrm{c}}{\partial \varepsilon_{aa}^2} + \frac{\partial^2 T_\mathrm{c}}{\partial \varepsilon_{bb}^2} + \frac{\partial^2 T_\mathrm{c}}{\partial \varepsilon_{cc}^2} \right) - \left( \frac{\partial^2 T_\mathrm{c}}{\partial \varepsilon_{ab}^2} + \frac{\partial^2 T_\mathrm{c}}{\partial \varepsilon_{ac}^2} + \frac{\partial^2 T_\mathrm{c}}{\partial \varepsilon_{bc}^2} \right) \right. \\
& \qquad \left. +4 \left( \frac{\partial^2 T_\mathrm{c}}{\partial \varepsilon_{aa} \partial \varepsilon_{bb}} + \frac{\partial^2 T_\mathrm{c}}{\partial \varepsilon_{aa} \partial \varepsilon_{cc}} + \frac{\partial^2 T_\mathrm{c}}{\partial \varepsilon_{bb} \partial \varepsilon_{cc}} \right) \right\} \Bigg) .
\end{aligned} \tag{4.4.12}$$

The derivatives of $T_\mathrm{c}$ could be measured on single crystals, with the first and second derivatives in the normal strain components extracted from a direct $T_\mathrm{c}(\sigma_{ii})$ measurement such as Fietz *et al.*'s [140] on REBCO. New measurement techniques may be required to measure single-crystal $T_\mathrm{c}$ under shear strain, and the method to measure the mixed partial derivatives is less obvious.

To reduce the complexity of equation 4.4.12, we can neglect second-derivatives of the normal strains and all mixed partial derivatives, leaving only the second derivatives with shear strain and first derivatives with normal strains. Neglecting the higher order normal strain terms is supported by the linear response of REBCO single crystals to uniaxial strain [140] over the available strain range.

The $T_\mathrm{c}$ response can then be written in terms of hydrostatic and deviatoric strains:

$$\begin{aligned}
\langle \Delta T_\mathrm{c} \rangle = {} & \varepsilon_\mathrm{hyd} \left( \frac{\partial T_\mathrm{c}}{\partial \varepsilon_{aa}} + \frac{\partial T_\mathrm{c}}{\partial \varepsilon_{bb}} + \frac{\partial T_\mathrm{c}}{\partial \varepsilon_{cc}} \right) + \frac{3}{40} \varepsilon_\mathrm{dev}^2 \left( \frac{\partial^2 T_\mathrm{c}}{\partial \varepsilon_{ab}^2} + \frac{\partial^2 T_\mathrm{c}}{\partial \varepsilon_{ac}^2} + \frac{\partial^2 T_\mathrm{c}}{\partial \varepsilon_{bc}^2} \right) + \\
& \frac{1}{10} (\varepsilon_{xy}^2 + \varepsilon_{xz}^2 + \varepsilon_{yz}^2) \left( \frac{\partial^2 T_\mathrm{c}}{\partial \varepsilon_{ab}^2} + \frac{\partial^2 T_\mathrm{c}}{\partial \varepsilon_{ac}^2} + \frac{\partial^2 T_\mathrm{c}}{\partial \varepsilon_{bc}^2} \right) ,
\end{aligned} \tag{4.4.13}$$

where the deviatoric component follows the definition used by ten Haken *et al.* [164], $\varepsilon_\mathrm{dev}^2 = \frac{8}{9}(I_1^2 - I_2)$. For a material with no applied shear strains, the change in $T_\mathrm{c}$ will be controlled by the hydrostatic strains when the single-crystal is more strongly affected by normal strains, and controlled by deviatoric strain when the single crystal behaviour is determined by shear strains. This provides a justification for the use of deviatoric strain as a parameter for the strain response of polycrystalline materials.

### 4.4.2 Nb$_3$Sn strain measurements

Nb$_3$Sn is an intermetallic compound which is used for a number of high-field applications.

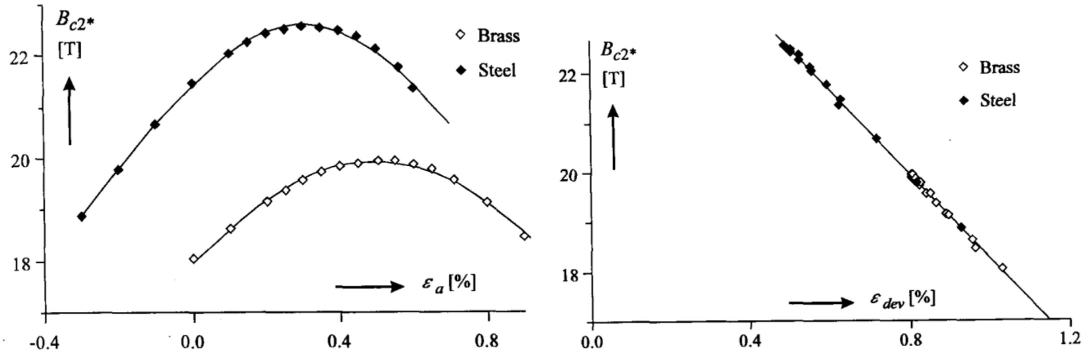

Figure 4.5: Measurements of $B_{c2}^*$ under uniaxial applied strain in Nb3Sn tapes with two different bending beam materials with different Poisson ratios and thermal expansivities. The different materials give different $y$-strains for a given $x$-strain. Left: as a function of applied $x$-strain. Right: as a function of calculated deviatoric strain. Figure from [164]. The thermal expansion coefficients used in the calculation of deviatoric strain are fitted to produce the straight line observed here.

As a brittle material it is challenging to make wound cables from, and a common form of degradation is through brittle failure of individual strands.

Within the reversible strain region, Nb3Sn is also highly strain sensitive, with a parabolic-like behaviour near zero strain and evidence of a weaker drop-off at larger strains [173].

Nb3Sn is almost always produced as a polycrystalline material with a grain size of roughly 100 nm [174]. Some equiaxed grains are observed, but due to the large number of grains and lack of control over texture, an isotropic model for Nb3Sn is likely to be a reasonable approximation.

Figure 4.5 shows measurements on Nb3Sn tapes by ten Haken *et al.* [164] which are well-described by a deviatoric strain model. The thermal expansion coefficients have been fitted to bring the data onto a straight line, with the fitted values approximately 10% smaller than the literature values quoted in the paper. The deviatoric component plotted in figure 4.5 is $\varepsilon_{\text{dev}} = \sqrt{\frac{2}{9}\sum_{i,j}(\varepsilon_i - \varepsilon_j)^2}$ which can be expressed in terms of the principal invariants as $\varepsilon_{\text{dev}}^2 = \frac{8}{9}(I_1^2 - I_2)$.

In ten Haken *et al.*'s work, the $y$-strain is calculated using the Poisson ratio of the bending beam, which implicitly assumes that the bending beam is much stiffer and therefore much thicker than the Nb3Sn. The $z$-strain is calculated using the Poisson ratio for Nb3Sn and the thermal pre-strain is calculated from the thermal expansivity of the bending beam material, again assuming that the beam is thick so determines the mechanical properties of the system. External constraints are neglected so that the thermal contraction of the bending beam can be assumed to be isotropic, and thermal contraction of the Nb3Sn is ignored. The material properties used are given in table 4.4.

The strain state is calculated using [164]

| | Brass | Steel | Nb$_3$Sn |
|---|---|---|---|
| Poisson ratio | 0.25 | 0.25 | 0.4 |
| Thermal strain (measured) (%) | -0.52 | -0.32 | - |
| Thermal strain (ten Haken fit) (%) | -0.47 | -0.29 | - |
| Thermal strain (re-fitted for $I_2$) (%) | -0.49 | -0.31 | - |

Table 4.4: Material properties used to calculate the strain state from ten Haken *et al.*'s measurements [164] for figure 4.5. All parameters apart from the re-fitted thermal strain are taken from ten Haken *et al.*'s paper. The re-fitted thermal expansivities are calculated assuming $B_{\mathrm{c2}}^2 \propto I_2$.

$$\begin{pmatrix} \varepsilon_{xx} \\ \varepsilon_{yy} \\ \varepsilon_{zz} \end{pmatrix} = \begin{pmatrix} 1 \\ 1 \\ \frac{-2\nu}{1-\nu} \end{pmatrix} \delta + \begin{pmatrix} 1 \\ -\nu_{\mathrm{b}} \\ \frac{-\nu(1-\nu_{\mathrm{b}})}{1-\nu} \end{pmatrix} \varepsilon_{\mathrm{a}}, \tag{4.4.14}$$

where $\delta$ is the thermal strain, $\nu$ the Poisson ratio of the Nb$_3$Sn, $\nu_{\mathrm{b}}$ the Poisson ratio of the bending beam and $\varepsilon_{\mathrm{a}}$ the applied strain.

Other strain invariants can equally well describe the data, which imply different results in unmeasured regions of phase space. As ten Haken *et al.* fitted the thermal expansivities, there is considerable scope for choosing a different invariant. Had they chosen the second principal invariant of the total strain, $I_2$, a better agreement would have been found with the measured (literature) thermal expansivities for brass and steel. I have performed a new fit to their data to optimise the thermal expansivities assuming that $B_{\mathrm{c2}}^2 \propto I_2$, shown in figure 4.6, which gives closer values to the measured expansivities than used in ten Haken's fit (see table 4.4). This indicates that $B_{\mathrm{c2}}^2 \propto I_2$ may be a more accurate model for these data, and demonstrates that other strain invariants can give reasonable descriptions of the strain response.

However, ten Haken *et al.*'s data do show that strain invariants linear in the eigenvalues of the strain state, such as $I_1$, do not adequately describe the response, and invariants including quadratic terms, such as $I_2$, $J_2$, $\boldsymbol{\varepsilon} : \boldsymbol{\varepsilon}$, or $\varepsilon_{\mathrm{dev}}$ are needed to model the strain response of Nb$_3$Sn.

We can compare equation 4.4.13 with the measurements by ten Haken *et al.* [164]. Since Nb$_3$Sn is largely a cubic material, we expect the strain derivatives in different crystallographic directions to be equal or at least of the same sign and similar magnitude. This rules out a cancellation by summation of terms of opposite signs in equation 4.4.13, sot the observations of deviatoric strain having greater effect than hydrostatic in Nb$_3$Sn suggests that $\frac{\partial^2 T_{\mathrm{c}}}{\partial \varepsilon_{ab}^2} \gg \frac{\partial T_{\mathrm{c}}}{\partial \varepsilon_{aa}}, \frac{\partial^2 T_{\mathrm{c}}}{\partial \varepsilon_{aa}^2}, \frac{T_{\mathrm{c}}}{\partial \varepsilon_{aa} \partial \varepsilon_{bb}}$ for Nb$_3$Sn.

ten Haken *et al.* have reported $B_{\mathrm{c2}}$ values calculated from extrapolations of Kramer fits to $I_{\mathrm{c}}$ measurements. As the description above for polycrystalline strain response is written in terms of $T_{\mathrm{c}}$, we need to relate $B_{\mathrm{c2}}$ variations to $T_{\mathrm{c}}$ variations. The critical temperature can be written as $\frac{T_{\mathrm{c}}(\varepsilon)}{T_{\mathrm{c}}(0)} = 1 + k\varepsilon_{\mathrm{dev}}^2$. Using the relation $B_{\mathrm{c2}}(\varepsilon) = B_{\mathrm{c2}}(0)(\frac{T_{\mathrm{c}}(\varepsilon)}{T_{\mathrm{c}}(0)})^w$ [161], this can be rewritten for small changes in $T_{\mathrm{c}}$ as $\frac{B_{\mathrm{c2}}(\varepsilon)}{B_{\mathrm{c2}}(0)} = 1 + wk\varepsilon_{\mathrm{dev}}^2$. The model predicts a different exponent of the deviatoric strain than in the linear relation found by ten Haken *et al.*.

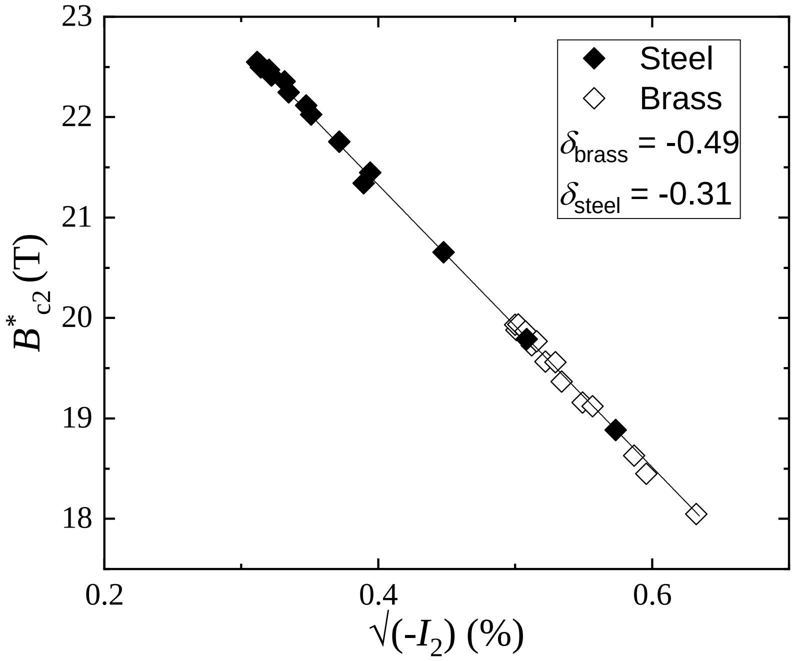

Figure 4.6: The $B_{c2}$ data from ten Haken *et al.* [164] shown in figure 4.5, plotted against the second principal invariant of the total strain, $I_2$, with the thermal expansion coefficients re-fitted for $B_{c2}^2 \propto I_2$.

There does not appear to be sufficient literature on single-crystal $Nb_3Sn$ measurements to determine the relative shear and normal strain dependencies directly.

## 4.5 Scaling law

A scaling law has been developed [173] based on measurements in $Nb_3Sn$, which can predict the critical surface $J_c(B, T, \varepsilon)$. The scaling law was initially developed for LTS, but has subsequently been applied to HTS [161, 175].

The scaling law takes the form:

$$J_c = A(\varepsilon)[T_c^*(\varepsilon)(1 - t^2)]^2[B_{c2}^*(T, \varepsilon)]^{n-3} b^{p-1}(1 - b)^q \tag{4.5.1}$$

The final terms, $J_c \propto b^{p-1}(1 - b)^q$ is similar to the Kramer form for pinning force [176], where in Kramer's derivation $p = 0.5$, $q = 2$.

Kramer calculates the pinning force for flux line shear, and assumes that there is a regular array of strong line pinning sites at a lower density than the flux lattice, such that flux motion occurs by shearing the flux lattice in regions between pins. $p = 0.5$, $q = 2$ are therefore applicable to systems where pinning sites are stronger than the flux line lattice shear strength, and only in sufficiently large applied fields where the flux spacing is smaller than the pin spacing.

Dew-Hughes [177] calculates the pinning force for a variety of pinning types and geometries, both for pinning from normal material and from superconducting regions with different properties. These are sometimes used to diagnose the type of pinning present in a superconductor from measurements of the pinning force. In Dew-Hughes' calculations, $p$ ranges from 0 to 2 and $q$ from 1 to 2 depending on the pinning type. While detailed reference to these pinning types is not made here, it demonstrates that a range of $p$ and $q$ values are expected in real measurements with non-ideal microstructures.

## 4.6 Conclusions

This chapter has discussed some basic properties of REBCO and its manufacture, noting the challenges in producing high-$I_\mathrm{c}$ CCs due to the short coherence length and difficulty in growing thick defect-free layers. The pseudo-single-crystal nature of high-$J_\mathrm{c}$ CCs leads to many interesting behaviours, with the crystallographic orientation of particular importance, which will be discussed in greater detail in chapter 8. The tapes measured for this thesis are ISD, which opens up particularly interesting research possibilities, both with more complex interactions of crystallographic orientation and macroscopic factors such as pinning, and particularly by allowing the possibility of transport current with a component in the $c$-axis direction.

Existing literature on single-crystal strain measurements and elastic properties of REBCO have been summarised, which will be used in a new model for the strain response of CCs, outlined in chapter 8. Finally, existing models for understanding strain behaviour in REBCO and $Nb_3Sn$ have been outlined which provide the basis for understanding and predicting the strain response of CCs to inform the design of large magnets and other systems with CCs in complicated strain states.

Chapter 5

# Miniature Strain Board for Resistivity Measurements

## 5.1 Introduction

This chapter describes a new strain board design for performing low-current measurements on strain samples in a much smaller volume than is possible for existing strain apparatus. A brief outline of irreversibility field measurements is given in section 5.2. Simulation results are presented for the expected performance of the strain board in section 5.3.

Performing measurements in high magnetic fields opens up new regions of phase space to probe the critical surface of superconductors. Typically for high-field magnets, the bore size is relatively small, which limits the space available for large current leads or bulky strain apparatus. Here in Durham, we have a physical properties measurement system (PPMS) which can apply magnetic fields up to 9 T and variable temperature from room temperature to roughly 4 K. In such a system, high-cross-section current leads which are required for large transport currents would not be compatible with the sealed cryostat, and would cause unacceptable heat losses by conduction even if the PPMS were modified. Additionally, the field is fixed to be parallel to the magnet bore, which limits the range of field angles available.

To overcome the limitation of the magnetic field angle, a rotator can be used which uses a drive-shaft to rotate a small platform within the magnet bore to change the relative orientation of the sample to the applied field. This limits the available space for apparatus to a hemisphere defined by the rotating platform with a radius equal to the shortest distance to the magnet bore walls.

Despite high-current measurements not being possible in the PPMS, the high degree of flexibility from automatic control of magnetic field, temperature and angle with wide ranges of each allows for many measurements that could not be performed as easily with a high-current probe. Additionally, there are a number of high-field facilities around the world which provide much stronger magnetic fields than can be generated by the PPMS, and typically have similar size restraints, so experimental apparatus for the PPMS could also be used in these high-field facilities. This would allow for strain measurements to be made under a greater range of conditions than are possible at present.

## 5.2 Resistivity measurements

An alternative to a transport current measurement that does not require large currents is a resistivity measurement. In this case, a small fixed current, typically of order 0.1 A, is applied and either the temperature or magnetic field is swept to cause a transition. From this measurement, the irreversibility field at a given temperature, strain and angle can be calculated.

Some authors have measured the irreversibility field of REBCO as a function of strain by extrapolation of pinning force curves [157, 178]. This method allows for the calculation of the irreversibility field from transport measurements by extrapolating to $J_\mathrm{c} = 0$, but if the irreversibility field is above the experimentally available field, an error associated with the extrapolation is present. The measurements by Shin *et al.* [178] have small extrapolations from 5 T for all $B_\mathrm{irr}(\varepsilon)$ and in van der Laan *et al.*'s measurements [157], some of the high temperature measurements are within the 8 T they measured to, but some measurements were extrapolated as far as 25 T with large associated uncertainties.

Measurements made within the group here in Durham [92, 179] have been able to determine the irreversibility field as a function of strain in a SuperPower tape up to 14 T using a transport probe with a variable temperature cup. While these measurements go to higher fields and consequently lower temperatures than are available in the PPMS, they are considerably more expensive to run due to the helium boil-off associated with the horizontal magnet and large current leads.

Irreversibility fields have also been measured at much larger magnetic fields but not as a function of strain [3, 127, 180, 130]. A strain probe which is compatible with the PPMS and high-field magnet facilities would be of great use to measure the irreversibility field as a function of strain more cheaply in the PPMS or at much higher fields in a high-field facility.

## 5.3 Miniature strain board design

The key challenge for such a device is to miniaturise the strain application apparatus. The volume available on the PPMS rotator is a 13 mm radius hemisphere and a maximum width of 16 mm, which is considerably smaller than the existing strain boards within the group.

Several designs were considered, with the final design chosen for its relatively large strain range and good degree of strain homogeneity. The strain board is made from Berylco, as are the strain boards used in the group for transport measurements, for its large elastic limit which is essential to reach high strains without catastrophic failure at cryogenic temperatures. Berylco is also solderable which makes sample mounting much more straightforward. The strain is applied by threaded rods and nuts, which can be made out of non-magnetic steel. The design tolerances are such that the two nuts have to be tightened while the flat surface of one is facing the other to avoid the corners of the nuts fouling each other. A drawing of the design is shown in figure 5.1. To apply tensile

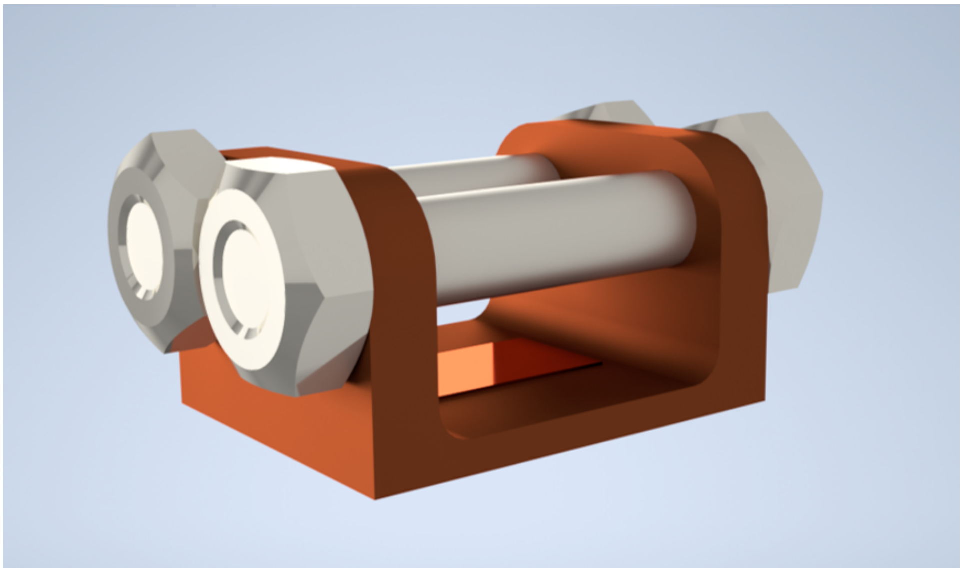

Figure 5.1: CAD drawing of the miniature strain board design. The Berylco component is 14 × 11 mm on the base and 8 mm tall, and the strain is applied by tightening the nuts on the threaded rods.

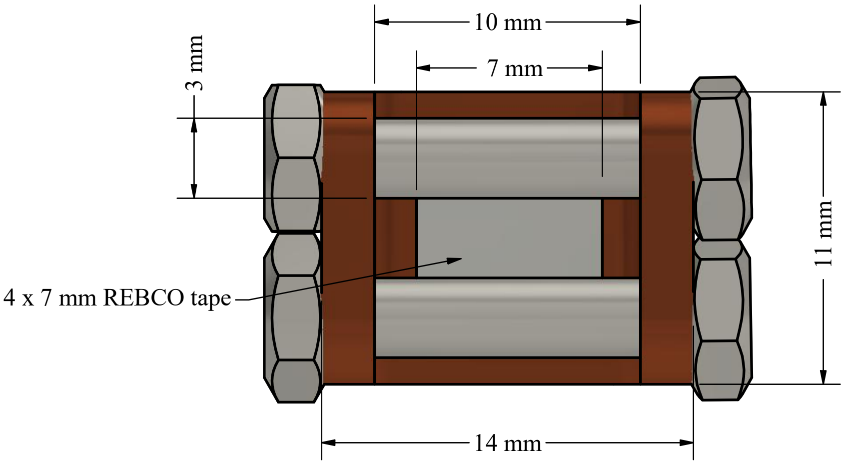

Figure 5.2: Top-down scale schematic of the miniature strain board design, including the threaded rods, nuts and sample.

strains to the bed, the nuts can be placed on the inside and moved outwards to push the walls outwards. The strain board is designed for a sample that is 4 mm wide and 7 mm long. Strain is applied a room temperature, but a large number of measurements could be made at a fixed strain in the PPMS. The room temperature application of strain does have the limitation of a thermal cycle between strains, so a larger number of strains and thermal cycles may be required to account for any random variation between properties on a thermal cycle to room temperature.

Finite element analysis (FEA) simulations have been performed to evaluate the expected performance of the design. The strain distribution across a sample is challenging to measure experimentally, so simulations give a good idea of the uniformity and likely strain range.

Simulations have been performed in Autodesk Inventor. The design gives a highly uniform

$X$-strain across the width of the sample, with the strain components and a tensile simulation shown in figures 5.3-5.6. As is usually the case for uniaxial strain boards, the simulations indicate a much more uniform strain distribution than is possible on the 2D strain board used for measurements in chapter 8.

The effective Poisson ratio of the strain board is much lower than the material Poisson ratio due to the shape, with an effective Poisson ratio of -0.09 at the centre of the sample, and -0.17 when 0.2 mm from the edge of the sample. The stiffer end pieces are not under any significant $X$-strain so do not have a large $Y$-strain generated by the Poisson effect. As these parts are mechanically stiffer than the sample region, they cause the $Y$-strain at the sample to be lower than would be expected from the Poisson ratio of the material. The use of a capital $X$, $Y$ are to specify that the strains refer the co-ordinates of the strain board.

The $Y$-tension on the strain board is limited to the edges of the board as the centre of the board is constrained by the thicker end pieces to have close to zero $Y$-strain, whereas the top edges are free to be in $Y$-tension from the Poisson ratio effect. A similar mechanism is seen for the localised $Y$-tension in the tape (the red regions in figure 5.4), where the bottom surface of the tape and the central region of the tape are constrained to have very small $Y$-strains by the strain board it is bonded to (which is in turn constrained to have small $Y$-strain by the stiffer end-pieces), whereas the top edges are free to be under $Y$-tension as would be expected from the Poisson ratio as the sample is under $X$-compression. This effect works the other way for the $X$-strain on the sample, where a green band of very low $X$-strain is seen on the top corner at the end of the sample in figure 5.3 where the edge causes a region where the force from the board is not transmitted to the sample and therefore a small region of much lower $X$-compression. The shear strains are small compared to the applied $X$-strain, which is desirable as they are challenging to measure experimentally. Slightly larger $Y$-strains are observed in tension (figure 5.7) than in compression, but these remain small.

Simulations of the Poisson ratio are particularly important as the commercially available $xy$-strain gauges used for the biaxial measurements are too large for the small sample area available in this design. Uniaxial strain gauges are likely to be used measuring only the $X$-strain, and the $Y$-strain would be inferred from the simulated effective Poisson ratio.

A high degree of uniformity of $Y$-strain is also achieved by the design, and shear strains are very small (see figure 5.5). Because the nuts are hand-tightened, a possible mismatch in the force from each rod is possible. Simulations have been performed to check how sensitive the design is to such a mismatch. Figure 5.8 shows a simulation with a 10% difference in the force on each rod. The gradient in the strain is well within the required tolerances, so even force mismatches well in excess of 10% are not likely to compromise experimental measurements. This result gives confidence that the design is robust to mismatched tightening and no controls are required beyond ensuring by eye that the number of turns are equal on both rods.

A prototype miniature strain board has been constructed to the design shown above. Room-temperature tests were undertaken using a small 1D strain gauge manufactured by HBM (1-LY15-0.3/120) [181]. The board was measured at -0.7636(4)% strain on the

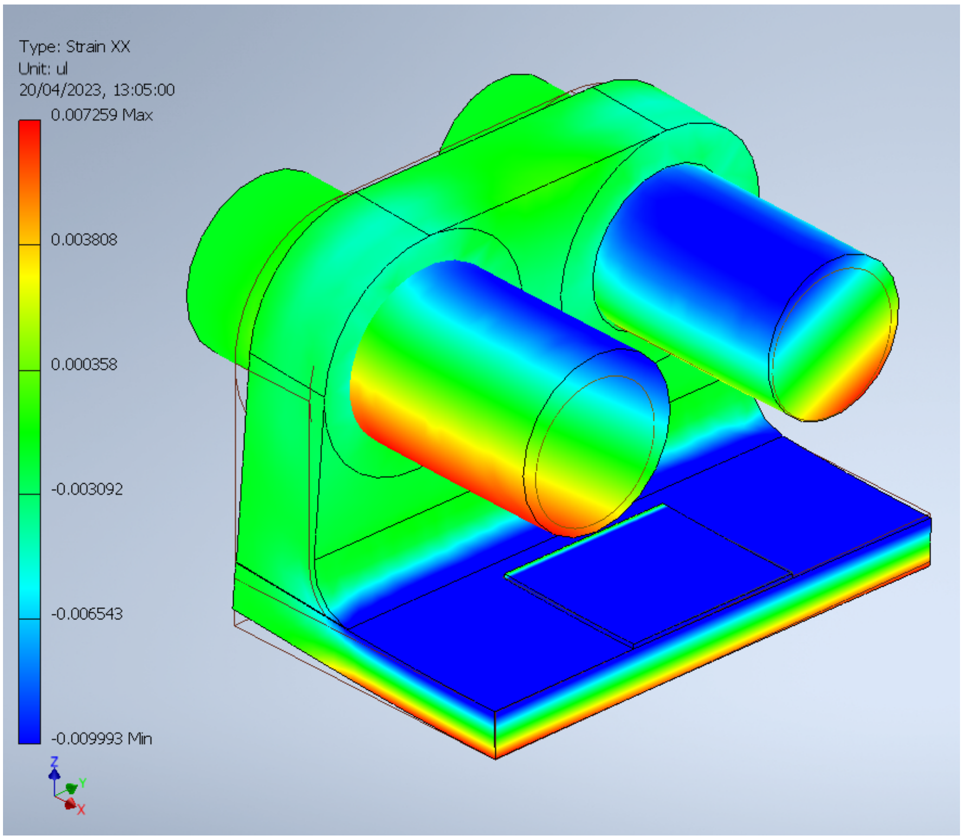

Figure 5.3: FEA simulation of the $X$-strain profile on the new design with -1% strain applied. Only half of the board is simulated and appropriate boundary conditions applied due to the symmetry of the board. A high degree of strain uniformity is observed across the majority of the sample.

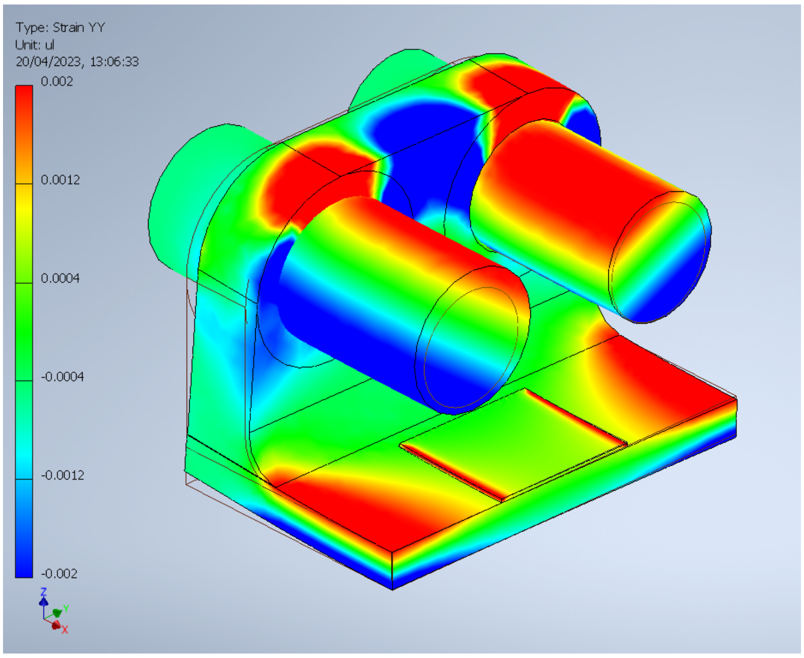

Figure 5.4: FEA simulation of the $Y$-strain profile on the new design with $\varepsilon_X = -1\%$, showing only very small off-axis strain components at the sample.

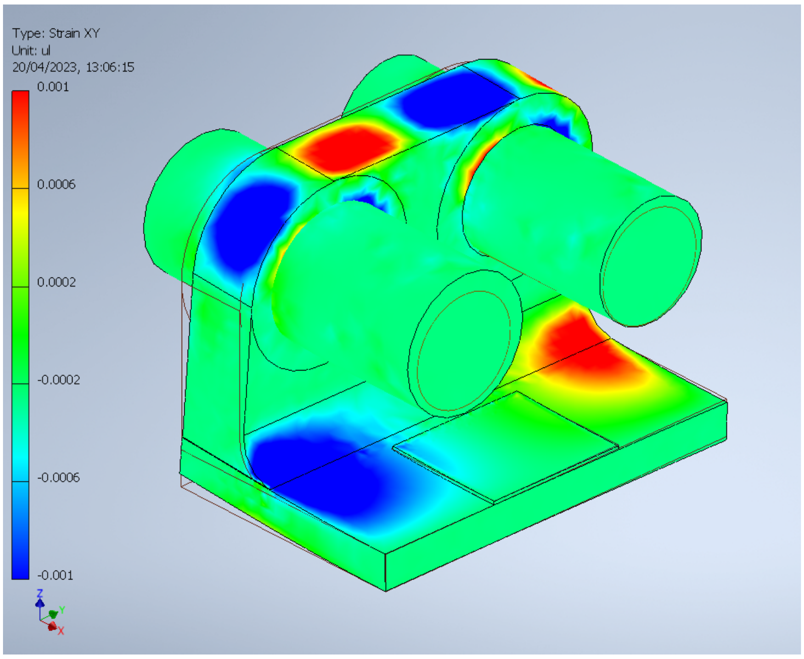

Figure 5.5: FEA simulation of the $XY$-shear strain profile on the new design with $\varepsilon_X = -1\%$, showing extremely small shear strains applied to the sample.

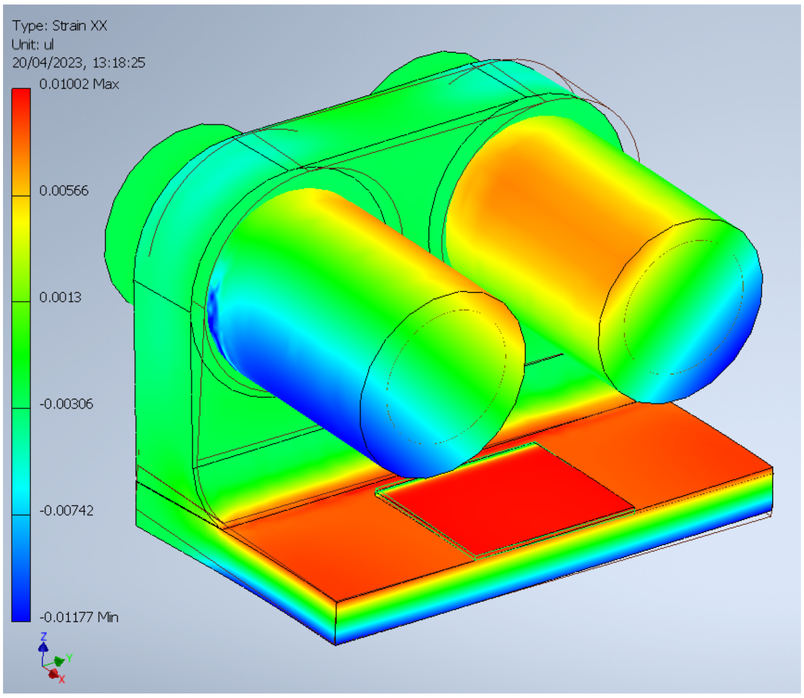

Figure 5.6: FEA simulation of the $X$-strain profile on the new design, with $\varepsilon_X = 1\%$.

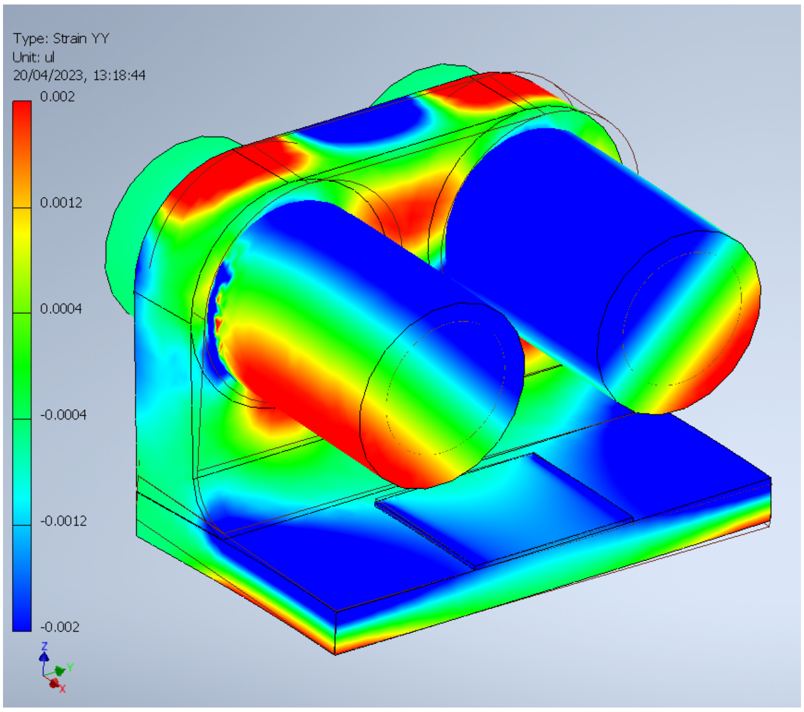

Figure 5.7: FEA simulation of the $Y$-strain profile on the new design, with $\varepsilon_X = 1\%$.

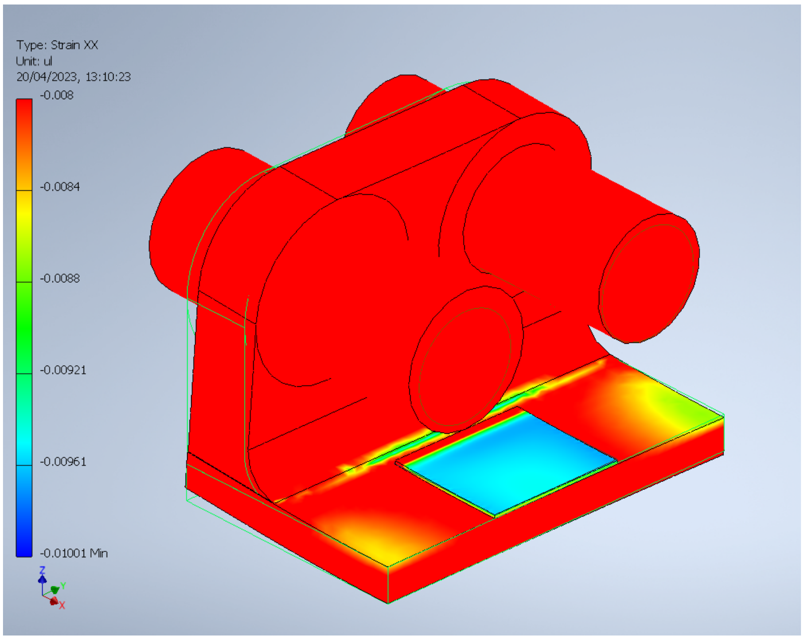

Figure 5.8: FEA simulation of the $X$-strain profile on the new design, with a 10% difference in the force applied by each rod. Note that the colour bar is much more zoomed-in than for the previous figures, to show the degree of variation. The strain gradients across the sample are extremely small even with the mismatched loads.

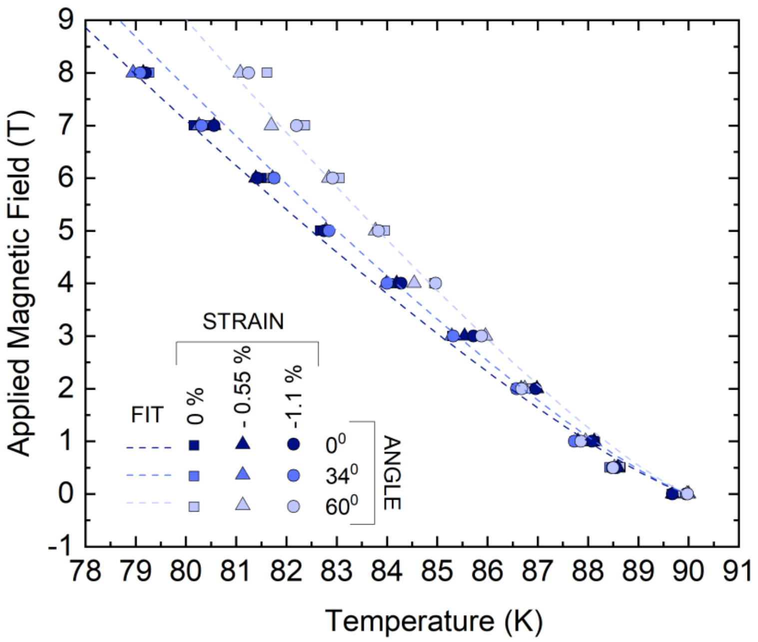

Figure 5.9: Measurements of the irreversibility field of a CC as a function of temperature, magnetic field angle and strain performed by Gillard *et al.* on a version of the miniature strain board design presented in this chapter. Figure from [182].

sample surface with a simultaneous strain of 0.5926(3)% on the back surface of the board. The strain board was taken to a higher strain of 0.9879(9)% strain on the back surface but with no reading made on the sample surface due to a strain gauge leg failure during strain application. If the ratio from front to back remained linear, this would correspond to a sample strain of -1.273(1)% at room temperature with no observable damage to the strain board, with a slight plastic deformation observed on release of the strain. As strain is applied only at room temperature, catastrophic failure would not occur at strains above the elastic limit, and strains in excess of -1.3% are likely to be achievable. The strain gauge failure could be made much less likely by the construction of a dedicated strain application rig to eliminate board motion during strain application.

Performing cryogenic measurements on the miniature board to measure CCs were not possible within the timeframe of this thesis, but the design has been taken forward and a further iteration of the design has been used by Emma Gillard, also a member of the Durham University Superconductivity Group. She has been able to measure the irreversibility field of a SuperPower CC as a function of strain using the PPMS [182]. Data measured by Gillard *et al.* up to 8 T at different field angles are shown in figure 5.9.

The strain range of the miniature board and the potential for high-field measurements over a large range of phase space make this an exciting avenue for future measurements to better understand the behaviour of CCs in magnetic applications.

## 5.4 Conclusions

A new design of strain board has been made and a prototype constructed and found to exceed the minimum design strain range. A miniaturised strain board has the potential to make high-field measurements at facilities with magnet bores too narrow for high-current measurements, or with the use of an inserted rotator to allow for field rotation within a vertical magnet. An iteration of the miniaturised strain board design has been used by another member of the group to make strain measurements in the PPMS.

Chapter **6**

# Metrology of Biaxial Strain Measurements of Coated Conductors

## 6.1 Introduction

This chapter details the experimental setup for strain measurements and modifications to a new biaxial strain probe. Many of the data shown in this chapter were first published in the author's paper presented at EUCAS 2019 [1]. A straightforward mechanical scribing technique is demonstrated that can safely be used to reduce the width of the samples without damaging them. Features of the angular variation of $I_c$ in ISD CCs are investigated, including the large change in $J_c$ that occurs when the direction of the magnetic field is reversed, associated with the changes in surface pinning. Other details key for experimental procedures are investigated, including heat treatments and using short samples.

## 6.2 Experimental setup

The samples measured for this thesis are 12 mm wide $GdBa_2Cu_3O_{7-\delta}$ ISD CCs fabricated by THEVA. During their fabrication, MgO is deposited on a Hastelloy C-276 (UNS N10276) substrate, inclined at an angle to the vapour spray to produce a faceted biaxially textured surface for REBCO growth. The crystallographic orientation of the MgO buffer layer controls the orientation of the CuO superconducting *ab*-planes, which are inclined at $\sim 30°$ to the tape surface [183]. The REBCO layer is coated with silver and the whole tape coated with copper as a stabiliser. The REBCO layer thickness is $\sim 3.5\,\mu m$.

All data presented here are derived from electric field–current density, $E$-$J$, transport measurements. Typical data are shown in figure 3.2, with a noise level $< 3\,\mu V\,m^{-1}$, well below the transition onset threshold of $10\,\mu V\,m^{-1}$. These data are used to extract the values of the critical current, $I_c$, defined using an electric field criterion of $100\,\mu V\,m^{-1}$ and the index of transition, $N$, calculated between $10\,\mu V\,m^{-1}$ and $100\,\mu V\,m^{-1}$.

Strain measurements have been made on a newly commissioned biaxial strain probe, designed by Jack Greenwood [179]. The probe is designed to deliver high currents to a sample board which sits within a 40 mm magnet bore. A field is applied by an external split-pair electromagnet with a Dewar between the magnet poles which contains the sample board and probe end. A water-cooled copper electromagnet has been used for measurements which can deliver a field up to 0.7 T and the superconductor is cooled with liquid nitrogen at 77 K. The probe has successfully delivered 700 A to samples and may well support higher currents, especially if more of the busbars were cooled in a longer Dewar. Higher currents were not necessary for the measurements made here as the self-field $I_\mathrm{c}$ of THEVA CCs is just under 700 A at 77 K.

Current is measured from the voltage across a calibrated shunt in series with the probe. Sample voltage is measured by a pair of voltage taps soldered onto the sample approximately 1 cm apart, and amplified by a factor of $5 \times 10^4$ before measurement with a Keithley voltmeter.

The new biaxial strain probe has *in situ* control over $X$-strain from a movable rod that runs the length of the probe and can be moved by a strain jack at the room-temperature end. The $Y$-strain can be applied on the bench with bolts but necessarily includes a thermal cycle to room temperature to change the $Y$-strain. A capital $X$ and $Y$ are used to specify the co-ordinates along the length and across the width of the strain board respectively.

As biaxial strains are applied, a measurement of the 2D strain state is required. This was achieved by using an $xy$-rosette strain gauge manufactured by HBM (1-XY91-1.5/120) [181]. The strain gauge contains two grids of wire laid on top of each other with a 90° rotation. Each grid is highly sensitive to one particular strain orientation with the majority of the wire oriented in that direction. The change in length of the wire changes the resistance which is measured by a 4-point resistance measurement. As a high precision resistance measurement is required to accurately measure strains, the voltage response from the strain gauge is time-averaged with a constant current, and a polarity switch is employed to remove any zero-offset error, implemented in in LabView. Details of this and other code used for this thesis can be found in appendix C.

Due to design constraints, the strain is not uniform over a large area of the strain board, so strain measurements within the measurement region are required. As the strain gauge is mounted within the voltage tap region, the size of commercially available 2D strain gauges presents a practical lower limit on gauge length and therefore sample size for strained measurements. The strain gauges used are 5 mm wide, so voltage taps were typically 7 mm apart for short samples.

Care is needed with the contacts on the strain gauge as poor quality of contacts can lead to drifts in voltage at constant strain, which may be due to heating. Each grid has a small transverse sensitivity, so a correction is applied when determining the actual strain state from the measurements:

$$\boldsymbol{\varepsilon} = \frac{1}{1-\tau^2}\begin{pmatrix} 1 & -\tau \\ -\tau & 1 \end{pmatrix} \boldsymbol{\varepsilon}_{\mathrm{meas.}} \tag{6.2.1}$$

where $\tau$ is the transverse sensitivity, which for the strain gauges used is 0.8%.

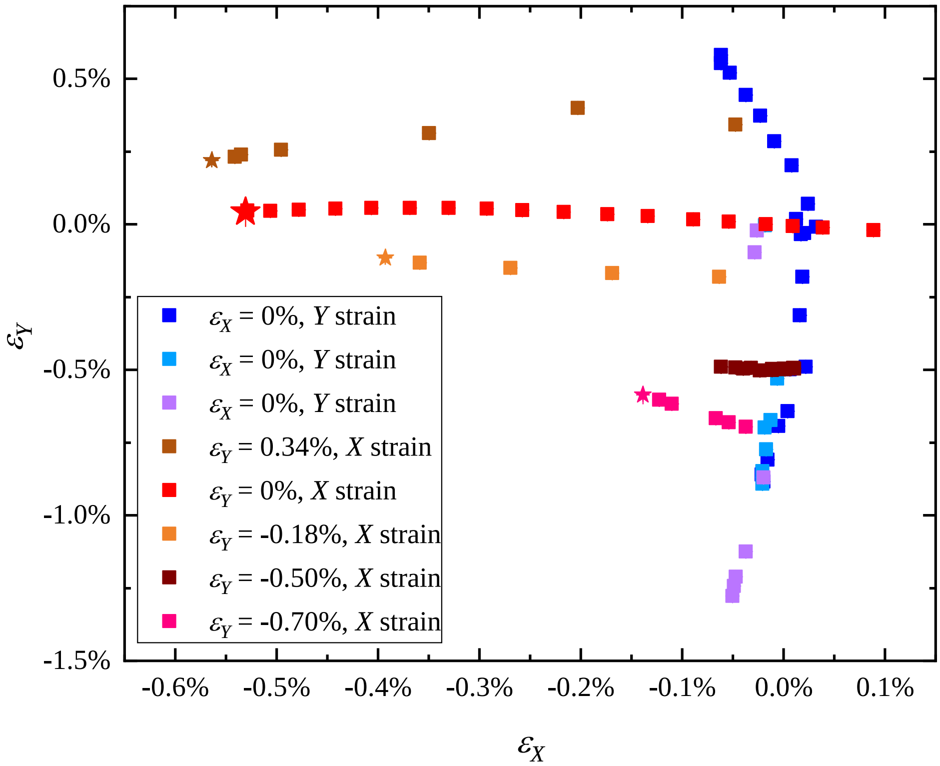

Figure 6.1: Strains measured at room temperature on the top surface of the 1 mm thick strain board. Stars represent the points at which the board was deflection limited.

In all cases for cryogenic measurements, the zero-strain is measured on initial cooldown and all subsequent strains measured on the same sample are made relative to this initial strain. Measuring relative to first cooldown eliminates any temperature dependence of the strain gauge resistance, but it does mean that the change in thermal strain between room temperature and 77 K is not included and in each case only the strains due to mechanical bending of the strain board are measured. If further measurements were to be made then the temperature sensitivity of the strain gauges could be calibrated by attaching them to a material with known thermal expansivity, which would enable the thermal strain induced by cooling down the strain board to be measured. To obtain the true strain state of the REBCO, the thermal strains generated by the manufacturing process would also need to be accounted for. This could be determined by measuring the crystallographic axis lengths, for example using X-ray diffraction [146].

## 6.3 Modifications to biaxial strain probe

As a newly designed piece of equipment, a number of changes were required to make it operational and several other modifications and improvements have been made. The initial design called for a 1 mm thick strain board, which the author tested at room temperature. The results obtained are shown in figure 6.1.

Calibration between the top and bottom faces of the strain board showed a good agreement between the $Y$-strains for all $X$-strains (figure 6.2). However, the equivalent relationship between the $X$-strain states on the top and bottom depended on the $Y$-strain state, as

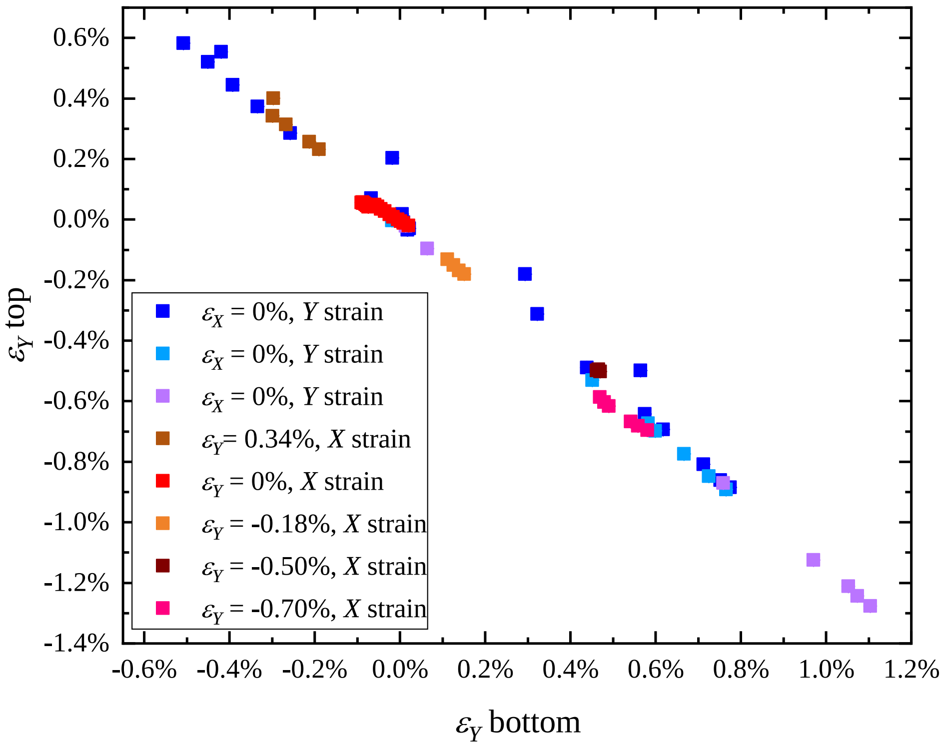

Figure 6.2: Calibration between the $Y$-strains on the top and bottom surfaces of the 1 mm thick strain board, measured at room temperature.

shown in figure 6.3.

The strain range of the original board was limited by the space available to the board under strain and is indicated by the stars in figure 6.1. To increase the strain range, the strain application rod was thinned down to increase the space available for deflection and the strain board thickened. A thicker strain board increases the distance of the sample from the neutral axis which increases the strain for a given deflection.

Simulations of the board performance were made using FEA in Autodesk Inventor. These simulations are linear and do not account for plastic deformation, but give an idea of the likely strain homogeneity for a particular geometry.

The change in sign of Poisson's ratio observed in figure 6.1 when applying positive or negative $y$-strain is not reproduced in FEA modelling, and was also not observed on the new 2 mm thick board. FEA for the 1 mm board under $Y$-tension is shown in figure 6.4. The simulated Poisson ratio for $Y$-strain in this geometry is 0.13, compared to the measured 0.08 in $Y$-compression and -0.18 in $Y$-tension. The calculated Poisson ratio for applied $X$-strain is 0.017, in agreement with the very shallow gradient of the applied $X$-strain measurement (in red in figure 6.1).

As the pillars for $Y$-strain application provide a stiffening effect, the peak strain under $X$-strain application is not centred in the measurement region. This is illustrated in figure 6.5 which shows a reasonably uniform strain of 0.5% around the measurement region with applied $X$-strain, but a peak strain in excess of 1% along the current path. A practical consequence of this is a reduced strain range, as the board will catastrophically fail long before the measurement region reaches the plastic limit of beryllium copper. This was

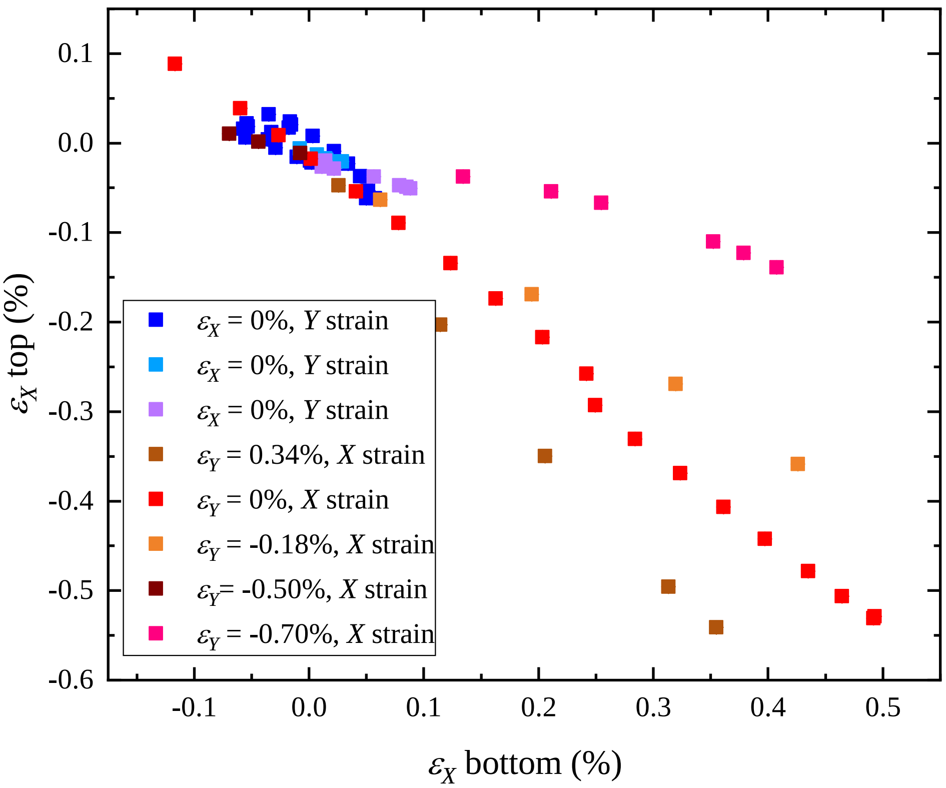

Figure 6.3: Calibration between the $X$-strains on the top and bottom surfaces of the 1 mm thick strain board, measured at room temperature.

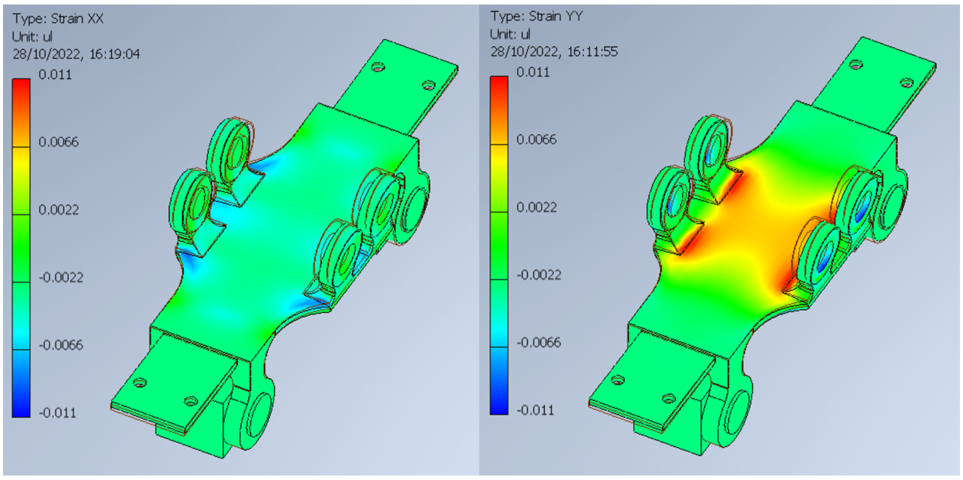

Figure 6.4: FEA simulation in Autodesk Inventor of the 1 mm strain board with an applied $Y$-tension of $\varepsilon_Y = 0.74\%$ in the center. Left: $X$-strain distribution. Right: $Y$-strain distribution.

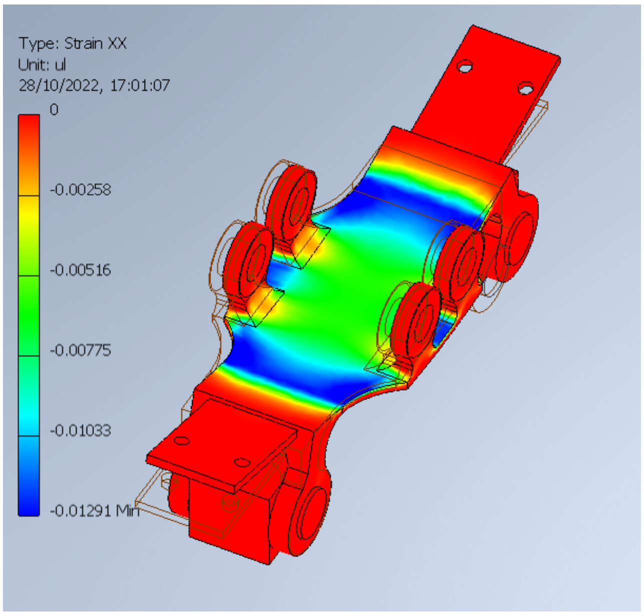

Figure 6.5: FEA simulation in Autodesk Inventor of the 1 mm strain board with an applied $X$-strain of $\varepsilon_X = -0.5\%$ in the center.

observed on the thin (1 mm) board which snapped at a sample strain of -0.56% in cryogenic conditions.

For long samples which cross the peak strain region, it is hoped that current transfer is sufficiently good that current shunted through the copper stabiliser when the peak strain region has $I_c$ suppressed can re-enter the REBCO layer before reaching the measurement region. The short transfer length between the copper stabiliser and the REBCO layer in commercial CCs of order 0.1 mm [184, 185, 186] means that only if current is shunted into the strain board or a large degree of heating occurs would this cause a problem. Heating from current shunting would likely suppress $I_c$, which would manifest as steeper decreases in $I_c$ with strain and possibly shallower increases depending on the strain profile.

The electrodes on the strain board were redesigned to move the current injection to the top surface of the sample and extend the beryllium copper surface so the sample is soldered onto one continuous piece, ensuring a high precision flat surface. It is preferable to mount samples with the superconducting layer up (i.e. on the top surface) to avoid the REBCO needing to support the stress require to bend the Hastelloy substrate. This reduces the chance of sample failure. With the superconductor nearest the top surface of the tape, current injection to the top surface is also preferable to reduce the injection length and associated heating.

Some components were also redesigned to allow for additional insulation to be added and eliminate shorts discovered upon assembly.

## 6.4 Error analysis

Strain measurement errors are derived primarily from the noise of the voltage signal. Because the measurement is of a small difference, systematic errors in the current source and voltmeter are relatively unimportant unless they drift between measurements.

Some uncertainty arises from the copper layer between the REBCO and the strain gauge. As a soft material, this could plastically deform generating a strain gradient that is hard to predict. In the worst case, the copper could debond from the silver/REBCO causing the strain gauge to under-read the strain state of the REBCO. Any delamination or plastic flow between the REBCO layer and the strain board will be transmitted to the strain gauge and is therefore automatically accounted for. A small correction could be applied for the increased distance of the strain gauge from the neutral axis. While the geometry of the strain board makes a precise determination of the neutral axis challenging,

For critical current measurements, a wide range of errors are included. As there are multiple stages of fitting, the errors need to be propagated appropriately. The first step in the calculation of $I_\mathrm{c}$ is to perform a baseline correction. This fits a straight line through the first section of the trace, which is extrapolated through the transition and subtracted from the measurement. This eliminates any background voltage (zero-offset error) and any linear resistive component within the voltage tap region.

The $N$-value is unaffected by multiplicative changes to current and voltage measurements, so the only errors that need to be considered are the baseline correction and the error in the fit of $N$ to the transition. Uncorrelated errors can be combined using the standard result $(\Delta a)^2 = \sum_i \left( (\frac{\partial a}{\partial x_i} \Delta x_i)^2 \right)$ [187]. An error is expected due to current shunting through parallel current paths. The degree of current shunting is determined by the shunt resistance which is challenging to measure at cryogenic temperatures. The shunt resistance would typically be determined by making a measurement just above $T_\mathrm{c}$ of the superconductor to find the cryogenic resistance with the effect of the superconductor subtracted. As variable temperature measurements were not possible with the biaxial probe, this has not been done for the measurements presented here. The effect is expected to be small, with Branch *et al.* [175] finding a shunted current fraction of roughly $10^{-3}$ on the unixaial strain board used in the group. For short samples, discussed in more detail below, the question of current shunting is more pressing due to the reduced superconducting length and a comparison between short and long samples is required to provide an estimate of the current shunting.

## 6.5 Mechanical scribing to reduce cross-section

Reducing the cross-section of the tape allows for measurements of higher critical current densities which opens up new areas of phase-space at low fields. Bridges have been patterned on CCs using chemical etching [128, 188, 189], photolithography [190, 191, 192] and laser ablation [193, 194, 195]. Mechanical scribing has also been used as a means of reducing AC losses [196].

Here, a simple scribing method has been used to reduce $I_\mathrm{c}$. The REBCO cross-section is reduced by scribing deep tracks into the tapes using a diamond-tipped scribe and a template. The bridge has an 8 mm region of constant width and curved ends to minimise crack nucleation at corners. The regions outside the bridge are heavily scored to prevent

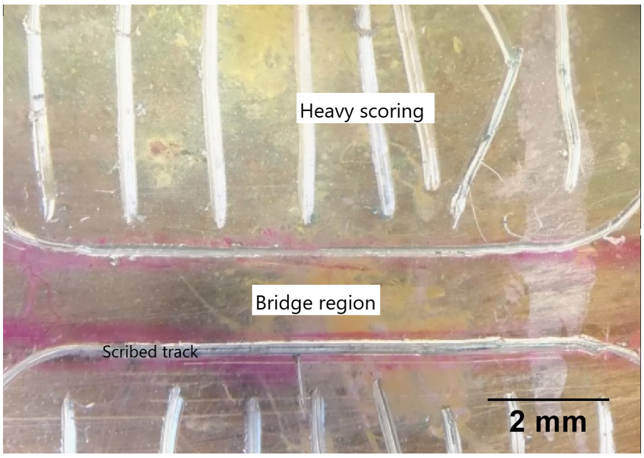

Figure 6.6: Image of a scribed bridge. The bridge is 8 mm×1.5 mm and simply produced with a diamond-tipped scribe and template.

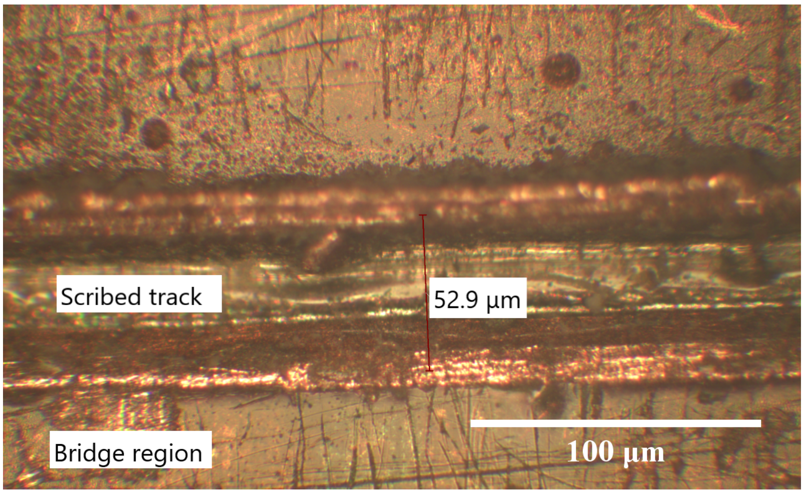

Figure 6.7: Magnified image of a scribed part of a bridge, showing that the material is cut down to the Hastelloy substrate. The groove left by this scribe is measured to be 53 µm wide.

any effects of current leakage across the tracks. A typical bridge is shown in figure 6.6 which is 1.5 mm wide. The tracks are roughly 50 µm wide and have cut through the copper, REBCO and buffer layers to the Hastelloy substrate, as shown in figure 6.7. Figure 6.8 shows that $I_c$ scales linearly with the bridge width over the range of fields measured, and the shape of the angular variation is preserved (figure 6.9). $I_c$ is too high to make low-field measurements on the as-supplied 12 mm tape on the previous probe available in the group. While the new biaxial strain probe does allow for the full low-field range on 12 mm width tapes, the phase space available would still be much greater at lower temperatures where the increased $J_c$ would limit the field range available without scribing. $J_c$ has been calculated using the measured bridge width and a nominal thickness of 3.5 µm, with the uncertainty associated predominantly with the width of the damaged region.

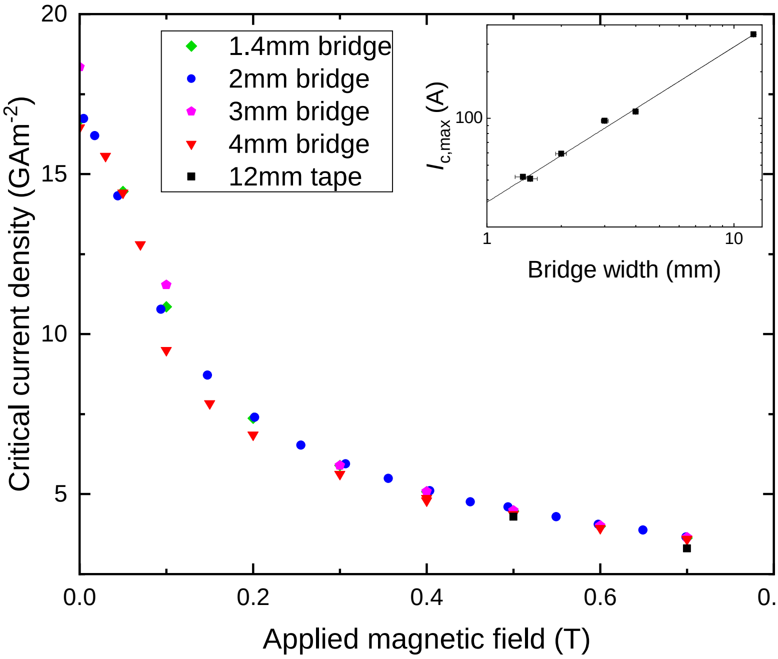

Figure 6.8: A comparison between the field dependence of $J_\mathrm{c}$ for bridges of different widths at 77 K for $B \parallel c$. The different bridge widths show good agreement across the field-range. Inset: $I_\mathrm{c}$ variation with bridge width when $B \parallel ab$, with a linear fit through the origin.

## 6.6 Angular $J_\mathrm{c}$ measurements

The angular dependence of $J_\mathrm{c}$ is shown in figure 6.10, measured up to 0.7 T. The inclined CuO planes shift the peak in $J_\mathrm{c}$ away from 0° to $\sim 30°$. A shoulder feature at $B \perp$ tape is also observed, which is weaker at low fields. A similar feature, a peak at $B \perp$ tape rather than a shoulder, has been seen in an ISD tape previously [128]. The data reported here are from a number of different samples with differing bridge widths, as not all measurements were made on every sample. Unmounting the sample damaged the tape, so some measurements which were introduced later could only be performed on a limited set of the samples. The $J_\mathrm{c}$ data for all samples measured are broadly similar (once scaled by the bridge width).

An empirical relationship between $J_\mathrm{c}$ and the index of transition, $N$, has been found in LTS [197], with

$$N(B,T,\varepsilon) = 1 + r(T,\varepsilon)[J_\mathrm{c}(B,T,\varepsilon)]^{s(T,\varepsilon)}. \tag{6.6.1}$$

This is observed, as shown in figure 6.11 for $B \parallel c$, for a sample with a 4 mm bridge. The deviations at higher currents are attributed to heating during the transition. Figure 6.12 shows this relation also applies for $J_\mathrm{c}$ measurements over a range of angles, with similar $r$ and $s$ values as shown in table 6.1.

The $N$ values are similar ($\approx 20$ for $B = 0.5\,\mathrm{T}$) for both the 1.4 mm and 4 mm bridge widths, suggesting that the damage region is small compared to the bridge-width. Reliable $N$ values were not obtained on the full-width tape due to heating at the high currents. Some bridged samples also exhibited heating effects (i.e. inconsistent $N$ values), which

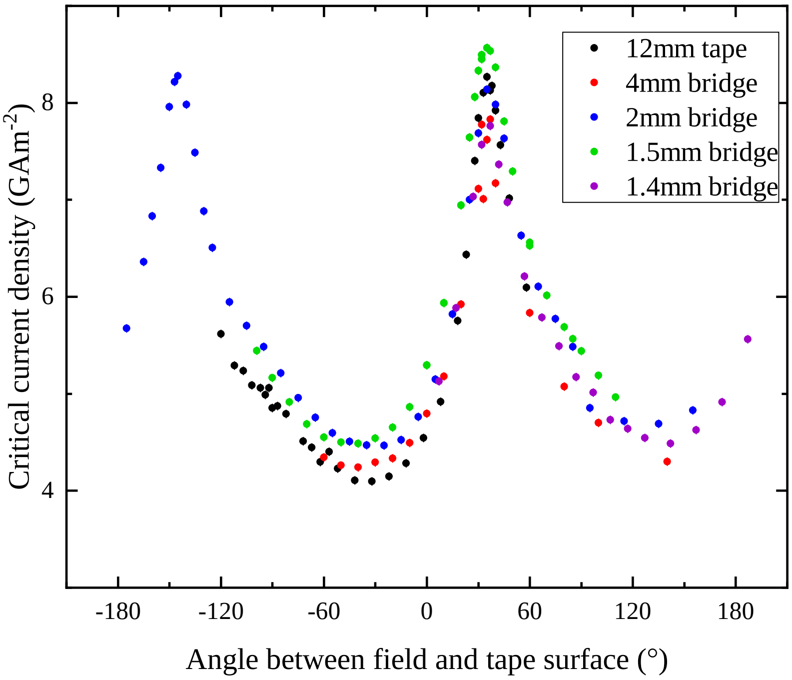

Figure 6.9: The angular variation of $J_c$ for the as-supplied 12 mm tape and different bridge widths. All measurements are at 0.5 T and 77 K. The angular dependent shape is preserved to within a relatively small error in the scaling factor.

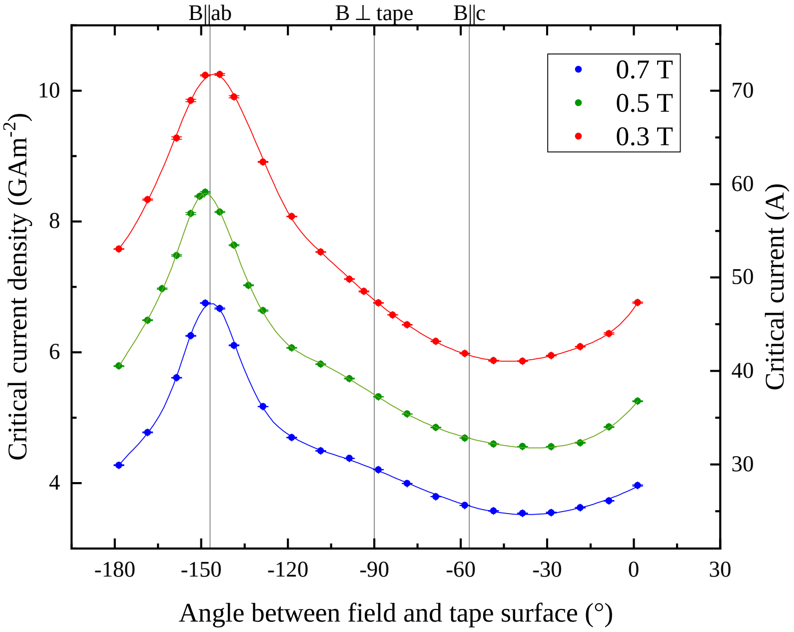

Figure 6.10: The angular dependence of $J_c$ at three magnetic fields on a sample with a 2 mm bridge. The *ab*-peak is shifted by 30° due to the angle between the *ab*-planes and the tape substrate. Also apparent is a shoulder feature when $B \perp$ tape.

is attributed to the resistance of the current injection point. $N$ values for these samples have not been reported.

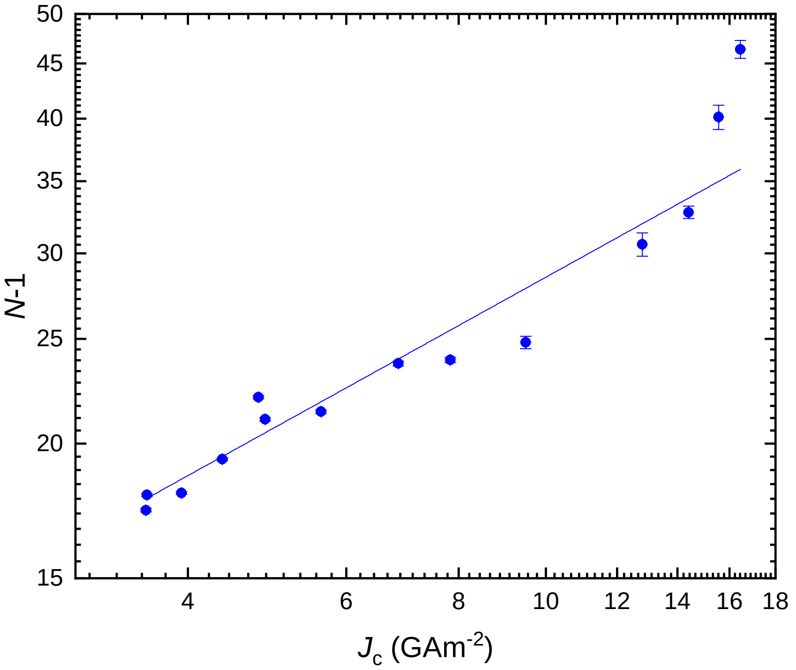

Figure 6.11: Index of transition versus critical current density with $B \parallel$ c for a 4 mm bridge. The non-linear behaviour at higher currents is attributed to heating during the transition.

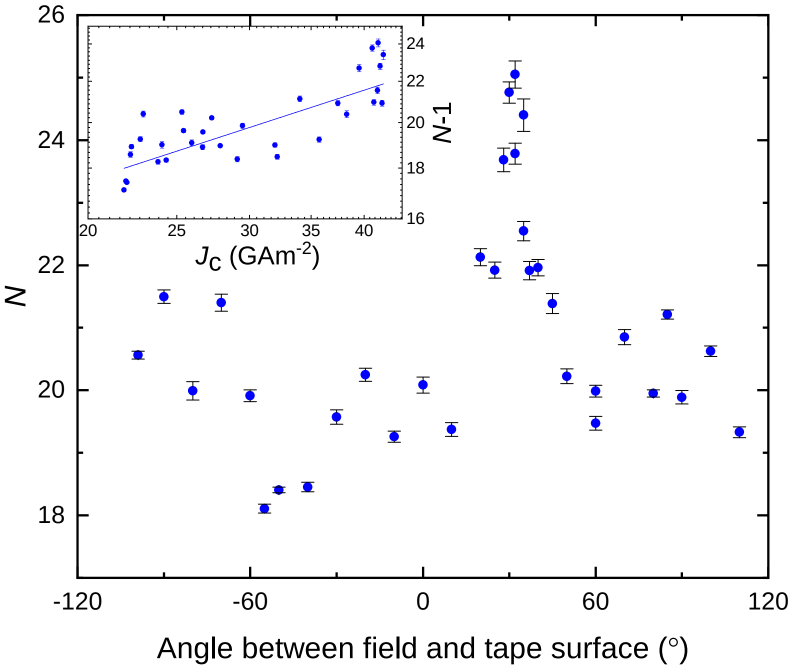

Figure 6.12: The angular dependence of $N$ at 0.5 T on a sample with a 1.4 mm bridge. The peak in $N$ occurs at 30° when $J_c$ is at its peak value and $B \parallel ab$. Inset: data replotted as $N-1$ vs. $J_c$ on a logarithmic scale.

## 6.7 Asymmetry on field inversion

A marked change in $J_c$ after rotating the sample by 180° is observed. An asymmetry of similar magnitude has been observed previously [198, 199, 200, 201], weakly at 1 T [202],

| | $r((\mathrm{GA\,m^{-2}})^{-s})$ | $s$ |
|---|---|---|
| $B \parallel$ c, varying field (figure 6.11) | 9.8(3) | 0.46(5) |
| $B = 0.5\,\mathrm{T}$, varying angle (figure 6.12) | 11.7(3) | 0.30(4) |

Table 6.1: $r$ and $s$ values calculated using equation 6.6.1 for the data in figures 6.11 and 6.12.

and on an ISD tape [128]. To ensure our asymmetry results are not due to magnetic history effects, a sample with a 1.5 mm bridge was measured with three different magnetic histories, as shown in figure 6.13. To check for hysteretic effects the magnetic field was kept constant at 0.3 T and the angle between the direction of the field and the tape surface monotonically increased during the sequence of $J_\mathrm{c}$ measurements, producing set 1. In set 2, the magnetic field angle was monotonically decreased. The sweep with increasing angle was extended for 360° to measure the region with opposite Lorentz force direction (set 4). Another set of hysteretic measurements (set 3) were taken, where the magnetic field was ramped to 0.7 T at the new angle before returning to 0.3 T for the measurement. The $J_\mathrm{c}$ data for set 1 with angle increasing (highest average $J_\mathrm{c}$) is on average $0.13(8)\,\mathrm{GA\,m^{-2}}$ higher than the equivalent data with hysteretic field ramps taken during set 3 (lowest average $J_\mathrm{c}$) with the largest difference in $J_\mathrm{c}$, $0.271(10)\,\mathrm{GA\,m^{-2}}$, occurring at 15°. The change in $J_\mathrm{c}$ on field inversion is shown in the inset of figure 6.13, which has a maximum change of $0.89(3)\,\mathrm{GA\,m^{-2}}$ at 0°. This is significantly larger than any change from magnetic field history in these samples and therefore cannot be attributed to field hysteretic effects.

This marked asymmetry is due to the difference in surface pinning between the buffer layer-superconducting layer and the silver coating-superconducting layer. The surface that the flux nucleates on is controlled by direction of flux flow, or equivalently the direction of the Lorentz force on the fluxons, or the relative direction of the applied field and the current. As the maximum in surface pinning is not aligned with maximum intrinsic pinning, the two $J_\mathrm{c}$ peaks are not 180° apart. In tapes where the *ab*-planes are parallel to the tape surface, only a change in peak height of $J_\mathrm{c}$ is seen with no angular shift. The effect is weaker at higher fields (see figure 6.14).

## 6.8 The effect of heat treatment on ISD REBCO

REBCO stability at elevated temperatures is a concern for sample preparation involving heat treatments. In particular, samples prepared for strain measurements have a strain gauge applied, which require a heat treatment for glue curing, with the recommended thermal history a gradual increase in temperature at $2\,\mathrm{K\,min^{-1}}$ from 50 °C to 170 °C followed by 120 min at 170 °C, and may experience a degradation in $J_\mathrm{c}$. Prior to any measurements (and the curing process), the sample was soldered to the strain board, requiring a couple of minutes at 200 °C to 230 °C.

Extrapolating Preuss *et al.*'s [122] linear temperature-dependent decay constant data down to the 170 °C gives $\tau = 2.7^{+3.6}_{-1.6}\times 10^5\,\mathrm{s}$ at 170 °C in the relation

$$\frac{I_\mathrm{c}}{I_\mathrm{c0}} = \exp\left(\frac{-t}{\tau}\right), \tag{6.8.1}$$

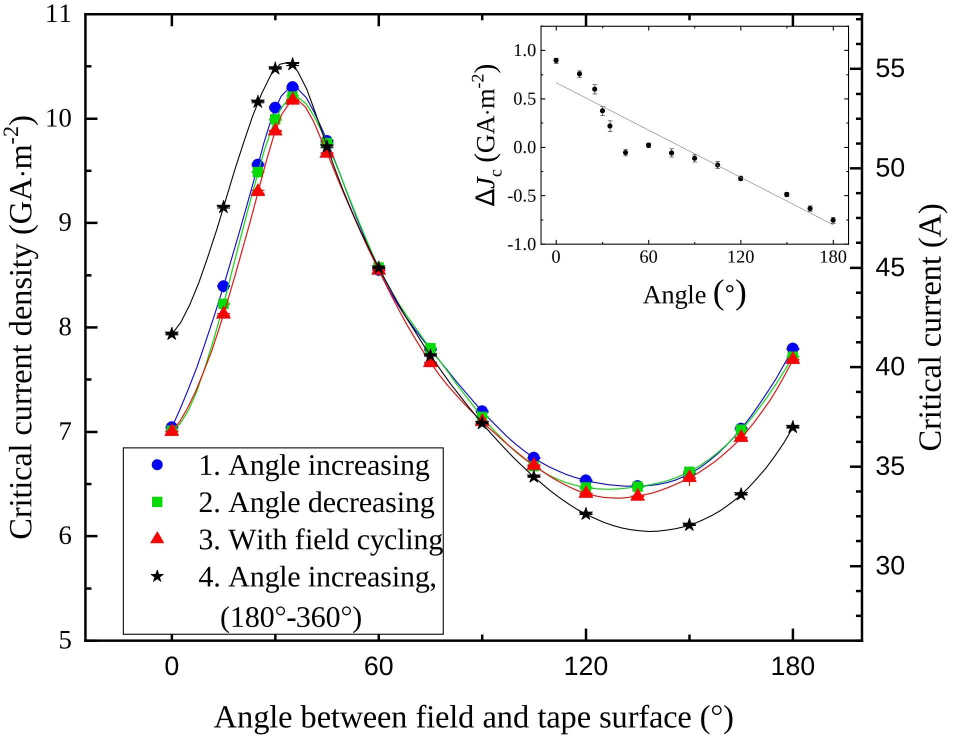

Figure 6.13: The angular dependence of $J_c$ at 0.3 T for different magnetic field histories. To rule out magnetic field hysteretic effects, three measurement scenarios have been used. For set 1 (●) and set 2 (■), the magnetic field was kept at 0.3 T and the sample rotated with the angle increasing or decreasing respectively. For set 3 (▲), the magnetic field was cycled to 0.7 T at the new angle before each measurement. Set 1 was extended to the full 360°, giving the data labelled as set 4 ($\star$) which have been replotted minus 180°, so they can included here. Inset: the difference in $J_c$ on rotating the magnetic field by 180°, derived from the data of sets 1 and 4.

and predicts a heat treatment of 170 °C for 120 min would give a $2.6^{+3.2}_{-1.5}$ % drop in $I_c$, which would have a significant effect on the $I_c$ measurements.

The changes in $J_c$ as critical parameters change are calculated using a standard volume pinning force, $F_p$, expression (eq. 4.5.1) [173, 203, 204] with $p = 0.5$, $q = 2$ [176], $n = 2.5$, and $A$ is a fixed constant. The Ginzburg-Landau parameter $\kappa$ is found from the thermodynamic critical field ($B_c$) and the two-fluid model

$$B^*_{c2}(T) = \sqrt{2}\kappa(T)B^*_c(0)\left(1-\left(\frac{T}{T_c}\right)^2\right). \tag{6.8.2}$$

Ossandon *et al.*'s data [119] predict a change of oxygen deficiency from 0.06 to 0.11, and a commensurate $\sim 20\,\%$ decrease in $J_c$ at 0.3 T and 77 K. Figure 6.15 shows the effect on $J_c$ from changing the oxygen content at 77 K and 4.2 K, using Ossandon *et al.*'s data and the scaling law in equation 4.5.1. Note that the peak $J_c$ is at a higher oxygen content for 4.2 K, 14 T, than for 77 K, 0.3 T, due to the peak $B^*_{c2}(0)$ being at a higher oxygen content than the peak in $T_c$. This implies that the optimal oxygen content for low-temperature operation does not necessarily give the maximum $T_c$. A linear interpolation of the data in figure 6.15 gives a change in oxygen deficiency from 0.060 to 0.064 is associated with a change in $J_c$ of 1.5 % at 77 K and 0.3 T.

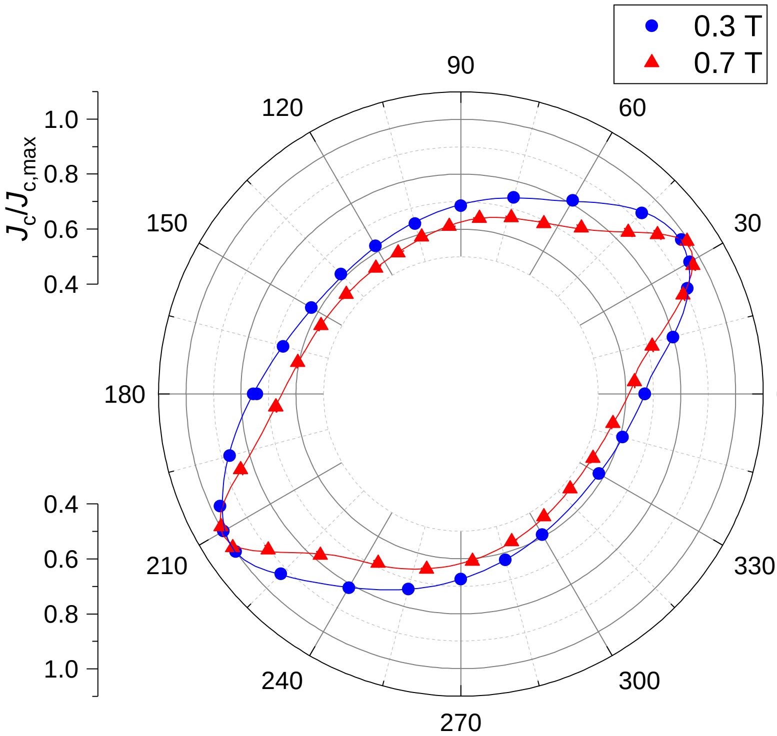

Figure 6.14: A normalised polar plot of $J_c$ vs. angle for two field strengths. The sample had a bridge width of 1.5 mm. $J_c$ is not symmetric on a 180° rotation, with the difference more pronounced at 0.3 T than at 0.7 T.

If oxygen diffusion is limited by the diffusivity through REBCO rather than through a barrier at the superconductor/silver interface, degradation is expected to be sensitive to crystallographic orientation. Oxygen diffusivity is much larger in the *ab*-planes than in the *c*-axis direction [205, 206], with Rothman *et al.* [206] finding $D_{ab} \geq 10^6 D_c$ at 400 °C.

In an ISD tape, the distance along the *ab*-plane to the nearest surface can be much shorter (the maximum distance in the samples tested is $\sim$ 2 µm) than for other manufacturing methods. In a tape with *c*-axis perpendicular to the tape surface, the distance between the surfaces at the ends of the *ab*-planes is approximately the width of the tape (i.e. typically a few mm), or at least $\frac{t}{\sin(\theta)}$ for misalignment angle $\theta$, rather than the thickness of the superconducting layer. If oxygen diffusion out of the REBCO layer is responsible for thermal degradation, the much shorter diffusion distance in ISD could in principle lead to significant $I_c$-decay during the heat treatment necessary to attach strain gauges to them.

To investigate whether significant thermal degradation is occurring in ISD CCs, two samples were measured before and after the strain gauge glue curing process, with several room temperature to 77 K cycles applied to the second sample to check whether the cryogenic thermal cycle between room temperature and 77 K could be causing any changes in $J_c$. The thermal histories of the two samples are summarised in table 6.2.

Figures 6.16 and 6.17 present the data measured for the two samples before and after the curing process. I have fitted parabolas have been fitted to the data and found that $J_c$ in sample 1 decreased by 2.0(5) % and in sample 2 increased by 2.9(2) % after the curing heat treatment. These changes are similar to the changes in $J_c$ observed on thermal cycling from 77 K to room temperature, which have a standard deviation of 1.5 %. No systematic

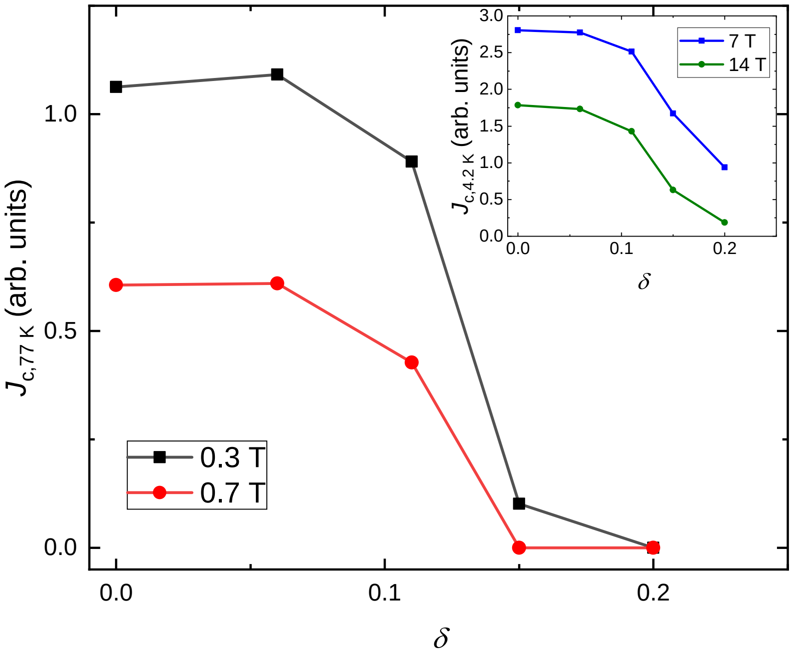

Figure 6.15: A calculation of $J_c$ in-field at 77 K versus oxygen deficiency, $\delta$, for $REBa_2Cu_3O_{7-\delta}$ tape using $B^*_{c2}$ and $T_c$ thermal data from [119] and the scaling law in equation 4.5.1. Inset: equivalent $J_c$ calculations for 4.2 K.

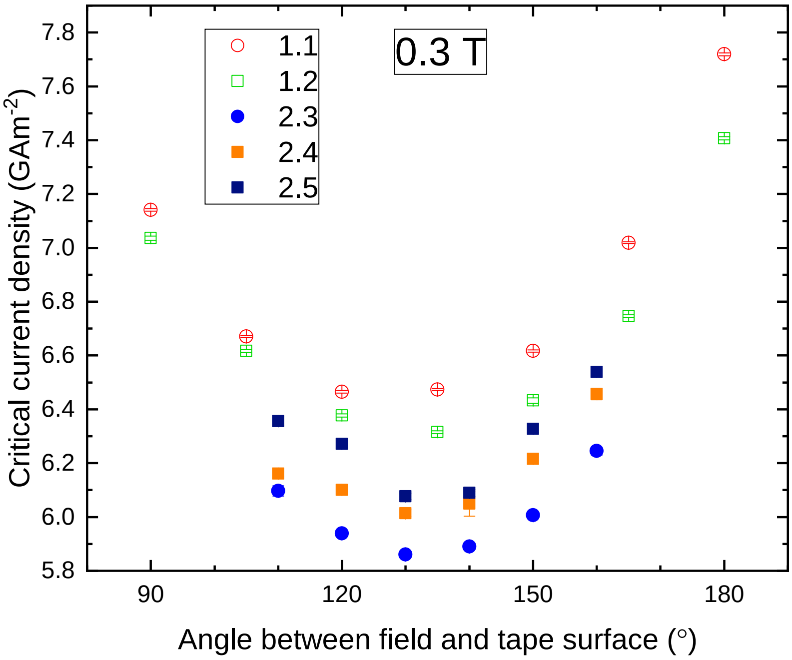

Figure 6.16: Angular measurements near the minimum $J_c$ for two samples after different thermal cycles. A summary of thermal history is given in table 6.2. Measurements were made at $B = 0.3$ T. Open symbols are for sample 1. Closed symbols are for sample 2. Circles and squares are for pre- and post-curing respectively.

decrease in $J_c$ has been observed, although I cannot rule out a small degradation, consistent with the lower bounds of the extrapolation from the data presented by Preuss *et al.* [122]. Our data show no evidence for any degradation. If degradation occurs, there is no evidence it is significantly greater than is expected for tapes with $c \perp$ tape, despite the much shorter

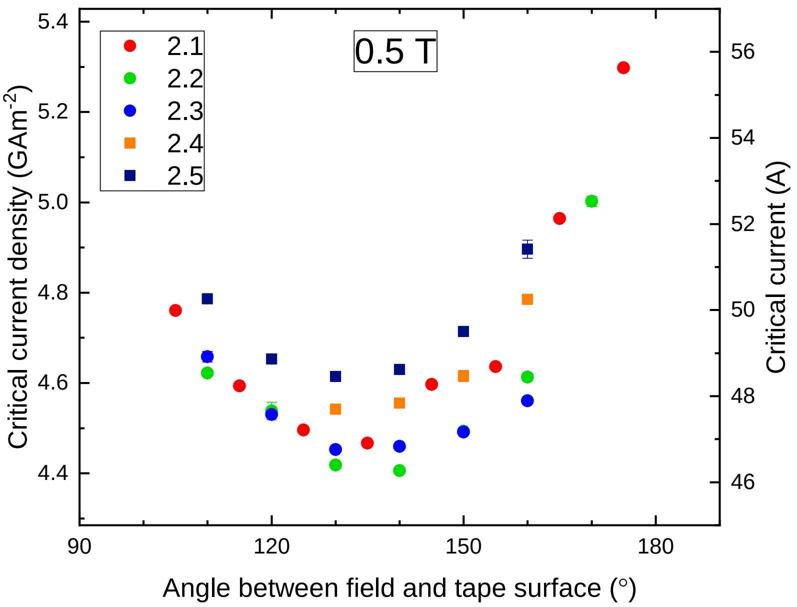

Figure 6.17: Measurements of critical current density with magnetic field angle at 0.5 T for sample 2. The data 2.1-3 show the variation on cycling from 77 K to room temperature, and data 2.4-5 (squares) are after the heat treatment for strain gauge glue curing.

| **Sample 1** | 1.5 mm bridge |
|---|---|
| 1.1 | As-supplied |
| 1.2 | Strain gauge applied |
| **Sample 2** | 3 mm bridge |
| 2.1 | As-supplied |
| 2.2 | One room temperature - 77 K cycle |
| 2.3 | Two room temperature - 77 K cycles |
| 2.4 | Strain gauge applied |
| 2.5 | Further room temperature - 77 K cycle |

Table 6.2: Thermal history of the samples in figures 6.16 and 6.17. After each thermal process $J_c$ was measured at fixed field as a function of angle.

diffusion distance for oxygen through REBCO in ISD CCs.

## 6.9 Short samples

It may be desirable to be able to rotate the sample relative to the strain board, particularly for THEVA CCs. This allows two things, both the rotation of the sample crystallographic axes relative to the strain direction, and the rotation of the applied current relative to the sample axes. Rotation of the sample is only possible with lengths that are shorter than the width of the strain board, and when applying current perpendicular to the conventional direction, the maximum sample length is the width of the tape, in this case 12 mm.

Measurements have been performed on square 12 mm × 12 mm. Potential limitations for short samples include current injection lengths, uniformity of current flow direction and heating.

If the current injection length is comparable or longer than the distance between the current lead and the measurement region, current will still be carried by the copper stabiliser and an accurate measurement of the REBCO $J_c$ will not be obtained. Measurements on the transfer length due to interfacial resistances within the REBCO tape [184, 185, 186] suggest that the transfer length in a variety of tapes is of the order 0.1 mm, which is sufficiently short compared to the roughly mm distances available in the short samples. This suggests that if current can be delivered to the CC copper stabiliser then it will injected into the REBCO layer unless some delamination or other damage occurs.

Current injection close to the measurement region can cause unwanted heating effects as the Ohmic heating of the copper current leads and joint will cause heating of the REBCO layer. This would be observed as a decrease in $I_c$ and possibly a thermal voltage in the measurement signal if a temperature gradient occurs.

A comparison between a long (64 mm) and short (12 mm) sample is given in figures 6.18 and 6.19, showing a good agreement between the $I_c$ and $N$-values on full-width unscribed samples, indicating that any additional heating or poor current injection from short samples is not causing significant changes to the measurements.

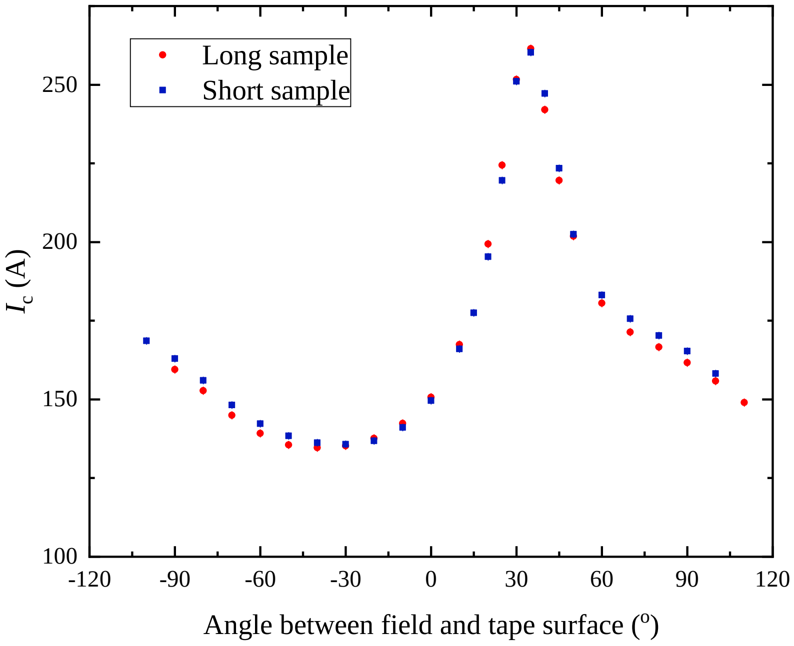

Figure 6.18: A comparison between critical current as a function of magnetic field angle for long (64 mm) and short (12 mm) samples of the same THEVA CC reel. Both samples are 12 mm wide and unscribed, and measured with an applied field of 0.7 T at 77 K.

## 6.10 Conclusions

The cross-section of REBCO coated conductor tapes has successfully been reduced by patterning a current bridge with a diamond tipped scribe. This patterning has been found to reduce $I_c$ linearly with the width of the bridge over all angles and fields up to 0.7 T at 77 K. These bridges can be used to access measurements of $J_c$ in the low-field regions of phase space otherwise inaccessible on a full-width tape. The angular dependence

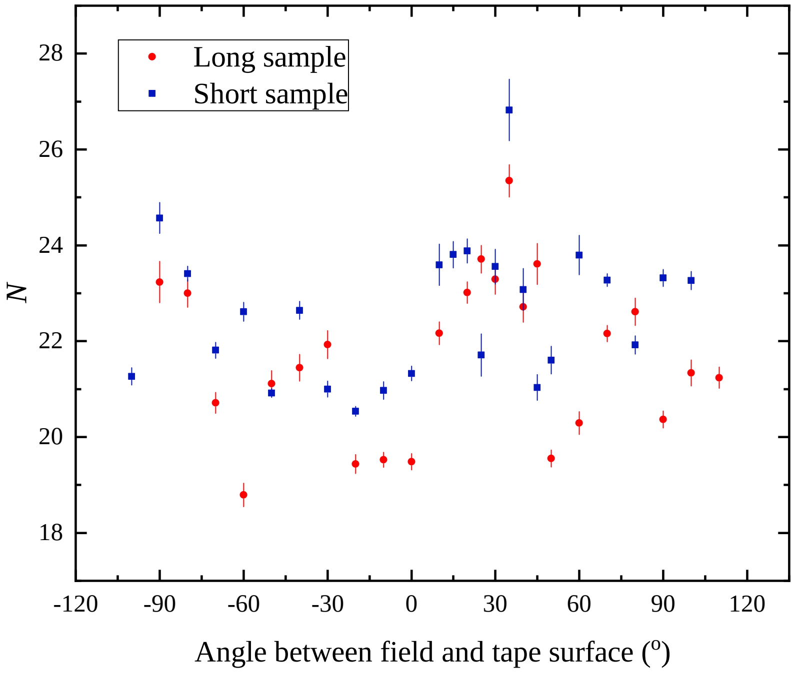

Figure 6.19: A comparison between $N$ values as a function of magnetic field angle for long (64 mm) and short (12 mm) samples of the same THEVA CC reel. Both samples are 12 mm wide and unscribed, and measured with an applied field of 0.7 T at 77 K.

of $J_c$ has been measured using sample bridges, and the lack of 180° rotational symmetry has been shown to be stronger than can be attributed to magnetic field hysteretic effects.

It has also been observed that the heat treatment used to mount a strain gauge does not systematically degrade $J_c$, with changes that are similar to those attributed to thermal cycling between room temperature and 77 K. Short samples, current bridges and the heat treatment for strain gauge mounting can all be used with confidence that it is not significantly affecting these samples.

Chapter 7

# Self-field Effects

## 7.1 Introduction

In the low-field limit, the critical current of a superconductor is not predominantly determined by the external field, but instead flux flow can be initiated by the self-field of the superconductor, the field generated by the current it carries. For very small systems with low currents, this self-field does not play a significant role, and instead the depairing current or defects limit $J_\mathrm{c}$. Descriptions of JJs are useful models for such systems, with the work Fink [100] describing the junction depairing current for narrow JJs and Clem [97] describing the applied-field dependence of wide JJs. These have been combined and extended to large applied-fields by Blair & Hampshire [99], with their parameterisation given in equation 3.5.8. This approach is effective when describing low currents and in large applied fields, but fails to accurately capture the low-field behaviour of high-$J_\mathrm{c}$ materials such as CCs.

Although Blair & Hampshire's solutions are written in terms of net field and therefore give well-behaved low field values for $J_\mathrm{c}$, the empirical approximation proposed by Blair & Hampshire (equation 3.5.8) diverges in low-fields so is clearly unsuitable as a descriptor for the low-field behaviour of superconductors which have finite $J_\mathrm{c}$. The standard flux pinning model (equation 4.5.1) also diverges for small applied fields so equally cannot be used unmodified.

While for many applications of CCs, the operational conditions are in large applied fields, applications such as power transmission and the quality control of CCs for all applications involve measurements in low magnetic fields so it is important to understand low-field and self-field behaviour.

Many of the results in this chapter have been published in the author's paper presented at EUCAS 2021 [2].

## 7.2 Josephson junctions in low magnetic fields

The parameterisation given in equation 3.5.8 can be improved by replacing it with a form that ensures $J_\mathrm{c}$ remains finite even in zero field given by:

$$J_{\mathrm{c}}(B,T) = c_0 \left( \frac{\Phi_0 \tanh \frac{B}{B_0}}{B w_{\mathrm{s}}^2} \right)^{c_1} J_{\mathrm{DJ}}(B,T), \tag{7.2.1}$$

and more closely approaches the envelope of the sinc function and the Bessel function found in Clem's work [97]. Again, $c_0$ and $c_1$ are constants, and I have introduced the constraint

$$B_0 = \frac{\Phi_0}{w_{\mathrm{s}}^2} c_0^{\frac{1}{c_1}} \tag{7.2.2}$$

so that in the low-field limit $J_{\mathrm{c}} = J_{\mathrm{DJ}}(0,T)$. Capturing the low-field behaviour with equation 7.2.1 eliminates the singularities that occur at zero-field in equation 3.5.8 and avoids non-physical solutions. The parameters $c_0$ and $c_1$ are calculated by fitting equation 7.2.1 to Clem's low field numerical solutions for $J_{\mathrm{c}}$ through a JJ [97] as a function of the aspect ratio of the superconducting electrodes in the junction and shown in figure 3.3. It is observed that $c_0 \approx c_1 \approx 0.6$ for an aspect ratio of 1.

As both $c_0$ and $c_1$ decrease monotonically with aspect ratio, the relation between the two can be described using

$$c_1 = a_0 \cdot \ln(c_0) + a_1, \tag{7.2.3}$$

where $a_0$ and $a_1$ are constants given by $a_0 = 0.357$ and $a_1 = 0.656$ when fitted to the peaks of the data in figure 3.3 and $a_0 = 0.181$ and $a_1 = 0.759$ when fitted to field-averaged values. In both cases, aspect ratios $0.05 < L/w_{\mathrm{s}} < 5$ are used where $L$ is the length of the superconducting electrodes. Equation 7.2.3 can be used to reduce the number of free parameters in equation 7.2.1. The variation of $c_0$ and $c_1$ with junction aspect ratio is shown for both peak- and average-fits in figure 7.1.

The most straightforward approach to the normal state properties of the junction (described within $J_{\mathrm{DJ}}(B,T)$ - equation 3.5.4) has been adopted, where $\alpha_{\mathrm{n}}$ has a linear temperature dependence above $T_{\mathrm{cn}}$ and $\beta_{\mathrm{n}}$ is a temperature independent constant. For these fits, the value of $T_{\mathrm{c}}$ is taken to be 90 K and the values of $B_{\mathrm{c2}}$ at 77 K and 4.2 K to be 8 T and 115 T respectively. The free parameters are listed in table 7.1 below - the form proposed enables us to describe both variable field and variable temperature $J_{\mathrm{c}}$ data [99]. It should also be noted that the conclusions in this chapter about the role of self-field are not sensitive to the precise details of the functional form used for $J_{\mathrm{DJ}}(B,T)$.

## 7.3 Self-field effects

To extend the JJ model to real systems including self-field, a model is proposed. The system is considered as a series of parallel JJs, where there is a characteristic length along the current direction and a characteristic width of each junction. The junctions are assumed to have a sufficiently thick barrier between them that coupling of the phase of the superconducting wavefunction between adjacent junctions can be neglected.

Multiple junctions in parallel are needed because the $J_{\mathrm{c}}$ from Clem's model decreases with junction width and becomes far lower than experimental measurements for mm scale CCs. Maintaining phase coherence over such large distances would not occur in the real

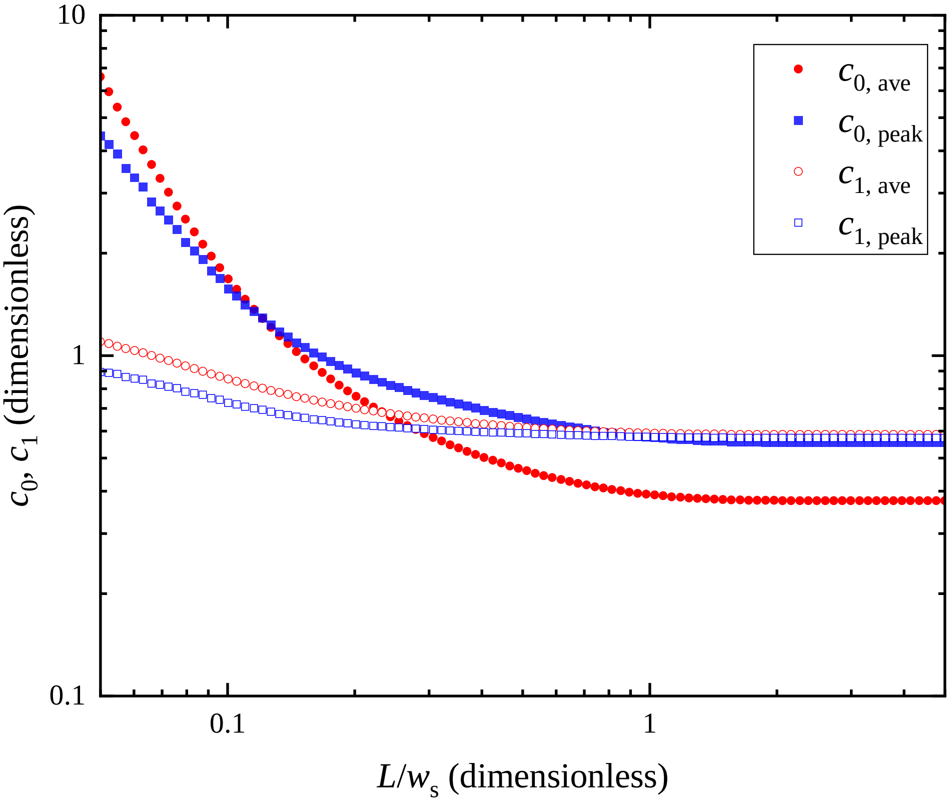

Figure 7.1: The constants $c_0$ & $c_1$ derived from fits using equation 7.2.1 to Clem's expression for the critical current density through a JJ [97], as shown in figure 3.3, for JJs with electrodes of different aspect ratios $L/w_\mathrm{s}$.

system, so a consideration of a single JJ is not applicable in this case. As the JJs need to be much narrower than the system to give a physical $J_\mathrm{c}$, it is reasonable to assume that the local field does not vary significantly within each junction for the vast majority of junctions. This allows the Clem solution for uniform applied field to be used for any individual JJ. The local field seen by any individual junction can then be found using the Biot-Savart law from the current distribution in the other junctions throughout the conductor cross-section. A self-consistent solution needs to be found which satisfies both the local $J_\mathrm{c}(B)$ relation everywhere and has a magnetic field distribution which matches the field generated from each current element. It is assumed that the current distribution when the tape at $J_\mathrm{c}$ is such that every individual junction is also at its $J_\mathrm{c}(B_\mathrm{local})$.

Clem's solution is derived for thin films where the thickness is less than the penetration depth. For REBCO, $\lambda_c(T=0) = 0.89\,\mu\mathrm{m}$ [82] and using the GL temperature dependence, $\lambda(T) = \lambda(0)(1-\frac{T}{T_\mathrm{c}})^{-0.5}$, and a $T_\mathrm{c}$ of 90 K gives $\lambda_c(T = 77\ \mathrm{K}) = 2.63\,\mu\mathrm{m}$. This means that for thick CCs, they are not strictly in the thin film limit used by Clem. As the width of the junctions is predicted to be much narrower than the thickness of the tape (see below), a reasonable physical picture would be to have several junctions through the thickness of the tape so that their dimensions are not more than an order of magnitude greater in one direction than the others. This would mean that each individual junction is thinner than the coherence length for REBCO, so the thin film model from Clem applies within each junction as the field is not varying in the $z$-direction within a junction.

The cross-over field where self-field becomes more significant than the applied field can be estimated by considering a thin cylindrical shell carrying a uniform current density flowing in the direction of the axis of the shell.

From symmetry, the magnetic field is entirely circumferential and from Ampère's law, the volumetrically averaged magnetic field within the cylindrical shell itself $B_{\mathrm{cyl}}$ is given by $B_{\mathrm{cyl}} w_{\mathrm{shell}} = \mu_0 I/2$, where $w_{\mathrm{shell}}$ is the circumference of the shell. It can be assumed that at the cross-over field, the applied field is sufficiently large to rotate the net field everywhere throughout the shell into the direction of the applied field which gives the condition $B_{\mathrm{app}} = B_{\mathrm{cr}} = B_{\mathrm{cyl}}$, and using $J = I/w_{\mathrm{shell}} t$ leads to an expression for the cross-over field given by

$$B_{\mathrm{cr}} = \frac{\mu_0 J_{\mathrm{c}}(B_{\mathrm{app}} \leq B_{\mathrm{cr}}) t}{2}. \tag{7.3.1}$$

Using the approximate power-law field dependence implicit in either equation 3.5.8 or 7.2.1 for $J_{\mathrm{c}}$ in magnetic fields above $B_{\mathrm{cr}}$, the thickness dependence of $J_{\mathrm{c}}(0)$ in self-field can be found. Consider two tapes of thickness $t_1$ and $t_2$ of identical quality so that in high magnetic fields $J_{\mathrm{c}}$ for the two tapes is the same. Using equation 7.3.1 and the power law for $J_{\mathrm{c}}$ gives the self-field values for the two tapes as

$$\frac{J_{\mathrm{c}}^{t_2}(B_{\mathrm{app}} = 0)}{J_{\mathrm{c}}^{t_1}(B_{\mathrm{app}} = 0)} = \left(\frac{t_1}{t_2}\right)^{\frac{c_1}{1+c_1}}, \tag{7.3.2}$$

which given that $c_1$ is typically 0.6, shows a strong thickness dependence. For example, if the thickness of a tape is doubled while retaining the same $J_{\mathrm{c}}$ in high fields, the self-field $J_{\mathrm{c}}$ can be expected to decrease by $\sim 20\,\%$. A decrease in self-field $J_{\mathrm{c}}$ with thickness has been seen by many authors [207, 208, 209, 210, 211, 212] (but not all [115]) and is often attributed to defects.

This result does not agree with the scaling law from Talantsev *et al.* [213], as their model predicts that CCs thicker than $\lambda$ see no increase in $I_{\mathrm{c}}$ for additional thickness. The Talantsev scaling law implies that supercurrents only flow within $\lambda/2$ of the surface of the tape, so that in the self field regime, superconductors thicker than $\lambda$ have a region in the centre which does not carry current. It also predicts the current distribution to be uniform across the width of the sample. While some authors do see no increase in $I_{\mathrm{c}}$ for additional thickness [207], several authors do see $I_{\mathrm{c}}$ continue to increase in thick CCs [209, 210, 115], which contradicts the prediction from Talantsev *et al.*. The scaling also only allows for changes in self-field $J_{\mathrm{c}}$ due to changes in $\lambda$ and $\kappa$ between tapes and no possible microstructural contribution. When the model is used to fit $\lambda$, a factor of 2 variation in $\lambda$ is seen between samples [214], so either the penetration depth in REBCO is highly variable and therefore the scaling law is very challenging to apply, or other factors such as microstructure are contributing to $I_{\mathrm{c}}$. It is the author's view that a self-field controlled model is more compelling than the surface-current model from Talantsev *et al.*, particularly as $I_{\mathrm{c}}$ is seen to increase with thicknesses above $\lambda$ in CCs.

## 7.4 Self-field calculations

Self-field calculations for local spatially varying $J_{\mathrm{c}}(B)$ have been made by a number of authors for thin strips [215, 216, 217, 218] using for example the Kim model [219].

The expression for the magnetic vector potential of a thin strip in terms of the current distribution [215] is used to find the magnetic field where

$$B_z(y) = B_{\mathrm{app}} + \frac{\mu_0 t}{2\pi}\int_{-w_t/2}^{w_t/2} \frac{J_{\mathrm{c}}(B_z(u))}{y-u}\mathrm{d}u, \tag{7.4.1}$$

$w_t$ is the width of the tape, $t$ its thickness and $B_{\mathrm{app}}$ is the applied field. This gives a width-independent solution for $B_z(y)$ where the self-field is linear with thickness. A 2D version of this could be used, but since for many CCs the thickness is smaller than or equal to $\lambda$, variations in magnetic field through the thickness are expected to be small and not significantly affect the results, so the analysis is limited here to the 1D case.

Because the relation for the field dependence of $J_{\mathrm{c}}(B)$ is strongly peaked around $B = 0$ (see equation 7.2.1), unlike the Kim model, it cannot be assumed that the gradient in the magnetic field is small everywhere and have to include higher-order terms to find accurate solutions. The second derivative terms are most important where the local field is zero and the current density at its peak value.

A Taylor expansion to second order in the derivative of the current is made to evaluate the integral at each grid point from $y_i - \Delta y/2$ to $y_i + \Delta y/2$:

$$\begin{gathered}\frac{\pi}{\mu_0 b}\left(B(y_j) - B_{\mathrm{app}}\right) \approx \sum_i \ln\left(\frac{y_i + \frac{\Delta y}{2} - y_j}{y_i - \frac{\Delta y}{2} - y_j}\right) J(y_i) \\ + \left(\Delta y - (y_i - y_j)\ln\left(\frac{y_i + \frac{\Delta y}{2} - y_j}{y_i - \frac{\Delta y}{2} - y_j}\right)\right) \left.\frac{\mathrm{d}J}{\mathrm{d}y}\right|_{y_i} + \\ \left((y_i - y_j)^2 \ln\left(\frac{y_i + \frac{\Delta y}{2} - y_j}{y_i - \frac{\Delta y}{2} - y_j}\right) - (y_i - y_j)\,\Delta y\right) \left.\frac{\mathrm{d}^2 J}{\mathrm{d}y^2}\right|_{y_i}.\end{gathered} \tag{7.4.2}$$

When the grid spacing $\Delta y \ll |y_i - y_j|$, this reduces to the expected $\sum J/(y_i - y_j)$, but for the points $j-1, j, j+1$ the additional contributions are not small. Including these gradient terms from the point of interest and its nearest neighbours gives:

$$\begin{aligned}\frac{\pi B(y_j)}{\mu_0 b \Delta y} &= \sum_{i \neq j} \frac{J(y_i)}{y_i - y_j} - \left.\frac{\mathrm{d}J}{\mathrm{d}y}\right|_{y_j} + (\ln(3) - 1) \\ &\times \left( J(y_{j+1}) - J(y_{j-1}) - \left.\frac{\mathrm{d}J}{\mathrm{d}y}\right|_{y_{j+1}} - \left.\frac{\mathrm{d}J}{\mathrm{d}y}\right|_{y_{j-1}} \right. \\ &\left. + \frac{1}{2}\left.\frac{\mathrm{d}^2 J}{\mathrm{d}y^2}\right|_{y_j+1} - \frac{1}{2}\left.\frac{\mathrm{d}^2 J}{\mathrm{d}y^2}\right|_{y_j-1} \right).\end{aligned} \tag{7.4.3}$$

Typically approximately 100 grid points are used across the strip. Equation 7.4.3 is then used with equation 7.2.1, where $B$ is taken to be the local magnetic field, and they are solved iteratively to find the spatial variation of the critical current density across the

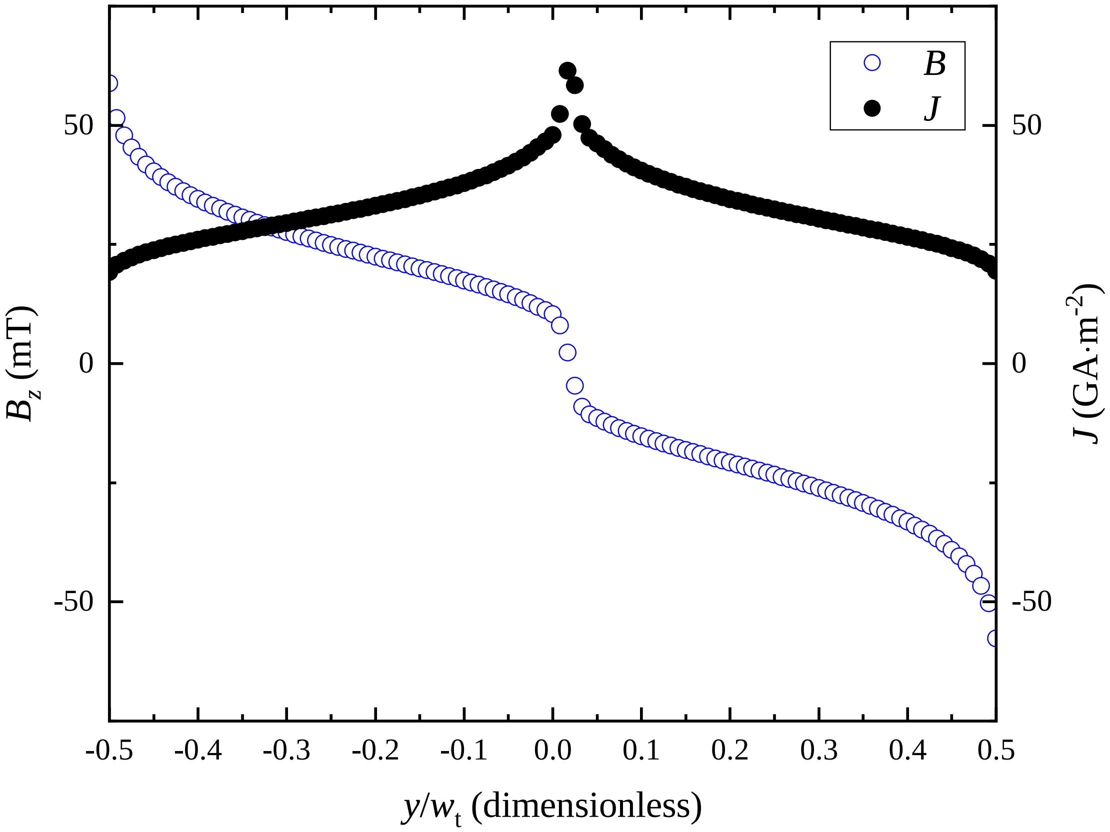

Figure 7.2: The spatial distribution of the magnetic field in the $z$-direction and the critical current density within the tape, where the width of the component JJs $w_\mathrm{s} = 200\,\mathrm{nm}$, and the applied field $B_\mathrm{app} = 1\,\mathrm{mT}$. Note that the local magnetic field in the tape is much larger than the applied field.

strip and hence the total critical current of the tape. Similar field distributions have been found experimentally [220, 221, 213, 222, 223].

In figure 7.2, the spatially varying field and current density are shown for the Fujikura fit-parameters with $w_\mathrm{s} = 200\,\mathrm{nm}$. The average magnitude of the field and the average of the current density are approximately related by equation 7.3.1 in figure 7.2 which demonstrates that the cross-over field can equally be considered the condition for the applied field to equal the average $z$-component of the self-field.

Figure 7.3 shows how the variation of $w_\mathrm{s}$ in equation 7.2.1 affects the low-field results. The other parameters in the model have been adjusted to compensate for the change in $w_\mathrm{s}$ such that the high field behaviour is the same. As shown in the figure, the cross-over field is broadly in agreement with equation 7.3.1 - only dependent on $J_\mathrm{c}$ and $t$ and independent of $w_\mathrm{s}$. Below the cross-over field, $J_\mathrm{c}$ is broadly constant. For large widths, the self-field correction means that the whole-tape behaviour is relatively insensitive to the junction width.

## 7.5 Comparison to experimental results

Figure 7.4 shows experimental data from the Robinson Research Institute database from CCs made by four different manufacturers. The cross-over field from equation 7.3.1 is

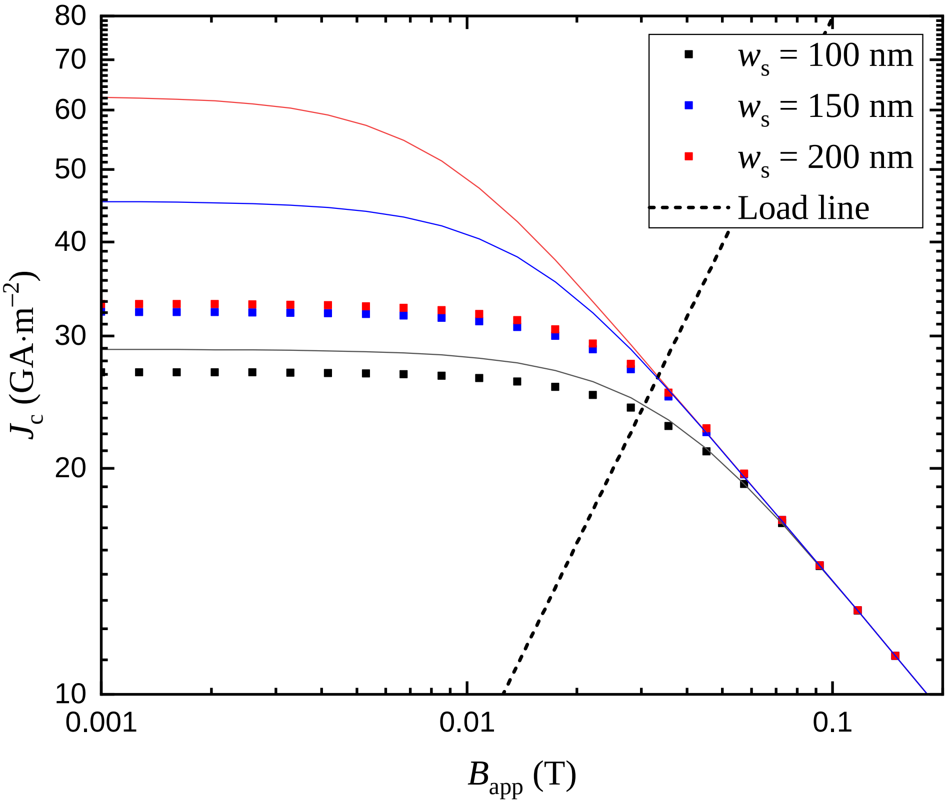

Figure 7.3: The effect of self-field on $J_c(B)$ for a range of junction widths, $w_s$. The other parameters have been rescaled for each width to match the Fujikura in-field $J_c(B)$ data at 77 K from [224]. Lines show the local $J_c(B)$ relation from equation 7.2.1, points are the average of the $J_c$ distribution with self-field. Also shown is the load line given by equation 7.3.1. At fields below the load line, the average $J_c$ is not strongly dependent on the local $J_c$ relation.

| Parameter | Fujikura | SuNAM | THEVA |
|---|---|---|---|
| $\tilde{\beta}_n$ | 0 | 0 | 0 |
| $T_{cn}$ (K) | 1.27 | 1.27 | 1.27 |
| $\tilde{m}_n/\tilde{\Upsilon}_n(0)$ | 4.56 | 4.56 | 4.56 |
| $d$ (nm) | 3.28 | 2.96 | 3.72 |
| $w_s$ (nm) | 100 | 108 | 67 |
| $c_1$ | 0.56 | 0.57 | 0.56 |
| $t$ (µm) | 2 | 1.5 | 3.5 |

Table 7.1: Fit parameters for equation 7.2.1

a good predictor of the change from power-law behaviour to field-independent critical current in three of the tapes - Fujikura, SuperPower and SuperOx. The cross-over point in the fourth tape, SuNAM, is at larger applied fields than predicted by the self-field cross-over. This indicates that a different mechanism is responsible for reducing $J_c$ relative to the power-law behaviour in larger fields. This could be explained by the JJ model in equation 7.2.1 as $J_c$ is independent of magnetic field for small fields, with the cross-over point determined by the width of the junction. This model predicts that the cross-over is independent of temperature, so a vertical line could be drawn on the plots in figure 7.4 with its position dependent on the junction width. For sufficiently high $J_c$, the self-field

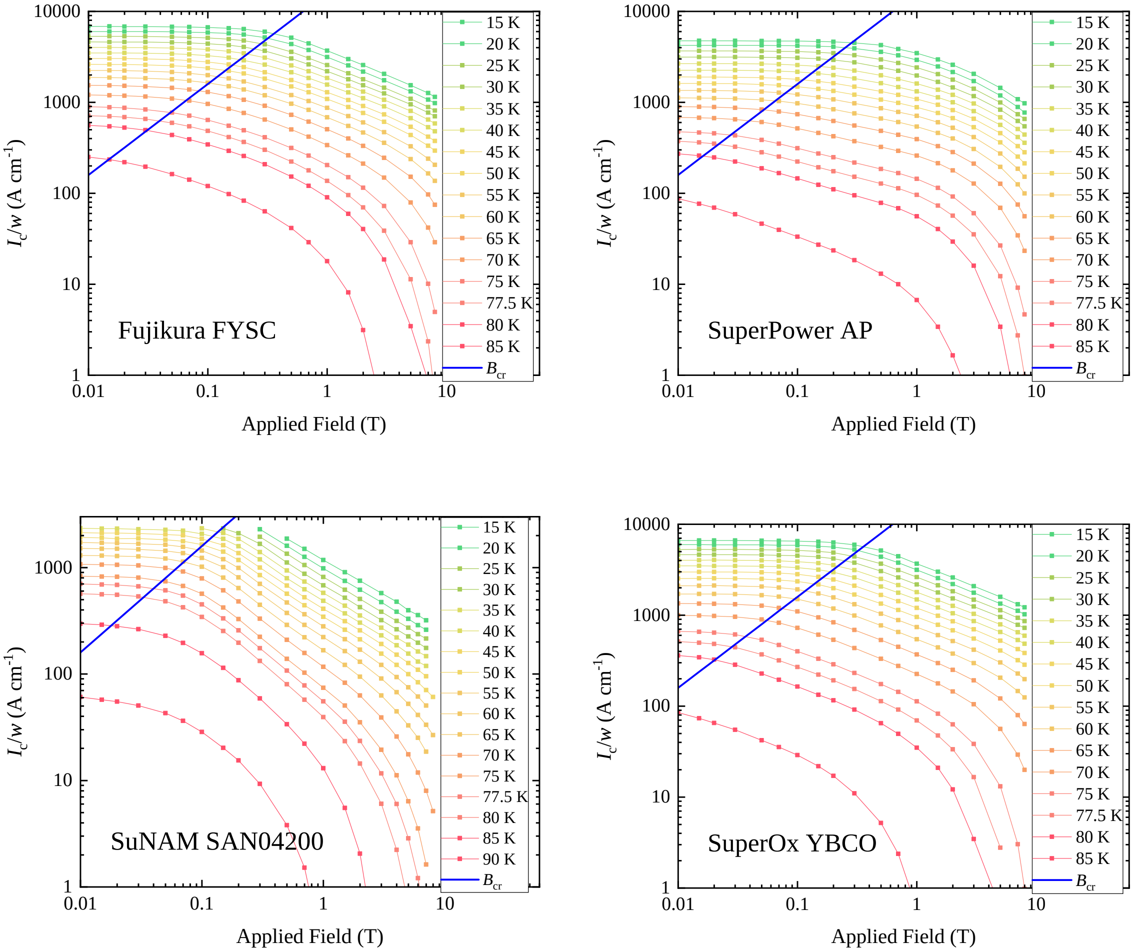

Figure 7.4: $I_c$ scaled by width as a function of applied field measured on CCs from four different manufactures. The crossover field (equation 7.3.1) is plotted for each. All measurements are with the applied field perpendicular to the tape surface. The data are taken from [225, 226].

would then start to dominate the low-field behaviour and the cross-over would move onto the $B_{cr}$ line where they intersect. This appears to be a plausible description of the SuNAM data, with a junction-width crossover occurring at approximately 0.05 T for the high-temperature data and following the self-field crossover at lower temperatures. This would correspond to a junction width of $w_s = \sqrt{\frac{\Phi_0}{B_0} c_0^{\frac{1}{c_1}}} = 98\,\mathrm{nm}$ when $c_1 = 0.6$ and $c_0 = 0.42$. This model predicts that the junction widths within the other tapes are sufficiently larger that the junction-width cross-over is at a lower field than the self-field cross-over for the range of measurements shown here.

In this chapter, fits are made to the experimental data from Tsuchiya *et al.* [224], who have measured a number of different commercial REBCO tapes at 4.2 K and 77 K, as well as the author's data on THEVA tapes at 77 K [1]. First the free parameters for equation 7.2.1 were found by fitting the $J_c$ above 0.5 T at both 4.2 K and 77 K. I have imposed a minimum value of 0.56 on $c_1$, see figure 7.1. Good fits were only obtained with small $\tilde{\beta}_n$, so this has been set to 0. The values of the parameters used are listed in table 7.1. The fit values for the normal state properties $T_{cn}$ and $\tilde{m}_n/\tilde{\Upsilon}_n(0)$ from the Fujikura tape were fixed for the SuNAM tape, with the junction geometry parameters, $d$, $w_s$ and $c_1$, kept free. For the THEVA data, a fit is made including a self-field correction to the $B_{app} = 0$ point

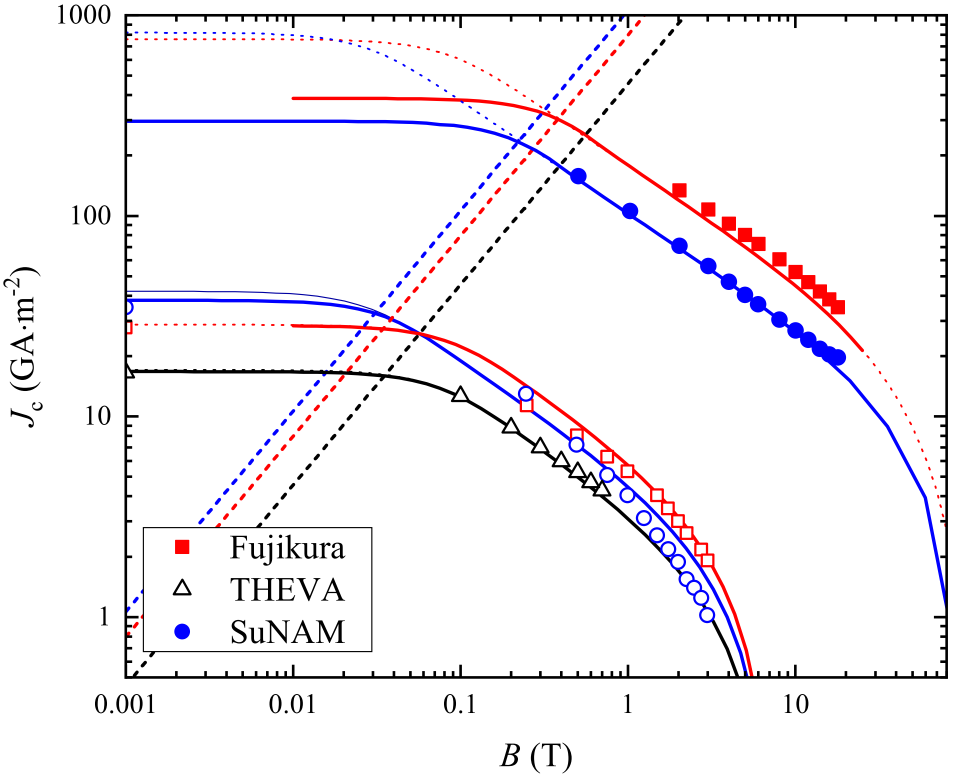

Figure 7.5: Critical current density as a function of applied field at 4.2 K and 77 K for a Fujikura and a SuNAM tape [224], and at 77 K for a THEVA tape [1]. Open symbols are experimental data at 77 K and closed symbols are at 4.2 K. Solid lines are fits to the experimental data and dotted lines are the local $J_c(B)$ input data used. Also shown are dashed lines for the cross-over fields given by equation 7.3.1.

to constrain the relation between $d$ and $w_s$ in the absence of temperature variation. Then using equation 7.2.1 to define $J_c$ as a function of the local magnetic field, equation 7.4.3 was used to find $J_c$ as a function of applied field with the self-field corrections included. As shown in figure 7.5 from the $J_c$ at 4.2 K, the self-field correction reduces the currents measured at the low fields and increases the field at which there is a cross-over from the field independent regime for $J_c$ to the power-law regime for $J_c$. It should be noted that the uncertainties in the free parameters are relatively large because the crossover field is not precisely measured in the data. Equation 7.3.1 has also been plotted and good agreement with the experimental cross-over field is demonstrated.

## 7.6 Conclusions

This chapter presents an analysis of the critical current density of REBCO tapes for low applied magnetic fields:

i) The high field expression for $J_c$ has been extended to low applied fields and proposed a functional form that correctly crosses over to the self-field regime at low field (see equation 7.2.1). This has value for computational parameterisation because it ensures that non-physical very high values of $J_c$ are avoided and is particularly useful for characterisation of the properties of tapes for use in magnet design.

ii) Numerical calculations have been completed that provide the spatial variation of the current density and $z$-component of the magnetic field in thin REBCO tapes that are useful when the self-field is larger than or of a similar magnitude to the applied field. A method is demonstrated, that by including higher order terms, can be used to self-consistently calculate the current density of a wide tape with self-field corrections.

iii) By considering the properties of an infinitesimally thin cylindrical shell, an expression is found, equation 7.3.1, for the cross-over field between low fields, where the self-field is larger than the applied field and high fields where the opposite holds. This cross-over field is important because the mechanism for dissipation changes completely from fluxons and anti-fluxons penetrating at opposite sides of the tape with fluxon-antifluxon annihilation above $J_\mathrm{c}$ at low fields, to fluxons entering one side of the tape, traversing the tape and leaving through the other side in high fields above the cross-over field. Different dissipative processes, along with a commensurately different mechanism for determining $J_\mathrm{c}$ below and above the crossover field provide a natural explanation for the well-know lack of correlation between $J_\mathrm{c}$ measured in zero applied field and $J_\mathrm{c}$ in high magnetic fields [227, 228]. This cross-over field expression is sufficiently simple to provide a means to determine from a single measurement of $J_\mathrm{c}$ in low fields whether it is above or below the cross-over field. The magnitude of the cross-over field also provides a useful minimum value for the local field when optimising the performance of high field superconducting systems using tapes. It is also noted that if a film with good uniform pinning properties is made thicker, equation 7.2.1 will lead to a significant reduction in $J_\mathrm{c}$ measured in zero applied field because of self-field effects.

iv) A comparison has been made between the predicted cross-over field and data from the Robinson Research Institute on CCs from a range of manufacturers, showing good agreement for a change in behaviour of $J_\mathrm{c}$ at the cross-over field. Data have been fitted in low fields at two different temperatures that self-consistently included the spatial distribution of $J_\mathrm{c}$ and demonstrated that relevant free parameters and self-consistent solutions can be found for the macroscopic $J_\mathrm{c}$ that agree with data from the literature.

Chapter 8

# Biaxial Strain Effects on Intra- and Interplanar Current

## 8.1 Introduction

This chapter describes the measurements performed on CCs manufactured by THEVA GmbH, with biaxial strain measurements and interplanar current measurements.

Measurements on a long sample with biaxial applied strain are presented in section 8.2, which are to the best of the author's knowledge, the first biaxial strain measurements on an ISD CC and the first *in situ* $X$-strain measurements with variable $Y$-strain on a CC.

Section 8.2.2 details strain measurements on short samples, with a discussion of the significant shortcomings seen in the data measured on short samples. Measurements on interplanar current, also measured on short samples, are presented in section 8.3, with a calculation of the expected relation between $ab$-current and interplanar current strain responses. These are the first measurements of interplanar currents under strain. In section 8.5, a theoretical model is outlined, based on single-crystal literature data and a comparison is made between the predictions from this model and the experimental data presented in this chapter and other literature measurements on different CC architectures.

These measurements are the first to be made on the new biaxial strain probe. The previous measurements (presented in chapter 6) were made on an older probe with a lower maximum current so a wider range of measurements are possible here. Full-width (12 mm) samples can be measured in self-field at 77 K, and in applied fields up to the 0.7 T limit of the resistive magnet used, with *in situ* variable magnetic field angle and $X$-strain. Further details on the new strain probe are given in chapter 6.

Table 8.1 gives a summary of the samples measured under strain. The effective width is either the full width of the sample for unscribed samples, or the width of the scribed bridge when present.

| Sample name | Length (mm) | Effective width (mm) | Notes |
|---|---|---|---|
| Long sample | 64 | 12 | |
| Short 1 | 12 | 1.7 | scribed |
| Short 2 | 12 | 1.8 | scribed |
| Short 3 | 12 | 12 | |
| Short 4 | 12 | 12 | |
| Short 5 | 12 | 12 | |
| Interplanar | 12 | 8.9 | sample rotated by 90° |

Table 8.1: List of samples measured under strain.

## 8.2 Biaxial strain measurements on THEVA tapes

Measurements have been made on ISD CCs manufactured by THEVA, using the biaxial strain board discussed in section 6.2. This allows for *in situ* variation of $x$-strain and variable $y$-strain set at room temperature. Measurements have been made on a 64 mm long sample at the full 12 mm width supplied by the manufacturer.

There are three different co-ordinate systems of interest for the measurement and analysis of ISD CCs. The first is the co-ordinate system based on the strain board, which will be used for the experimental results and strains in the board co-ordinated are written as $\varepsilon_X$, $\varepsilon_Y$ with a capital $X$ or $Y$. These refer to the two strain orientations that can be independently varied on the biaxial strain board.

The second co-ordinate system is associated with the REBCO tape. For a conventional $ab$-current measurement, the direction along the length of the tape reel is aligned with the $X$-direction on the strain board, but this is not always the case as the tape can be rotated relative to the strain board. The tape co-ordinates are given by $\varepsilon_{xx}$, $\varepsilon_{xy}$ etc. A double subscript is used since the full tensorial strain state is considered for analysis. For the $ab$-current measurements presented in this chapter, the board and tape are aligned so these two co-ordinate systems are identical. For the interplanar current measurements, the sample is rotated by 90°, so the co-ordinates are simply $\varepsilon_X = \varepsilon_{yy}$, $\varepsilon_Y = \varepsilon_{xx}$. If the analysis were extended to other orientations of the sample on the strain board, a rotation (equation 8.5.2) would need to be applied to convert between these.

The final co-ordinate system is that based on the crystallographic axes, and is given by $\varepsilon_{aa}$, $\varepsilon_{ab}$ etc.

Figure 8.1 shows the strain values measured on the long THEVA sample. The effective Poisson ratio for the biaxial strain board with no applied $y$-strain is seen to be -0.263(7), compared to -0.33 for bulk copper beryllium [229]. A smaller effective Poisson ratio of -0.131(9) is observed when $Y$-compression is applied. This attributed to the increased stiffness in the $Y$-direction caused by the $Y$-strain application rods which were not present for the uniaxial measurements. For the measurements with an applied $Y$-compression of -0.185%, a non-monotonic behaviour of the strain was measured. As this behaviour was only observed when increasing the $X$-strain (with the expected behaviour seen when the strain was decreasing) and at no other values of $Y$-compression, this behaviour is believed to be due to an issue with the strain gauge and not reflective of the strain state seen by the sample. The measured $Y$-strain values are not reflected in changes of $I_\mathrm{c}$, which would be expected if the sample strain state was changing. The measured resistance of the $Y$-strain grid was slightly lower than expected, which could indicate a very minor short developing as the strain board deformed that changed the resistance by a few tenths of a percent. The $X$-strain behaviour remained exactly as expected, with monotonic and reversible behaviour. After this measurement sequence, the insulation of the strain gauge wires was rechecked and no subsequent problems were observed, with the $\varepsilon_Y = -0.262\%$ data behaving as expected with the same strain gauge.

The $X$-strain range chosen was informed by the likely safe range for the board and sample. The compressive limit of -0.5% was chosen to avoid board failure which was observed at -0.56% on the thinner design, and a tensile limit of roughly 0.2% is to avoid irreversible sample degradation from crack propagation. A more cautious strain range was used when $Y$-strains were applied both because the Poisson ratio effect from $Y$-compression generates $X$-tension, which makes brittle failure of the REBCO layer more likely if further tension is applied, and the additional forces on the strain board may lead to a lower board failure point. The strain range was chosen to have a low risk of sample or board failure. A thorough investigation of the failure points of the new strain board design may allow for slightly larger strain ranges, but the brittle nature of the samples is unlikely to allow for much larger tensile strains, and the stress concentration caused by the struts for $Y$-strain application means the compressive strain range cannot be significantly extended without a change in design. Other (uniaxial) strain board designs have been able to reach larger compressive strains, with Branch *et al.* [92] measuring a CC at -1% strain, and Keys & Hampshire [230] reaching -2.15% strain on a $Nb_3Sn$ sample, albeit on a spring which was plastically deformed by such a large strain. The lower strain range accessible here is one of the compromises that were required for biaxial strain application.

The strain measurements on the long sample are shown in figure 8.2. A significant variation in $I_\mathrm{c}$ was observed between measurements with no applied $Y$-strain, with a 4% difference between the highest and lowest $I_\mathrm{c}$ values (the two strain cycles ‘day 1’ and ‘day 2’, with the initial measurement in between). Unfortunately, this variation is of a similar magnitude to the variations with strain that are being measured. Within one measurement sequence, the variation is much smaller, with a clear linear and reversible response observed. The gradients of the two strain measurement sequences with no applied $Y$-strain are in good agreement with each other (figure 8.3) and consistent at the two magnetic field strengths measured. This variation in $I_\mathrm{c}$ is of a similar magnitude than was seen between thermal cycles on the same sample when measuring on a different probe (see figures 6.16 & 6.17). As the measurements from chapter 6 were made over a range of angles, the variation there was not attributable to an angle misalignment and must be due to the thermal cycle from 77 K to room temperature and back. A similar effect may well be responsible for the variation observed on the biaxial strain probe. This large variation highlights the importance of *in situ* strain control. Unfortunately this does mean that the variation in $I_\mathrm{c}$ with $Y$-strain is not greater than the variation between measurements and cannot be used to form any strong conclusions. A much larger (irreversible) change in $I_\mathrm{c}$ was seen for the $Y$-tension measurements, included in the inset for figure 8.2. The changes in gradient

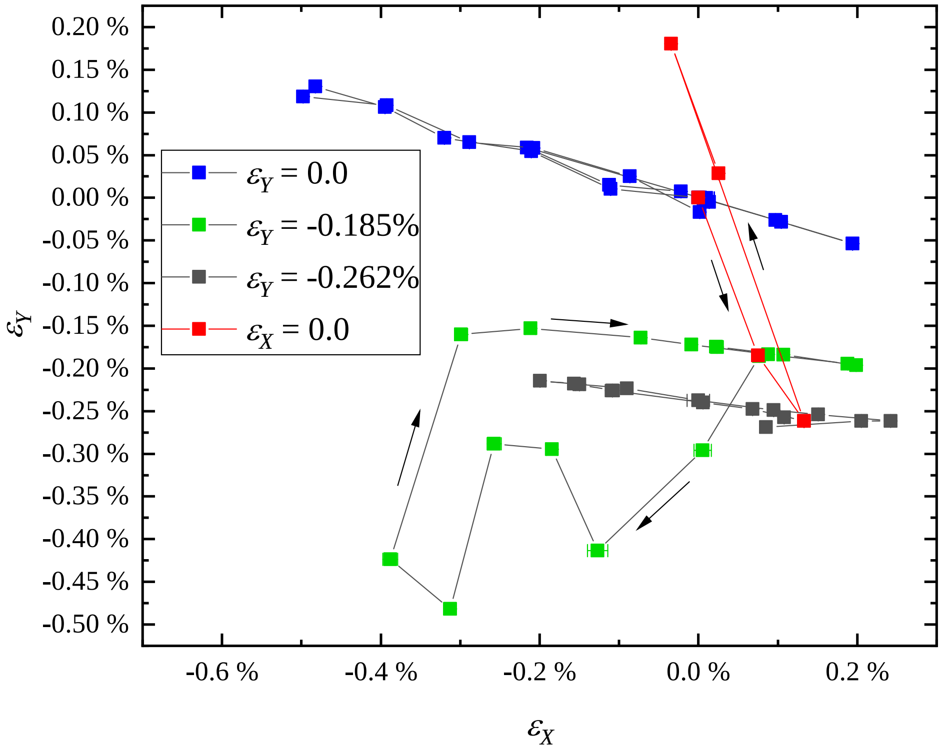

Figure 8.1: Strain values for measurements on the long sample mounted on a 2 mm thick strain board. The blue, green and black data are for *in situ* variations of $X$-strain at 77 K with a fixed separation of the $Y$-strain legs of the strain board. The red data are changes in $Y$-strain made at room temperature with no applied $X$-stress, measured at 77 K. The non-monotonic changes in $Y$-strain for the green data are not believed to reflect the strain state of the sample but are attributed to problems with the strain gauge. The spuriously large $Y$-strains are only present when increasing $X$-compression, the monotonic behaviour and expected values were recovered when the $X$-strain was decreasing.

within each strain sweep as a result of varying the applied $Y$-strain are meaningful as they are measured while the sample remains at cryogenic temperatures.

For uniaxial applied $X$-strain (figure 8.3), a clear linear bevahiour of $I_c$ is observed, with reversible changes in $I_c$ over the measured strain range and a consistent gradient at the two field strengths of

$$\frac{1}{J_c(0)}\frac{dJ_c}{d\varepsilon_X} = -7.0(3)\%/\%. \tag{8.2.1}$$

This gradient is consistent with the uniaxial measurements on ISD CCs in the literature [157]. The measurements presented here extend the compressive strain range previously measured on ISD CCs at liquid nitrogen temperatures by van der Laan *et al.* [157], which were between -0.2% and +0.25% at 75.9 K, although the strain range here is comparable to their measurements at 65 K.

Measurements with an additional constant $Y$-compression applied are shown in figures 8.4 and 8.5. The strain sensitivity is slightly lower with applied $Y$-strain, with a gradient of

$$\frac{1}{J_c(0)}\frac{dJ_c}{d\varepsilon_X} = -5.3(4)\%/\% \tag{8.2.2}$$

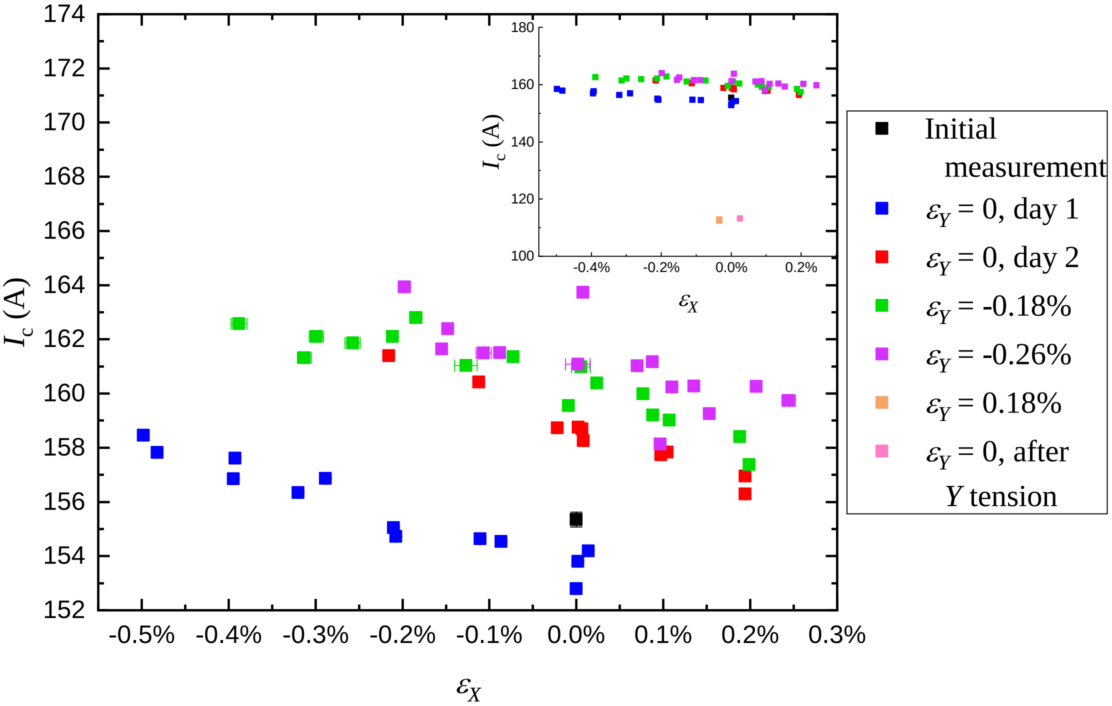

Figure 8.2: Measurements of critical current on the THEVA CC long sample with applied strains at 77 K. All measurements are for an applied field of 0.7 T. Between each colour is a room temperature cycle, with the order of the legend matching the order of measurements. Inset: including the $Y$-tension data, which showed an irreversible decrease in $I_c$

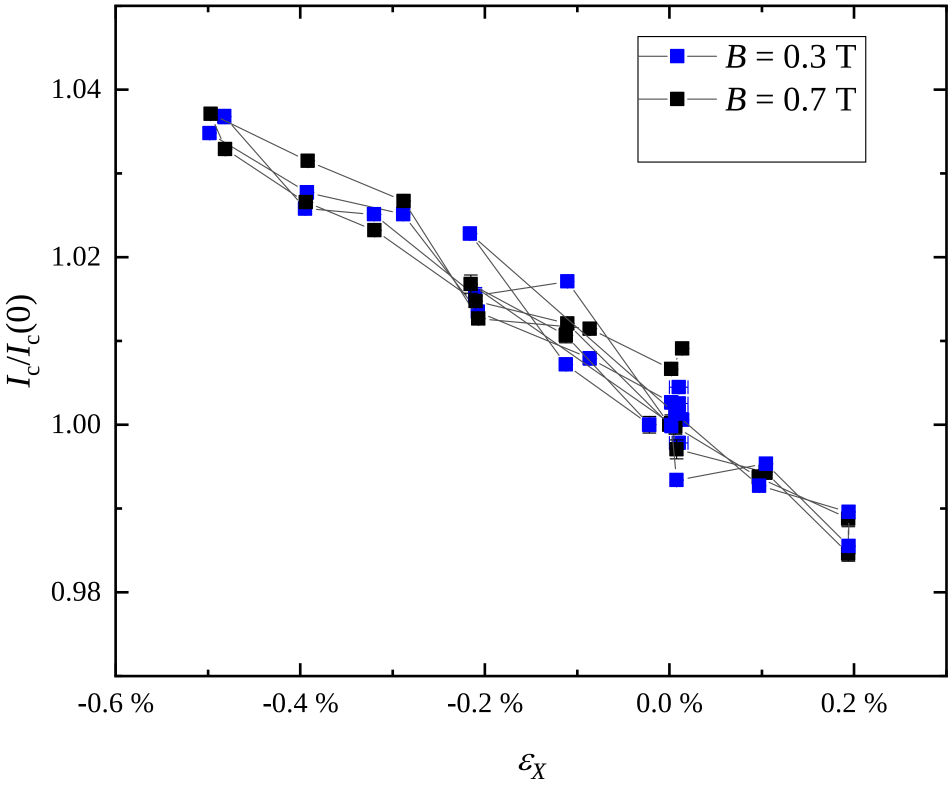

Figure 8.3: Normalised critical currents on the THEVA long sample with uniaxial applied $X$-strain at 77 K and no applied $Y$-strain. The data are taken from two different measurement sets which have been normalised separately to eliminate the change on a thermal cycle.

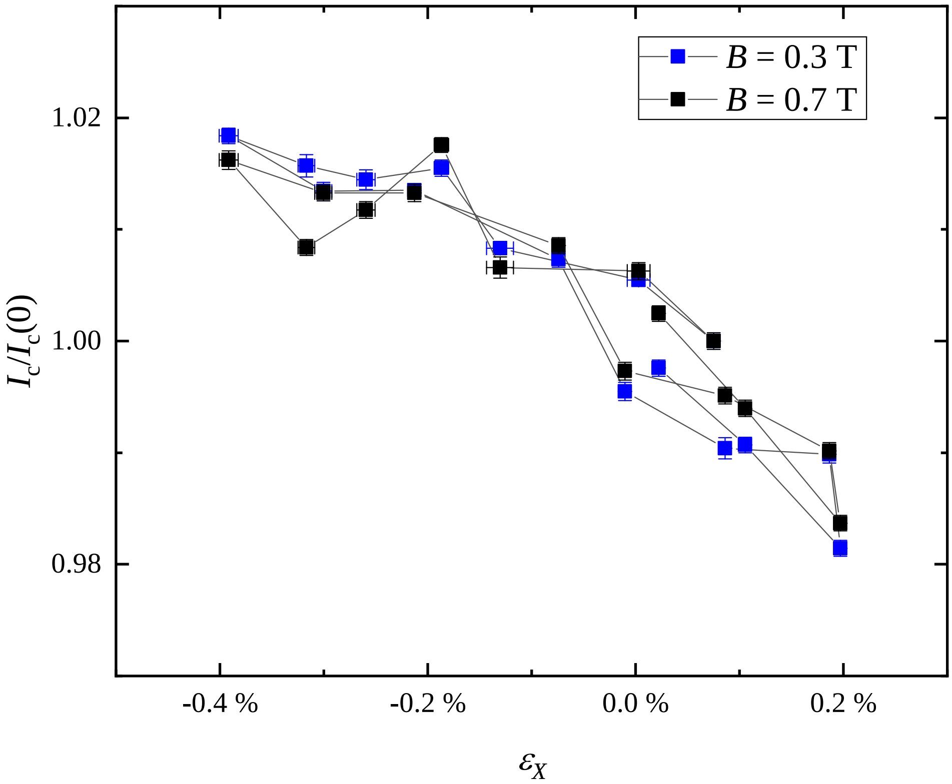

Figure 8.4: Normalised critical currents on the long sample with varying $X$-strain and an applied $Y$-strain of -0.185%.

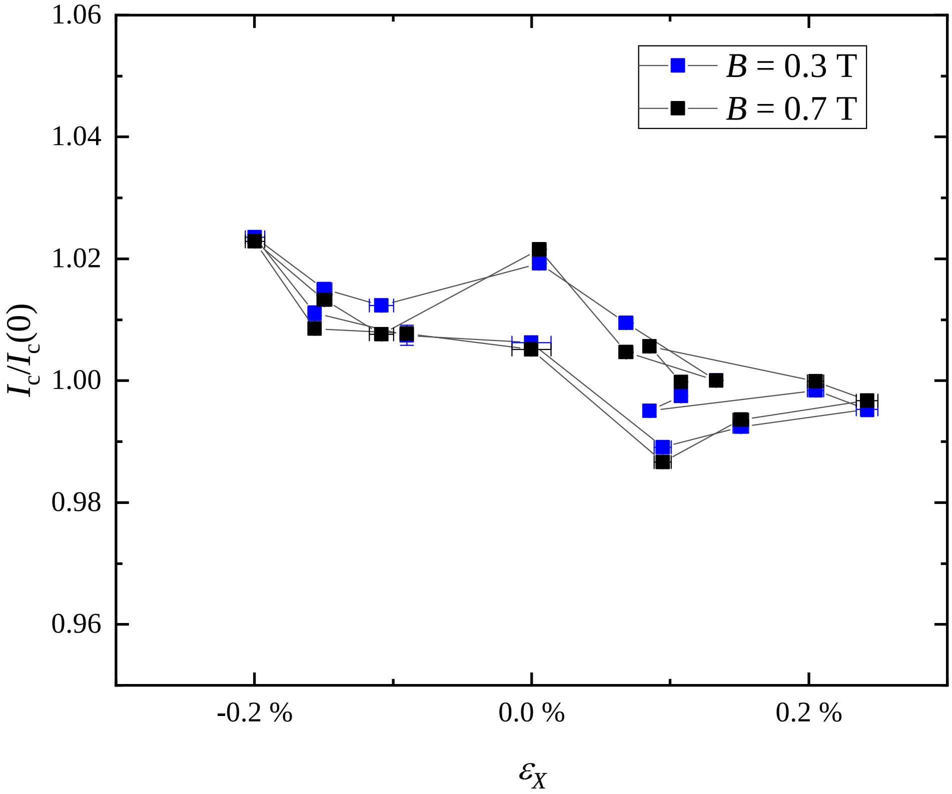

Figure 8.5: Normalised critical currents on the long sample with varying $X$-strain and an applied $Y$-strain of -0.262%.

with an additional applied $\varepsilon_Y$ of -0.185%, and

$$\frac{1}{J_c(0)}\frac{dJ_c}{d\varepsilon_X} = -5.7(10)\%/\% \tag{8.2.3}$$

for an applied $\varepsilon_Y$ of -0.262%.

Also notable is the less clear linear behaviour with applied $Y$-strain. For $\varepsilon_Y$ = -0.185%, there is a decrease in gradient for larger compressive $X$-strains which is not seen in the uniaxial data.

The reduced strain range measured at the largest compressive $Y$-strain means that the quality of the linear trend is reduced significantly. As $X$-strains beyond -0.2% were not measured for $\varepsilon_Y$ = -0.262%, it is not known whether the decrease in gradient seen at the intermediate $Y$-compression would also be present for larger $Y$-compressions.

### 8.2.1 $y$-tension

The sample failed with significant irreversible decrease in $J_c$ of 28% at 0.7 T and 37% in self-field when a $y$-tension of 0.18% was applied, as well as an irreversible 40-50% reduction in $N$-value. The combined reduction in $I_c$ and $N$ is a strong indicator of sample damage. This could be due to crack propagation under $y$-tension. The nature of the substrate provides an explanation for why the sample would fail at this $y$-strain but not at an equivalent $x$-tension. The MgO buffer layer is faceted as a result of the angled deposition, which provides the 30° tilt for the $ab$-planes without the height of the buffer layer changing significantly over the width. The corners associated with these facets lie parallel to the $x$-direction, which means that they will be most likely to nucleate cracks for perpendicular strains in the $y$-direction. These sharp angles may be causing crack nucleation and growth at much lower tensile strains than are needed to cause failure in the $x$-direction. Figure 8.6 is a scanning transmission electron microscopy (STEM) image showing these facets, measured by Lao *et al.* [128].

Interplanar strain measurements (in section 8.4.1) were made for $y$-tension in the tape axis, for strains up to $\varepsilon_{yy}$ = 0.14% without observing this dramatic irreversible drop in $I_c$. If these two samples are taken to be indicative of all samples, the threshold for damage would be between $\varepsilon_{yy}$ = 0.14% and 0.18%.

Further work is needed to determine if this failure is repeatable and determine the reversible limit for this orientation of strain.

### 8.2.2 Strain on short samples

Strain measurements on short samples with the experimental apparatus used for this thesis were significantly compromised.

The strain board is constructed of beryllium copper, which is chosen for its large elastic limit and its solderability. The sample is soldered to the strain board to provide a good mechanical contact that is robust to changing strains under cryogenic conditions, with

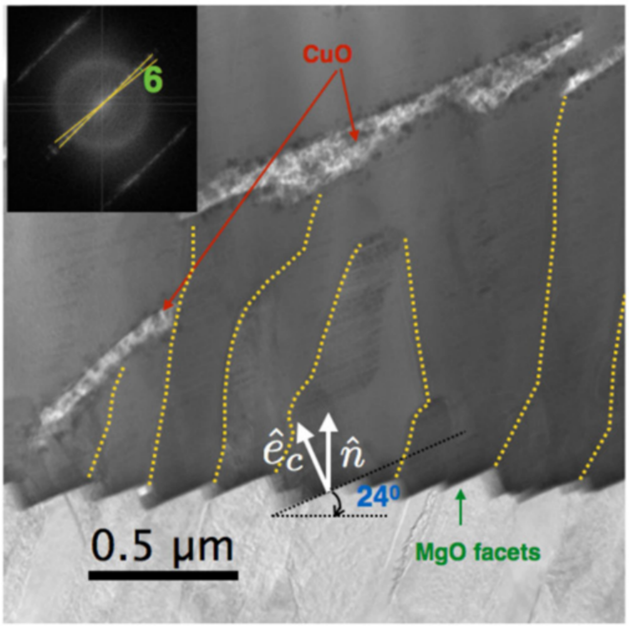

Figure 8.6: An annular bright field STEM image measured by Lao *et al.* [128] of the buffer layer and lower part of the REBCO layer in an ISD CC. Current in the *ab*-direction would be applied into the page.

comparatively easy mounting and removal of samples. The electrical contact between the sample and the strain board is not typically an issue for measurements as the superconductor has no resistance and therefore carries all of the current when below $J_c$, and a parallel current path needs to be present to prevent runaway heating of the sample during transition when the REBCO becomes an insulator. The copper coating on the surfaces of the tape provides this parallel current path, with the beryllium copper strain board not affecting this mechanism under normal conditions.

Figures 8.7 and 8.8 show the new design for current leads on the strain board. The leads are designed to maximise the surface area for current injection into the short sample given the very short length available. They are also designed to have a sufficiently large cross section to avoid excessive heating during a high-current measurement and minimise their electrical resistance compared to the parallel current path. The design thickness of 1 mm is a compromise between minimising electrical resistance and minimising the perturbation of the strain state which would occur for very thick current leads.

Current leads were also designed and made for samples rotated by 45°, shown in figure 8.9, although these current leads were not used for $I_c$ measurements due to the difficulties encountered with the straight current leads under strain.

For 12 mm short samples, the ends of the sample are within the high strain region on the board, and therefore at least part of the current leads and the joint to the superconductor are also in the high strain region. The current leads therefore need to be mechanically connected to the strain board to avoid significant stress concentration in the solder joint between the current leads and the sample. The current leads were mechanically bonded to the strain board with solder along with the sample. The measurements on unstrained samples showed good agreement with long samples (see figure 6.18), giving confidence that current was flowing through the superconductor as intended, which is still much

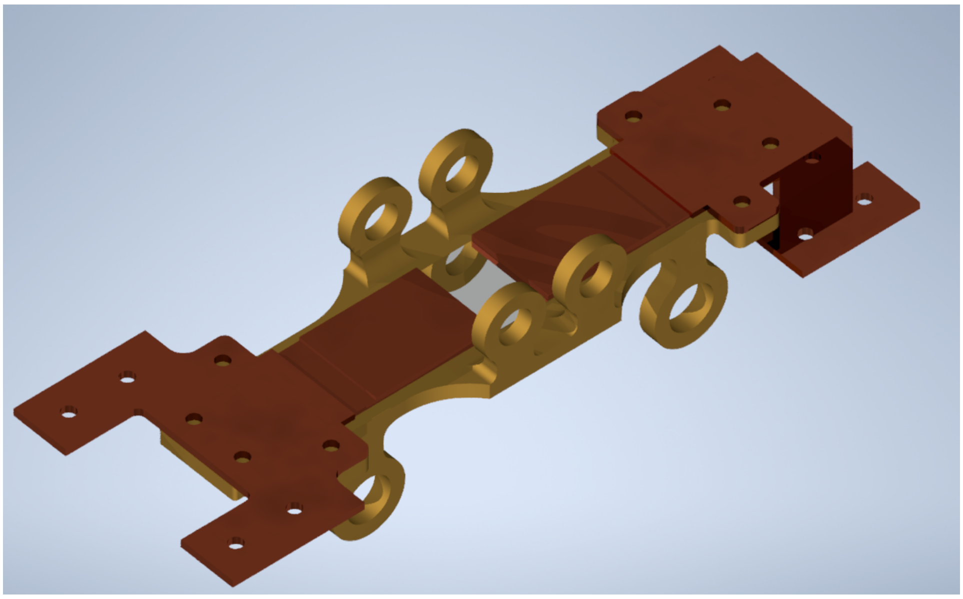

Figure 8.7: Sample board with current leads for short samples. Copper current leads are soldered onto the beryllium copper strain board for mechanical stability to ensure the strain in the board is distributed through the current leads. The electrical contact between the current leads and strain board through this solder joint has led to a degree of current shunting which varied with strain, attributed to the joints between the current leads and CC sample (shown in silver) degrading with strain.

Figure 8.8: Current leads for a short sample, showing the joint between the copper and the CC.

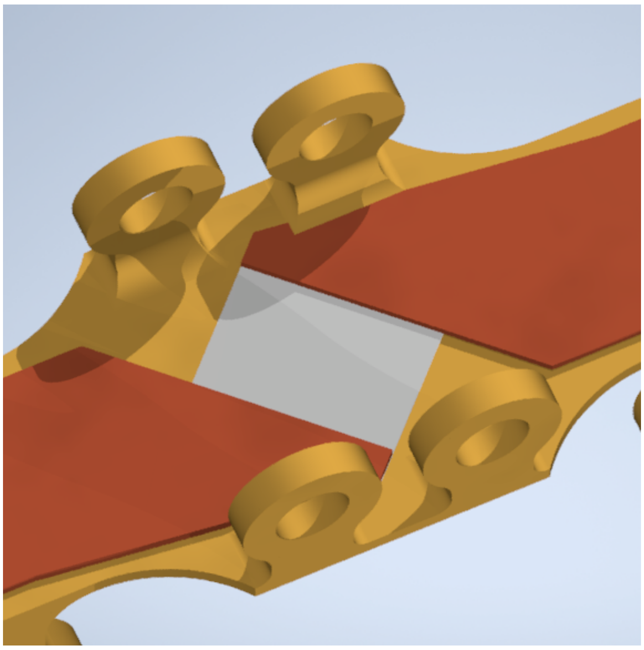

Figure 8.9: Design for current leads to a short sample rotated by 45°.

lower resistance than the strain board.

Unfortunately, when strains above a few tenths of a percent were applied, the apparent $I_c$ would often suddenly increase. This is attributed to an increase in the resistance of the joint between the current leads and the sample when strain is applied, causing an alternative current path out of the current leads into the strain board to become closer in resistance to the sample and cause a few percent of the current to travel through this parallel current path. The unpredictable nature of these increases make comparisons between measurements extremely difficult.

These changes were seen on a number of samples, both for interplanar and *ab*-currents. On samples where multiple voltage taps were used to determine the spacial variation of the transition voltage, a divergence between the behaviour of the centre and edge was observed once a larger strain is applied.

A schematic of the short sample is shown in figure 8.10, with the location of the voltage taps shown. When only one pair of voltage taps is used, they are located at the 'centre voltage taps' locations, and when an additional pair of voltage taps are used they are placed near the edge of the sample. Multiple voltage taps were only possible on unbridged samples.

On short sample 5, both voltage taps produced irreversible increases of roughly 10% when the strain was taken to -0.25%. The edge voltage tapes gave a slightly higher $I_c$ before strain application, but this gap increased notably when the irreversible jump occurred between -0.2% and -0.25% (figure 8.11). A corresponding increase in the resistance of the whole strain board occurred when the sample is placed into compression and again when taken into tension (figure 8.12), indicating damage along the current path occurring which would cause current shunting. Additionally, a large baseline voltage was picked up on this sample after the jump in $I_c$ occurred (figure 8.13), indicating a significant degree of current shunting in the voltage tap region.

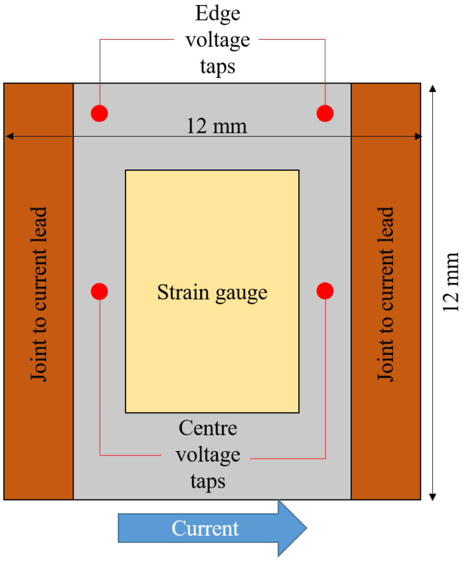

Figure 8.10: A scale diagram of the setup for a short sample. The brown regions are the solder joints to the copper current leads. Where multiple sets of voltage taps were used, one pair are in the centre of the current flow path and another pair mounted near to the edge of the sample.

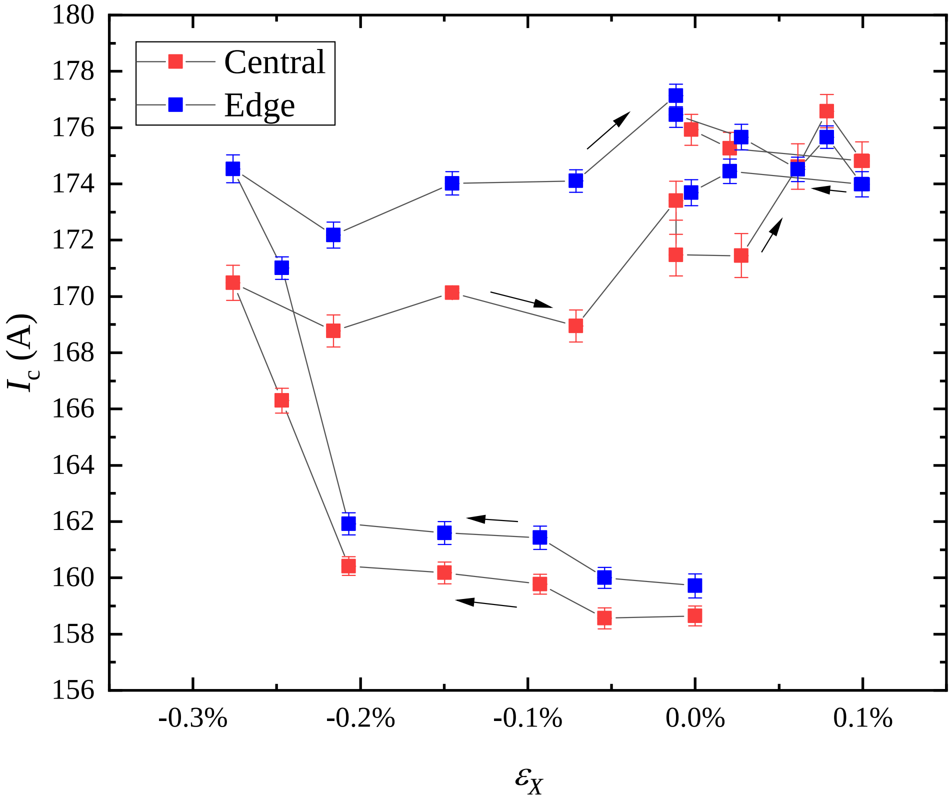

Figure 8.11: Critical current as a function of $X$-strain measured on short sample 5 with two different voltage tap pairs, one in the centre of the sample and the other at the edge of the sample. All measurements are for 0.7 T perpendicular to the tape. A shallow increase in $I_c$ is seen as expected up to -0.2% strain, when a sudden increase in $I_c$ occurs and the difference between centre and edge increases. Once the sample is taken into tension, the central voltage tap switches to having a slightly higher measured $I_c$ than the edge.

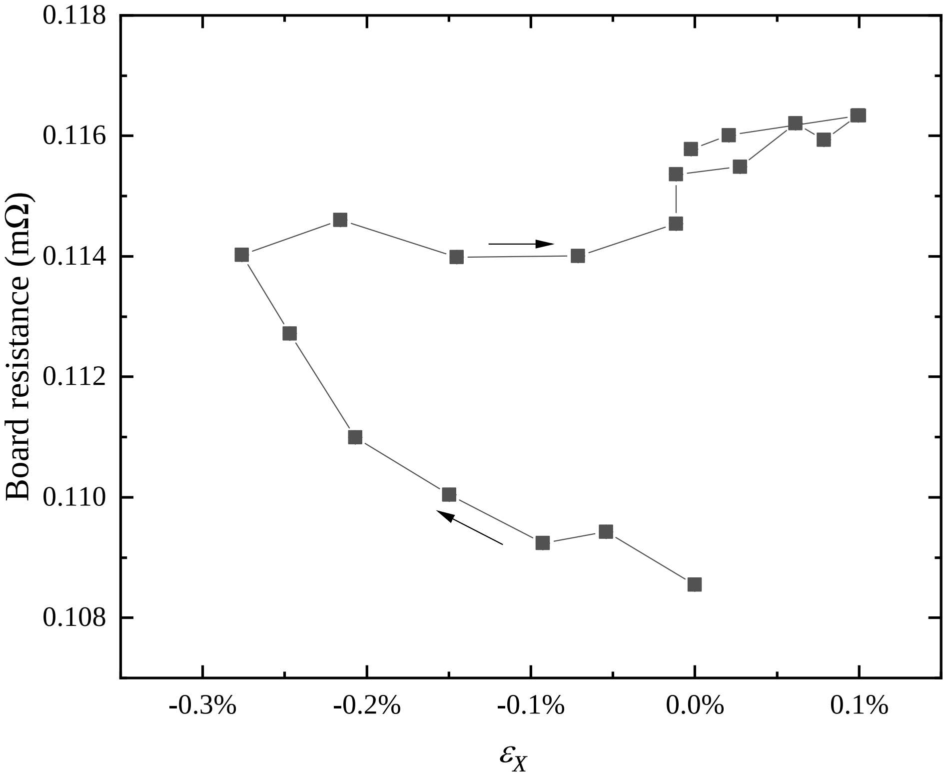

Figure 8.12: The resistance of the whole strain board as strain is applied with short sample 5. The resistance increases as compressive strain is applied, and again as the board is taken into tension. This increase in resistance implies the degradation of a joint or the sample as strain is applied, with cracks generated in compression opening as the sample is taken into tension.

A similar picture is seen for short sample 3, with a large discrepancy between the central and edge voltage taps appearing at the point of a large current jump, albeit at a larger applied strain of -0.35% (see figure 8.14). For this sample, the two voltage taps retained the large difference in $I_c$ as the strain was removed and the traces became increasingly degraded. The resistive baseline measured on the central voltage taps once larger strains had been applied was much steeper than measured at the edge, and by the time 0.1% tension was applied the baseline was too severe to measure a transition.

The divergence between centre and edge voltage taps indicates that whatever change is occurring to irreversibly change the measured critical current is spatially varying. This indicates a change close to the sample which could change the current distribution through the sample as a result of damage. A degradation of either the sample or the joint between the current leads and the sample is most likely to explain this discrepancy between the edges and the centre. The short length and low aspect ratio of the sample is likely to be sufficient to support a non-uniform current distribution across the width. If the joint into the superconductor were to degrade at the edge, the current density is likely to be higher in the centre of the sample, causing the voltage measured at the edge to be lower and consequently a higher total current would be required to reach the $I_c$ threshold.

Measurements of the strain board voltage show an increase in the effective resistance of the strain board through the series of measurements on the interplanar current sample (discussed in section 8.22). This supports the interpretation of an increase in resistance

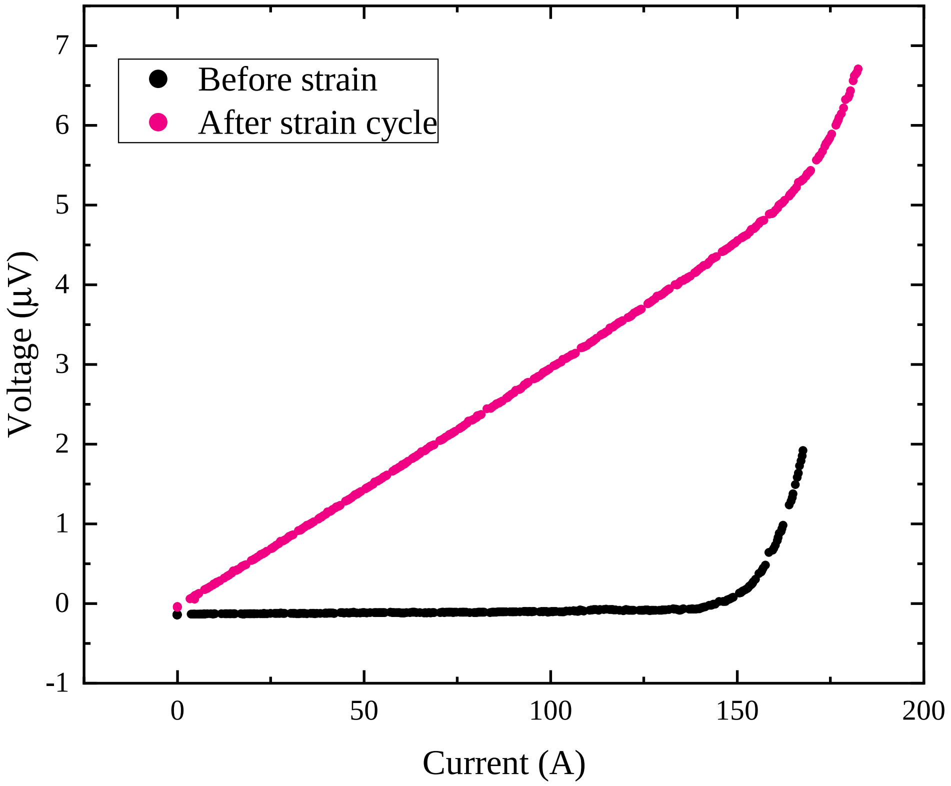

Figure 8.13: Raw $I$-$V$ traces measured on short sample 5. Both are for an applied field of 0.7 T perpendicular to the tape, no applied strain and measured on the central voltage taps. The pink data are taken after the strain sweep to -0.28% compression, 0.1% tension and returned to 0, showing a large resistive baseline and a significant increase in $I_c$.

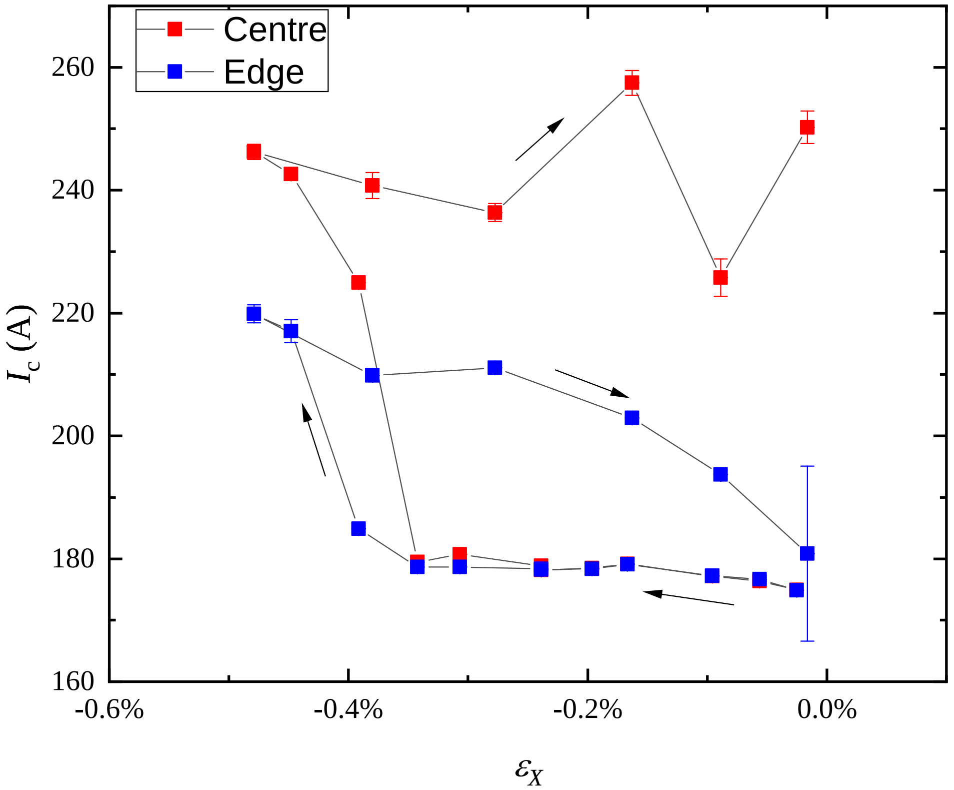

Figure 8.14: Critical currents measured on short sample 3 as a function of $X$-strain with two different voltage tap pairs, one in the centre of the sample and the other at the edge of the sample. All measurements are for 0.7 T perpendicular to the tape.

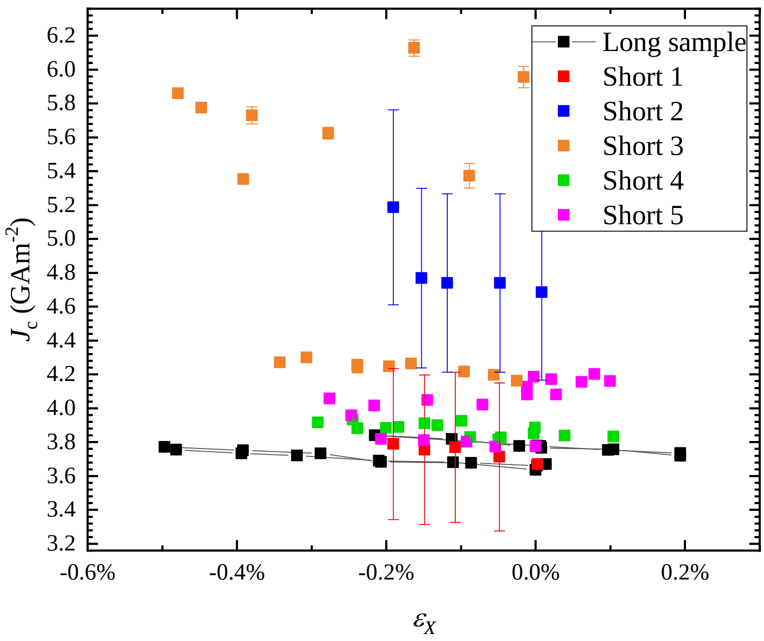

Figure 8.15: Measurements of critical current density as a function of uniaxial $X$-strain on the *ab*-current samples. The applied field is 0.7 T perpendicular to the tape. The large error bars for short samples 1 and 2 are due to the error on the scribed bridge widths used for the calculation of $J_c$. Figure 8.16 is normalised plot of these data and the measurements at different field strengths on the same samples, which allows for a comparison of strain gradients.

increasing the measured $I_c$. Extra insulation was added at the ends of the strain board to electrically isolate all components from the strain board apart from the sample and on-board current leads which are soldered down. This did not affect the increased $I_c$ value, indicating that the change in $I_c$ is due to a change within the strained region. Significant changes in the current lead properties are unlikely, so the behaviour can be attributed to either the joint between the current leads and the sample or to some change in sample properties. It is possible that some delamination or other damage occurs which dramatically increases the current injection length. While this is not seen on the long sample, there could be some stress concentration associated with the joint causing the damage.

The parallel current path must be sufficiently far from the sample to not show up as a significant resistive baseline on the measurements, although some measurements did pick up a resistive baseline in addition, suggesting current flow through the copper tape surround. The measurements with resistive baselines may indicate damage internally in the tape preventing current transfer between layers.

A comparison of strain in long and short samples is given in figures 8.15 and 8.16. Excluding data points after abrupt increases in $I_c$, some short samples have gradients of $J_c$ with strain within error of the long sample behaviour, and others show a steeper gradient (but all within two standard deviations). The weighted average of the gradients for the short samples is -8.4(7) %/%, showing a consistently slightly greater change of $I_c$ with strain. The large changes of $I_c$ are largely discrete, but the same mechanism causing these increases could also be increasing the $I_c$ gradient with strain in some of the samples.

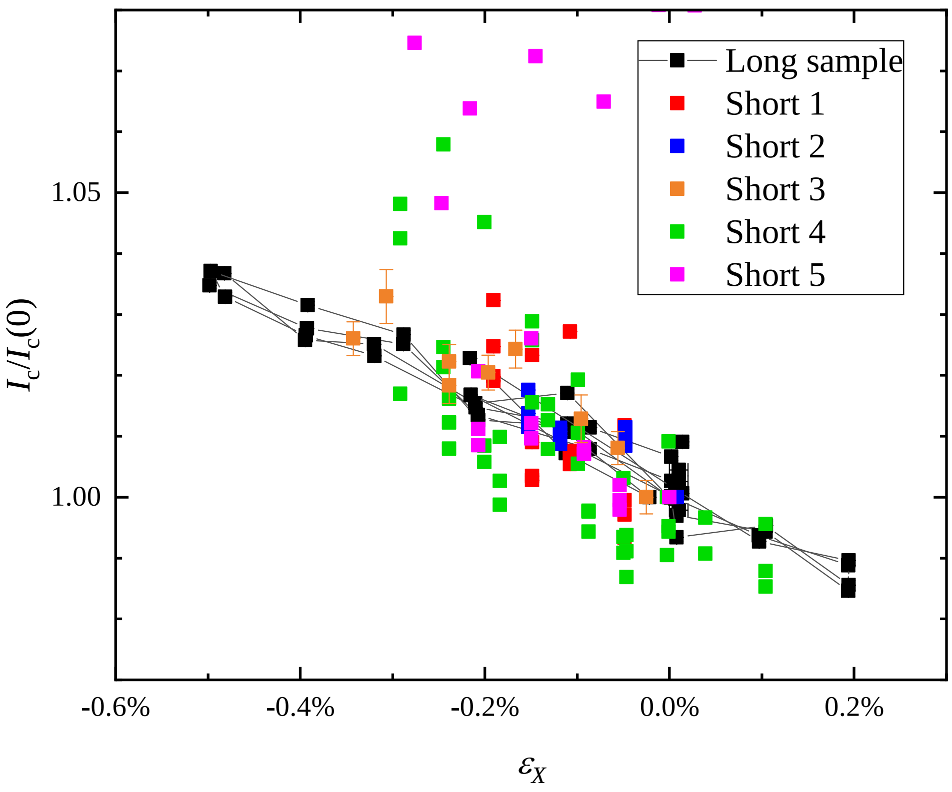

Figure 8.16: Normalised critical current as a function of uniaxial $X$-strain on a number of short samples with $ab$-current. The reversible strain range is much smaller than for the long sample (shown in black), due to the sensitivity of the measurements to the quality of the joints to the REBCO tape. Sudden increases in current are seen when larger strains are applied, which can be seen here in the sample sample 5 (pink) data. The increase seen in sample 3 (green) was reversible, with the original $I_c$ being recovered when the strain was removed. For sample 5 a much larger increase was observed (off the scale of the plot) which was not reversible. Samples 2 (blue) and 3 (orange) also had an irreversible sudden increase, too large to appear on this plot. Sample 1 failed at roughly -0.2% $x$-strain with a sudden increase in $y$-strain and loss of superconductivity. See table 8.1 for a summary of the samples.

This current shunting issue could be addressed by changing the material of the strain board to something much more resistive and/or electrically isolating the sample from the strain board. The mechanical bonding would be much more challenging but may be possible for future research. Alternatively, a complete redesign of the strain apparatus specifically for small samples may be able to avoid the problems encountered here with the joint to the sample under relatively large strains by decreasing the strained volume to exclude the joints.

## 8.3 Interplanar current measurements

Measurements have been made on short samples of the interplanar currents in THEVA ISD CCs. Section 4.2.4 looked at the limited existing literature addressing interplanar currents.

Measurements are made in the same manner as for short samples with $ab$-current, but with a rotation of the sample by 90°. Figure 8.17 shows measurements with varying magnetic

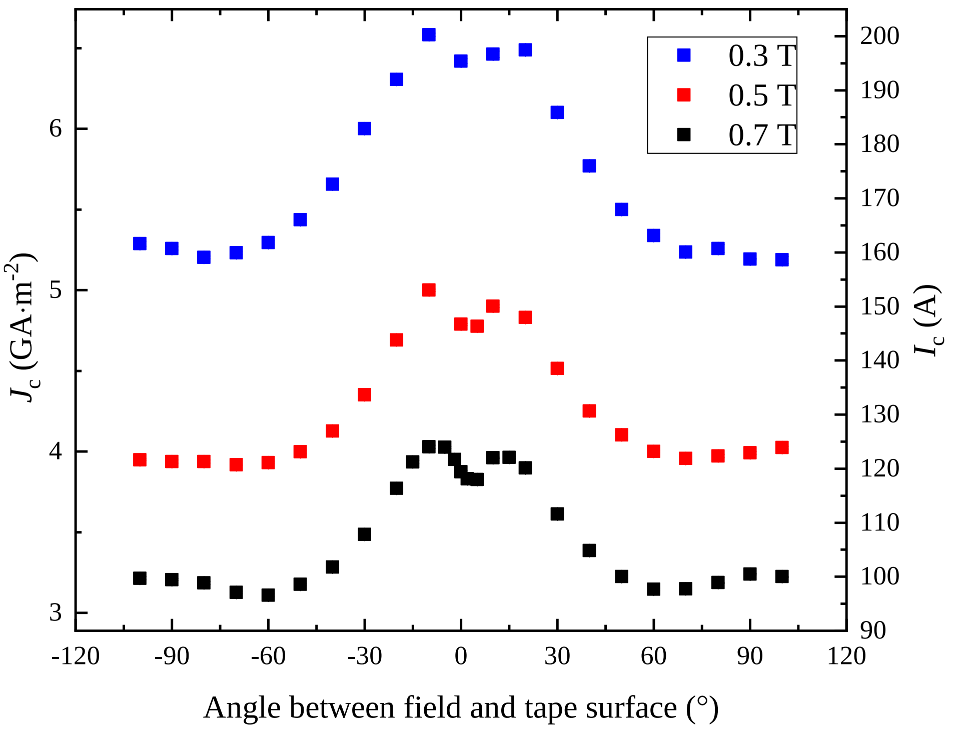

Figure 8.17: Critical current as a function of magnetic field angle on THEVA CCs with interplanar current, where current is applied perpendicular to the *ab*-current direction such that current is forced to travel between *ab*-planes. The magnetic field is rotated in the maximum-Lorentz-force configuration.

field rotated such that the field remains perpendicular to the current flow (maximum Lorentz force). An angle of 0° still corresponds to the field parallel to the tape surface, which is now parallel to the *ab*-planes in the interplanar configuration.

The flux-channelling trough at $B \parallel ab$ is observed clearly in the data along with a slight asymmetry. The variation in $N$-value with angle is shown in figure 8.18, which for an applied field of 0.7 T shows a clear increase in $N$ around $B \parallel ab$ which does not correspond to an increase in $J_c$ and is therefore not attributable to heating from large currents. The data at lower fields and correspondingly higher currents are less clear with much more scatter on the $N$-values, which are extremely sensitive to the quality of the traces. In this case, the increased scatter is likely to be due to a small amount of sample heating at the higher currents with the very short injection lengths available in short samples. A peak in transition index near $B \parallel ab$ is seen, a feature that is also seen for *ab*-current (see figure 6.12), although for interplanar currents the *ab*-planes are parallel to the tape (0°) rather than at 30°.

A comparison between $J_c(B)$ of *ab*-current and interplanar current is shown in figures 8.19 & 8.20 and a comparison of the $N$-values is shown in figure 8.21. For both samples, the field is applied perpendicular to the tape, which means that the field and fluxon state should be identical between samples and only the current flow direction is changed. At other angles, an equivalent field state in *ab*- and interplanar currents would have different Lorentz forces and therefore not be directly comparable $J_c$ values. The critical current has the same power law behaviour in-field for both current configurations, but scaled by a factor of approximately 20%. In low-fields, the interplanar current is suppressed

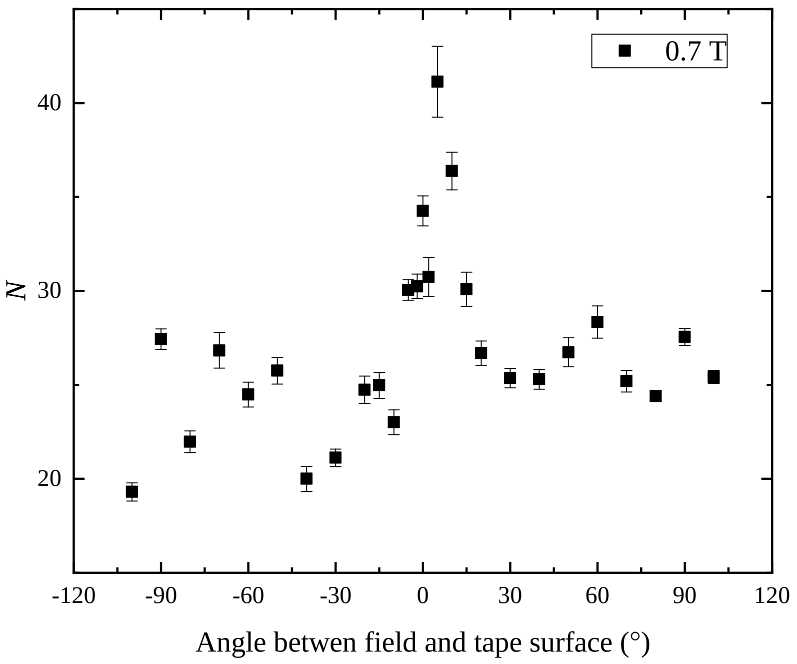

Figure 8.18: The transition index, $N$, as a function of magnetic field angle for the 0.7 T data shown in figure 8.17.

more strongly relative to the $ab$-current direction, being 40% lower in self-field. This is contradictory to the prediction from equation 7.3.1, which suggests that self-field $J_\mathrm{c}$ would scale as

$$J_\mathrm{c}(\mathrm{SF}) = J_\mathrm{c}(B)^{\frac{1}{1+c_1}}. \tag{8.3.1}$$

A tape limited by the cross-over field would give a 12% increase in self-field $J_\mathrm{c}$ from a 20% increase in in-field $J_\mathrm{c}$, which differs from the increased suppression of $J_\mathrm{c}$ seen in the samples measured here. This could suggest that a different mechanism is limiting the self-field critical current for interplanar currents. The specific mechanism for this is not understood at present. The author is not aware of any published measurements of this comparison between in-field and self-field with equivalent magnetic states, so future measurements of this in other regions of phase space such as variable temperature measurements may shed more light on the mechanism determining self-field $J_\mathrm{c}$ for interplanar currents.

The stronger $J_\mathrm{c}$ suppression in self-field is also contrary to the prediction from a JJ model neglecting self-field. If the system is described as being limited by JJs in the $ab$-direction and by thicker or more resistive JJs in the interplanar direction, the larger $\tilde{\xi}_\mathrm{n}$ at lower fields (see equation 3.5.4) would lead to a weaker relative suppression at small fields. This supports an argument that the low $J_\mathrm{c}$ in self-field is due to a different dissipation mechanism or current distribution when interplanar currents are applied.

The transition indices, $N$, are the same within error for $ab$-currents and interplanar currents in-field, which may indicate that a similar mechanism for flux flow is present for both current configurations. There is a discrepancy in self-field, although unfortunately there is a relatively large uncertainty in $N$ when currents are large in short samples. The

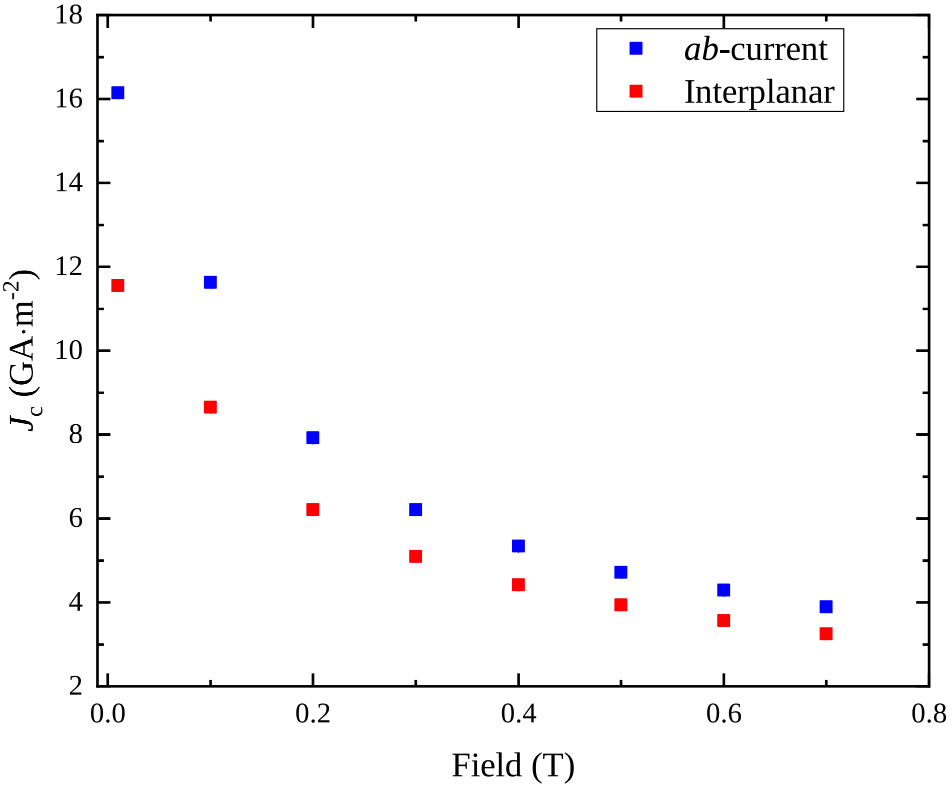

Figure 8.19: A comparison between the critical current density as a function of applied field for a short sample with *ab*-current and interplanar currents. The short sample is full width (12 mm) and the interplanar current sample is 8 mm wide. For both samples, the field is applied perpendicular to the tape.

error bars in figure 8.21 refer to the calculation of $N$ (see appendix B) and does not account for factors such as heating which give a systematic change in the transition index.

## 8.4 Strain effects on interplanar currents

The effect of strain on interplanar current could help to understand the underlying mechanisms determining $J_c$ in REBCO and give information about the importance of the layered structure. The plane separation will change under strain, particularly when strain is applied with a component in the $c$-direction.

For *ab*-current, the efficacy of scaling laws such as equation 4.5.1 suggests that changes in critical currents can be attributed to changes in $T_c$ and $B_{c2}$. $B_{c2}$ can also be described in terms of $T_c$, although it is also sensitive to changes in pinning and microstructure. Some analyses of strain behaviour [175, 161] have described $B_{c2}$ purely in terms of $T_c$, which would mean that for *ab*-current the change in plane spacing is not expected to have a significant effect beyond the small change in $T_c$ from $c$-oriented strains. For interplanar current, however, the current is forced to travel in the $c$-direction, meaning that current flow through the weakly superconducting regions of the unit cell occurs. This is understood as coupled layers where the separation is sufficiently small for a high degree of tunnelling through the weakly superconducting regions, particularly in light of the modest reduction in $J_c$ at high temperatures. For a system of coupled planes, it may be expected that

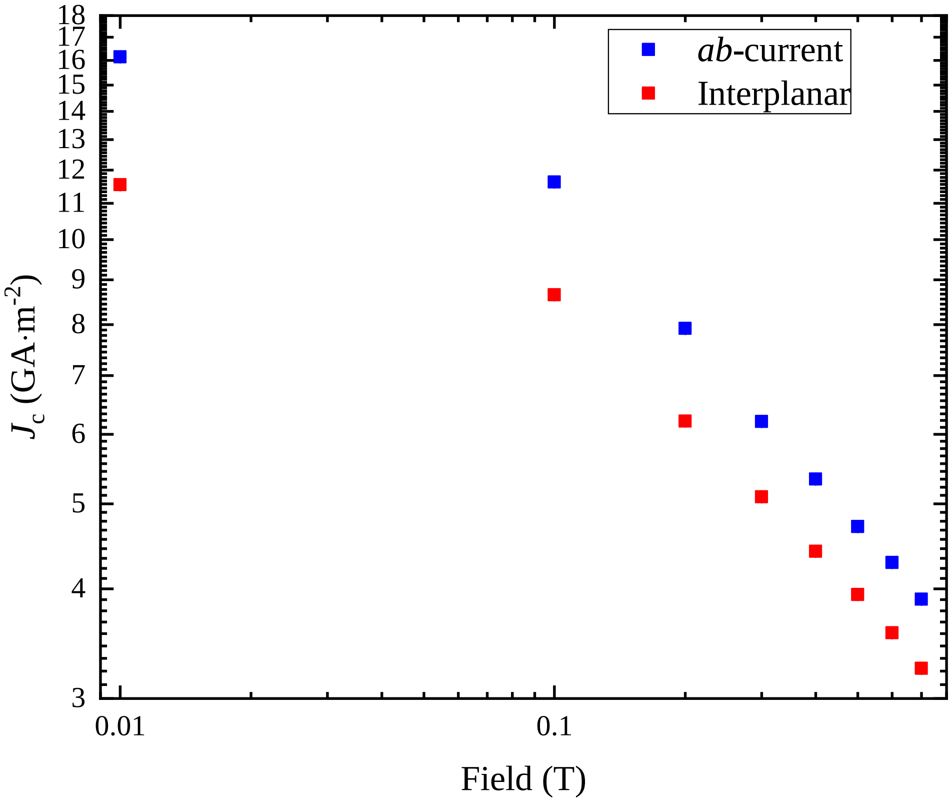

Figure 8.20: The same measurements of critical current density as a function of applied field as in figure 8.19, presented on a log graph. This shows an almost identical power law exponent in-field for both measurements, but a lower cross-over field in the interplanar configuration. The switch to self-field behaviour for interplanar currents does not appear to be controlled by the load line discussed in section 7.3.

the critical current is highly sensitive to the plane separation, which would mean that the strain sensitivity is stronger. The critical current would increase in compression and decrease in tension if the plane spacing is strongly affecting the critical current.

The strength of this effect can be simply estimated by assuming that the planes act as JJs with the strongly superconducting planes as the electrodes and the gap between them as junctions.

Using equation 3.5.4, the critical current through the junction depends exponentially on the thickness. This means that the change in $J_\mathrm{c}$ with thickness can be expressed as

$$\frac{\mathrm{d}J_\mathrm{c}}{\mathrm{d}d} = \frac{-1}{\xi_\mathrm{n}} J_\mathrm{c}, \tag{8.4.1}$$

and with the chain rule this can be expressed as

$$\frac{\Delta J_\mathrm{c}}{J_\mathrm{c}} = \frac{-\Delta d}{\xi_\mathrm{n}}. \tag{8.4.2}$$

As we do not have the relevant information to determine the material parameters of the normal region for the interplanar current's JJ system, we shall assume that the normal region has the same properties as the normal barriers which limit current flow for *ab*-current and that the difference in $J_\mathrm{c}$ can be attributed purely to an increased thickness of normal

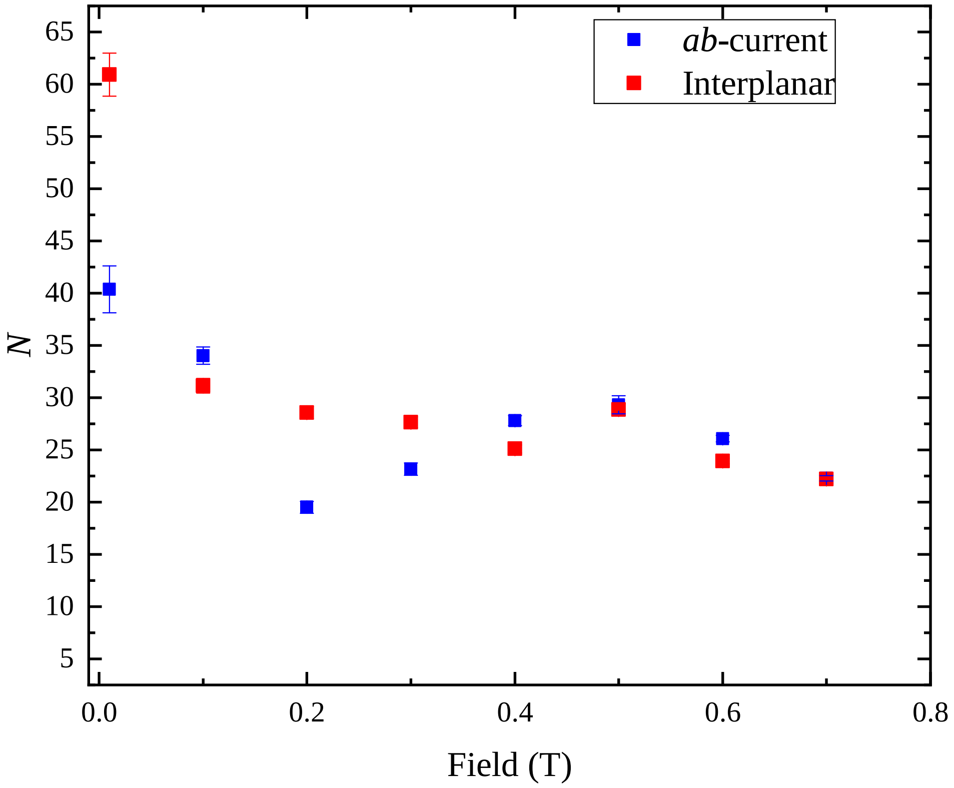

Figure 8.21: A comparison between the transition indices as a function of applied field of the *ab*-current to the interplanar current measurements. The transition indices are the same within error apart from in self-field, where a greater discrepancy between the critical currents is also observed.

barrier. The material properties of JJs along the current path are expected in general to differ from the weakly-superconducting interplanar regions.

Making this assumption, the relative critical currents for *ab*- and interplanar currents can be written as

$$\ln\left(\frac{J_c(ab)}{J_c(\text{interplanar})}\right) = \frac{1}{\xi_n}(d_{\text{interplanar}} - d_{ab}). \tag{8.4.3}$$

Using the normal state parameters determined for THEVA tapes in table 7.1, the relative condensation parameter at 77 K is $\tilde{\alpha}_n = -2.748$ and the normal state coherence length at 0.7 T, 77 K is 1.688 nm. Combining this coherence length with the calculated $d_{ab} = 3.27$ nm (table 7.1), equation 8.4.3 becomes

$$\frac{d_{\text{interplanar}}}{\xi_n} = 2.427. \tag{8.4.4}$$

The fractional change in junction thickness (neglecting anisotropic effects) can be given by $\frac{\Delta d}{d} = \varepsilon_{cc}$, which combined with equation 8.4.4 means that the change in $J_c$ from plane separation is

$$\frac{\Delta J_c}{J_c} = -2.427\varepsilon_{cc}. \tag{8.4.5}$$

| Elastic constants | $\frac{\Delta J_\mathrm{c}}{J_\mathrm{c}\varepsilon_X}$ |
|---|---|
| Reichardt [147] | -0.22 |
| Ledbetter [148] | -0.43 |
| Lei [149] | -0.25 |
| Murphy [150] | -0.30 |
| Favre [151] | -0.06 |

Table 8.2: Predicted change in interplanar $J_\mathrm{c}$ with strain from the effect of changing $c$-axis length, from equation 8.4.5.

The $c$-strain can be found using equation 8.5.6, (noting that for interplanar current, $J \parallel \varepsilon_{yy}$) giving $\varepsilon_{cc} = -0.454\varepsilon_{xx} - 0.018\varepsilon_{yy}$ when Lei *et al.*'s elastic constants are used. The $y$-contribution is so small in this case because the $z$-strain generated from the Poisson ratio effect almost cancels the component from the $y$-strain.

Using equation 8.4.5, the predicted change in $J_\mathrm{c}$ from changes in plane-spacing at 0.7 T, 77 K is

$$\frac{\Delta J_\mathrm{c}}{J_\mathrm{c}} = 1.102\varepsilon_{xx} + 0.044\varepsilon_{yy}, \tag{8.4.6}$$

where strains and the fractional change in $J_\mathrm{c}$ are both expressed as a percentage.

The magnitude for the correction from this effect on uniaxial strain measurements can be calculated by using the effective Poisson ratio of the strain board. For the biaxial strain board with no applied $Y$-strain, the Poisson ratio is -0.263. Performing the above calculation for all sets of elastic constants, the predicted changes during a uniaxial strain measurement (when $\varepsilon_X = \varepsilon_{yy}$ is applied) are given in table 8.2.

The experimental configuration for the measurements presented in this chapter allows for *in situ* $y$-strain control in the interplanar current configuration, which means that the effect of plane-spacing on the measurements is expected to be relatively small. As the strain variation observed in the $ab$-current direction is $\frac{\Delta J_\mathrm{c}}{J_\mathrm{c}} = -7.0(3)\varepsilon_X$ (equation 8.2.1), the $T_\mathrm{c}$ variation is expected to have a much larger effect than changes from plane-spacing at 77 K. At lower measurement temperatures, the effect of changes in plane spacing would get stronger as $\xi_\mathrm{n}$ decreases, and the change of $J_\mathrm{c}$ with $T_\mathrm{c}$ becomes weaker. Using the same material parameters, the normal state coherence length decreases to 1.206 nm at 10 T, 4.2 K, which gives $\frac{\Delta J_\mathrm{c}}{J_\mathrm{c}} = -3.397\varepsilon_{cc}$. The expected strain dependence from plane spacing at 10 T, 4.2 K using Lei *et al.*'s constants [149] is therefore

$$\frac{\Delta J_\mathrm{c}}{J_\mathrm{c}} = 1.54\varepsilon_{xx} + 0.06\varepsilon_{yy}. \tag{8.4.7}$$

### 8.4.1 Strain measurements on interplanar currents

The problems described in section 8.2.2 were present in short samples for both $ab$- and interplanar currents, but as short samples were the only option for interplanar currents, all strain measurements on interplanar currents have been compromised in this way. The

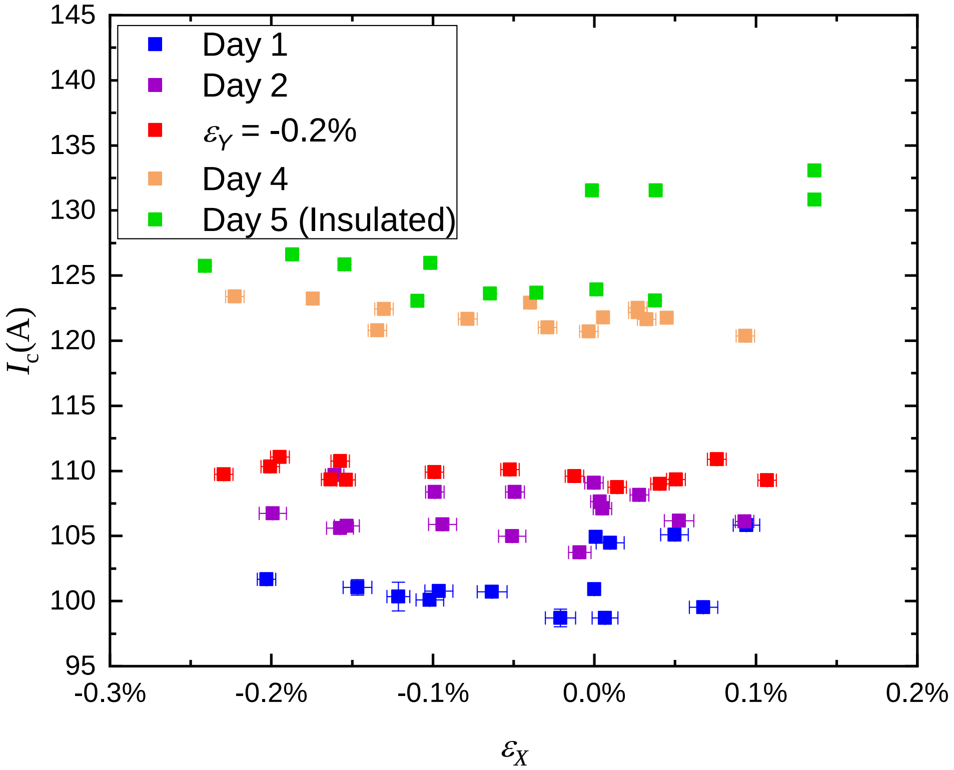

Figure 8.22: Critical current measurement with applied $X$-strain on the interplanar current sample over a number of strain cycles. The blue data are on the initial strain cycle, which showed an irreversible increase in $I_c$ when the sample was taken into tension, which was retained when the sample was subsequently measured after a thermal cycle to room temperature (purple). Several further jumps occurred, including the significant jump in the 5th strain cycle under tension again (green). All cycles are for $\varepsilon_Y = 0$ except for the red data which have an applied strain of $\varepsilon_Y = -0.2\%$

variation in $I_c$ for the only interplanar sample measured is shown in figure 8.22. As this problem was not overcome in this work, strain on interplanar current was not reliably measured in a repeatable fashion. Nevertheless, the data are presented here and limited conclusions drawn from the results.

Some information can be extracted from this if it is assumed that the joint/sample degradation is sudden and discrete. The changes in $I_c$ with strain which show gradual and monotonic changes can be attributed to changes in superconducting properties and sudden jumps which can be attributed to damage.

Normalising each strain sweep to the zero-strain values allows for a comparison of the gradient of $J_c$ with strain, shown in figure 8.23. The data sets for each measurement day have been normalised to the first measurement of each set, which is made with no applied $X$-strain. Also shown on this figure is the strain variation of the *ab*-current long sample within this strain range, suggesting a reasonable agreement of the gradients of *ab*- and interplanar current.

The gradients of the measurements that have been made on interplanar currents have been extracted by normalising and removing all data points on a particular strain sweep after any abrupt change occurs. The gradients for each measurement day are given in table 8.3. The average gradient for all measurements with no applied $Y$-strain is within error

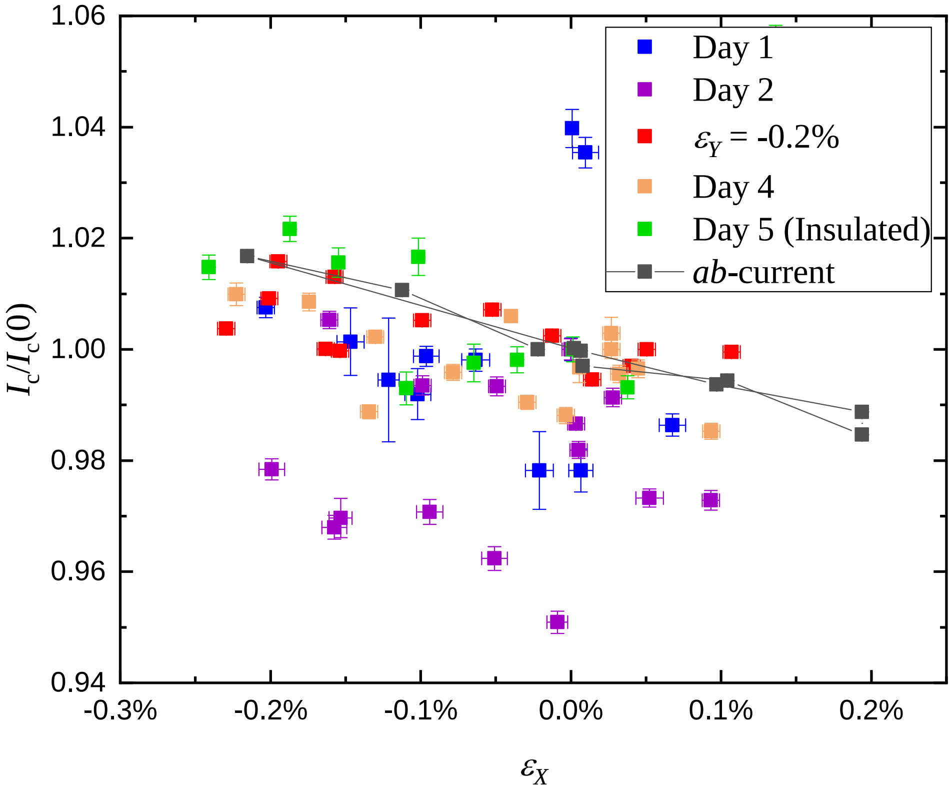

Figure 8.23: The same measurements of interplanar current as a function of applied $X$-strain presented in figure 8.22, but normalised to the initial $I_c$ for each strain cycle. This shows the sudden jump in tension for days 1 and 5 (blue and green), and a small decrease in the critical current on the 2nd strain cycle (purple) when it was taken into compression. The *ab*-current strain data for the same strain range is also presented. The average gradient with strain across samples is within error of of the *ab*-current long-sample once the discrete jumps in $I_c$ are removed by this normalisation.

of the gradient observed in the long *ab*-current sample. This agrees with the prediction above that the change in plane space should have a much smaller effect than changes in $T_c$, and is an indication that changes in $T_c$ remain the dominant mechanism for changing $J_c$ with strain at 77 K for interplanar current. The quality of the data obtained does limit the strength of this conclusion, but no large change in behaviour has been observed. The average strain gradient of all interplanar-current uniaxial strain measurements is

$$\frac{1}{J_c(0)}\frac{\mathrm{d}J_c}{\mathrm{d}\varepsilon_X} = -7.6(13)\%/\%. \tag{8.4.8}$$

Also in agreement with the *ab*-current data, the measurements with applied $Y$-compression also have a shallower gradient than the uniaxial measurements.

## 8.5 A model for strain response

Due to the highly textured nature of CCs, an obvious approach is to model its behaviour using the data from the literature on single-crystals. There are a number of differences that need to be acknowledged, but it remains a useful tool for understanding CCs. The strain state of a free-standing single-crystal under uniaxial or hydrostatic pressure will

| | $\frac{\Delta J_c}{J_c \varepsilon}$ (% / %) |
|---|---|
| Interplanar Day 1 | -8(3) |
| Interplanar Day 2 | -12(3) |
| Interplanar $\varepsilon_Y = -0.2\%$ | -3.4(13) |
| Interplanar Day 4 | -4(2) |
| Interplanar Day 5 (Insulated) | -10(3) |
| Average of interplanar ($\varepsilon_Y = 0$) | -7.6(13) |
| Average of all interplanar | -5.5(9) |
| *ab*-current, long sample | -7.0(3) |

Table 8.3: Strain gradients for measurements of interplanar currents. All interplanar measurements are on the same sample, with repeated strain cycles. Days 1, 2, 4, and 5 have no applied $Y$-strain. Additional insulation was added for day 5, which did not prove to remedy the issue with jumps in $I_c$. For all interplanar measurements, only data points before abrupt changes in $I_c$ are included. The averages are weighted by the errors in each gradient, and the value for the long sample with *ab*-current is included for comparison. Values are given as percent change in $I_c$ per percent strain (% / %).

be different to the strain states seen by the REBCO layer in a CC, due to both the possibility for twisting and shear forces on the tape, and the mechanical interaction with other elements within the tape structure. To make a detailed comparison between single-crystal REBCO and CCs, the strain state in a CC needs to be understood, and an appropriate model for extrapolating the strain behaviour chosen as many regions of the phase space of possible strain states have not to the author's knowledge been measured on high-quality single-crystals. There are in general 9 degrees of freedom in the strain state of an orthotropic material such as REBCO, and only 3 of these are typically measured on single-crystals [140]. A biaxial strain board with rotatable samples also gives access to 3 degrees of freedom in the strain state, but they are not the same ones so an appropriate model is required to predict the change in superconducting properties for regions of phase space not measured on single-crystals. Another key difference between CCs and single-crystals is that single-crystals tend to be optimised for high purity and lack of defects, whereas CCs are designed to have the highest possible $J_c$ for the desired operational conditions, so typically have a large number of pinning sites in the form of defects or APCs. This is harder to account for when comparing to single-crystals, so shall just be understood as a limitation of the predictions. It has been noted in section 4.3.1 that the strain response is highly sensitive to oxygen concentration, so only single-crystals with close to optimum oxygen doping are useful comparisons to CCs. This also leaves the possibility that the defects present in high performance CCs cause significant changes in strain response, both from the strain field typically generated by a defect, and from the possibility of oxygen depletion near a pinning site or grain boundary.

The starting point for the model is to determine how single-crystal REBCO would respond to the strain state seen by the CC.

We first need to find the response of a single crystal to a given strain state. Using equation 4.3.2, the expected values of $\frac{\mathrm{d}T_c}{\mathrm{d}\varepsilon}$ can be found from the single crystal $\frac{\mathrm{d}T_c}{\mathrm{d}\sigma}$ measurements summarised in table 4.2, and the elastic constants summarised in table 4.3.

The calculated values of $\frac{\partial T_c}{\partial \varepsilon}$ from the possible combinations of elastic constants and strain

| | $\frac{\partial T_\mathrm{c}}{\partial \varepsilon_{aa}}$ (K/%) | $T_\mathrm{c}$ versus pressure measurements | | | |
|---|---|---|---|---|---|
| | | Welp [139] | Kraut [135] | Kund [136] | Fietz [140] |
| Elastic constants | Reichardt [147] | 3.00 | 3.75 | 1.30 | 1.29 |
| | Ledbetter [148] | 4.02 | 5.44 | 2.19 | 1.94 |
| | Lei [149] | 2.33 | 2.60 | 0.82 | 0.87 |
| | Murphy [150] | 2.42 | 2.82 | 0.98 | 0.97 |
| | Favre [151] | 3.54 | 4.21 | 1.52 | 1.46 |

Table 8.4: Calculated $a$-strain dependence of critical temperature, $\frac{\partial T_\mathrm{c}}{\partial \varepsilon_{aa}}$ (K/%), from the combinations of elastic constants and pressure dependencies measured by different authors. The literature constants are shown in tables 4.2 and 4.3.

| | $\frac{\partial T_\mathrm{c}}{\partial \varepsilon_{bb}}$ (K/%) | $T_\mathrm{c}$ versus pressure measurements | | | |
|---|---|---|---|---|---|
| | | Welp [139] | Kraut [135] | Kund [136] | Fietz [140] |
| Elastic constants | Reichardt [147] | -2.07 | -3.79 | -2.33 | -1.55 |
| | Ledbetter [148] | -3.62 | -5.97 | -3.32 | -2.36 |
| | Lei [149] | -2.17 | -4.14 | -2.52 | -1.69 |
| | Murphy [150] | -2.06 | -3.89 | -2.25 | -1.56 |
| | Favre [151] | -2.91 | -5.43 | -3.12 | -2.17 |

Table 8.5: Calculated $b$-strain dependence of critical temperature, $\frac{\partial T_\mathrm{c}}{\partial \varepsilon_{bb}}$ (K/%), from the combinations of elastic constants and pressure dependencies measured by different authors. The literature constants are shown in tables 4.2 and 4.3.

| | $\frac{\partial T_\mathrm{c}}{\partial \varepsilon_{cc}}$ (K/%) | $T_\mathrm{c}$ versus pressure measurements | | | |
|---|---|---|---|---|---|
| | | Welp [139] | Kraut [135] | Kund [136] | Fietz [140] |
| Elastic constants | Reichardt [147] | 0.55 | 0.56 | -0.31 | 0.07 |
| | Ledbetter [148] | 0.43 | 0.40 | -0.34 | 0.02 |
| | Lei [149] | 0.17 | 0.16 | -0.59 | -0.11 |
| | Murphy [150] | 0.50 | 0.71 | -0.17 | 0.14 |
| | Favre [151] | 0.84 | 1.30 | -0.23 | 0.27 |

Table 8.6: Calculated $c$-strain dependence of critical temperature, $\frac{\partial T_\mathrm{c}}{\partial \varepsilon_{cc}}$ (K/%), from the combinations of elastic constants and pressure dependencies measured by different authors. The measured constants are shown in tables 4.2 and 4.3.

dependencies using equation 4.3.2 are shown in tables 8.4-8.6.

The full range of combinations are calculated to quantify the error associated with the calculation. A large range of strain sensitivities are obtained, highlighting the sensitivity of the predictions to the literature values chosen.

The strain sensitivity measurements by Fietz *et al.* are deemed to be more reliable than other available measurements on all three crystallographic axes, as a relatively large number of different pressures have been measured and $T_\mathrm{c}$ measured directly, rather than inferred from heat capacity and expansivity measurements. It should be noted that the discrepancies between authors are relatively large, up to a factor of two between strain sensitivities in the $a$- and $b$-directions and large variations in the $c$-axis sensitivity. The elastic constants provided by Lei [149] *et al.* may be the most reliable as they are the most recent values which are experimentally measured.

Combining Fietz and Lei's constants gives among the smallest strain sensitivity of the combinations shown in tables 8.4-8.6.

The large range of predicted values indicates that either the literature measurements are unreliable or that there is a large variation between samples, both of which mean that conclusions for CCs are necessarily limited in their precision.

### 8.5.1 Strain model for THEVA tapes

The crystallographic axes and applied strain are not aligned in ISD CCs such as those manufactured by THEVA which means that an appropriate coordinate transformation is required to calculate the crystallographic strains. The *ab*-planes are inclined at an angle, $\theta \approx 30°$ to the tape surface and within the *ab*-planes, the *a*- and *b*-axes are rotated by $\varphi = 45°$ from the current flow direction. This can be expressed as a rotation matrix, $\boldsymbol{v}' = \mathbf{R}\boldsymbol{v}$, where $\boldsymbol{v}'$ is in terms of the crystallographic axes and $\boldsymbol{v}$ uses the tape axes, and

$$\mathbf{R} = \begin{pmatrix} \cos(\varphi) & \cos(\theta)\sin(\varphi) & \sin(\theta)\sin(\varphi) \\ -\sin(\varphi) & \cos(\theta)\cos(\varphi) & \sin(\theta)\cos(\varphi) \\ 0 & -\sin(\theta) & \cos(\theta) \end{pmatrix}. \tag{8.5.1}$$

The appropriate transformations for the strain tensor and stiffness tensor are

$$\boldsymbol{\varepsilon}' = \mathbf{R}\boldsymbol{\varepsilon}\mathbf{R}^{\mathrm{T}}, \;\; \varepsilon'_{ij} = \mathrm{R}_{ik}\mathrm{R}_{jl}\varepsilon_{kl} \tag{8.5.2}$$

$$\mathbf{C}' = \mathbf{RRCR}^{\mathrm{T}}\mathbf{R}^{\mathrm{T}}, \;\; \mathrm{C}'_{ijkl} = \mathrm{R}_{im}\mathrm{R}_{jn}\mathrm{R}_{ko}\mathrm{R}_{lp}\mathrm{C}_{mnop}. \tag{8.5.3}$$

The $x$- and $y$-strains are measured directly in experiments, but the $z$-strain needs to be inferred. Because the REBCO layer extends over almost all of the width of the tape, the Poisson ratio for $z$-strain can be considered purely from the REBCO elastic properties and neglect the mechanical effect of the copper coating at the edges.

The Poisson ratio for REBCO can be calculated from the same elastic constants that are used to translate the single-crystal measurements to strain. As stresses are applied along the tape axes, the stiffness tensor needs to be transformed into the tape axes using equation 8.5.3. An added complication is the microtwinning present in CCs, which mean that the elastic constants switch between domains. As a large number of domains are present within the tape and measurement region, the effect of twinning can be approximated by averaging the stiffness of the *a*- and *b*-oriented regions. It should be noted that this does not strictly satisfy all of the appropriate boundary conditions at the interfaces between domains, and a more detailed model would be required for a more rigorous result. For stresses parallel to the twin-boundaries, this is the appropriate average to make, but for stresses perpendicular to the twin boundaries, the appropriate average would be to average the inverses of the stiffness tensor. Since the stress state of the REBCO layer is determined by the much stiffer substrate, there will be both $x$- and $y$-stresses present in the layer and a sophisticated approach would be needed to accurately capture the boundary conditions. For simplicity, the stiffness tensor is averaged here between the two domains, which is not expected to have a significant effect on the predictions, especially given the relatively large range of elastic constants from the literature.

| | $\nu_x$ | $\nu_y$ | $\nu$ |
|---|---|---|---|
| Reichardt [147] | 0.596 | 0.547 | 0.667 |
| Ledbetter [148] | 0.397 | 0.406 | 0.457 |
| Lei [149] | 0.527 | 0.597 | 0.546 |
| Murphy [150] | 0.540 | 0.525 | 0.587 |
| Favre [151] | 0.483 | 0.463 | 0.450 |

Table 8.7: Calculated Poisson ratios in the tape-frame using the elastic constants from a range of authors in table 4.3. The values are the solutions to $\varepsilon_{zz} = -\nu(\varepsilon_{yy} + \varepsilon_{zz})$ (for crystallographic axes aligned with tape axes) and $\varepsilon_{zz} = -\nu_x \varepsilon_{xx} - \nu_y \varepsilon_{yy}$ (for ISD CCs), with applied stresses purely in the $xy$-plane.

To find the Poisson ratio of the REBCO layer, Hooke's law can be solved in the case where $\sigma_{zz} = \sigma_{xz} = \sigma_{yz} = 0$ to find the $z$-strain as a function of $x$- and $y$-strains. With the appropriate rotations into the tape-axes for an ISD CC, Hooke's law becomes $\sigma_{ij} = \mathrm{R}_{mi}\mathrm{R}_{nj}\mathrm{R}_{ok}\mathrm{R}_{pl}\mathrm{C}'_{mnop}\varepsilon_{kl}$.

For the elastic constants from Lei *et al.*, and using the averaging procedure above to account for twinning, the following relation is obtained:

$$\varepsilon_{zz} = -0.527\varepsilon_{xx} - 0.597\varepsilon_{yy}. \tag{8.5.4}$$

Table 8.7 shows the values for other authors' elastic constants to indicate the sensitivity of this value to the elastic constants. Also shown are the Poisson ratios for tapes with the crystallographic axes aligned with the principal tape axes, such as for SuperPower CCs.

With this Poisson ratio for REBCO, the $z$-strain can be calculated from the measured $x$- and $y$-strains.

Using Lei *et al.*'s elastic constants [149], the strain state in the REBCO layer is given by

$$\boldsymbol{\varepsilon} = \begin{pmatrix} \varepsilon_{xx} & \varepsilon_{xy} & -0.145\varepsilon_{xy} \\ \varepsilon_{xy} & \varepsilon_{yy} & 0.068\varepsilon_{xx} - 0.208\varepsilon_{yy} \\ -0.145\varepsilon_{xy} & 0.068\varepsilon_{xx} - 0.208\varepsilon_{yy} & -0.527\varepsilon_{xx} - 0.597\varepsilon_{yy} \end{pmatrix}, \tag{8.5.5}$$

which can be rotated into the crystallographic axes using equation 8.5.2 and combined with equation 4.3.2 to find the predicted strain sensitivity of $T_\mathrm{c}$.

The strain state in the crystallographic axes for Lei *et al.*'s elastic constants is given by

$$\varepsilon' = \begin{pmatrix} 0.464\varepsilon_{xx} + 0.794\varepsilon_{xy} + 0.210\varepsilon_{yy} & -0.536\varepsilon_{xx} + 0.210\varepsilon_{yy} & -0.137\varepsilon_{xx} - 0.442\varepsilon_{xy} - 0.563\varepsilon_{yy} \\ -0.536\varepsilon_{xx} + 0.210\varepsilon_{yy} & 0.464\varepsilon_{xx} - 0.794\varepsilon_{xy} + 0.210\varepsilon_{yy} & -0.137\varepsilon_{xx} + 0.442\varepsilon_{xy} - 0.563\varepsilon_{yy} \\ -0.137\varepsilon_{xx} - 0.442\varepsilon_{xy} - 0.563\varepsilon_{yy} & -0.137\varepsilon_{xx} + 0.442\varepsilon_{xy} - 0.563\varepsilon_{yy} & -0.454\varepsilon_{xx} - 0.018\varepsilon_{yy} \end{pmatrix}. \tag{8.5.6}$$

Unfortunately, for the ISD geometry the shear components in the crystallographic axes are not small compared to the strain components along crystallographic axes. This means that neglecting the sensitivity to shear components could significantly change the predictions of the model. Measuring single-crystals is well outside the scope of this thesis, but further research in this area to measure shear strains on REBCO single-crystals would be greatly beneficial to this understanding of strain in CCs. As the single-crystal measurements

| | $\frac{\partial T_c}{\partial \varepsilon_{xx}}$ (K/%) | $T_c$ versus pressure measurements<br>Welp [139] | <br>Kraut [135] | <br>Kund [136] | <br>Fietz [140] |
|---|---|---|---|---|---|
| Elastic constants | Reichardt [147] | 0.13 | -0.38 | -0.34 | -0.18 |
| | Ledbetter [148] | 0.02 | -0.27 | -0.44 | -0.23 |
| | Lei [149] | 0.00 | -0.79 | -0.52 | -0.33 |
| | Murphy [150] | -0.07 | -0.50 | -0.52 | -0.21 |
| | Favre [151] | 0.02 | -0.82 | -0.56 | -0.35 |

Table 8.8: Calculated $x$-strain sensitivity, $\frac{\partial T_c}{\partial \varepsilon_{xx}}$ (K/%), for an ISD CC for different combinations of elastic constants and single-crystal pressure measurements.

| | $\frac{\partial T_c}{\partial \varepsilon_{yy}}$ (K/%) | $T_c$ versus pressure measurements<br>Welp [139] | <br>Kraut [135] | <br>Kund [136] | <br>Fietz [140] |
|---|---|---|---|---|---|
| Elastic constants | Reichardt [147] | 0.20 | -0.05 | -0.25 | -0.07 |
| | Ledbetter [148] | 0.13 | -0.11 | -0.32 | -0.11 |
| | Lei [149] | 0.03 | -0.33 | -0.35 | -0.17 |
| | Murphy [150] | 0.08 | -0.24 | -0.30 | -0.14 |
| | Favre [151] | 0.15 | -0.40 | -0.45 | -0.21 |

Table 8.9: Calculated $y$-strain sensitivity, $\frac{\partial T_c}{\partial \varepsilon_{yy}}$ (K/%), for an ISD CC for different combinations of elastic constants and single-crystal pressure measurements.

available in the literature have not measured the variation in $T_c$ with shear stresses or shear strains, we have set $\frac{dT_c}{d\varepsilon_{ab,ac,bc}}$ to zero.

The shear strains generated by the strain board are expected to be small from the FEA calculations, so we can set $\varepsilon_{xy}$ to be zero. Since the crystallographic strain components $\varepsilon_{aa}$ and $\varepsilon_{bb}$ are strongly dependent on the applied shear strain $\varepsilon_{xy}$, a direct measurement of the $xy$-shear applied to the tape would be preferable in a future experiment to confirm whether the effect of shear strains is negligible.

For the combination of Fietz *et al.*'s single-crystal measurements and Lei *et al.*'s elastic constants, the predicted strain sensitivity neglecting all the shear components mentioned above is given by

$$\Delta T_c = -0.33\varepsilon_{xx} - 0.17\varepsilon_{yy}, \tag{8.5.7}$$

where strains are expressed in % and the changes of $T_c$ in K. The full set of strain sensitivities from the literature values presented earlier are given in tables 8.8 & 8.9.

The model predicts that the $xy$-shear component is the only component that differs between $a$- and $b$-domains in ISD CCs. If the $xy$-shear is large for the specific experimental setup, this should be observed in a deviation from linear strain dependence as the two domains would have different behaviours and the chain rule (equation 4.3.3) would be applied, generating a parabola-like strain dependence. The linear dependence on strain observed in the experimental results presented in this thesis gives confidence that the $xy$-shear strain is relatively small compared to the $x$- and $y$-strains. This is supported by FEA simulations of the strain-board which find $xy$- shear strains in the centre of the board of less than 3% of the smaller of the $x$- and $y$-strains when pure $x$- or pure $y$-stresses are applied.

To perform a comparison between the predicted changes in $T_c$ with experimental $J_c$ measurements, a scaling law needs to be used. For this comparison, the Durham scaling

| | |
|---|---|
| $w$ | 2.2 |
| $s$ | 1.26 |
| $B_{c2}(0,0)(B \parallel c)$ | 98.7 T |
| $B_{c2}(0,0)(B \parallel ab)$ | 185 T |
| $T_c(0)$ | 90.1 K |
| $p$ | 0.706 |
| $q$ | 2 |

Table 8.10: Parameters used for the scaling law (equation 4.5.1) to convert between $T_c$ and $J_c$. The paramters are taken from Greenwood *et al.* [161].

| | $\frac{1}{J_c(0)}\frac{dJ_c}{d\varepsilon_X}$ | $T_c$ versus pressure measurements | | | |
|---|---|---|---|---|---|
| | | Welp [139] | Kraut [135] | Kund [136] | Fietz [140] |
| Elastic constants | Reichardt [147] | 1.0 | -4.7 | -3.5 | -2.1 |
| | Ledbetter [148] | -0.2 | -3.1 | -4.6 | -2.6 |
| | Lei [149] | -0.1 | -9.0 | -5.5 | -3.7 |
| | Murphy [150] | -1.2 | -5.6 | -5.7 | -2.2 |
| | Favre [151] | -0.2 | -9.2 | -5.7 | -3.8 |

Table 8.11: Expected $J_c$ gradient with applied $X$-strain. The value is calculated using the Durham scaling law and chain model, and includes the effective Poisson ratio of the strain board. Values are calculated for an applied field of 0.3 T at 77 K, and expressed as % change in $J_c$ per % strain.

| | $\frac{1}{J_c(0)}\frac{dJ_c}{d\varepsilon_X}$ | $T_c$ versus pressure measurements | | | |
|---|---|---|---|---|---|
| | | Welp [139] | Kraut [135] | Kund [136] | Fietz [140] |
| Elastic constants | Reichardt [147] | 1.4 | -4.7 | -3.9 | -2.2 |
| | Ledbetter [148] | 0.1 | -3.3 | -5.1 | -2.7 |
| | Lei [149] | -0.1 | -9.5 | -6.1 | -3.9 |
| | Murphy [150] | -1.1 | -6.0 | -6.1 | -2.4 |
| | Favre [151] | 0.1 | -9.8 | -6.5 | -4.1 |

Table 8.12: Expected $J_c$ gradient with applied $X$-strain and a constant applied $Y$-strain. The value is calculated using the Durham scaling law and chain model, and includes the effective Poisson ratio (-0.131) of the strain board when a fixed $Y$-strain is applied. Values are calculated for an applied field of 0.3 T at 77 K, and expressed as % change in $J_c$ per % strain.

law is chosen (equation 4.5.1) and REBCO parameters drawn from Greenwood *et al.* [161]. The variation of $B_{c2}$ with $T_c$ is given by $B_{c2}(T,\varepsilon) = B_{c2}(0,0)(\frac{T_c(\varepsilon)}{T_c(0)})^w(1-t)^s$ [161], with the scaling law constants used given in table 8.10.

The effective Poisson ratio of the board is included in the calculation, with

$$\varepsilon_X = \varepsilon_{xx} = \frac{1}{\nu_{\text{eff}}}\varepsilon_{yy}, \tag{8.5.8}$$

where the effective Poisson ratio, $\nu_{\text{eff}}$ is -0.263(7) for uniaxial $X$-strain and -0.131(9) when an additional $Y$-compression is applied.

As can be seen in table 8.11, the experimental gradient of -7.0(3) is within the range of predictions from single-crystal but close to the largest negative predictions. The predicted behaviour of a linear negative gradient is in agreement with experimental observations, but the single-crystal model appears to be predicting a smaller gradient than is observed.

| | $\frac{1}{J_\mathrm{c}(0)}\frac{\mathrm{d}J_\mathrm{c}}{\mathrm{d}\varepsilon_X}$ | $T_\mathrm{c}$ versus pressure measurements | | | |
|---|---|---|---|---|---|
| | | Welp [139] | Kraut [135] | Kund [136] | Fietz [140] |
| Elastic constants | Reichardt [147] | 1.9 | 0.4 | -2.3 | -0.6 |
| | Ledbetter [148] | 1.2 | -1.0 | -3.1 | -1.1 |
| | Lei [149] | 0.2 | -1.8 | -2.9 | -1.3 |
| | Murphy [150] | 1.0 | -1.9 | -2.5 | -1.4 |
| | Favre [151] | -1.9 | -2.5 | -4.0 | -1.6 |

Table 8.13: Expected $J_\mathrm{c}$ gradient for interplanar currents with applied $X$-strain. The value is calculated using the Durham scaling law and chain model, and includes the effective Poisson ratio (-0.263) of the strain board. A correction for the effect of changing plane-spacing with interplanar currents has also been applied. Values are calculated for an applied field of 0.3 T at 77 K, and expressed as % change in $J_\mathrm{c}$ per % strain.

This could be due to the crystallographic shear components which were neglected in this model. If the change in shear components contributes to changes in $T_\mathrm{c}$ with the same sign as the linear components, then a steeper gradient would be seen. Alternatively, the large range of values for different elastic constants and single-crystal measurements could be sufficient to explain the experimental results, especially as the precise oxygen doping of the experimental samples is unknown.

The experimental results for varying $X$-strains with an applied $Y$-strain (figures 8.4 and 8.5) are not quite so well explained. The deviations from linear observed in figure 8.4 are not predicted by the model, as the smaller effective Poisson ratio of the strain board when a fixed $Y$-strain is applied should provide a small increase in the magnitude of the gradient (see table 8.12). Instead, a shallower gradient with strain is observed experimentally. Some other factor appears to be contributing to the difference in gradients.

The same calculation can be done for the interplanar current configuration. In this case, the mapping $\varepsilon_X = \varepsilon_{yy}$, $\varepsilon_Y = \varepsilon_{xx}$ needs to be made to account for the rotation of the tape relative to the strain board. A correction can also be made to account for the effect of the changing plane spacing with strain, as described in section 8.4.1. Here, we calculate the expected change in $J_\mathrm{c}$ using the scaling law and simply add the predicted change in $J_\mathrm{c}$ with plane spacing. The combination of the $T_\mathrm{c}$ variations with the correction for plane spacing for the different combinations of elastic constants and single-crystal $T_\mathrm{c}$ measurements are given in table 8.13. These values are systematically smaller than the *ab*-current predictions, principally because the $y$-strain sensitivity is generally predicted to be smaller than the $x$-strain sensitivity (tables 8.8 and 8.9). Since the applied strain $\varepsilon_X = \varepsilon_{yy}$, this leads to a weaker predicted strain response, with a range of values (excluding the least reliable single-crystal data set from Welp) from 0.4 to -4.0.

The experimental strain gradient for interplanar currents is shallower than the results on short *ab*-current samples, as suggested by the predictions from this model. The average of the interplanar short-sample measurements is a gradient of -7.6(13) which does fall outside the range of predictions from the model. Since the short-sample *ab*-current measurements do provide a steeper gradient than the long-sample *ab*-current measurements, a similar effect could be present in the interplanar measurements causing an overestimate of the strain gradient, although the discrepancy between the model and the interplanar experimental measurements is significantly greater than the difference between long and short samples observed with *ab*-currents.

### 8.5.2 Strain model for SuperPower tapes

The geometrical considerations are much simpler for a SuperPower tape. The crystallographic axes are aligned with the tape axes so no coordinate transformations are required. The strain sensitivities calculated in tables 8.4-8.6 can be used directly in the tape frame. The *c*-axis strain can be calculated using the Poisson ratios given in table 8.7. As the *a*- and *b*-domains differ for SuperPower tapes (unlike THEVA tapes with no applied *xy*-shear), the chain rule (equation 4.3.3) needs to be applied.

The model presented here has been compared to experimental data with biaxial strain on SuperPower CCs with APCs measured by Greenwood *et al.* [160, 161], published in 2018 and 2019. To perform a direct comparison, a few parameters need to be assumed. As for the THEVA predictions, these values are drawn where appropriate from Greenwood *et al.* [161]. The change in $T_c$ in each domain is calculated exactly as outlined above using constants from Fietz *et al.* [140] and Lei *et al.* [149].

The chain rule (equation 4.3.3) and Durham scaling law (equation 4.5.1) are then used to calculate $J_c$ as a function of $T_c$, with $N = 20$ and $f = 0.5$.

Figure 8.24 shows the experimental data and model predictions for a combination of the two different data sets published in each paper [160, 161]. A moderate agreement is found with the correct general shape. The model does not correctly capture the $X$-compression region of the 2019 data set, predicting a smaller decrease in $J_c$, but is in good agreement in the compressive regime. For much of the 2018 data set, a good agreement is seen, but the measurements have a large increase in $J_c$ when in the $X$-tension region, which is not predicted by the model. The model is not a fit to the data other than by using the same constants as Greenwood *et al.* for $J_c(T_c)$, so there is no prior expectation for the model to agree with the data. The relatively large variation in predictions from different sets of elastic constants and single-crystal measurements does allow some freedom to more closely match the experimental data.

Uniaxial strain data can also be compared to this model with information about the Poisson ratio of the strain apparatus. Typically the strain board would be much stiffer than the REBCO tape, so the $Y$-strain can be assumed to be entirely due to the Poisson ratio of the strain board. For example, the uniaxial strain boards commonly used in the group here in Durham are 2.5 mm thick, which is more than an order of magnitude thicker than a typical REBCO tape (0.1-0.2 mm depending on the thickness of the copper stabiliser and substrate chosen by the manufacturer). The $Z$-strain can be calculated from this calculated $Y$- and the measured $X$-strain using the REBCO Poisson ratios derived in table 8.7.

### 8.5.3 A deviatoric model for REBCO?

As a deviatoric model has been successfully used in the literature for $Nb_3Sn$ (see section 4.4), it may be worthwhile to investigate its possible application to REBCO.

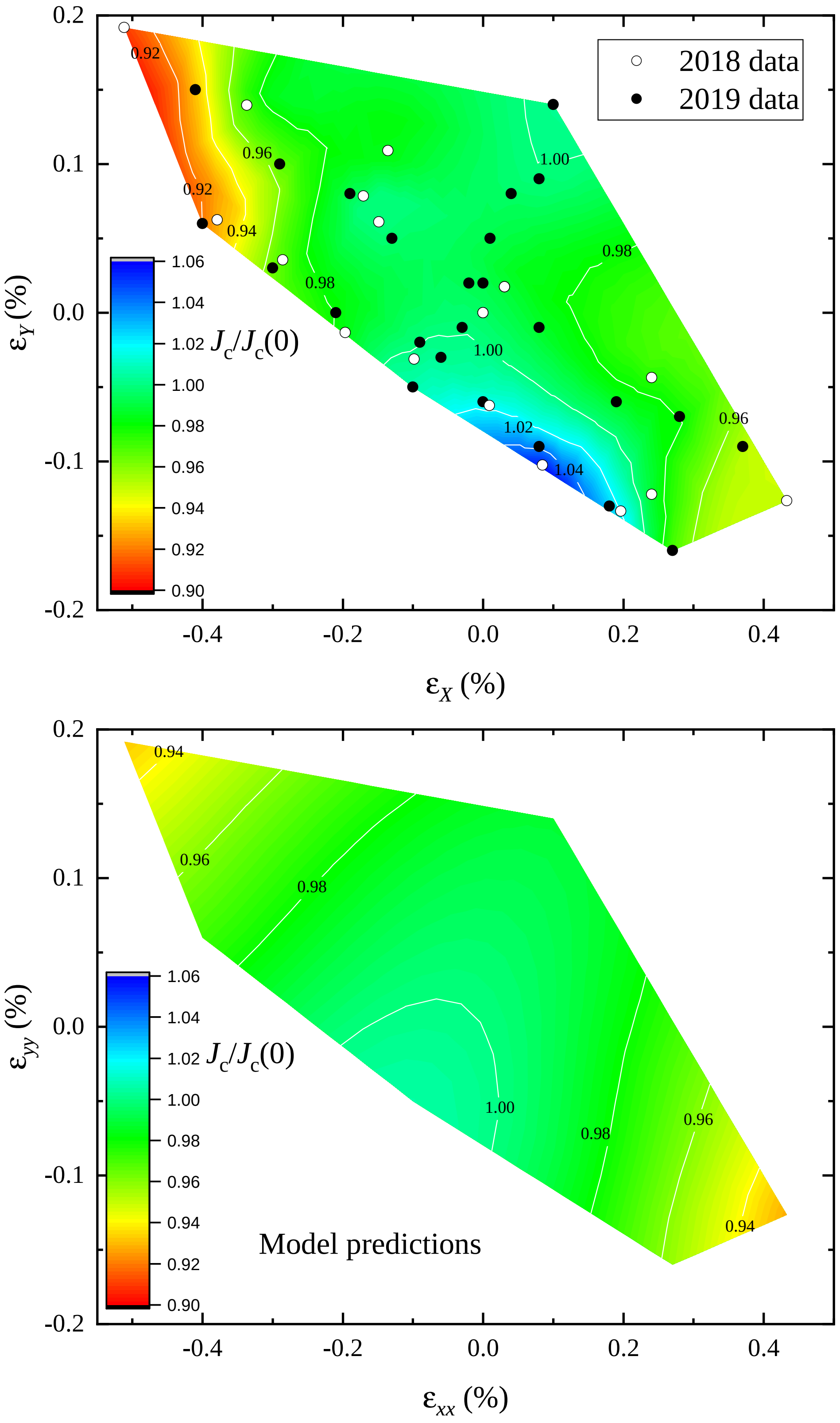

Figure 8.24: Top: A contour plot of experimental normalised critical current with biaxial strain data from Greenwood *et al.* 2018 [160] and 2019 [161]. The applied field is 0.3 T and parallel to the *c*-axis. The increase in $J_\mathrm{c}$ around $\varepsilon_X = 0.1\%, \varepsilon_Y = -0.1\%$ is only seen in the 2018 data so may not be representative of a general tape behaviour. Bottom: Predictions for normalised critical current as a function of strain from the single-crystal strain model presented in this chapter with an applied field of 0.3 T parallel to the *c*-axis, using the literture constants from Fietz *et al.* [140] and Lei *et al.* [149].

As the REBCO in CCs is not isotropic, some modifications need to be made. Firstly, the orientation of the strain relative to the crystallographic axes affects the behaviour, so all strains will be considered relative to the crystallographic axes. Additionally, the single-crystal behaviour of $a$- and $b$-strains causing similar but opposite changes in $T_\mathrm{c}$ does not appear to agree with a deviatoric model as both $a$- and $b$-strains would have the same deviatoric strain. This can be accommodated by noting that the $T_\mathrm{c}$ of REBCO increases as the longer $b$-axis is in compression and as the shorter $a$-axis is in tension. The available strain range of measurements in the literature is not sufficient to determine the behaviour when the $a$- and $b$-lattice constants become equal, but for this model it will be assumed that the maximum $T_\mathrm{c}$ is when the lattice constants are equal. The zero-strain point will therefore be set at $a = b$ rather than the force-free strain state, with a free parameter for the length of $a, b$. For simplicity, the zero-strain $c$-axis length is taken to be the zero-force $c$-axis length, rather than accounting for the Poisson ratio effects from constraining $a = b$.

The model will assume that $T_\mathrm{c}$ can be described by

$$T_\mathrm{c}(\varepsilon) = T_\mathrm{c}(0) - A\sqrt{\varepsilon_\mathrm{dev} : \varepsilon_\mathrm{dev}}, \tag{8.5.9}$$

where $A$ and the $a, b$-axis length are free parameters, determined from a fit to single-crystal data. The double-dot product of the deviatoric strain tensor is equivalent up to a multiplicative constant to the scalar deviatoric strain calculated by ten Haken *et al.* [164] and others.

The strain-state for the single-crystal measurements is calculated using the stiffness constants from Lei *et al.* [149], and the force-free lattice constants set to be $a = 0.3818\,\mathrm{nm}$, $b = 0.3884\,\mathrm{nm}$ [126]. The strain gradients and measured strain ranges are taken from [140], and the $a, b$-length and $A$ from equation 8.5.9 are determined by fitting to equation 8.5.9 over the measured strain range, with the $a, b$-length found to be $0.3849\,\mathrm{nm}$ and $A = 1.60\,\mathrm{K}/\%$. Figure 8.25 shows this fit applied to the single crystal data measured by Fietz *et al.*, producing a reasonable straight line through all three orientations of applied pressure.

The successful fit of the deviatoric model demonstrates that the single-crystal literature data can be described in this way. The principal difference in the prediction of the deviatoric model, aside from the deviations from linear in figure 8.26, is in its treatment of shear components. Unlike the model described earlier in this section which neglected the shear components' contribution to changes in $T_\mathrm{c}$, they are automatically accounted for when considering the deviatoric strain. Measurements on configurations which produce large shears in the crystallographic axes, such as those presented in this thesis on THEVA CCs, are precisely the measurements needed to distinguish between these models.

Using equation 8.5.6 and the fitted zero-deviatoric-strain lattice parameters, the deviatoric strain in a THEVA tape is given by

$$\varepsilon_\mathrm{dev} : \varepsilon_\mathrm{dev} = 1.21\varepsilon_{xx}^2 + 1.39\varepsilon_{yy}^2 + 0.45\varepsilon_{xx}\varepsilon_{yy} - 4.8 \times 10^{-4}\varepsilon_{xx} - 1.2 \times 10^{-4}\varepsilon_{yy} + 1.47 \times 10^{-4}. \tag{8.5.10}$$

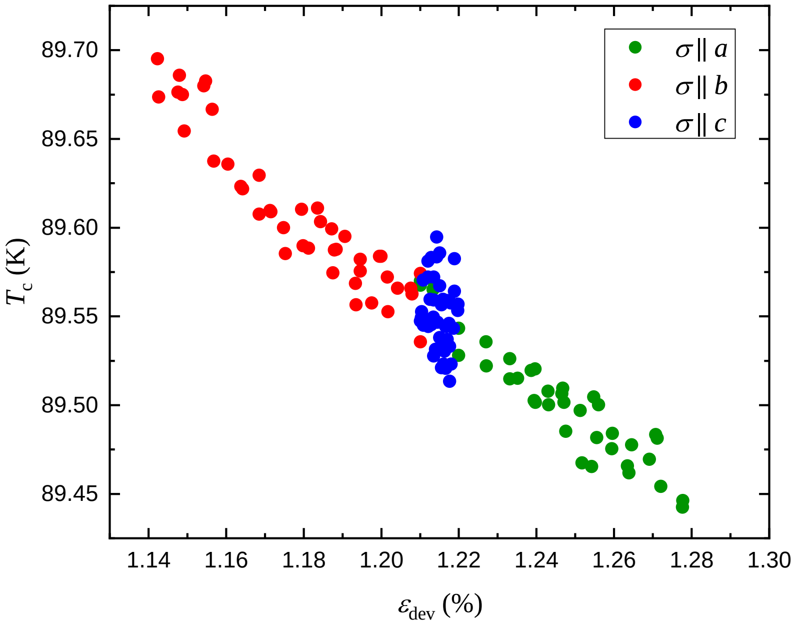

Figure 8.25: Fit to equation 8.5.9 of critical temperature as a function of deviatoric strain for single-crystal strain measurements from Fietz *et al.* [140], with deviatoric strain calculated using REBCO elastic constants [149].

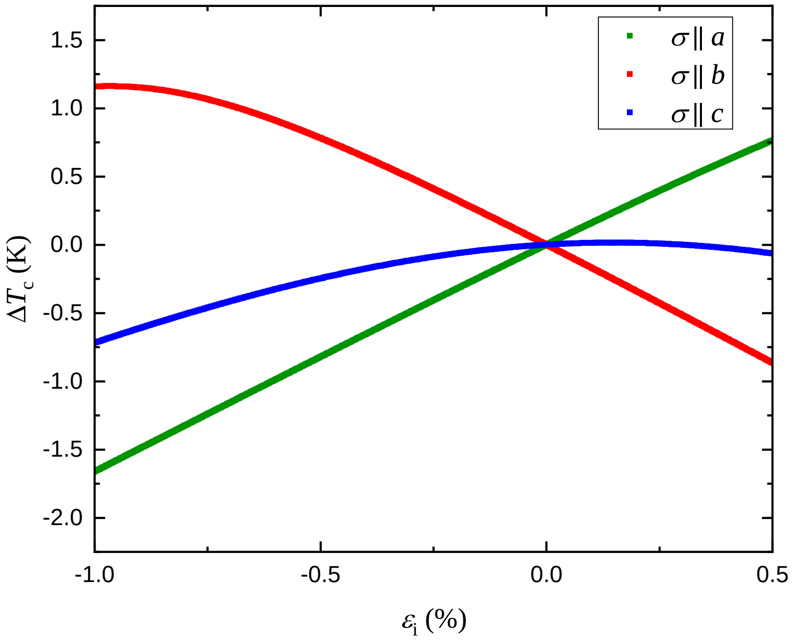

Figure 8.26: Calculated change in $T_c$ from equation 8.5.9. Each direction is for uniaxial pressure along a crystallographic axis, plotted as a function of the strain component along that axis. The strain range is chosen to be slightly larger than than typical experimental strain ranges on CCs, which is much greater than the strain range available in single-crystal measurements.

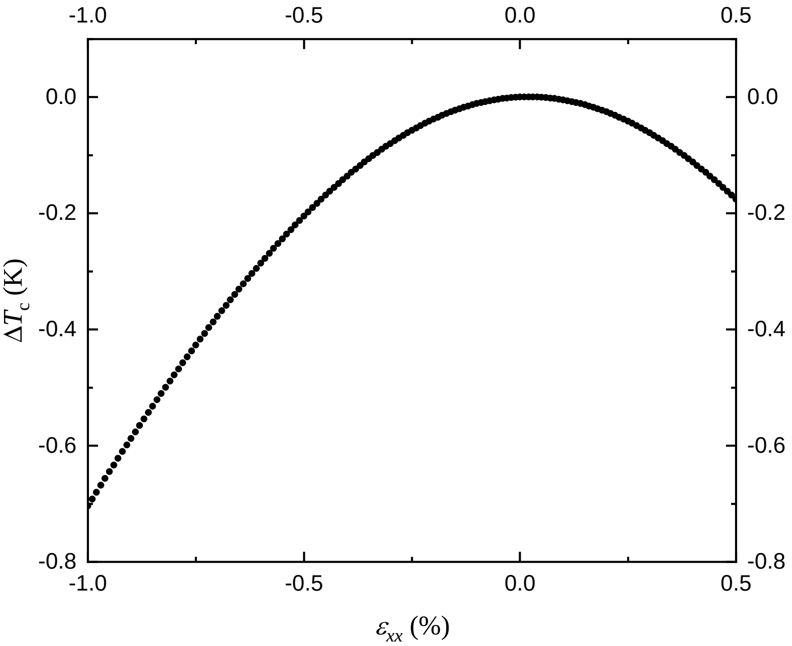

Figure 8.27: Predicted change in $T_\mathrm{c}$ from variations in $x$-strain using the deviatoric model for a THEVA tape. Here the $y$-strain and $xy$-shear is set to zero.

The deviatoric strain from zero-applied strain is 1.21%, due to the non-equal $a$ and $b$ lattice parameters with no applied strain.

The predicted change in $T_\mathrm{c}$ from variations in $x$-strain is shown in figure 8.27. For this figure, the $y$-strain is set to zero, but the Poisson ratio of the board makes only minor changes to the shape. The key feature of this plot is that the critical temperature decreases for both tensile and compressive strains, with the peak $T_\mathrm{c}$ at sufficiently small strains to be captured by the experimental measurements. This behaviour is not reflected in the experimental measurements presented in this thesis, which show an increase in $T_\mathrm{c}$ for compressive strain. The increase in deviatoric strain in both directions even though a large initial deviatoric strain is present is caused by the large crystallographic shear strains generated when strains are applied in the tape axis.

The deviatoric model can suitably explain single-crystal data and would therefore also describe strain data on a SuperPower architecture where shear components are small. The experimental data on THEVA tapes where the shear components have a large effect are in fundamental disagreement with the predictions of the deviatoric model as the large quadratic component of the predicted strain response in this deviatoric model is not seen experimentally. The model neglecting shear components presented earlier in this chapter is a more accurate description of the measurements, with the correct prediction of a linear response to strain and a measured strain gradient within the predicted range. The model neglecting shear components is therefore a better description of the experimental data.

The key difference between the strain behaviour of LTS and CCs is from the symmetries of the material. In polycrystalline materials such as $Nb_3Sn$, the orientation of the strain cannot change the response unless there is a preferential crystallographic alignment. Of course, the direction of strain applied to a macroscopic object could still change the behaviour if a different strain distribution results from the anistropy of the macroscopic object, but at a length-scale where the material is uniform the response will be orientation-independent. An analysis in terms of some combination of invariant quantities is the only way to capture this isotropy, although the choice of the specific combination allows for some freedom and will affect the predictions in unmeasured regions of phase space. As outlined in section 4.4, the available data is not sufficient to distinguish between choosing the deviatoric component $J_2$ from other quadratic components.

In CCs, however, the rotational symmetry is broken by the highly-textured nature of the material. This means that the range of possible descriptions of the strain state is much larger as the material can respond differently depending on the orientation of the strain. This greatly increases the complexity of the model, as instead of three degrees of freedom in the strain state for an isotropic system, there are now six. The available measurements on single-crystal data are not sufficient to determine fully the strain behaviour of REBCO with only up to three degrees of freedom constrained. At present some assumption of the response to shear strains needs to be made, but measurements on CCs such as those presented in this thesis are able to provide further constraints. The shear strains present in the THEVA measurements made here can eliminate a treatment of shear strains using a deviatoric model, and treating $T_c$ as independent of crystallographic shear strains gives the correct qualitative behaviour, if possibly too shallow a strain gradient. Further measurements on ISD CCs could more tightly constrain the understanding of shear strain, as would measurements of shear strains in single-crystals.

## 8.6 Comparing REBCO strain response to $Nb_3Sn$

The single-crystal measurements on REBCO do not measure the shear strain, but the reasonable description of both ISD and more conventional tape architectures with no crystallographic shear contribution outlined in this chapter suggests that shear components can be neglected. Using equation 4.4.12, the predicted behaviour of $T_c$ in a polycrystalline REBCO sample may include a substantial hydrostatic component. Since the effects of strain along the $a$ and $b$-axes have opposite signs, the sum of normal strain responses (i.e. the change of $T_c$ with hydrostatic pressure) is much smaller than the individual normal strain sensitivities. This means we cannot rule out a deviatoric dependence for the polycrystalline material, since the shear strain dependencies could be smaller than the normal strain dependencies but still produce a greater net effect than the normal strain components when summed in equation 4.4.12. It is unclear therefore whether the response of a polycrystalline REBCO sample would be best described by hydrostatic or deviatoric strains or some combination of them. The underlying mechanism for changes in $T_c$ is likely to differ from $Nb_3Sn$, even if both were to have a deviatoric response. For $Nb_3Sn$, the cubic crystal symmetry rules out large but cancelling normal strain components, meaning that behaviour dominated by the shear components is expected.

Strain modelling for REBCO bulks has been performed using the deviatoric component [231, 232]. The analysis presented in this chapter suggests that the hydrostatic component is also likely to contribute to the behaviour of bulk polycrystalline REBCO, and may be an important correction to stress analyses of bulks. Of course, our analysis is designed for CCs, which are manufactured as pseudo-single-crystals to eliminate the effect of grain boundaries, so we have been able to neglect grain boundaries. In polycrystalline HTS materials such as REBCO bulks, the grain boundaries are expected to have a large effect on $J_\mathrm{c}$ and therefore an analysis incorporating strain effects on grain boundaries is likely to be required to accurately capture the strain behaviour of REBCO bulks.

## 8.7 Conclusions

This chapter presents the first biaxial strain measurements on ISD CCs, measured on a new biaxial strain probe. These measurements agree with the existing uniaxial strain measurements and extend the available phase space of measurements to understand CC strain behaviour and predict its response in new applications and new magnet configurations. A new detailed model is presented which uses single-crystal strain data and elastic constants to predict the response of CCs. This model correctly reproduces the qualitative behaviour of the measurements discussed in this chapter, namely the linear negative gradient of $I_\mathrm{c}$ with strain seen in ISD tapes and the shape of the biaxial strain response in SuperPower tapes. Predictions are made using different combinations of literature values for elastic constants and single-crystal measurements. Four sets of single-crystal strain measurements which use high-$T_\mathrm{c}$ detwinned samples with three axes of strain are combined with a selection of measured and calculated elastic constants. A detailed outline of the method to convert from single-crystal measurements to a CC configuration is given using these constants. The quality of the data available in the literature limits the model's quantitative agreement with the measured data, as a large range of predictions are seen when different authors' constants are used, with a range of values of $\frac{1}{J_\mathrm{c}(0)}\frac{\mathrm{d}J_\mathrm{c}}{\mathrm{d}\varepsilon_{xx}}$ from +1.0 to -9.2 %/%. Excluding the data-set from Welp *et al.*, the model predicts a range of values of $\frac{1}{J_\mathrm{c}(0)}\frac{\mathrm{d}J_\mathrm{c}}{\mathrm{d}\varepsilon_{xx}}$ from -2.1 to -9.2 %/%.

The model is sufficient to explain the experimental results when neglecting contributions from crystallographic shear strains as the experimental measurements are within the range of the model predictions, with an experimentally measured value of $\frac{1}{J_\mathrm{c}(0)}\frac{\mathrm{d}J_\mathrm{c}}{\mathrm{d}\varepsilon_{xx}} = -7.0(3)$ on a THEVA CC. Further measurements on single-crystal samples, and particularly on the response to shear strain, would significantly improve this model's predictive power.

An alternative model based on deviatoric strains is presented, which accounts for the effect of shear strains automatically. While the deviatoric model is able to explain the single-crystal measurements and CCs with strains along crystallographic axes, the shear strains generated in the ISD measurements presented in this chapter demonstrate that the deviatoric model does not correctly predict the response of CCs.

The model for strain response suggests that it is reasonable to neglect the single-crystal shear-strain sensitivity. This is in contrast to $\mathrm{Nb_3Sn}$ which appears to have a strong single-crystal sensitivity to shear strains and a weak or negligible effect from normal strain sensitivities. This result is consistent with a different mechanism for $T_\mathrm{c}$ variation with strain for $\mathrm{Nb_3Sn}$ and REBCO.

An invariant description of $Nb_3Sn$ is required as it is a polycrystalline material, whereas the pseudo-single-crystal CC require a different framework to explain their strain response. The inferred difference in the relative importantance of shear and normal strain components to the single-crystal behaviour of $Nb_3Sn$ and REBCO means that the two materials are expected to have different strain responses, even when comparing $Nb_3Sn$ to a polycrytalline REBCO material. Alternatively if a pseudo-single-crystal $Nb_3Sn$ material existed it would be expected to have a shear-dominated strain response, unlike experimental observations on REBCO CCs.

Measurements on interplanar currents are presented in this chapter. These measurements are made possible by the ISD architecture and relatively wide tapes measured. Characterisation of interplanar currents at 77 K shows the expected flux channelling effects and relatively small reduction of $I_c$ compared to *ab*-currents.

The first measurements of interplanar currents under strain are presented here, showing a similar response to strain as is seen with *ab*-currents. Unfortunately the measurements of strain in short samples were severely hampered by current leaking when joint resistances changed under strain, so a change of design or material of the strain board may be needed to produce more reliable results over a larger strain range on the short samples. The single-crystal model for strain response predicts a decrease in strain sensitivity for the $\varepsilon_{yy}$ direction, which is not seen in the experimental measurements. A JJ model for coupled *ab*-planes predicts only a small change in behaviour for strain in interplanar currents, which is consistent with the measurements.

Chapter 9

# Concluding Comments and Future Work

## 9.1 Future work

This section outlines some areas of research which could be undertaken if more time were available for this project, as well as some possible avenues of research informed by the work presented in this thesis.

### 9.1.1 Single-crystal measurements

While making single-crystal measurements was not part of this thesis research, the theoretical calculations in chapter 8 rely heavily on both single crystal strain measurements and elastic constants for REBCO, many of which are rather old measurements. Further measurements of these properties would improve the precision of the predictions, and in particular, making measurements of shear strain on single-crystals would provide significant insight into the description of CCs. As to the authors knowledge, measurements of shear strain have not been made on a high-quality (optimally doped) single-crystal, this area of research may be fruitful and provide new insights.

### 9.1.2 Short samples

Significant difficulties were encountered in this research when applying strain to short REBCO samples. The irreversible increases in measured $I_\mathrm{c}$ are attributed to a degrading joint and relatively low resistance parallel current path leading to increased shunting. Improvements could be made in a number of ways. If the parallel current path is much higher resistance (by an order of magnitude or more), the effect would be much smaller. This could be achieved by replacing the strain board with another material that still has a high elastic limit but higher resistance, such as titanium, which has been used for strain measurements [233]. Mechanical bonding to titanium is more challenging as conventional soldering is not possible, which is why copper-beryllium was used for the measurements in this thesis. Another method of bonding the sample to the strain board could also provide an insulating layer between the sample and the strain board. The challenges with this are to have sufficient elastic or low-temperature plastic deformation to transmit the applied strains. More work would be required to determine how an alternative bonding procedure would perform at large applied strains. A third alternative would be to redesign the strain board in such a way that there is not stress experienced by the joint between the current leads and the sample. This is likely to require a smaller strain applicator that is not compatible with long-length samples, and may require wider samples such as the 12 mm wide THEVA tapes measured here to be reduced in width if the homogeneous strain region shrinks accordingly.

If strain application to short samples can be reliably achieved, this provides an opportunity to investigate the effect of strain on interplanar currents thoroughly. The measurements presented here imply that the change in $T_c$ independent of current orientation dominates, but measurements at lower temperatures where the change in plane spacing is likely to have a stronger effect may improve our understanding of the degree of coupling between CuO planes.

Another major benefit of short samples is the ability to rotate the sample relative to the strain orientation. This allows for the relative normal and shear strain components to be varied, potentially continuously if appropriate current leads are designed. This provides an extra degree of freedom in the measurements which could provide further constraints for models for strain response. With the present design, different current leads are required for each angle, but given the difficulties associated with demounting and remounting samples, each angle which could be measured at is likely to be a different sample and bespoke current leads would be less prohibitive.

Rotation of the sample to provide this additional degree of freedom could also be applied to interplanar current measurements in much the same fashion.

The biaxial strain probe can be used to measure CCs from other manufacturers, both on long samples, and if the current injection problems are overcome for short samples to provide a comprehensive picture of the 2D strain response in a large range of CCs.

### 9.1.3 High field measurements

The new biaxial strain probe can be used in larger magnetic fields such as those available from the 15 T split-pair superconducting magnet in Durham. As the probe does not allow for temperature control within the 40 mm magnet bore, the measurements would be limited to the temperature of the liquid helium coolant for the magnet at 4.2 K. Nevertheless, the possibility of applying large fields at low temperatures opens up more possibilities, and the ability to make biaxial strain measurements at low temperatures would provide new measurements. If the sample cross-section is reduced, such as by mechanical scribing as described in section 6.5, lower applied fields could be reached without exceeding the critical current limit of the probe. Combining this with the high design current of the probe should allow for lower field measurements at 4.2 K than have been made previously in Durham and potentially provide new insights into the self-field regime at liquid helium temperatures if sufficient sample cross-section reduction can be achieved.

### 9.1.4 Resitivity measurements

The design for a miniature strain applicator for resistivity measurements (chapter 5) has already been taken forward by Emma Gillard to make strained measurements in the PPMS. These measurements could be made on a wide range of CCs to provide characterisation in a region of phase space not typically measured. In particular, the miniaturised design makes measurements at international high-field facilities more straightforward, and measurements of $B_{\mathrm{irr}}$ could be made as a function of strain at higher fields and correspondingly lower temperatures to better understand the critical surface for CCs. The miniature design could also be applied to situations where large samples are not possible. This is particularly relevant to irradiated samples where larger sample volumes incur more stringent radiation shielding requirements, so smaller samples make measurements logistically much easier. There is scope for many new measurements to be made on the interaction between strain in CCs and radiation damage, which could be possible using a miniature strain board.

### 9.1.5 Self-field calculations

The calculations of the self-field response of CCs presented in chapter 7 could be extended in a number of ways. At present the calculations are performed in 1D, by assuming that the field and current distribution do not vary significantly across the thickness of the tape. The variations in the field across the thickness are likely to be small for commercial CCs as the thickness is typically similar to the penetration depth. The current distribution could vary on smaller lengthscales however. As the model assumes that the current is only determined by the net field at that point, a field that is uniform through the thickness would cause a uniform current distribution, but surface effects could be included which would cause a variation through the thickness. Additionally, performing the integration of the Biot-Savart law in 2D would introduce some minor geometrical variations, although the aspect ratio of the REBCO layer is typically so high ($> 10^3$) that this effect is expected to be small.

The calculations could also be extended to a scenario where the applied field is not parallel to the self-field, and the angular response of the REBCO is included to account for the relative angle of the net field.

The most significant assumption present in the calculations is that neighbouring regions of the superconductor do not interact with each other. The Blair & Hampshire calculations assume a single JJ with insulating boundary conditions, which may not be accurate for a real material. It would be reasonable to assume that the boundaries to the electrodes would be of similar thickness and properties to the junction regions. An analytical calculation or simulation is therefore required to determine the effect of multiple JJs in parallel. While the grid points for the simulation are not representative of individual JJs, the $J_{\mathrm{c}}(B)$ relation is presently for an isolated JJ. If a calculation for JJs in parallel can be performed, the self-field analysis could be repeated with the local $J_{\mathrm{c}}(B)$ relation replaced with the one found for JJs in parallel. Provided the length scale for interaction of the JJs is much smaller than the width of the system (and especially if it is smaller than $\lambda$), the assumption that calculation points for the self-field can be treated independently would be reasonable. If the relevant length scale is smaller than the system but larger than $\lambda$ then a correction for the gradient of the field at each calculation point may be required.

## 9.2 Conclusions

This thesis investigates the critical current of coated conductors, a promising material with many potential applications in high-field magnets and nitrogen-cooled superconducting applications. The experimental and theoretical work presented here is largely focused on high temperatures (77 K), and low to moderate applied magnetic fields. The measurements presented in chapters 6 and 8 are made with liquid nitrogen cooling to 77 K and in magnetic fields up to 0.7 T. These results include the first measurements with biaxial applied strain on an ISD CC, and the first measurements on the effect of strain for interplanar currents. More work is required, particularly on short samples as outlined in the previous section, which would enable a more complete picture of the behaviour of these materials. Nevertheless, the measurements presented are in reasonable agreement with the theoretical predictions for strain response and support the model presented in chapter 8.

Chapter 7 details a theoretical model for self-field in CCs. The model takes the work of Blair & Hampshire [99] which predicts the behaviour of a wide JJ in large applied fields and assigns this response to local regions of the superconductor. The regions are treated as independent and a self-consistent solution to the field and current distribution using the Blair & Hampshire $J_c(B)$ relation and Maxwell's equations is found for a thin strip. This approach extends the high-field work of Blair & Hampshire to low fields and wide tapes where the self-field contribution dominates the behaviour and allows a description of technological superconducting tapes over the entire applied field range.

Chapter 8 includes a new detailed model for the strain response of CCs based on extrapolation from single crystal measurements. Existing literature measurements for the uniaxial pressure dependences of $T_c$ in single-crystal REBCO is combined with measurements of the elastic constants of REBCO to predict how $T_c$ varies with strain. The relevant rotations for an ISD CC are performed and comparisons made to the strain measurements presented in this thesis.

The results presented here can be used to inform our understanding of regimes outside those directly measured, particularly the theoretical understanding of strain mechanisms which can be combined with a scaling law to predict the properties of a superconductor in a wide range of conditions.

Appendix A

# Fusion CDT

The author is a member of the EPSRC centre for doctoral training in the science and technology of fusion energy (Fusion CDT). The Fusion CDT is a collaboration between the universities of Durham, Liverpool, Manchester, Oxford and York, providing doctoral students with a broad basis in fusion disciplines to support their specialised research. Training courses and assignments are distributed through the first 9 months of the PhD, with courses on a range of topics delivered by each of the participating universities. Some courses are modules from the York University MSc in Fusion Energy, the others are bespoke courses for doctoral students. A summary of the courses taken is given in table A.1. In addition to the training courses, the Fusion CDT organises a yearly student conference in York, Frontiers of Fusion.

Table A.1.

| **Course Name** | **Location** | **Result** |
|---|---:|---:|
| Introduction to fusion plasmas | York | Distinction |
| Computation techniques | York | Distinction |
| Introduction to materials | York | Distinction |
| Materials applications | Oxford | Distinction |
| Radiation damage | Oxford | Distinction |
| Fusion technology | York | Pass |
| Plasma surface interactions | Liverpool | Distinction |
| Analytical / characterisation tools | Oxford<br>Manchester | Pass<br>Distinction |
| Materials for nuclear power | Oxford | Distinction |
| Finite element modelling | Manchester | Pass |
| Integrated systems and project management (group project) | Durham | Pass |

Table A.1: First year courses attended as part of the Fusion CDT.

Appendix **B**

# Errors in Critical Current Measurements

The baseline fit errors are determined from the linear regression error, with the error in the offset and the gradient labelled as $\Delta B_0$ and $\Delta B_1$ respectively. Propagating these errors through to the $N$-value calculation, the error in $N$ is given by

$$(\Delta N)^2 = (\Delta N_{\text{fit}})^2 + \left(\frac{\Delta B_0}{V_{\text{c}} \ln I_{\text{c}}}\right)^2 + \left(\frac{(I_{\text{c}} - I_0)\Delta B_1}{V_{\text{c}} \ln I_{\text{c}}}\right)^2, \tag{B.0.1}$$

where $\Delta N_{\text{fit}}$ is the linear regression error in the calculation of $N$ and $I_0$ is the midpoint of the baseline fitting region.

$I_{\text{c}}$ is extracted by fitting the expression $V_{\text{c}} = C I_{\text{c}}^N$ to the experimental data. The errors that need to be considered are from voltage measurement errors, $\Delta V$, such as voltmeter errors and measurement gauge length errors, current measurement errors, $\Delta I$, such as the error on the shunt used to measure current, errors from the calculation of $C$ from the fit, $\Delta C_{\text{fit}}$, and the baseline and $N$-value errors described above.

Including all these sources of error, the error for an $I_{\text{c}}$ measurement is estimated to be

$$\begin{aligned}\left(\frac{\Delta I_{\text{c}}}{I_{\text{c}}}\right)^2 = &\left(\frac{\ln\left(\frac{V_{100}}{V_{10}}\right)}{2N^2}\Delta N\right)^2 + \left(\frac{\Delta B_0}{N V_{\text{c}}}\right)^2 + \left(\frac{(I_{\text{c}} - I_0)}{N V_{\text{c}}}\Delta B_1\right)^2 \\ &+ \left(\frac{\Delta C_{\text{fit}}}{N C}\right)^2 + \left(\frac{\Delta V}{N V_{\text{c}}}\right)^2 + \left(\frac{\Delta I}{I_{\text{c}}}\left(1 + \frac{B_1 I_{\text{c}}}{N V_{\text{c}}}\right)\right)^2, \end{aligned} \tag{B.0.2}$$

where $V_{100}$ and $V_{10}$ are the upper and lower bounds of the transition region, set at $100\,\mu\text{V}\,\text{m}^{-1}$ and $10\,\mu\text{V}\,\text{m}^{-1}$ respectively.

Appendix C

# Summary of Code Used

Much of the code used for the work presented in this thesis has been collected in a git repository.

The repository contains:

- Python code for the extraction of $I_c$, $N$ from raw $V$-$I$ data, which performs baseline fitting and calculates the error in the $N$-value and $J_c$.
- Python code to calculate $J_c$ in a single junction as a function of applied field using the work of Clem [97], and fit the parameters $c_0$ and $c_1$ to these solutions.
- Python code for the calculation of current and field distributions with self-field included, as outlined in section 7.3.
- Python code to perform fitting of the self-field solutions to experimental data.
- LabView code for measurement of strain gauges.
- Mathematica scripts for calculating tensor operations and integrations for the single-crystal strain model.

Please contact me or Professor Damian Hampshire if you would like access to this repository.

# Bibliography

[1] C. W. A. Gurnham, V. Große, and D. P. Hampshire, "Angular $J_\mathrm{c}$ measurements at 77 K in-field, on an ISD REBCO coated conductor using a straightforward mechanical scribing technique to reduce tape width," *J. Phys: Conf. Ser.*, vol. 1559, p. 012036, 2020.

[2] C. W. A. Gurnham and D. P. Hampshire, "Self-field effects in a Josephson junction model for $J_\mathrm{c}$ in REBCO tapes," *IEEE Trans. Appl. Supercond.*, vol. 32, no. 4, p. 8000205, 2022.

[3] T. Sekitani, N. Miura, S. Ikeda, Y. H. Matsuda, and Y. Shiohara, "Upper critical field for optimally-doped $\mathrm{YBa_2Cu_3O_{7-\delta}}$," *Physica B*, vol. 346–347, pp. 319–24, 2004.

[4] P. Sunwong, J. S. Higgins, and D. P. Hampshire, "Probes for investigating the effect of magnetic field, field orientation, temperature and strain on the critical current density of anisotropic high-temperature superconducting tapes in a split-pair 15 T horizontal magnet," *Rev. Sci. Instrum.*, vol. 85, no. 6, p. 065111, 2014.

[5] S. Awaji, K. Watanabe, H. Oguro, H. Miyazaki, S. Hanai, T. Tosaka, and S. Ioka, "First performance test of a 25 T cryogen-free superconducting magnet," *Supercond. Sci. Technol.*, vol. 30, p. 065001, 2017.

[6] E. Berrospe-Juarez, F. Trillaud, V. M. R. Zermeño, F. Grilli, H. W. Weijers, and M. D. Bird, "Screening currents and hysteresis losses in the REBCO insert of the 32 T all-superconducting magnet using $T$-$A$ homogenous model," *IEEE Trans. Appl. Supercond.*, vol. 30, no. 4, p. 4600705, 2020.

[7] J. R. Miller, "The NHMFL 45-T hybrid magnet system: Past, present, and future," *IEEE Trans. Appl. Supercond.*, vol. 13, no. 2, pp. 1385–90, 2003.

[8] S. Izquierdo Bermudez *et al.*, "Progress in the development of the $\mathrm{Nb_3Sn}$ MQXFB quadrupole for the HiLumi upgrade of the LHC," *IEEE Trans. Appl. Supercond.*, vol. 31, no. 5, p. 4002007, 2021.

[9] Y. Lvovsky and J. Jarvis, "Superconducting systems for MRI – present solutions and new trends," *IEEE Trans. Appl. Supercond.*, vol. 15, no. 2, pp. 1317–25, 2005.

[10] NHS England, "Diagnostic imaging dataset statistical release," 2023, accessed 03/03/2023. [Online]. Available: www.england.nhs.uk/statistics/wp-content/uploads/sites/2/2023/02/Statistical-Release-16th-February-2023-PDF-468KB.pdf

[11] T. C. Arnold, C. W. Freeman, B. Litt, and J. M. Stein, "Low-field MRI: Clinical promise and challenges," *J. Magn. Reson. Imaging*, vol. 57, no. 1, pp. 25–44, 2023.

[12] N. Gudino and S. Littin, "Advancements in gradient system performance for clinical and research MRI," *J. Magn. Reson. Imaging*, vol. 57, no. 1, pp. 57–70, 2023.

[13] ITER. Accessed 08/08/2022. [Online]. Available: www.iter.org

[14] B. N. Sorbom *et al.*, "ARC: A compact, high-field, fusion nuclear science facility and demonstration power plant with demountable magnets," *Fusion Eng. Des.*, vol. 100, pp. 378–405, 2015.

[15] D. Whyte, "Small, modular and economically attractive fusion enabled by high temperature superconductors," *Philos. Trans. R. Soc. A*, vol. 377, no. 2141, p. 20180354, 2019.

[16] ITER. ITER magnets. Accessed 07/09/2022. [Online]. Available: https://www.iter.org/mach/magnets

[17] S. B. L. Chislett-McDonald, E. Surrey, and D. P. Hampshire, "Could high H98-factor commercial tokamak power plants use Nb-Ti toroidal field coils?" *IEEE Trans. Appl. Supercond.*, vol. 29, no. 5, p. 4200405, 2019.

[18] T. Sunn Pedersen *et al.*, "Confirmation of the topology of the Wendelstein 7-X magnetic field to better than 1:100,000," *Nat. Commun.*, vol. 7, no. 1, p. 13493, 2016.

[19] A. Schaper, "Arms control at the stage of research and development? – the case of inertial confinement fusion," *Sci. Glob. Secur.*, vol. 2, no. 4, pp. 279–99, 1991.

[20] J. Tollefson and E. Gibney, "Nuclear-fusion lab achieves 'ignition': what does it mean?" *Nature*, vol. 612, pp. 597–8.

[21] Intergovernmental Panel on Climate Change, "Climate change 2022: Impacts, adaptation and vulnerability," 2022.

[22] Durham University. (2022) Highest ever temperature recorded in durham. Accessed 08/08/2022. [Online]. Available: https://www.durham.ac.uk/news-events/latest-news/2022/07/durham-records-highest-temperature

[23] B. Nayak, "Reactivities of neutronic and aneutronic fusion fuels," *Ann. Nucl. Energy*, vol. 60, pp. 73–7, 2013.

[24] M. Gilbert, T. Eade, C. Bachmann, U. Fischer, and N. Taylor, "Waste assessment of european demo fusion reactor designs," *Fusion Eng. Des.*, vol. 136, pp. 42–8, 2018.

[25] NNB Generation Company (HPC) Ltd., "Redacted public version HPC PCSR3: Chapter 21 – decommissioning," 2017.

[26] R. P. Rechard, “Historical background on performance assessment for the waste isolation pilot plant,” *Reliab. Eng. Syst. Saf.*, vol. 69, no. 1, pp. 5–46, 2000.

[27] World nuclear news, “Application lodged for construction of French repository,” 2023, accessed 27/03/2023. [Online]. Available: https://www.world-nuclear-news.org/Articles/Application-lodged-for-construction-of-French-repo?

[28] S. Grape, S. Jacobsson Svärd, C. Hellesen, P. Jansson, and M. Åberg Lindell, “New perspectives on nuclear power—Generation IV nuclear energy systems to strengthen nuclear non-proliferation and support nuclear disarmament,” *Energy Policy*, vol. 73, pp. 815–9, 2014.

[29] B. Bornschein, C. Day, D. Demange, and T. Pinna, “Tritium management and safety issues in ITER and DEMO breeding blankets,” *Fusion Eng. Des.*, vol. 88, no. 6, pp. 466–71, 2013.

[30] H. W. Weber, “Radiation effects on superconducting fusion magnet components,” *Int. J. Mod. Phys. E*, vol. 20, no. 6, pp. 1325–78, 2011.

[31] P. A. Hahn, H. Hoch, H. Weber, R. C. Birtcher, and B. S. Brown, “Simulation of fusion reactor conditions for superconducting magnet materials,” *J. Nucl. Mater.*, vol. 141–3, pp. 405–9, 1986.

[32] L. S. Topchishvili and A. I. Naskidashvili, “Critical current in NbTi wires irradiated by neutrons at 20 K,” *J. Nucl. Mater.*, vol. 271–2, pp. 505–7, 1999.

[33] D. Parkin and A. Sweedler, “Neutron irradiation of $Nb_3Sn$ and NbTi multifilamentary composites,” *IEEE Trans. Magn.*, vol. 11, no. 2, pp. 166–9, 1975.

[34] P. A. Hahn, M. W. Guinan, L. T. Summers, and T. Okada, “Fusion neutron irradiation effects in commercial $Nb_3Sn$ superconductors,” *J. Nucl. Mater.*, vol. 179, pp. 1127–30, 1990.

[35] S. Haindl, M. Eisterer, R. Müller, R. Prokopec, H. W. Weber, M. Müller, H. Kirchmayr, T. Takeuchi, and L. Bargioni, “Neutron irradiation effects on A15 multifilamentary wires,” *IEEE Trans. Appl. Supercond.*, vol. 15, no. 2, pp. 3414–7, 2005.

[36] H. Bauer, E. J. Saur, and D. G. Schweitzer, “Effect of neutron irradiations on superconducting properties of A-15 compounds undoped and doped with $^{10}B$ and $^{235}U$,” *J. Low Temp. Phys.*, vol. 19, pp. 171–87, 1975.

[37] A. Nishimura, T. Nakamoto, M. Yoshida, M. Iio, M. Yamazaki, T. Toyama, Y. Hishinuma, H. Oguro, and S. Awaji, “Effect of neutron irradiation on $Nb_3Sn$ wire,” *Supercond. Sci. Technol.*, vol. 32, p. 024004, 2019.

[38] T. Okada and Y. Hayashiuchi, “Neutron irradiation effect on NbTi and $Nb_3Sn$ and their application in superconducting magnets for fusion reactors,” *J. Nucl. Mater.*, vol. 72, no. 1, pp. 177–81, 1978.

[39] A. R. Sweedler and D. E. Cox, “Superconductivity and atomic ordering in neutron-irradiated $Nb_3Al$,” *Phys. Rev. B*, vol. 12, no. 1, pp. 147–56, 1975.

[40] T. Baumgartner, M. Eisterer, H. W. Weber, R. Flükiger, C. Scheuerlein, and L. Bottura, “Effects of neutron irradiation on pinning force scaling in state-of-the-art $Nb_3Sn$ wires,” *Supercond. Sci. Technol.*, vol. 27, no. 1, p. 015005, 2014.

[41] T. Baumgartner, M. Eisterer, H. W. Weber, R. Flükiger, C. Scheuerlein, and L. Bottura, “Performance boost in industrial multifilamentary $Nb_3Sn$ wires due to radiation induced pinning centers,” *Sci. Rep.*, vol. 5, p. 10236, 2015.

[42] A. Nishimura, T. Takeuchi, S. Nishijima, H. Oguro, K. Ochiai, K. Watanabe, and T. Shikama, “Fast neutron irradiation effect on superconducting properties of $Nb_3Sn$ and $Nb_3Al$ strands,” *AIP Conf. Proc.*, vol. 1435, no. 1, pp. 217–24, 2012.

[43] M. C. Frischherz, M. A. Kirk, J. Farmer, L. R. Greenwood, and H. W. Weber, “Defect cascades produced by neutron irradiation in $YBa_2Cu_3O_{7-\delta}$,” *Physica C*, vol. 232, no. 3, pp. 309–27, 1994.

[44] M. Chudy, R. Fuger, M. Eisterer, and H. W. Weber, “Characterization of commercial YBCO coated conductors after neutron irradiation,” *IEEE Trans. Appl. Supercond.*, vol. 21, no. 3, pp. 3162–5, 2011.

[45] H. W. Weber, H. P. Wiesinger, W. Kritscha, F. M. Sauerzopf, G. W. Crabtree, J. Z. Liu, Y. C. Chang, and P. Z. Jiang, “Critical currents in neutron irradiated YBCO and BiSCCO single crystals,” *Superconductor Science and Technology*, vol. 4, no. 1S, pp. S103–5, 1991.

[46] B. Hensel, B. Roas, S. Henke, R. Hopfengärtner, M. Lippert, J. P. Ströbel, M. Vildić, G. Saemann-Ischenko, and S. Klaumünzer, “Ion irradiation of epitaxial $YBa_2Cu_3O_{7-\delta}$ films: effects of electronic energy loss,” *Phys. Rev. B*, vol. 42, no. 7, pp. 4135–42, 1990.

[47] L. Civale, “Vortex pinning and creep in high-temperature superconductors with columnar defects,” *Supercond. Sci. Technol.*, vol. 10, pp. A11–28, 1997.

[48] L. Civale, A. D. Marwick, T. K. Worthington, M. A. Kirk, J. R. Thompson, L. Krusin-Elbaum, Y. Sun, J. R. Clem, and F. Holtzberg, “Vortex confinement by columnar defects in $YBa_2Cu_3O_7$ crystals: enhanced pinning at high fields and temperatures,” *Phys. Rev. Lett.*, vol. 67, no. 5, pp. 648–51, 1991.

[49] A. K. Jha, K. Matsumoto, T. Horide, S. Saini, P. Mele, A. Ichinose, Y. Yoshida, and S. Awaji, “Tailoring the vortex pinning strength of YBCO thin films by systematic incorporation of hybrid artificial pinning centers,” *Supercond. Sci. Technol.*, vol. 28, no. 11, 2015.

[50] M. Chudy, Z. Zhong, M. Eisterer, and T. Coombs, “$n$-Values of commercial YBCO tapes before and after irradiation by fast neutrons,” *Supercond. Sci. Technol.*, vol. 28, no. 3, p. 035008, 2015.

[51] M. Eisterer, R. Fuger, M. Chudy, F. Hengstberger, and H. W. Weber, “Neutron irradiation of coated conductors,” *Supercond. Sci. Technol.*, vol. 23, no. 1, p. 014009, 2010.

[52] J. Emhofer, M. Eisterer, and H. W. Weber, “Stress dependence of the critical currents in neutron irradiated (RE)BCO coated conductors,” *Supercond. Sci. Technol.*, vol. 26, no. 3, 2013.

[53] R. Prokopec, D. X. Fischer, H. W. Weber, and M. Eisterer, “Suitability of coated conductors for fusion magnets in view of their radiation response,” *Supercond. Sci. Technol.*, vol. 28, no. 1, p. 014005, 2015.

[54] M. Jirsa, M. Rameš, I. Ďuran, T. Melíšek, P. Kováč, and L. Viererbl, “Electric currents in REBaCuO superconducting tapes,” *Superconductor Science and Technology*, vol. 30, no. 4, p. 045010, 2017.

[55] R. Fuger, M. Eisterer, and H. W. Weber, “YBCO coated conductors for fusion magnets,” *IEEE Trans. Appl. Supercond.*, vol. 19, no. 3, pp. 1532–5, 2009.

[56] S. Tönies, A. Vostner, and H. W. Weber, “Determination of inter- and intragranular currents in high temperature superconducting tapes and coated conductors,” *J. Appl. Phys.*, vol. 92, no. 5, pp. 2628–33, 2002.

[57] D. X. Fischer, R. Prokopec, J. Emhofer, and M. Eisterer, “The effect of fast neutron irradiation on the superconducting properties of REBCO coated conductors with and without artificial pinning centers,” *Supercond. Sci. Technol.*, vol. 31, no. 4, p. 044006, 2018.

[58] W. Iliffe, K. Adams, N. Peng, G. Brittles, R. Bateman, A. Reilly, C. Grovenor, and S. Speller, “The effect of *in situ* irradiation on the superconducting performance of $\mathrm{REBa_2Cu_3O_{7-\delta}}$-coated conductors,” *MRS Bull.*, vol. 48, 2023.

[59] H. Thomas, A. Marian, A. Chervyakov, S. Stückrad, D. Salmieri, and C. Rubbia, “Superconducting transmission lines - sustainable electric energy transfer with higher public acceptance?” *Renew. Sustain. Energy Rev.*, vol. 55, pp. 59–72, 2016.

[60] M. Noe and M. Steurer, “High-temperature superconductor fault current limiters: concepts, applications, and development status,” *Supercond. Sci. Technol.*, vol. 20, no. 3, pp. R15–29, 2007.

[61] D. Boussard, E. Chiaveri, E. Haebel, H. P. Kindermann, R. Losito, S. Marque, V. Rödel, and M. Stirbet, “The LHC superconducting cavities,” *Proc. 1999 Part. Accel. Conf.*, vol. 2, pp. 946–8, 1999.

[62] H. S. Padamsee, “Superconducting radio-frequency cavities,” *Annual Rev. Nucl. Part. Sci.*, vol. 64, no. 1, pp. 175–96, 2014.

[63] J. Clarke, “Geophysical applications of SQUIDs,” *IEEE Trans. Magn.*, vol. 19, no. 3, pp. 288–94, 1983.

[64] H. Kamerlingh Onnes, "Further experiments with liquid helium. G. on the electrical resistance of pure metals, etc. VI. on the sudden change in the rate at which the resistance of mercury disappears," *Verslagen van de Afdeeling Natuurkunde der Kon. Akad. van Wetenschappen te Amsterdam*, vol. 124c, pp. 799–802, 1911.

[65] W. Meissner and R. Ochsenfeld, "Ein neuer Effekt bei Eintritt der Supraleitfähigkeit," *Naturwissenschaften*, vol. 21, pp. 787–8, 1933.

[66] T. G. Berlincourt and R. R. Hake, "Superconductivity at high magnetic fields," *Phys. Rev.*, vol. 131, no. 1, pp. 140–58, 1963.

[67] B. T. Matthias, T. H. Geballe, S. Geller, and E. Corenzwit, "Superconductivity of $Nb_3Sn$," *Phys. Rev.*, vol. 95, no. 6, p. 1435, 1954.

[68] F. London and H. London, "The electromagnetic equations of the supraconductor," *Proc. R. Soc. Lond. A*, vol. A149, pp. 71–88, 1935.

[69] V. L. Ginzburg and L. D. Landau, "On the theory of superconductivity," *Zh. Eksp. Teor. Fiz.*, vol. 20, pp. 1064–82, 1950.

[70] J. Bardeen, L. N. Cooper, and J. R. Schrieffer, "Theory of superconductivity," *Phys. Rev.*, vol. 108, no. 5, pp. 1175–1204, 1957.

[71] M. K. Wu, J. R. Ashburn, C. J. Torng, P. H. Hor, R. L. Meng, L. Gao, Z. J. Huang, Y. Q. Wang, and C. W. Chu, "Superconductivity at 93 K in a new mixed-phase Y-Ba-Cu-O compound system at ambient pressure," *Phys. Rev. Lett.*, vol. 58, no. 9, pp. 908–10, 1987.

[72] Y. Kamihara, H. Hiramatsu, M. Hirano, R. Kawamura, H. Yanagi, T. Kamiya, and H. Hosono, "Iron-based layered superconductor: LaOFeP," *J. Am. Chem. Soc.*, vol. 128, no. 31, pp. 10 012–3, 2006.

[73] J. E. Hirsch and F. Marsiglio, "Unusual width of the superconducting transition in a hydride," *Nature*, vol. 596, no. 7873, pp. E9–10, 2021.

[74] J. E. Hirsch and F. Marsiglio, "Clear evidence against superconductivity in hydrides under high pressure," *Matter Radiat. Extremes*, vol. 7, no. 5, p. 058401, 2022.

[75] E. Snider, N. Dasenbrock-Gammon, R. McBride, M. Debessai, H. Vindana, K. Vencatasamy, K. V. Lawler, A. Salamat, and R. P. Dias, "Room-temperature superconductivity in a carbonaceous sulfur hydride," *Nature*, vol. 586, no. 7829, pp. 373–7, 2020.

[76] J. F. Annett, *Superconductivity, Superfluids and Condensates.* Oxford University Press, New York, U.S.A, 2004.

[77] H. Traüble and U. Essmann, "Flux line arrangement in superconductors as revealed by direct observation," *J. Appl. Phys.*, vol. 39, no. 9, pp. 4052–9, 1968.

[78] J. Carlström, E. Babaev, and M. Speight, "Type-1.5 superconductivity in multiband systems: Effects of interband couplings," *Phys. Rev. B*, vol. 83, no. 17, p. 174509, 2011.

[79] S. B. L. Chislett-McDonald, “Designing a fusion power plant with superconducting training magnets,” PhD thesis, Durham University, 2022.

[80] C. P. Poole, H. A. Farach, R. J. Creswick, and R. Prozorov, *Superconductivity*, 2nd ed. Amsterdam, Netherlands: Academic Press, 2007.

[81] R. Klemm, *Layered Superconductors, volume 1.* Oxford University Press, 2012.

[82] G. Wang, M. J. Raine, and D. P. Hampshire, “How resistive must grain-boundaries be to limit $J_\mathrm{c}$ in polycrystalline superconductors?” *Supercond. Sci. Technol.*, vol. 30, no. 10, p. 104001, 2017.

[83] E. Maxwell, “Isotope effect in the superconductivity of mercury,” *Phys. Rev.*, vol. 78, no. 4, p. 477, 1950.

[84] C. A. Reynolds, B. Serin, W. H. Wright, and L. B. Nesbitt, “Superconductivity of isotopes of mercury,” *Phys. Rev.*, vol. 78, no. 4, p. 487, 1950.

[85] D. R. Tilley and J. Tilley, *Superfluidity and Superconductivity*, 3rd ed. Bristol, UK: IOP, 1990.

[86] L. N. Cooper, “Bound electron pairs in a degenerate Fermi gas,” *Phys. Rev.*, vol. 104, no. 4, pp. 1189–90, 1956.

[87] R. A. Ogg, “Superconductivity in solid metal-ammonia solutions,” *Phys. Rev.*, vol. 69, pp. 243–4, 1946.

[88] A. Brown, M. W. Zemansky, and H. A. Boorse, “The superconducting and normal heat capacities of niobium,” *Phys. Rev.*, vol. 92, no. 1, pp. 52–8, 1953.

[89] L. P. Gor’kov, “Microscopic derivation of the Ginzburg-Landau equations in the theory of superconductivity,” *Zh. Eksp. Teor. Fiz.*, vol. 36, no. 6, pp. 1918–23, 1959.

[90] A. I. Lichtenstein and M. I. Katsnelson, “Antiferromagnetism and $d$-wave superconductivity in cuprates: A cluster dynamical mean-field theory,” *Phys. Rev. B*, vol. 62, pp. R9283–6, 2000.

[91] D. M. J. Taylor and D. P. Hampshire, “Properties of helical springs used to measure the axial strain dependence of the critical current density in superconducting wires,” *Supercond. Sci. Technol.*, vol. 18, pp. 356–68, 2005.

[92] P. Branch, Y. Tsui, K. Osamura, and D. P. Hampshire, “Weakly-emergent strain-dependent properties of high field superconductors,” *Sci. Rep.*, vol. 9, p. 13998, 2019.

[93] K. Tsuchiya *et al.*, “Critical current measurement of commercial REBCO conductors at 4.2 K,” *Cryogenics*, vol. 85, pp. 1–7, 2017.

[94] F. Warmont and H. Jones, “Angular effect of transport critical currents in high-temperature superconductor tapes,” *Supercond. Sci. Technol.*, vol. 14, pp. 145–51, 2001.

[95] B. D. Josephson, “Possible new effects in superconductive tunnelling,” *Phys. Lett.*, vol. 1, no. 7, pp. 251–3, 1962.

[96] B. D. Josephson, “Supercurrents through barriers,” *Adv. Phys.*, vol. 14, no. 56, pp. 419–51, 1965.

[97] J. R. Clem, “Josephson junctions in thin and narrow rectangular superconducting strips,” *Phys. Rev. B*, vol. 81, no. 14, p. 144515, 2010.

[98] J. Pearl, “Current distribution in superconducting films carrying quantized fluxoids,” *Appl. Phys. Lett.*, vol. 5, no. 4, pp. 65–6, 1964.

[99] A. I. Blair and D. P. Hampshire, “Critical current density of superconducting-normal-superconducting Josephson junctions and polycrystalline superconductors in high magnetic fields,” *Phys. Rev. Res.*, vol. 4, p. 023123, 2022.

[100] H. J. Fink, “Supercurrents through superconducting-normal-superconducting proximity layers. I. Analytic solution,” *Phys. Rev. B*, vol. 14, no. 3, pp. 1028–38, 1976.

[101] L. J. Neuringer and Y. Shapira, “Effect of spin-orbit scattering on the upper critical field of high-field superconductors,” *Phys. Rev. Lett.*, vol. 17, no. 2, pp. 81–4, 1966.

[102] A. Godeke, M. C. Jewell, C. M. Fischer, A. A. Squitieri, P. J. Lee, and D. C. Larbalestier, “The upper critical field of filamentary $Nb_3Sn$ conductors,” *J. Appl. Phys.*, vol. 97, no. 9, p. 093909, 2005.

[103] M. Xu, H. Kitazawa, Y. Takano, J. Ye, K. Nishida, H. Abe, A. Matsushita, N. Tsujii, and G. Kido, “Anisotropy of superconductivity from $MgB_2$ single crystals,” *Appl. Phys. Lett.*, vol. 79, no. 17, pp. 2779–81, 2001.

[104] Q. Li, M. Suenaga, J. Gohng, D. K. Finnemore, T. Hikata, and K. Sato, “Reversible magnetic properties of *c*-axis-oriented superconducting $Bi_2Sr_2Ca_2Cu_3O_{10}$,” *Phys. Rev. B*, vol. 46, no. 5, pp. 3195–8, 1992.

[105] K. Tsuchiya, X. Wang, S. Fujita, A. Ichinose, K. Yamada, A. Terashima, and A. Kikuchi, “Superconducting properties of commercial REBCO-coated conductors with artificial pinning centers,” *Supercond. Sci. Technol.*, vol. 34, no. 10, p. 105005, 2021.

[106] N. Miura, H. Nakagawa, T. Sekitani, M. Naito, H. Sato, and Y. Enomoto, “High-magnetic-field study of high-$T_c$ cuprates,” *Physica B*, vol. 319, no. 1, pp. 310–20, 2002.

[107] J. D. Jorgensen *et al.*, “Oxygen ordering and the orthorhombic-to-tetragonal phase transition in $YBa_2Cu_3O_{7-x}$,” *Phys. Rev. B*, vol. 36, no. 7, pp. 3608–16, 1987.

[108] S. E. Babcock and D. C. Larbalestier, “Bicrystal studies of high transition temperature superconductors,” *J. Phys. Chem. Solids*, vol. 55, no. 10, pp. 1125–36, 1994.

[109] D. Dimos, P. Chaudhari, and J. Mannhart, "Superconducting transport properties of grain boundaries in $YBa_2Cu_3O_7$ bicrystals," *Phys. Rev. B*, vol. 41, no. 7, pp. 4038–49, 1990.

[110] SuperPower Inc., "2G HTS wire specification," 2022, accessed 29/09/2022. [Online]. Available: https://www.superpower-inc.com/specification.aspx

[111] Y. Iijima, N. Tanabe, O. Kohno, and Y. Ikeno, "In-plane aligned $YBa_2Cu_3O_{7-x}$ thin-films deposited on polycrystalline metallic substrates." *Appl. Phys. Lett.*, vol. 60, no. 6, pp. 769–71, 1992.

[112] J. H. Durrell and N. A. Rutter, "Importance of low-angle grain boundaries in $YBa_2Cu_3O_{7-\delta}$ coated conductors," *Supercond. Sci. Technol.*, vol. 22, p. 013001, 2009.

[113] J.-H. Lee, H. Lee, J.-W. Lee, S.-M. Choi, S.-I. Yoo, and S.-H. Moon, "RCE-DR, a novel process for coated conductor fabrication with high performance," *Supercond. Sci. Technol.*, vol. 27, no. 4, p. 044018, 2014.

[114] A. Markelov *et al.*, "2G HTS wire with enhanced engineering current density attained through the deposition of HTS layer with increased thickness," *Progr. Supercond. Cryogen.*, vol. 21, no. 4, pp. 29–33, 2019.

[115] M. Dürrschnabel, Z. Aabdin, M. Bauer, R. Semerad, W. Prusseit, and O. Eibl, "$DyBa_2Cu_3O_{7-x}$ superconducting coated conductors with critical currents exceeding 1000 A $cm^{-1}$," *Supercond. Sci. Technol.*, vol. 25, no. 10, p. 105007, 2012.

[116] J. D. Weiss *et al.*, "Introduction of the next generation of CORC® wires with engineering current density exceeding 650 $Amm^{-2}$ at 12 T based on SuperPower's ReBCO tapes containing substrates of 25 μm thickness," *Supercond. Sci. Technol.*, vol. 33, no. 4, p. 044001, 2020.

[117] THEVA Dünnschichttechnik GmbH, "Pro-line product overview," 2022, accessed 07/11/2022. [Online]. Available: https://www.theva.de/wp-content/uploads/2022/09/Product_Overview_2022.pdf

[118] A. Molodyk *et al.*, "Development and large volume production of extremely high current density $YBa_2Cu_3O_7$ superconducting wires for fusion," *Sci. Rep.*, vol. 11, p. 2084, 2021.

[119] J. G. Ossandon, J. R. Thompson, D. K. Christen, B. C. Sales, H. R. Kerchner, J. O. Thomson, Y. R. Sun, K. W. Lay, and J. E. Tkaczyk, "Influence of oxygen deficiency on the superconductive properties of grain-aligned $YBa_2Cu_3O_{7-\delta}$," *Phys. Rev. B*, vol. 45, no. 21, pp. 12 534–47, 1992.

[120] S. I. Schlachter, W. H. Fietz, K. Grube, T. Wolf, B. Obst, P. Schweiss, and M. Kläser, "The effect of chemical doping and hydrostatic pressure on $T_c$ of $Y_{1-y}Ca_yBa_2Cu_3O_x$ single crystals," *Physica C*, vol. 328, no. 1, pp. 1–13, 1999.

[121] A. A. Zhukov *et al.*, “Influence of oxygen stoichiometry on the irreversible magnetization and flux creep in $R\mathrm{Ba_2Cu_3O_{7-\delta}}$ ($R$ = Y,Tm) single crystals,” *Phys. Rev. B*, vol. 51, no. 18, pp. 12 704–14, 1995, pRB.

[122] A. Preuss, W. H. Fietz, F. Immel, S. Kauffmann-Weiss, and M. J. Wolf, “Critical current degradation of coated conductors under soldering conditions,” *IEEE Trans. Appl. Supercond.*, vol. 28, no. 4, p. 6601105, 2018.

[123] J. Lu, Y. Xin, B. Jarvis, and H. Y. Bai, “Oxygen out-diffusion in REBCO coated conductor due to heating,” *Supercond. Sci. Technol.*, vol. 34, no. 7, p. 075004, 2021.

[124] Y. Tsui, E. Surrey, and D. P. Hampshire, “Soldered joints - an essential component of demountable high temperature superconducting fusion magnets,” *Supercond. Sci. Technol.*, vol. 290, p. 075005, 2016.

[125] Y. Tsui, R. Mahmoud, E. Surrey, and D. P. Hampshire, “Superconducting and mechanical properties of low-temperature solders for joints,” *IEEE Trans. Appl. Supercond.*, vol. 26, no. 3, p. 6900204, 2016.

[126] K. Osamura, S. Machiya, Y. Tsuchiya, H. Suzuki, T. Shobu, M. Sato, and S. Ochiai, “Microtwin structure and its influence on the mechanical properties of REBCO coated conductors,” *IEEE Trans. Appl. Supercond.*, vol. 22, no. 1, 2012.

[127] C. Tarantini, J. Jaroszynski, F. Kametani, Y. L. Zuev, A. Gurevich, Y. Chen, V. Selvamanickam, D. C. Larbalestier, and D. K. Christen, “Anisotropy of the irreversibility field for Zr-doped $(\mathrm{Y,Gd})\mathrm{Ba_2Cu_3O_{7-x}}$ thin films up to 45 T,” *Phys. Rev. B*, vol. 84, no. 22, p. 224514, 2011.

[128] M. Lao, J. Bernardi, M. Bauer, and M. Eisterer, “Critical current anisotropy of GdBCO tapes grown on ISD-MgO buffered substrate,” *Supercond. Sci. Technol.*, vol. 28, no. 12, p. 124002, 2015.

[129] M. Lao, J. Hecher, M. Sieger, P. Pahlke, M. Bauer, R. Hühne, and M. Eisterer, “Planar current anisotropy and field dependence of $J_\mathrm{c}$ in coated conductors assessed by scanning Hall probe microscopy,” *Supercond. Sci. Technol.*, vol. 30, no. 2, p. 024004, 2017.

[130] A. P. Smith, M. J. Raine, E. Surrey, S. Awaji, T. Okada, and D. P. Hampshire, “3-D properties in (RE)BCO tapes measured in fields up to 35T,” *IEEE Trans. Appl. Supercond.*, vol. 29, no. 5, p. 6601005, 2019.

[131] R. A. Klemm, A. Luther, and M. R. Beasley, “Theory of the upper critical field in layered superconductors,” *Phys. Rev. B*, vol. 12, no. 3, pp. 877–91, 1975.

[132] M. Weigand, N. A. Rutter, S. Sahonta, and J. H. Durrell, “Critical current densities of MOCVD tapes for different current directions,” *IEEE Trans. Appl. Supercond.*, vol. 21, no. 3, pp. 3347–51, 2011.

[133] C. Meingast, B. Blank, H. Bürkle, B. Obst, T. Wolf, H. Wühl, V. Selvamanickam, and K. Salama, “Anisotropic pressure dependence of $T_\mathrm{c}$ in single-crystal $\mathrm{YBa_2Cu_3O_7}$ via thermal expansion,” *Phys. Rev. B*, vol. 41, no. 16, pp. 11 299–304, 1990.

[134] C. Meingast, O. Kraut, T. Wolf, H. Wühl, A. Erb, and G. Müller-Vogt, “Large $a$-$b$ anisotropy of the expansivity anomaly at $T_\mathrm{c}$ in untwinned $\mathrm{YBa_2Cu_3O_{7-\delta}}$,” *Phys. Rev. Lett.*, vol. 67, no. 12, pp. 1634–7, 1991.

[135] O. Kraut, C. Meingast, G. Bräuchle, H. Claus, A. Erb, G. Müller-Vogt, and H. Wühl, “Uniaxial pressure dependence of $T_\mathrm{c}$ of untwinned $\mathrm{YBa_2Cu_3O}_x$ single crystals for $x$=6.5–7,” *Physica C*, vol. 205, no. 1, pp. 139–46, 1993.

[136] M. Kund and K. Andres, “Anisotropic stress dependence of $T_\mathrm{c}$ in $\mathrm{YBa_2Cu_3O_{7-\delta}}$ single crystals deduced from thermal expansion, measured with a capacitive quartz-dilatometer,” *Physica C*, vol. 205, no. 1, pp. 32–8, 1993.

[137] C. Murayama, Y. Iye, T. Enomoto, N. Môri, Y. Yamada, T. Matsumoto, Y. Kubo, Y. Shimakawa, and T. Manako, “Correlation between the pressure-induced changes in the Hall coefficient and $T_\mathrm{c}$ in superconducting cuprates,” *Physica C*, vol. 183, no. 4, pp. 277–85, 1991.

[138] R. Benischke, T. Weber, W. H. Fietz, J. Metzger, K. Grube, T. Wolf, and H. Wühl, “The effect of high hydrostatic pressure on $T_\mathrm{c}$ of $\mathrm{YBa_2Cu_3O}_x$ as a function of the oxygen content,” *Physica C*, vol. 203, no. 3, pp. 293–8, 1992.

[139] U. Welp, M. Grimsditch, S. Fleshler, W. Nessler, J. Downey, and G. W. Crabtree, “Effect of uniaxial stress on the superconducting transition in $\mathrm{YBa_2Cu_3O_7}$,” *Phys. Rev. Lett.*, vol. 69, no. 14, p. 2130, 1992.

[140] W. H. Fietz, K. Weiss, and S. I. Schlachter, “Influence of intrinsic strain on $T_\mathrm{c}$ and critical current of high-$T_\mathrm{c}$ superconductors,” *Supercond. Sci. Technol.*, vol. 18, no. 12, pp. S332–7, 2005.

[141] W. H. Fietz *et al.*, “Joint features of pressure effects and specific heat of $R\mathrm{Ba_2Cu_3O}_x$ at distinct $n_\mathrm{h}$ values,” *Physica C*, vol. 341–8, pp. 347–50, 2000.

[142] C. Meingast, T. Wolf, M. Kläser, and G. Müller-Vogt, “Uniaxial pressure dependence of $T_\mathrm{c}$ in $(\mathrm{Y}_{1-y}\mathrm{Ca}_y)_1\mathrm{Ba_2Cu_3Ox}$ single crystals via high-resolution thermal expansion,” *J. Low Temp. Phys.*, vol. 105, no. 5, pp. 1391–1396, 1996.

[143] B. Bucher, E. Kaldis, C. Krüger, and P. Wachter, “Stoichiometry and pressure dependence of $T_\mathrm{c}$ of $\mathrm{YBa_2Cu_3O}_x$,” *Europhys. Lett.*, vol. 34, no. 5, pp. 391–394, 1996.

[144] P. Cayado, D. Hauck, D. Barthlott, M. Erbe, J. Hänisch, and B. Holzapfel, “Determination of the oxygen chain ordering in $\mathrm{REBa_2Cu_3O_{7-\delta}}$ by electrical conductivity relaxation measurements,” *ACS Appl. Electron. Mater.*, vol. 3, no. 12, pp. 5374–82, 2021.

[145] T. Suzuki, S. Awaji, H. Oguro, and K. Watanabe, “Applied strain effect on superconducting properties for detwinned $(\mathrm{Y},\mathrm{Gd})$BCO coated conductors,” *IEEE Trans. Appl. Supercond.*, vol. 25, no. 3, p. 8400704, 2015.

[146] S. Awaji, T. Suzuki, H. Oguro, K. Watanabe, and K. Matsumoto, “Strain-controlled critical temperature in $\mathrm{REBa_2Cu_3O}_y$-coated conductors,” *Sci. Rep.*, vol. 5, p. 11156, 2015.

[147] W. Reichardt, L. Pintschovius, B. Hennion, and F. Collin, "Inelastic neutron scattering study of $YBa_2Cu_3O_{7-x}$," *Supercond. Sci. Technol.*, vol. 1, no. 4, pp. 173–176, 1988.

[148] H. Ledbetter and M. Lei, "Monocrystal elastic constants of orthotropic $Y_1Ba_2Cu_3O_7$: an estimate," *J. Mater. Res.*, vol. 6, no. 11, pp. 2253–5, 1991.

[149] M. Lei, J. L. Sarrao, W. M. Visscher, T. M. Bell, J. D. Thompson, A. Migliori, U. W. Welp, and B. W. Veal, "Elastic constants of a monocrystal of superconducting $YBa_2Cu_3O_{7-\delta}$," *Phys. Rev. B*, vol. 47, no. 10, pp. 6154–6, 1993.

[150] S. T. Murphy, "A point defect model for $YBa_2Cu_3O_7$ from density functional theory," *J. Phys. Commun.*, vol. 4, no. 11, p. 115003, 2020.

[151] S. Favre, D. Ariosa, C. Yelpo, M. Mazini, and R. Faccio, "Depression of critical temperature due to residual strain induced by PLD deposition on $YBa_2Cu_3O_{7-\delta}$ thin films," *Mater. Chem. Phys.*, vol. 266, p. 124507, 2021.

[152] D. C. van der Laan, D. Abraimov, A. A. Polyanskii, D. C. Larbalestier, J. F. Douglas, R. Semerad, and M. Bauer, "Anisotropic in-plane reversible strain effect in $Y_{0.5}Gd_{0.5}Ba_2Cu_3O_{7-\delta}$ coated conductors," *Supercond. Sci. Technol.*, vol. 24, no. 11, p. 115010, 2011.

[153] K. Osamura, S. Machiya, and D. P. Hampshire, "Mechanism for the uniaxial strain dependence of the critical current in practical REBCO tapes," *Supercond. Sci. Technol.*, vol. 29, no. 6, p. 065019, 2016.

[154] M. Sugano, K. Osamura, W. Prusseit, R. Semerad, K. Itoh, and T. Kiyoshi, "Tensile fracture behaviour of RE-123 coated conductors induced by discontinuous yielding in Hastelloy C-276 substrate," *Supercond. Sci. Technol.*, vol. 18, no. 12, p. S344, 2005.

[155] M. Sugano, S. Machiya, K. Osamura, H. Adachi, M. Sato, R. Semerad, and W. Prusseit, "The direct evaluation of the internal strain of biaxially textured YBCO film in a coated conductor using synchrotron radiation," *Supercond. Sci. Technol.*, vol. 22, no. 1, p. 015002, 2009.

[156] S. Ochiai, H. Okuda, M. Sugano, K. Osamura, and W. Prusseit, "Influences of electroplated copper on tensile strain and stress tolerance of critical current in DyBCO-coated conductor," *IEEE Trans. Appl. Supercond.*, vol. 22, no. 1, p. 8400607, 2012.

[157] D. C. van der Laan, J. F. Douglas, L. F. Goodrich, R. Semerad, and M. Bauer, "Correlation between in-plane grain orientation and the reversible strain effect on flux pinning in RE-$Ba_2Cu_3O_{7-\delta}$ coated conductors," *IEEE Trans. Appl. Supercond.*, vol. 22, no. 1, p. 8400707, 2012.

[158] S. Ochiai, H. Okuda, T. Arai, M. Sugano, K. Osamura, and W. Prusseit, "Influence of copper volume fraction on tensile strain/stress tolerances of critical current in a

copper-plated DyBCO-coated conductor," *Mater. Trans.*, vol. 54, no. 3, pp. 269–75, 2013.

[159] M. Sugano *et al.*, "The effect of the 2D internal strain state on the critical current in GdBCO coated conductors," *Supercond. Sci. Technol.*, vol. 25, no. 5, p. 054014, 2012.

[160] J. R. Greenwood, E. Surrey, and D. P. Hampshire, "Biaxial strain measurements of $J_\mathrm{C}$ on a (RE)BCO coated conductor," *IEEE Trans. Appl. Supercond.*, vol. 28, no. 4, p. 8400705, 2018.

[161] J. R. Greenwood, E. Surrey, and D. P. Hampshire, "The biaxial strain dependence of $J_\mathrm{C}$ of a (RE)BCO coated conductor at 77 K in low fields," *IEEE Trans. Appl. Supercond.*, vol. 29, no. 5, p. 8002805, 2019.

[162] D. Arbelaez, A. Godeke, and S. O. Prestemon, "An improved model for the strain dependence of the superconducting properties of $\mathrm{Nb_3Sn}$," *Supercond. Sci. Technol.*, vol. 22, no. 2, p. 025005, 2008.

[163] B. ten Haken and H. H. J. ten Kate, "The degradation of the critical current density in a $\mathrm{Nb_3Sn}$ tape conductor due to parallel and transversal strain," *Fusion Eng. Des.*, vol. 20, pp. 265–70, 1993.

[164] B. ten Haken, A. Godeke, and H. H. J. ten Kate, "The influence of compressive and tensile axial strain on the critical properties of $\mathrm{Nb_3Sn}$ conductors," *IEEE Trans. Appl. Supercond.*, vol. 5, no. 2, pp. 1909–12, 1995.

[165] E. A. Kearsley, "Note: Strain invariants expressed as average stretches," *J. Rheol.*, vol. 33, no. 5, pp. 757–60, 1989.

[166] A. Godeke, B. ten Haken, and H. H. J. ten Kate, "The deviatoric strain description of the critical properties of $\mathrm{Nb_3Sn}$ conductors," *Physica C*, vol. 372–6, pp. 1295–8, 2002.

[167] W. D. Markiewicz, "Elastic stiffness model for the critical temperature $T_\mathrm{c}$ of $\mathrm{Nb_3Sn}$ including strain dependence," *Cryogenics*, vol. 44, pp. 767–82, 2004.

[168] A. Godeke, B. ten Haken, H. H. J. ten Kate, and D. Larbalestier, "A general scaling relation for the critical current density in $\mathrm{Nb_3Sn}$," *Supercond. Sci. Technol.*, vol. 19, pp. R100–116, 2006.

[169] Y. Ilyin, A. Nijhuis, and E. Krooshoop, "Scaling law for the strain dependence of the critical current in an advanced ITER $\mathrm{Nb_3Sn}$ strand," *Supercond. Sci. Technol.*, vol. 20, pp. 186–91, 2007.

[170] A. Nijhuis, Y. Ilyin, and W. Abbas, "Axial and transverse stress–strain characterization of the EU dipole high current density $\mathrm{Nb_3Sn}$ strand," *Supercond. Sci. Technol.*, vol. 21, no. 6, p. 065001, 2008.

[171] D. O. Welch, “Alteration of the superconducting properties of A15 compounds and elementary composite superconductors by nonhydrostatic elastic strain,” *Adv. Cryo. Eng.*, vol. 26, pp. 48–65, 1980.

[172] S. S. Andrews, “Using rotational averaging to calculate the bulk response of isotropic and anisotropic samples from molecular parameters,” *J. Chem. Educ.*, vol. 81, no. 6, pp. 877–85, 2004.

[173] D. M. J. Taylor and D. P. Hampshire, “The scaling law for the strain dependence of the critical current density in $Nb_3Sn$ superconducting wires,” *Supercond. Sci. Technol.*, vol. 18, pp. S241–52, 2005.

[174] P. X. Zhang, Y. Feng, X. H. Liu, C. G. Li, K. Zhang, X. D. Tang, and Y. Wu, “Microstructure and superconducting properties comparison of bronze and internal tin process $Nb_3Sn$ strands for ITER,” *Physica C*, vol. 469, no. 15-20, pp. 1536–40, 2009.

[175] P. Branch, K. Osamura, and D. Hampshire, “Weak emergence in the angular dependence of the critical current density of the high temperature superconductor coated conductor REBCO,” *Supercond. Sci. Technol.*, vol. 33, no. 10, p. 104006, 2020.

[176] E. J. Kramer, “Scaling laws for flux pinning in hard superconductors,” *J. Appl. Phys.*, vol. 44, no. 3, pp. 1360–70, 1973.

[177] D. Dew-Hughes, “Flux pinning mechanisms in type II superconductors,” *Philos. Mag.*, vol. 30, no. 2, pp. 293–305, 1974.

[178] H. S. Shin, A. Gorospe, A. R. Nisay, M. J. Dedicatoria, K. D. Sim, S. Awaji, and H. Oguro, “Macroscopic strain response of $i_c$ under magnetic fields in differently stabilized REBCO CC tapes,” *IEEE Trans. Appl. Supercond.*, vol. 25, no. 3, p. 6602104, 2015.

[179] J. R. Greenwood, “Percolative current flow through anisotropic high-field superconductors under strain,” PhD thesis, Durham University, 2023.

[180] Y. Ando *et al.*, “Resistive upper critical fields and irreversibility lines of optimally doped high-$t_c$ cuprates,” *Phys. Rev. B*, vol. 60, pp. 12 475–9, 1999.

[181] Hottinger Brüel & Kjær GmbH, “Strain gauges,” accessed 18/04/2023. [Online]. Available: www.hbm.com/fileadmin/mediapool/hbmdoc/technical/S01265.pdf

[182] E. G. Gillard, M. J. Raine, and D. P. Hampshire, “Resistivity measurements of the strain, temperature and angular dependence of the upper critical field of REBCO tapes up to 8 T,” *IEEE Trans. Appl. Supercond.*, vol. 33, no. 5, p. 8401205, 2023.

[183] M. Sieger *et al.*, “Influence of substrate tilt angle on the incorporation of $BaHfO_3$ in thick $YBa_2Cu_3O_{7-\delta}$ films,” *IEEE Trans. Appl. Supercond.*, vol. 27, no. 4, p. 7500504, 2017.

[184] N. Bagrets, G. Celentano, A. Augieri, R. Nast, and K. P. Weiss, “Investigation of soldered REBCO tape–copper joints for superconducting applications,” *IEEE Trans. Appl. Supercond.*, vol. 26, no. 4, p. 4800404, 2016.

[185] R. Hayasaka, S. Ito, and H. Hashizume, “Evaluation of interface resistance in a REBCO tape at different temperatures by contact-probing current transfer length method,” *IEEE Trans. Appl. Supercond.*, vol. 29, no. 5, p. 9000805, 2019.

[186] N. Bagrets, R. Nast, J. H. Fournier-Lupien, F. Sirois, G. Celentano, and K. P. Weiss, “Current transfer length and interfacial resistance between superconductors and metals in commercial REBCO tapes and cables,” *IEEE Trans. Appl. Supercond.*, vol. 31, no. 6, p. 6601508, 2021.

[187] J. R. Taylor, *An introduction to error analysis. The Study of Uncertainties in Physical Measuements.* University Science Books, 1982.

[188] A. Xu, V. Braccini, J. Jaroszynski, Y. Xin, and D. C. Larbalestier, “Role of weak uncorrelated pinning introduced by $BaZrO_3$ nanorods at low-temperature in $(Y, Gd)Ba_2Cu_3O_x$ thin films,” *Phys. Rev. B*, vol. 86, no. 11, p. 115416, 2012.

[189] O. Tsukamoto and M. Ciszek, “AC magnetization losses in striated YBCO-123/Hastelloy coated conductors,” *Supercond. Sci. Technol.*, vol. 20, no. 10, pp. 974–9, 2007.

[190] L. Peng, C. Cai, C. Chen, Z. Liu, J. Liu, B. Gao, and J. Zhang, “Formation of nanosized $BaZrO_3$ and the magnetotransport properties in $YBa_2Cu_3O_{7-\delta}$/YSZ quasi-multilayers,” *J. Phys. D*, vol. 41, no. 15, p. 155403, 2008.

[191] A. H. Puichaud, S. C. Wimbush, and R. Knibbe, “Enhanced low-temperature critical current by reduction of stacking faults in REBCO coated conductors,” *Supercond. Sci. Technol.*, vol. 30, no. 7, p. 074005, 2017.

[192] R. Hühne, V. S. Sarma, D. Okai, T. Thersleff, L. Schultz, and B. Holzapfel, “Preparation of coated conductor architectures on Ni composite tapes,” *Supercond. Sci. Technol.*, vol. 20, no. 7, pp. 709–14, 2007.

[193] H. Shin, M. J. Dedicatoria, H. S. Kim, N. J. Lee, H. S. Ha, and S. S. Oh, “Electro-mechanical property investigation of striated REBCO coated conductor tapes in pure torsion mode,” *IEEE Trans. Appl. Supercond.*, vol. 21, no. 3, pp. 2997–3000, 2011.

[194] A. Godfrin *et al.*, “Influence of the striation process and the thickness of the Cu-stabilization on the AC magnetization loss of striated REBCO tape,” *IEEE Trans. Appl. Supercond.*, vol. 27, no. 6, p. 5900809, 2017.

[195] M. Iwakuma *et al.*, “Relaxation of shielding current in test coils for MRI with REBCO superconducting scribed tapes,” *IEEE Trans. Appl. Supercond.*, vol. 26, no. 3, p. 4401505, 2016.

[196] I. Kesgin, G. Majkic, and V. Selvamanickam, “Fully filamentized HTS coated conductor via striation and selective electroplating,” *Physica C*, vol. 486, pp. 43–50, 2013.

[197] D. M. J. Taylor and D. P. Hampshire, “Relationship between the $n$-value and critical current in $\mathrm{Nb_3Sn}$ superconducting wires exhibiting intrinsic and extrinsic behaviour,” *Supercond. Sci. Technol.*, vol. 18, pp. S297–302, 2005.

[198] F. Grilli, F. Sirois, V. M. R. Zermeño, and M. Vojenčiak, “Self-consistent modeling of the $I_c$ of HTS devices: How accurate do models really need to be?” *IEEE Trans. Appl. Supercond.*, vol. 24, no. 6, p. 8000508, 2014.

[199] E. Pardo, M. Vojenčiak, F. Gömöry, and J. Šouc, “Low-magnetic-field dependence and anisotropy of the critical current density in coated conductors,” *Supercond. Sci. Technol.*, vol. 24, p. 065007, 2011.

[200] S. A. Harrington, J. L. MacManus-Driscoll, and J. H. Durrell, “Practical vortex diodes from pinning enhanced $\mathrm{YBa_2Cu_3O_{7-\delta}}$,” *Appl. Phys. Lett.*, vol. 95, no. 2, p. 022518, 2009.

[201] V. Selvamanickam *et al.*, “The low-temperature, high-magnetic-field critical current charatceristics of Zr-added $(\mathrm{Gd, Y})\mathrm{Ba_2Cu_3O}_x$ superconducting tapes,” *Supercond. Sci. Technol.*, vol. 25, p. 125013, 2012.

[202] V. Selvamanickam, Y. Chen, J. Xie, Y. Zhang, A. Guevara, I. Kesgin, G. Majkic, and M. Martchevsky, “Influence of Zr and Ce doping on electromagnetic properties of (Gd,Y)–Ba–Cu–O superconducting tapes fabricated by metal organic chemical vapor deposition,” *Physica C*, vol. 469, no. 23, pp. 2037–43, 2009.

[203] W. A. Fietz and W. W. Webb, “Hysteresis in superconducting alloys—temperature and field dependence of dislocation pinning in niobium alloys,” *Phys. Rev.*, vol. 178, no. 2, pp. 657–67, 1969.

[204] S. A. Keys, N. Koizumi, and D. P. Hampshire, “The strain and temperature scaling law for the critical current density of a jelly-roll $\mathrm{Nb_3Al}$ strand in high magnetic fields,” *Supercond. Sci. Technol.*, vol. 15, pp. 991–1010, 2002.

[205] S. I. Bredikhin, G. A. Emel’chenko, V. S. Shechtman, A. A. Zhokhov, S. Carter, R. J. Chater, J. A. Kilner, and B. C. H. Steele, “Anisotropy of oxygen self-diffusion in $\mathrm{YBa_2Cu_3O_{7-\delta}}$ single crystals,” *Physica C*, vol. 179, no. 4, pp. 286–90, 1991.

[206] S. J. Rothman, J. L. Routbort, U. Welp, and J. E. Baker, “Anisotropy of oxygen tracer diffusion in single-crystal $\mathrm{YBa_2Cu_3O_{7-\delta}}$,” *Phys. Rev. B*, vol. 44, no. 5, pp. 2326–33, 1991.

[207] S. R. Foltyn, Q. X. Jia, P. N. Arendt, L. Kinder, Y. Fan, and J. F. Smith, “Relationship between film thickness and the critical current of $\mathrm{YBa_2Cu_3O_{7-\delta}}$-coated conductors,” *Appl. Phys. Lett.*, vol. 75, no. 23, pp. 3692–4, 1999.

[208] S. I. Kim, A. Gurevich, X. Song, X. Li, W. Zhang, T. Kodenkandath, M. W. Rupich, T. G. Holesinger, and D. C. Larbalestier, “Mechanisms of weak thickness dependence of the critical current density in strong-pinning *ex situ* metal–organic-deposition-route $YBa_2Cu_3O_{7-x}$ coated conductors,” *Supercond. Sci. Technol.*, vol. 19, no. 9, pp. 968–79, 2006.

[209] H. Zhou *et al.*, “Thickness dependence of critical current density in $YBa_2Cu_3O_{7-\delta}$ films with $BaZrO_3$ and $Y_2O_3$ addition,” *Supercond. Sci. Technol.*, vol. 22, no. 8, p. 085013, 2009.

[210] H.-S. Ha, J.-H. Lee, R.-K. Ko, H.-S. Kim, H.-K. Kim, S.-H. Moon, C. Park, D.-J. Youm, and S.-S. Oh, “Thick SmBCO/IBAD-MgO coated conductor for high current carrying power applications,” *IEEE Trans. Appl. Supercond.*, vol. 20, no. 3, pp. 1545–8, 2010.

[211] M. Igarashi *et al.*, “High-speed deposition of RE123 film with large current capacity by hot-wall type PLD system,” *Physica C*, vol. 470, no. 20, pp. 1230–3, 2010.

[212] L. Liu, Y. Li, G. Xiao, and X. Wu, “Fabrication of thick REBCO–coated conductors with high performance on metal tapes by pulsed laser deposition process,” *J. Supercond. Nov. Magn.*, vol. 28, no. 2, pp. 403–6, 2015.

[213] E. F. Talantsev, W. P. Crump, and J. L. Tallon, “Universal scaling of the self-field critical current in superconductors: from sub-nanometre to millimetre size,” *Sci. Rep.*, vol. 7, p. 10010, 2017.

[214] E. F. Talantsev and J. L. Tallon, “Universal self-field critical current for thin-film superconductors,” *Nat. Commun.*, vol. 6, p. 7820, 2015.

[215] A. A. Babaei Brojeny and J. R. Clem, “Self-field effects upon the critical current density of flat superconducting strips,” *Supercond. Sci. Technol.*, vol. 18, no. 6, pp. 888–95, 2005.

[216] L. Rostila, J. Lehtonen, and R. Mikkonen, “Self-field reduces critical current density in thick YBCO layers,” *Physica C*, vol. 451, no. 1, pp. 66–70, 2007.

[217] A. Sanchez, C. Navau, N. Del-Valle, D.-X. Chen, and J. R. Clem, “Self-fields in thin superconducting tapes: Implications for the thickness effect in coated conductors,” *Appl. Phys. Lett.*, vol. 96, no. 7, p. 072510, 2010.

[218] Ö. Polat, J. W. Sinclair, Y. L. Zuev, J. R. Thompson, D. K. Christen, S. W. Cook, D. Kumar, Y. Chen, and V. Selvamanickam, “Thickness dependence of magnetic relaxation and $E$–$J$ characteristics in superconducting (Gd-Y)-Ba-Cu-O films with strong vortex pinning,” *Phys. Rev. B*, vol. 84, p. 024519, 2011.

[219] Y. B. Kim, C. F. Hempstead, and A. R. Strnad, “Magnetization and critical supercurrents,” *Phys. Rev.*, vol. 129, no. 2, pp. 528–35, 1963.

[220] X.-F. Li, A. B. Yahia, G. Majkic, M. Kochat, S. Kar, and V. Selvamanickam, “Reel-to-reel critical current measurement of REBCO coated conductors,” *IEEE Trans. Appl. Supercond.*, vol. 27, no. 4, p. 3800205, 2017.

[221] E. F. Talantsev, N. M. Strickland, S. C. Wimbush, and W. P. Crump, “The onset of dissipation in high-temperature superconductors: Self-field experiments,” *AIP Adv.*, vol. 7, no. 12, p. 125230, 2017.

[222] E. F. Talantsev, N. M. Strickland, S. C. Wimbush, J. Brooks, A. E. Pantoja, R. A. Badcock, J. G. Storey, and J. L. Tallon, “The onset of dissipation in high-temperature superconductors: magnetic hysteresis and field dependence,” *Sci. Rep.*, vol. 8, p. 14463, 2018.

[223] N. Chikumoto, S. Yamaguchi, and O. Shyshkin, “Transport current distribution in soldered joint of BSCCO and REBCO tapes,” *J. Phys.: Conf. Ser.*, vol. 1559, p. 012069, 2020.

[224] K. Tsuchiya *et al.*, “Critical current characterization of commercial REBCO coated conductors at 4.2 and 77 K,” *IEEE Trans. Appl. Supercond.*, vol. 27, no. 4, p. 6600205, 2017.

[225] Robinson Research Institute, “The Robinson Research Institute high-temperature superconducting wire critical current database,” accessed 05/12/2022. [Online]. Available: https://htsdb.wimbush.eu/

[226] S. C. Wimbush and N. M. Strickland, “A public database of high-temperature superconductor critical current data,” *IEEE Trans. Appl. Supercond.*, vol. 27, no. 4, p. 8000105, 2017.

[227] V. Selvamanickam, A. Xu, Y. Liu, N. D. Khatri, C. Lei, Y. Chen, E. Galstyan, and G. Majkic, “Correlation between in-field critical currents in Zr-added $(\mathrm{Gd},\mathrm{Y})\mathrm{Ba}_2\mathrm{Cu}_3\mathrm{O}_x$ superconducting tapes at 30 and 77 K,” *Supercond. Sci. Technol.*, vol. 27, no. 5, p. 055010, 2014.

[228] G. Majkic, R. Pratap, E. Galstyan, and V. Selvamanickam, “Correlation of in-field performance of thick REBCO films between 0-14 T and 4.2–77 K,” *IEEE Trans. Appl. Supercond.*, vol. 29, no. 5, p. 6602005, 2019.

[229] J. Millett, G. Whiteman, N. Park, S. Case, and G. Appleby-Thomas, “The effects of heat treatment upon the shock response of a copper-beryllium alloy,” *Acta Mater.*, vol. 165, pp. 678–85, 2019.

[230] S. A. Keys and D. P. Hampshire, “A scaling law for the critical current density of weakly and strongly-coupled superconductors, used to parameterise data from a technological $\mathrm{Nb}_3\mathrm{Sn}$ strand,” *Supercond. Sci. Technol.*, vol. 16, pp. 1097–108, 2003.

[231] F. Trillaud, K. Berger, B. Douine, and J. Lévêque, “Distribution of current density, temperature, and mechanical deformation in YBCO bulks under field-cooling magnetization,” *IEEE Trans. Appl. Supercond.*, vol. 28, no. 4, p. 6800805, 2018.

[232] K. Zhang, M. Ainslie, M. Calvi, S. Hellmann, R. Kinjo, and T. Schmidt, “Fast and efficient critical state modelling of field-cooled bulk high-temperature superconductors using a backward computation method,” *Supercond. Sci. Technol.*, vol. 33, no. 11, p. 114007, 2020.

[233] F. J. Ridgeon, M. J. Raine, D. P. Halliday, M. Lakrimi, A. Thomas, and D. P. Hampshire, “Superconducting properties of titanium alloys (Ti-64 and Ti-6242) for critical current barrels,” *IEEE Trans. Appl. Supercond.*, vol. 27, no. 4, p. 4201205, 2017.